Dynamics of Ultralight Flexible Spacecraft during Slew Maneuvers

Thesis by
Michael A. Marshall

In Partial Fulfillment of the Requirements for the
Degree of
Doctor of Philosophy

CALIFORNIA INSTITUTE OF TECHNOLOGY
Pasadena, California

2022
Defended 14 February 2022

Michael A. Marshall
ORCID: 0000-0002-4259-2484

ACKNOWLEDGEMENTS

A good friend is partial to saying that a PhD is primarily an exercise in tenacity. While I agree that tenacity is important, I think equally important are the contributions of the family, friends, colleagues, and collaborators who help along the way.

First and foremost, I want to thank my advisor, Professor Sergio Pellegrino, for his dedication to my both my personal and professional development. I still vividly remember meeting Sergio for the first time. He invited me to a Skype meeting after I submitted my application to Caltech for graduate school. After our conversation, I remember thinking something to the effect of, "Well there goes any chance I may have had to go to Caltech." To this day, I am not entirely sure what compelled Sergio to invite me to Caltech and welcome me into his research group, but I am very glad he did. If I use ultralight flexible spacecraft as a metaphor for my research, then Sergio maneuvered the spacecraft in such a way as to excite interesting and non-trivial dynamics while simultaneously providing sufficient feedback to prevent loss-of-control. From the very beginning, Sergio encouraged me to explore my own ideas and take charge of my research, which led to several interesting collaborations and significant contributions in areas beyond the scope of this thesis. In doing so, he pushed me to step out of my comfort zone and to strive for excellence in everything that I do. I am privileged to call Sergio both a mentor and a friend, and I look forward to continuing to cross paths with him in the future.

Next, I want to extend a special thanks to the members of my candidacy and defense committees: Professors Bobby Braun, Dan Meiron, Domniki Asimaki, Sigrid Leyendecker, and Soon-Jo Chung. Their contributions to my research have been invaluable, and I have done my best to incorporate their insights and suggestions here. I have particularly enjoyed my semi-irregular research meetings with Sigrid over the last year and a half. Sigrid has the uncanny ability to distill complex mathematical subjects into remarkably simple and intuitive explanations. Our collaboration has taught me most of what I know about the theory underlying discrete mechanics and variational integrators, and I hope we have the opportunity to collaborate again in the future.

I also want to thank Professors Harry Atwater and Ali Hajimiri, Sergio's co-investigators for the Caltech Space Solar Power Project (SSPP), along with the

rest of the SSPP team. The SSPP has been a compelling application for much of my research, and consequently, I am grateful for the team's many helpful comments and discussions about my work. I have likewise appreciated how the team's biweekly meetings have challenged me to think critically and creatively about the design and implementation of complex engineering systems. Dr. Rich Madonna, the Project Manager for the SSPP, deserves a special mention. I have had the pleasure of collaborating extensively with Rich on problems related to systems engineering and optimization of space solar power satellites. Incidentally, our collaboration has also taught me most of what I know about systems engineering. I am looking forward to continuing our conversations in Maryland.

I am thankful to have had the opportunity to collaborate with the Structural Dynamics Branch at NASA Langley Research Center as part of my NASA Space Technology Research Fellowship. In particular, I want to thank Dr. Keats Wilkie, Dr. Jay Warren. Dr. Olive Stohlmann, Dr. Matt Chamberlain, and Sarah Cook for being gracious hosts during my three Visiting Technologist Experiences, including my virtual Visiting Technologist Experience at the height of the COVID-19 pandemic. I thoroughly enjoyed working with and learning from all of you. My only regret is that we did not have more time to spend working together.

Caltech's greatest strength is its people. With that being said, I want to thank my wonderful colleagues and collaborators from the Space Structures Laboratory, both past and present, for their steadfast support, encouragement, and friendship. In particular, I want to acknowledge the contributions of Dr. Ashish Goel, Dr. Dan Scharf (an honorary member of the Space Structures Laboratory from JPL), Dr. Thibaud Talon, Gianfranco Canales, Dr. Antonio Pedivellano (our resident Abaqus master), and Dr. Jay Warren (another honorary member of the Space Structures Laboratory, this time from NASA Langley). Ashish and Dan taught me numerical trajectory optimization during my first forays into research, work that ultimately led to several publications on power-optimal guidance for space solar power satellites. Among other contributions, my conversations with Dan were also instrumental in helping me conceptualize the slew maneuver requirements introduced in Chapter 3. Thibaud introduced me to floating frame of reference formulations for flexible multibody dynamics. In doing so, he helped teach me many of the fundamentals that were incorporated into the finite element formulations in Chapters 5 and 6. Gianfranco suggested vectorizing the subsequent MATLAB® implementations of these finite elements. This saved me countless hours and was critical for realizing

the dynamic simulations in Chapter 8. Antonio developed the original Abaqus finite element model of the strips used in Chapter 7. He subsequently spent untold hours helping me modify his model for the homogenization studies described in this thesis. Jay suggested the two-step eigenanalysis algorithm for symmetric structures described in Chapter 7. Last but not least, I want to recognize my academic brother, Dr. Charles (Charlie) Dorn, for all his contributions to my Caltech experience, both inside and outside the lab.

I was fortunate to receive an invitation to the "Non-Nuclear Exploration of the Solar System" workshop organized by the W. M. Keck Institute for Space Studies in April 2021. This thesis benefited from ideas and discussions with Mike Paul Hughes from JPL and the other participants at the workshop.

The GALCIT Colloquia were a frequent source of inspiration for my research. Two colloquia stood out in particular. Professor Steve Brunton's colloquium (and the free download of his then-new textbook) introduced me to nonlinear, data-driven model reduction. At the time, I was studying nonlinear model reduction methods for geometrically nonlinear structural dynamics, and this gave me new insights into my problem. Professor Zac Manchester's colloquium and our subsequent discussions then introduced me to Lie group methods for describing rotations in 3D space. This later influenced parts of Chapters 5 and 6 in this thesis.

Many thanks to the GALCIT staff, especially Christine Ramirez, for making my problems disappear. It is not an understatement to say that many of us graduate students would be lost without them.

I am grateful to the Caltech Space Solar Power Project and NASA for financially supporting my research, the latter via a NASA Space Technology Research Fellowship. I likewise appreciate the fellowship from the Graduate Aerospace Laboratories of the California Institute of Technology (GALCIT) that supported me during my first year at Caltech.

I owe many thanks to Professors Jim Craig and Glenn Lightsey from Georgia Tech for their encouragement to go to graduate school and their tremendous support and mentorship over the years. Similarly, I am grateful for my friendship with Professor Keith Schwab at Caltech. Keith has not only been a staunch mentor for me, but he has also been the only other person at Caltech that I can nerd-out about soaring with.

I have had the pleasure of sharing my Caltech journey with many outstanding friends. I specifically want to mention Aayush Sharma, Alex Miller, and Kayla Watson, for

always being there when I needed it (I do not think I would be the same person today without the three of you); Ashish Goel and Charles Dorn, adventure buddies extraordinaire; the Monday night pizza crew: Lucia de Rose, Jeremy Bernstein, Stefan Lohaus, and later, Tristan Faschinger (I am still disappointed that pizzas are no longer $5, although the company certainly makes up for it); my GALCIT friends: Akshay Sridhar, Fabien Royer, Maria Sakovsky, Matt Leibowitz, Matt Schwab, and Serena Ferraro; and my soaring family: Rich Owen and the Zimmermans, Leigh and Sam. Forgive me if I have forgotten anyone. I hope this experience has not made me too much grumpier and more cynical. I likewise want to acknowledge Caltech's awesome trail running community, which has been a significant part of my social life in Pasadena. The Alpine Club trail runs have without a doubt been one of the things I looked forward to most each week. Additionally, I must recognize the certifiable badasses in the "Breakfast Club": Alice Baumgartner, Andrew Erwin, Andy Boyle, Aubrey Schonhoff, Brayden Aller, Cameron Hummels, Dan van Beveren, Emily Geyman, Jack Sayers, Kat de Kleer, Maria Carilli, Max Saccone, Noel Csomay-Shanklin, and Robert Webber. I am going to miss running and breakfasting with you all, but I know we have many more adventures together to look forward to.

None of this would have been possible without the support of my family: my parents, Donald and Heather Marshall; my brother, Dr. Ryan Marshall (a Caltech Applied Physics PhD); and my grandparents, Anne and Murray Pasternack. They have been and continue to be my biggest supporters. This thesis belongs as much to them as it does to me. Mom and Dad, I think it is safe to say that all the science camps, flying lessons, and my general shenanigans have paid off! My grandma Anne has always been my biggest cheerleader, and while I am sorry you are not here to celebrate my graduation with me, I know you are out there somewhere bragging to anyone and everyone who is willing to listen about your two grandsons with Caltech PhDs! This thesis is dedicated to you.

Lastly, I owe a debt of gratitude to Dr. Stephen Wolfram, for without *Mathematica*, none of this would have been possible.

ABSTRACT

Traditional spacecraft design paradigms rely on stiff structures with comparatively flexible appendages. More recent trends, however, trade deployed stiffness for packaging efficiency to stow increasingly large-area apertures inside existing launch vehicles. By leveraging recent advances in materials and structures, these ultralight, packageable, and deployable spacecraft, hereafter referred to as *ultralight flexible spacecraft*, are up to several orders of magnitude lighter and more flexible than the current state-of-the-art. They promise to deliver higher performance for a wide range of applications, but this comes at a cost, in this case, due to their very low-frequency structural dynamics. Structural dynamics can negatively interact with spacecraft attitude control systems and degrade pointing performance. These developments motivate the main objective of this thesis: to demonstrate the feasibility and limitations of maneuvering next-generation ultralight flexible spacecraft.

The thesis first proposes a framework that uses reduced-order modal models to determine structure-based performance limits for flexible spacecraft slew maneuvers. The framework fuses space mission requirements with the dynamic properties of a structure to produce slew time estimates tailored for specific missions and applications, leading to higher-performance, less-conservative spacecraft and mission designs. This aims to provide spacecraft designers with a preliminary design tool capable of answering the question of how fast flexible spacecraft can be slewed without excessive vibrations.

The thesis then turns to the development of a flexible multibody dynamics finite element model of a representative ultralight flexible spacecraft. The representative spacecraft uses the modular and scalable structural architecture developed by the Caltech Space Solar Power Project (SSPP). The SSPP architecture consists of slender, thin-shell structures, called strips, attached to diagonal booms via joints and assembled into a square aperture. For increased computational tractability, each strip is replaced with an equivalent beam model derived using an energy-equivalence-based homogenization procedure. The booms and strips are discretized using geometrically exact beam finite elements. Unlike many conventional elements, these elements are based on a quaternion parameterization of rotations and a spatial discretization that preserves the physical structure of the 1D continuum strain measures. This leads to an objective finite element formulation, i.e., a formulation invariant to superposed rigid body motions. Objectivity is important for simulating the large

rotations that occur during slew maneuvers. The same spatial discretization is then used to develop a quaternion variational integrator for the dynamics of geometrically exact beams in flexible multibody systems in order to take advantage of its structure-preserving properties in slew maneuver simulations. A procedure for designing booms for the expected slew maneuver loads is discussed, and a parametric modal analysis is used to investigate how structural design parameters affect the spacecraft's dynamic properties at different length scales.

A reduced-order modal model is subsequently derived from the flexible spacecraft finite element model and used to estimate structure-based slew maneuver performance limits. These estimates are validated using geometrically nonlinear simulations of slew maneuver dynamics with the full finite element model. Two integrators are used: a Lie group generalized-α method representative of standard structural dynamics integrators and a variational integrator. The results are somewhat unexpected: the generalized-α method exhibits better numerical stability than the variational integrator, even for long-duration slew maneuvers. The results also demonstrate that contrary to common assumptions, other constraints impose more restrictive limits on slew performance than the dynamics of the structure. Using attitude control system performance as an example, they show that the available momentum and torque are often significantly more limiting than the structure. Consequently, these results have significant implications for spacecraft design. In particular, they suggest that spacecraft structures can either be (i) maneuvered significantly faster, assuming suitable actuators are available, or (ii) built using lighter-weight, less-stiff, and lower-cost construction that moves the structure-based slew performance limits closer to those of the rest of the system. Thus, there is a significant opportunity to design less-conservative, higher-performance space systems.

PUBLISHED CONTENT AND CONTRIBUTIONS

[1] M. A. Marshall, R. G. Madonna, and S. Pellegrino, "Investigation of Equatorial Medium Earth Orbits for Space Solar Power," *IEEE Transactions on Aerospace and Electronic Systems*, 2021. DOI: 10.1109/TAES.2021.3122790,

M. A. Marshall developed and implemented the power-optimal guidance for constellations of space solar power satellites and helped write the manuscript.

[2] M. A. Marshall and S. Pellegrino, "Reduced-Order Modeling for Flexible Spacecraft Deployment and Dynamics," in *AIAA SciTech Forum*, AIAA 2021-1385, Virtual Event, 2021. DOI: 10.2514/6.2021-1385,

M. A. Marshall developed and implemented both the full-order model and the reduced-order modeling approach, performed the simulations, and wrote the manuscript. AIAA Spacecraft Structures Best Paper Award Winner.

[3] M. A. Marshall, A. Goel, and S. Pellegrino, "Power-Optimal Guidance for Planar Space Solar Power Satellites," *Journal of Guidance, Control, and Dynamics*, vol. 43, no. 3, pp. 518–535, 2020. DOI: 10.2514/1.G004643,

M. A. Marshall developed the theoretical framework and implemented the numerical algorithm for power-optimal guidance, conducted the systems study, and wrote the manuscript.

[4] M. A. Marshall, A. Goel, and S. Pellegrino, "Attitude maneuver design for planar space solar power satellites," in *29th AAS/AIAA Space Flight Mechanics Meeting*, AAS 19-287, Ka'anapali, Maui, Hawaii, 2019,

M. A. Marshall developed and implemented the trajectory optimization algorithm, analyzed the results, and wrote the manuscript.

TABLE OF CONTENTS

Chapter 1

INTRODUCTION

1.1 Background and Motivation

Since the dawn of the Space Age, structural dynamics has been an important consideration in the design and operation of spacecraft, particularly for spacecraft stability and control. In 1958, the Jet Propulsion Laboratory at the California Institute of Technology flew Explorer 1, the first American satellite to reach low Earth orbit. Explorer 1 was intended to be passively spin-stabilized about its minimum axis of inertia. Unbeknownst at the time, this minor axis spin proved to be unstable due to the neglected effects of structural compliance in its whip antennas, specifically the energy dissipated by structural damping [1, 2]. Although Explorer 1 was widely regarded as a success, its anomalous attitude dynamics were a warning for future space missions.

Sixty years later, a dominant trend in spacecraft design trades deployed structural stiffness against packaging efficiency to facilitate the construction of higher-performing, lighter-weight, and lower-cost spacecraft with structures that unfurl into increasingly large-area apertures. In particular, advances in materials and structures are leading to the development of aggressive new structural architectures with very low areal mass densities that can best be characterized as ultralight, packageable, and (self-)deployable.[1]. Such spacecraft are hereafter referred to as *ultralight flexible spacecraft*. Whereas traditional spacecraft design philosophies rely on architectures with a stiff bus and comparatively flexible appendages, ultralight flexible spacecraft are inherently very flexible to allow increasingly large apertures to stow within the confines of existing launch vehicles. This leads to first natural frequencies that may be up to several orders of magnitude lower than the current state-of-the-art and introduces new spacecraft dynamics and control challenges. Ultralight flexible spacecraft are currently envisioned for a variety of applications, ranging from solar system exploration [10] and space science [11] to communications, power transfer, remote sensing [12], and space solar power [13].

[1] Self-deployable refers to spacecraft structures that deploy from a packaged configuration via strain energy release (see e.g., [3–6]), as opposed to via mechanical actuation. Ultralight flexible spacecraft typically deploy via either strain energy release or a hybrid scheme (see e.g., [7, 8]), although there are exceptions, e.g., solar sails [9].

Spacecraft require maneuvers to change their orbits and orientations. A *slew maneuver* normally refers to any maneuver that changes a spacecraft's orientation. Large-angle slew maneuvers in particular are common, e.g., for reorienting high-gain antennas, solar arrays, and thrust vectors. Unlike a rigid spacecraft, i.e., a spacecraft that can be modeled as a rigid body, maneuvering a flexible spacecraft excites structural dynamics which can perturb its motion, interact with its attitude control system, and degrade its pointing performance. In some cases, structural dynamics can even lead to instabilities and loss-of-control.

Classical approaches for mitigating the effects of structural dynamics usually involve either maneuvering the spacecraft sufficiently "slowly" to reduce the excitation, or delaying operations with stringent pointing requirements until structural damping dissipates any vibrations. Both become increasingly difficult as the spacecraft's flexibility increases because the associated maneuvering and settling times also increase. This decreases the time available to a spacecraft for actually performing functions in support of its mission objectives. In particular, for sufficiently flexible spacecraft, the maneuvering and settling times may become prohibitively long. This emphasizes the importance of characterizing the dynamics of these spacecraft and developing new approaches for their subsequent mitigation. However, large space structures are notoriously difficult to test in representative 0-g environments before launch [14–18]. As a result, computational approaches play an outsize role in characterizing their structural dynamics and demonstrating that they are stable and controllable throughout their expected flight envelopes.

Modeling and simulation of flexible spacecraft dynamics are perennial problems plaguing spacecraft designers. Unsurprisingly, these modeling and simulation problems increase in difficulty as both the spacecraft size and flexibility increase. Several characteristics of ultralight flexible spacecraft further compound these challenges. For example, large size, low stiffness, and symmetry lead to very low (potentially sub-millihertz) natural frequencies with many closely spaced vibration modes. The resulting low-frequency structural dynamics can couple with the spacecraft's rigid body dynamics. Low stiffness can likewise lead to geometrically nonlinear elastic deformations due to environmental and inertial loads. Altogether, these challenges dictate the use of large-scale, geometrically nonlinear finite element models with sufficient fidelity to capture dynamic effects at multiple length and temporal scales.

Due to the importance of structural dynamics in spacecraft design, flexible spacecraft dynamics have been extensively studied in the literature; see e.g., [1, 19–22].

However, ultralight flexible spacecraft are largely new territory. As a result, this thesis aims to address several open problems related to the dynamics of ultralight flexible spacecraft.

1.2 Research Objectives

The main objective of this thesis is to demonstrate the feasibility and limitations of maneuvering next-generation ultralight flexible spacecraft. To that end, this thesis develops computational tools with varying degrees of fidelity for modeling ultralight flexible spacecraft dynamics. The computational tools span a breadth of applications, from preliminary design and analysis all the way to on-orbit operations and slew maneuvers. As a case study, the thesis focuses on the slew maneuver dynamics of a representative ultralight flexible spacecraft based on the Caltech Space Solar Power Project (SSPP) structural architecture [13].

This thesis specifically addresses the following four research objectives:

1. Development and validation of a framework for quantifying minimum slew times

A common assumption about flexible spacecraft is that their structures limit how fast they can be slewed. For highly compliant structures, very long slew times can make an otherwise promising mission infeasible. As a result, it is important to demonstrate the feasibility of slewing large flexible spacecraft early in the design process. However, there is no standard framework for rigorously quantifying how fast flexible spacecraft can be slewed. The most common heuristic states that the minimum slew time must be at least ten times the structure's lowest natural period. Such a heuristic is convenient but may lead to overly conservative, and in some cases, prohibitively conservative spacecraft designs and mission scenarios.

For these reasons, an important goal of this thesis is to propose and validate a framework for rigorously quantifying minimum slew times at the beginning of the space mission design cycle. For such a framework to be useful, it must use quantitative performance metrics rooted in a space mission's requirements and account for the dynamic properties of a spacecraft's structure, not simply its natural frequencies. It likewise must be sufficiently simple to use during preliminary design and sufficiently scalable to take advantage of the higher-fidelity finite element models available at later stages of the design cycle. Lastly, it must be applicable to a wide range of space mission concepts, from large conventional spacecraft with flexible appendages all the way to next-generation ultralight flexible spacecraft. Ultimately, fusing space mission requirements with the dynamic properties of a structure yields

slew time estimates that are tailored for specific missions and applications, leading to higher-performance, less-conservative spacecraft and mission designs. These slew time estimates are likely to be valuable for identifying the flexible spacecraft architectures most suitable for specific mission concepts and vice versa.

2. Tradeoffs between structural design and structural dynamic properties

It is well known that large space structures tend to have very low natural frequencies and many closely spaced vibration modes [23]. This can can make it difficult to ascertain which modes are the most dynamically significant, because, contrary to intuition, the most dynamically significant modes are not necessarily the lowest frequency ones. It is less well known that scaling a space structure from a smaller scale to a larger one may change which types of modes are the most dynamically significant. In other words, what is dynamically significant at smaller scales may not necessarily be representative of what happens at larger ones. This highlights an important practical challenge, namely that it is difficult to extrapolate the dynamic properties of smaller-scale test articles to those of a full-scale flight system. Thus, as spacecraft become larger and more flexible, it becomes increasingly important to understand how their structural designs influence their dynamic properties.

Unlike many other ultralight flexible spacecraft concepts, the SSPP architecture studied in this thesis uses bending-stiff elements to support the integration of functional elements. For this reason, the SSPP architecture is characteristic of a class of ultralight flexible spacecraft referred to as bending architectures [24], i.e., spacecraft structural architectures that derive their load carrying capacities from bending stiffness. While commonly used for large solar array wings on conventional spacecraft, bending architectures tend to be outliers among ultralight flexible spacecraft concepts. Consequently, their dynamic properties are not well understood. Motivated by these deficiencies, an objective of this thesis is to investigate the relationship between three important structural design parameters for the SSPP architecture — boom stiffness, areal density, and spacecraft size — to both improve the understanding of how its structural design affects its dynamic properties and to reveal potentially useful design insights for other similar structural concepts.

3. Prediction of slew maneuver dynamics using finite element models

Verification and validation of ultralight flexible spacecraft dynamics requires high-fidelity finite element models, both to counterbalance the difficulties associated with ground testing large space structures [14–18] and to reduce the risks associated with

high-performance maneuvers and complex on-orbit operations. In particular, finite element models capable of accurately predicting ultralight flexible spacecraft dynamics can reduce conservatism in mission planning by mitigating the uncertainties associated with higher-performance, i.e., faster, slew maneuvers. However, these simulations pose challenges due to the low stiffnesses, very low-frequency dynamics, and long time scales involved.

These challenges motivate the use of geometrically nonlinear finite element models that accurately describe large linear-elastic deformations and coupling between rigid body and flexible dynamics. They likewise suggest a requirement for time integration methods that exhibit excellent long-duration numerical stability. For these reasons, the thesis aims to demonstrate the use of geometrically nonlinear finite element models to predict the slew maneuver dynamics of a representative ultralight flexible spacecraft. It specifically focuses on moderate-fidelity simulations that are useful as both a proof-of-concept and for preliminary design trade studies, but the fundamental ideas are scalable to the higher-fidelities required for actual flight systems.

4. Demonstration of structure-preserving integrators for larger-scale finite element models

Structure-preserving integrators refer to numerical methods that respect the underlying physics of a problem. Most standard structural dynamics integrators, e.g., the generalized-α method [25], are not structure-preserving. Instead, they introduce artificial numerical dissipation to damp the high-frequency oscillations that often appear in the solution of numerically stiff differential equations. While this tends to increase the integrator's stability, it can also introduce pathological behaviors into a simulation, e.g., non-physical energy decay. Unlike standard structural dynamics integrators, structure-preserving ones are often able to achieve both stability and excellent long-term energy behavior without numerical dissipation.

Applications that require high-fidelity simulations of complex, nonlinear phenomena are increasingly turning to structure-preserving integrators. However, a recent review paper [26] stresses that most of the applications of structure-preserving integrators revolve around small-scale benchmark problems. Hence, it is unclear if and when structure-preserving integrators are useful for larger-scale engineering problems. Moreover, structure-preserving integrators often only preserve a subset of the physical properties of a system. For example, fixed-time step integrators are either symplectic-momentum conserving or energy-momentum conserving, but not both [27]. For this reason, it is often likewise unclear which properties of a physical

system are the most important to preserve with the integrator.

Simulating the low-frequency dynamics of ultralight flexible spacecraft inherently requires long-duration finite element simulations. As a result, ultralight flexible spacecraft dynamics are a possible engineering application that may benefit from the use of structure-preserving integrators. With this in mind, this thesis applies a specific type of structure-preserving integrator, a variational integrator [28, 29], to finite element simulations of ultralight flexible spacecraft dynamics. Variational integrators are a type of symplectic-momentum conserving integrator that inherit the structure of the underlying physical system and generally exhibit excellent long-term energy behavior. To evaluate the efficacy of these integrators, the thesis compares the performance of a variational integrator with a more traditional structural dynamics integrator for simulating flexible spacecraft slew maneuvers.

1.3 Outline of Thesis

The remainder of this thesis is organized into the eight chapters outlined below:

Chapter 2 presents a motivating example that emphasizes the often contradictory design requirements for ultralight flexible spacecraft. In particular, it describes a space solar power concept that requires ultralight flexible spacecraft with fast slew maneuver capabilities.

Chapter 3 proposes a framework for calculating slew times for flexible spacecraft. The chapter discusses canonical modeling approaches for flexible spacecraft dynamics, along with mode selection and the use of the Craig-Bampton method [30, 31] to transform complex finite element models into reduced-order modal models suitable for slew time calculations and attitude control system (ACS) analysis and design. Implementing and validating this framework requires a finite element model of a flexible spacecraft. Much of the remainder of the thesis is devoted to the development of such a model for a representative ultralight flexible spacecraft based on the Caltech SSPP architecture [13].

Chapters 4, 5, and 6 describe the geometrically exact beam finite elements and associated numerical methods implemented in the finite element model of the representative ultralight flexible spacecraft. Together, these chapters are self-contained, and hence, can be read independently of the rest of the thesis. Chapter 4 specifically reviews the quaternion parameterization of the 3D rotation group SO(3) and Reissner-Simo geometrically exact beam theory (GEBT) [32–34]. This provides the requisite background for Chapters 5 and 6. From there, Chapter 5 develops a

new quaternion-based geometrically exact beam finite element based on a structure-preserving spatial discretization. The spatial discretization accounts for the Lie group structure of $\mathrm{SO}(3)$ and leads to a strain-invariant finite element formulation, i.e., a formulation invariant to superposed rigid body motions. This is important for simulating the large rotations involved in flexible spacecraft slew maneuvers. Chapter 6 then uses this spatial discretization to derive a quaternion-based variational integrator for simulating the dynamics of geometrically exact beams.

Chapters 7 and 8 return to the problem of ultralight flexible spacecraft dynamics. Chapter 7 specifically describes the development and implementation of a flexible multibody dynamics finite element model of a representative ultralight flexible spacecraft based on the Caltech SSPP architecture. In doing so, it derives equivalent beam models for the thin-shell, ladder-like "strips" [35] that are a building block of the SSPP architecture. It then designs the booms that support the strips for the expected inertial loads during slew maneuvers. The equivalent beam models and boom designs feed into a parametric modal analysis that seeks to understand how the spacecraft's structural design influences its dynamic properties as functions of its size, areal mass density, and boom stiffness.

Chapter 8 studies the slew maneuver dynamics of the representative ultralight flexible spacecraft. It combines the framework from Chapter 3 with the modal analysis from Chapter 7 to estimate slew times for the reference spacecraft at different length scales. Comparisons are then made with slew time limits derived from representative ACS capabilities. From there, geometrically nonlinear finite element simulations validate the slew time predictions and reveal important insights into the spacecraft's slew maneuver dynamics. Finally, the chapter uses the slew maneuver simulations to compare the performance of a more traditional structural dynamics integrator, the Lie group generalized-α method [36–38], with the performance of the variational integrator from Chapter 6.

Lastly, Chapter 9 summarizes the important conclusions from the thesis and outlines possible directions for future research.

1.4 Note on Notation

Throughout this thesis, the prefix δ denotes infinitesimal variations. Gradients use the numerator-layout (Jacobian) convention; i.e., for a function $f(\mathbf{x}) : \mathbb{R}^n \to \mathbb{R}$, $\partial f/\partial \mathbf{x} \in \mathbb{R}^{1\times n}$. The symbols $\mathbf{I}_{n\times n}$ and $\mathbf{0}_{m\times n}$ denote the identity and null matrices in $\mathbb{R}^{n\times n}$ and $\mathbb{R}^{m\times n}$, respectively. In general, prime notation denotes (scalar) derivatives

of a function with respect to its argument; e.g., $f'(x) = \mathrm{d}f/\mathrm{d}x$ for a function $f(x) : \mathbb{R} \to \mathbb{R}$. Likewise, dot notation denotes derivatives with respect to the time variable t; e.g., $\dot{x} = \mathrm{d}x/\mathrm{d}t$ for $x \in \mathbb{R}$. Boldface letters signify vectors and matrices.

Chapter 2

A MOTIVATING EXAMPLE: SPACE SOLAR POWER

The work presented in this chapter is based on the following publications:

M. A. Marshall, A. Goel, and S. Pellegrino, "Attitude maneuver design for planar space solar power satellites," in *29th AAS/AIAA Space Flight Mechanics Meeting*, AAS 19-287, Ka'anapali, Maui, Hawaii, 2019.

M. A. Marshall, A. Goel, and S. Pellegrino, "Power-Optimal Guidance for Planar Space Solar Power Satellites," *Journal of Guidance, Control, and Dynamics*, vol. 43, no. 3, pp. 518–535, 2020. DOI: 10.2514/1.G004643.

2.1 Introduction

The purpose of this chapter is to describe a space mission concept that requires ultralight flexible space vehicles with fast slew maneuver capabilities. The space mission concept is the novel space solar power station architecture originally introduced by the Caltech Space Solar Power Project (SSPP)[1] in [13]. Preliminary studies of formation flying for this concept [41, 42] identify the requirement for a fast slew maneuver capability, whereas more recent works [39, 40] present detailed studies of these maneuvers and how they influence overall system efficiency.

Space solar power involves collecting solar power in space and wirelessly transmitting it to Earth. Compared to terrestrial solar power, it is advantageous because (i) it separates power generation from both terrestrial weather and diurnal and seasonal cycles, and (ii) it can dispatch power to almost any location on Earth at any time.

The original idea for space solar power dates to 1941 and is the stuff of science fiction [43]. Two decades passed before P. E. Glaser proposed what is widely regarded as the first engineering concept for a space solar power satellite [44]. In subsequent years, the engineering community proposed a variety of space solar power concepts (see e.g., [45–47]), most of which can be considered variations of Glaser's original concept. The defining characteristics of these "classical" concepts are the use of large, monolithic spacecraft and either mechanically steerable solar arrays, antennas, or reflectors that decouple antenna steering from sun pointing.

[1] https://www.spacesolar.caltech.edu/

In 2016, under the leadership of Professors Harry Atwater, Ali Hajimiri, and Sergio Pellegrino, the Caltech SSPP proposed a fundamentally different approach to space solar power [13]. The SSPP concept replaces the complex, monolithic satellites characteristic of classical concepts with a formation-flying phased array of ultralight flexible spacecraft, multiple of which can be packaged for launch in a single launch vehicle and self-deployed in space. By doing so, it aims to achieve economic viability by reducing the mass, cost, and complexity of the space-based power station by upwards of an order of magnitude compared to more classical concepts. This entails the use of simple structural architectures constructed out of ultralight, thin shells with low deployed stiffness.

A defining feature of the SSPP structural architecture is that it is plate-like (planar). Planarity facilitates efficient packaging [13]. However, it also couples the problems of orienting the photovoltaics towards the Sun and pointing the radio frequency (RF) beam towards the Earth. This coupling motivates the requirement for a fast slew maneuver capability. More specifically, this coupling results in a requirement for power-optimal guidance [40], i.e., orientation trajectories that maximize the power transmitted by the space solar power station. The power-optimal guidance solutions reveal that a fast slew maneuver capability maximizes the average transmitted power.

The modular, scalable space solar power architecture proposed by the Caltech SSPP is depicted in Fig. 2.1. The fundamental unit in the SSPP concept is referred to as a "tile" [12, 48, 49]. Each tile is an approximately 10 cm $\times$ 10 cm, multi-layer, flexible sandwich structure that integrates photovoltaic (PV) cells, direct current (DC) to RF converters, and microwave antennas — all the equipment required to independently collect sunlight and transmit it to Earth. Tiles are integrated into approximately 1 m-wide supporting structures called "strips" [35], which are then incorporated into a nominally 60 m $\times$ 60 m spacecraft (the "module"). The power station consists of a constellation of formation flying spacecraft operating as a single phased array [41, 42]. To eliminate PV shadowing by adjacent spacecraft, the spacecraft maintain their positions and orientations in a fixed plane [41, 42]. Thus, the power station in aggregate shares the same orientation as the individual spacecraft.

The baseline tile from the original SSPP concept [13] consists of two main layers: a top PV layer that converts sunlight into DC electrical power, and a bottom RF layer that converts DC electrical power into RF power radiated by patch antennas. This baseline tile architecture is referred to as single-sided PV, single-sided RF (PV1RF1). The performance of a power station with PV1RF1 tiles is constrained by

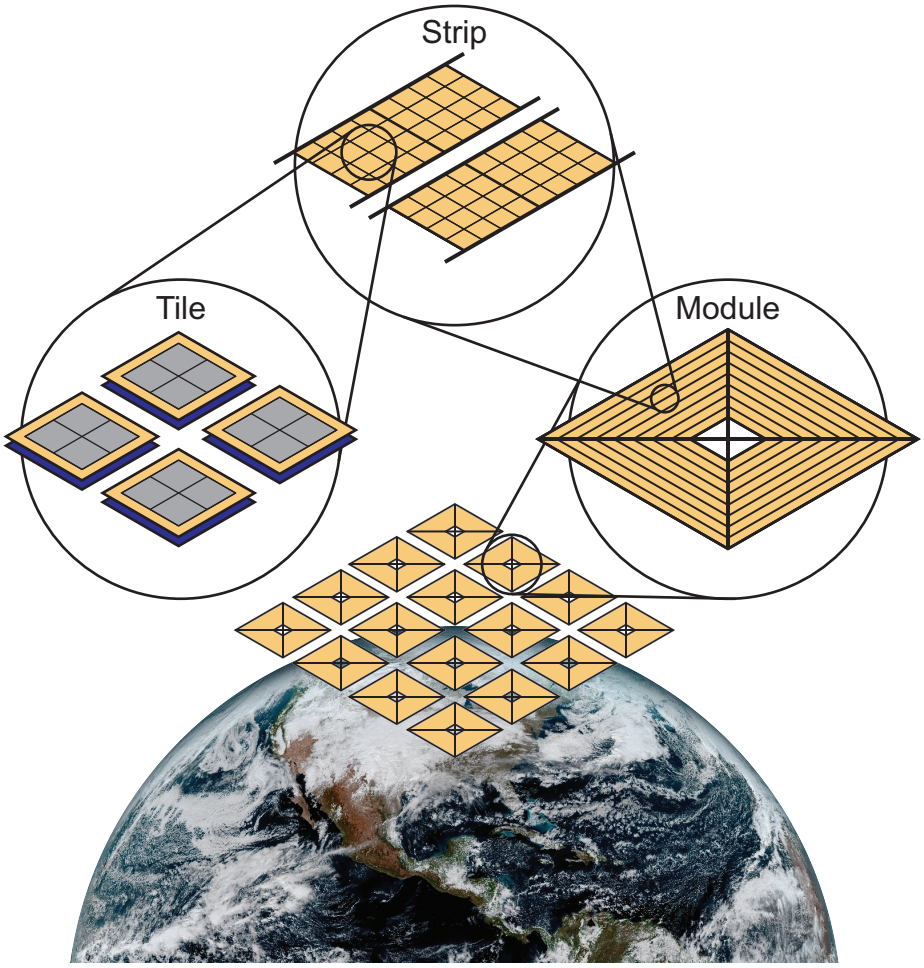

Figure 2.1: Overview of Caltech Space Solar Power Project concept originally introduced in [13].

the orbit geometry [40]. Hence, higher performance requires the use of a dual-sided tile. One possible dual-sided tile adds a layer of RF-transparent PV cells to the RF layer of the baseline tile. This modified tile is referred to as dual-sided PV, single-sided RF (PV2RF1). Dual-sided tiles facilitate uninterrupted power transfer when the receiving station falls between the Sun and the power station. Consequently, the use of a dual-sided tile can increase the overall system efficiency by upwards of 50% [40]. The two tile architectures are sketched in Fig. 2.2. Due to its higher efficiency, this chapter exclusively considers a PV2RF1 tile.

The goal of the remainder of this chapter is to demonstrate why the Caltech SSPP concept requires a fast slew maneuver capability. To that end, it calculates the power-optimal guidance for a representative mission scenario, that of a single power station in a geostationary Earth orbit (GEO) transmitting to a single receiving station. The

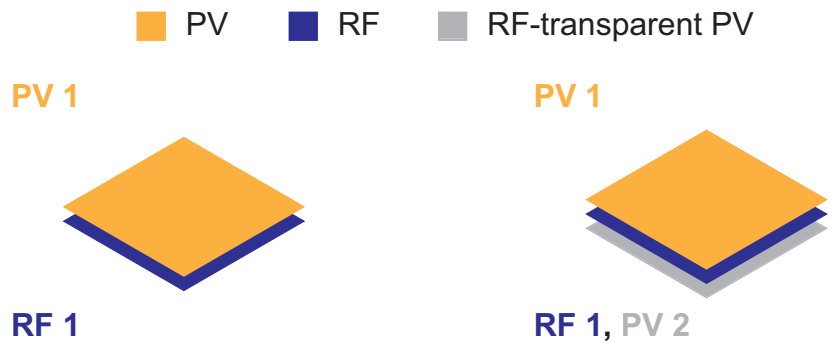

(a) (b)

Figure 2.2: Tile layering schematics for (a) single-sided PV, single-sided RF (PV1RF1) and (b) dual-sided PV, single-sided RF (PV2RF1).

chapter is organized as follows: Sec. 2.2 describes the orbit geometry and the power transmission model. Sec. 2.3 calculates the power-optimal guidance. Sec. 2.4 then briefly summarizes the chapter and how it fits into the rest of the thesis.

2.2 Problem Geometry and Power Transmission Model

This section describes the simplified geometric framework and power transmission model used for the power-optimal guidance calculations in Sec. 2.3. Unlike previous studies [39, 40], this section models the nonlinear power input-output relationship for a representative RF integrated circuit (RFIC) responsible for converting DC electrical power from the PV cells into RF output power.

The power-optimal guidance considers a power station in a circular, equatorial, geostationary Earth orbit (GEO) transmitting to an equatorial receiving station; see Fig. 2.3. In GEO, the power station's angular rate around the Earth equals the Earth's rotation rate about its axis (15 deg/hour). As a result, the power station's position appears fixed with respect to the receiving station. For simplicity, the power and receiving stations are located at the same longitude. Following [39, 40], Fig. 2.3 assumes that the Earth's orbital position around the Sun is fixed at the vernal equinox. This allows the Sun's apparent motion to be neglected and reduces the general 3D orbit geometry to 2D where the Earth's equatorial plane is coplanar with a great circle of the Sun. Due to the fixed Earth-Sun geometry, an Earth-Centered Inertial (ECI) reference frame can be defined with its origin at the center of the Earth and the orthonormal basis vectors $\{\hat{\mathbf{x}}, \hat{\mathbf{y}}, \hat{\mathbf{z}}\}$. With these assumptions, $\hat{\mathbf{x}}$ points towards the Sun, i.e., parallel to the unit sun vector $\hat{\mathbf{s}}$, $\hat{\mathbf{z}}$ is parallel to Earth's axis, and $\hat{\mathbf{y}} = \hat{\mathbf{z}} \times \hat{\mathbf{x}}$. Since the Earth's equatorial plane is coplanar with the ecliptic, the

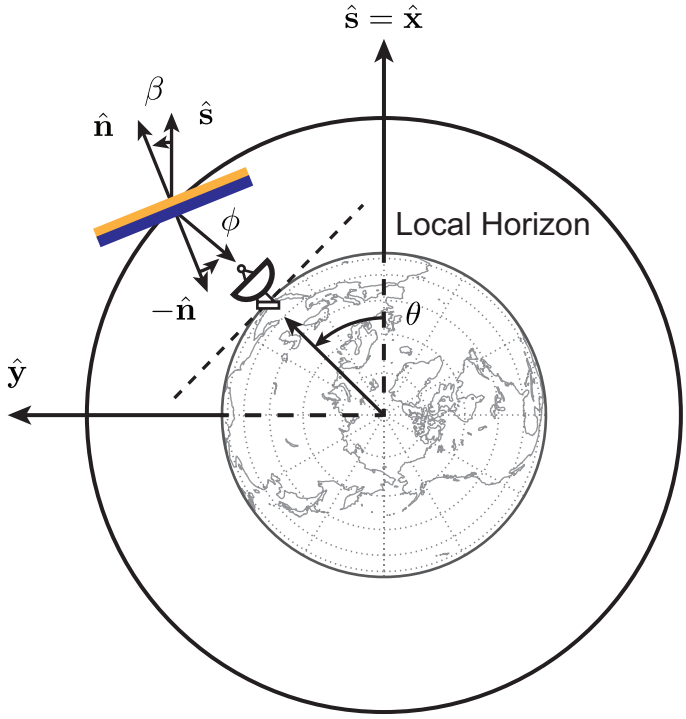

Figure 2.3: Problem geometry for a planar space solar power station in GEO. The power station's angular rate around the Earth is 15 deg/hour in GEO.

transmitted power is independent of Earth's axial tilt.

In 2D, the outward normal vector $\hat{\mathbf{n}}$ fully specifies the orientation of the power station. $\hat{\mathbf{n}}$ points outward from the power station's PV1 surface and is used to define the sun angle β and squint angle ϕ. β and ϕ are respectively the positive counterclockwise angles from $\hat{\mathbf{s}}$ to $\hat{\mathbf{n}}$ and from $-\hat{\mathbf{n}}$ to the slant vector pointing towards the receiving station.

Since the power station and receiving station are located at the same longitude, the angular position θ fully describes both of their positions in the ECI frame. Using the assumptions in this chapter, the relationship between β, ϕ, and θ is [40]

$$\beta + \phi = \theta \tag{2.1}$$

which is useful for writing the power-optimal guidance problem in Sec. 2.3 as a single-variable optimization problem.

Unlike previous studies [39, 40], this study neglects eclipsing. In GEO, eclipsing only occurs in the vicinities of the vernal and autumnal equinoxes. This assump-

tion contradicts the coplanarity assumption and results in an upper bound on the efficiency of the power station.

The power-optimal guidance calculations in Sec. 2.3 require an expression for the total transmitted power as a function of the orbital geometry, i.e., as a function β and ϕ. The total transmitted power is modified from [40] to account for the nonlinear power input-output relationship for the RFICs. These modifications result in the following expression for the total power transmitted by a single tile:

$$P_t(\beta, \phi) = \mathrm{IC}\left(W_{\mathrm{SF}} A_{\mathrm{PV}} \eta_{\mathrm{PV}} \,\mathrm{PV}(\beta)\right) \mathrm{RF}(\phi)\,\mathrm{AF}(\phi) \tag{2.2}$$

where

- W_{SF} is $1,361\ \mathrm{W/m^2}$ solar insolation (irradiance);
- A_{PV} is the effective PV area of a single tile (in this case, 72 mm × 72 mm);
- η_{PV} is the optical-to-electrical power conversion efficiency of the PV cells (assumed to be 25%, a value comparable to the current state-of-the-art for lightweight, low-cost space photovoltaics[2]);
- $\mathrm{PV}(\beta) = |\cos(\beta)|$ is the PV cell efficiency as a function of the sun angle for planar PV cells with unrestricted fields-of-view;
- $\mathrm{IC}(P_{\mathrm{in}})$ is the power input-output relationship for the RFICs (Fig. 2.4a);
- $\mathrm{RF}(\phi)$ is the efficiency of a single antenna in the phased array as a function of the squint angle (Fig. 2.4b); and
- $\mathrm{AF}(\phi) = |\cos(\phi)|$ is the phased array factor that accounts for the interactions between the antennas in the phased array [59, p. 283–333].

Here, the antenna efficiency $\mathrm{RF}(\phi)$ includes squint angle limits on the RF surface due to each antenna's limited field-of-view (the maximum squint angle in Fig. 2.4b is 76 deg) and the absolute values in $\mathrm{PV}(\beta)$ and $\mathrm{AF}(\phi)$ guarantee that $P_t \geq 0$.

[2] III-V multi-junction solar cells with efficiencies in excess of 30% are the current state-of-the-art for space photovoltaics [50]. However, III-V cells are expensive to manufacture [50] and require shielding to protect them from the high-energy particles responsible for radiation damage [51]. Moreover, despite the use of thin-film substrates (see e.g., [52]), the mass of the shielding fundamentally limits the specific power (i.e., the power per unit mass) achievable with III-V cells. Decreasing the cost per watt and increasing the specific power both require the use of lightweight photovoltaics, like perovskite [53–55] and nano-wire [56, 57] solar cells, that trade high efficiency for low cost and intrinsic radiation tolerance. State-of-the-art perovskite solar cells, for example, typically achieve maximum efficiencies on the order of 25% [55]. The economic viability of space solar power depends on low-cost, high specific power solar cells[58]

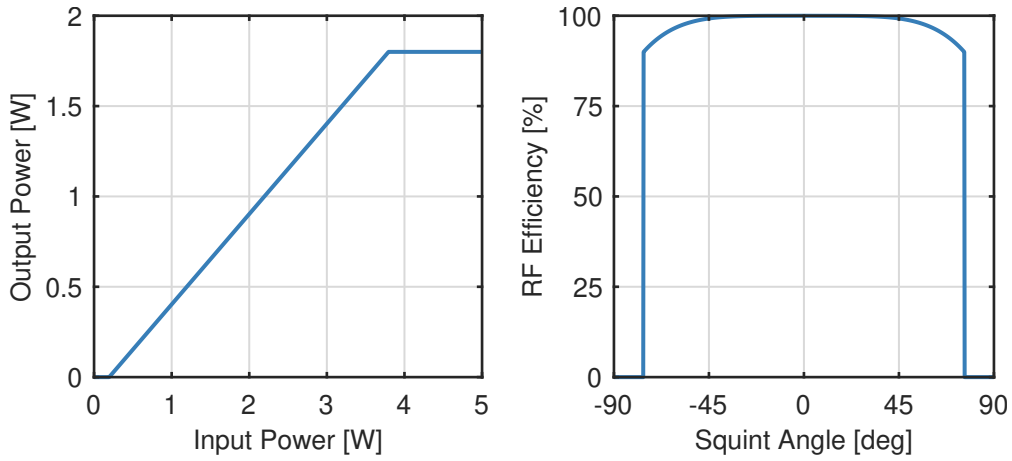

(a) (b)

Figure 2.4: (a) idealized power input/output relationship for high-performance RFICs and (b) antenna efficiency as a function of squint angle for near-isotropic patch antennas described in [48]. In (a), the RFICs turn on and saturate at input powers of 0.195 W and 3.795 W, respectively. In (b), the maximum allowable squint angle is 76 deg. These figures were produced using data provided by Dr. Austin Fikes and Professor Ali Hajimiri at Caltech.

To simplify Eq. (2.2) and the subsequent power-optimal guidance calculations, β is taken as the independent orientation variable and Eq. (2.1) is used to eliminate ϕ. Hence, the total transmitted power can be rewritten as

$$P_t(\beta) = \mathrm{IC}\left(W_{\mathrm{SF}} A_{\mathrm{PV}} \eta_{\mathrm{PV}}\, \mathrm{PV}(\beta)\right) \mathrm{RF}(\theta-\beta)\, \mathrm{AF}(\theta-\beta). \tag{2.3}$$

The instantaneous power transmission efficiency, i.e., the fraction of the total incident solar power $W_{\mathrm{SF}} A_{\mathrm{PV}}$ transmitted as RF output power, is then given by

$$\eta_t(\beta) = \frac{P_t(\beta)}{W_{\mathrm{SF}} A_{\mathrm{PV}}} \tag{2.4}$$

which is an input to the power-optimal guidance calculations in Sec. 2.3. Said another way, given 1 W of incident solar power, the power station transmits $\eta_t(\beta)$ W.

2.3 Power-Optimal Guidance

This section introduces and solves the power-optimal guidance problem for a power station in GEO.

The power-optimal guidance problem determines the optimal orientation trajectory $\beta^*(\theta)$ that maximizes the power transmitted to a receiving station. It is specifically defined as follows [40]:

$$\max_{\beta(\theta)} \quad \overline{\eta}_t(\beta(\theta)) \tag{2.5}$$

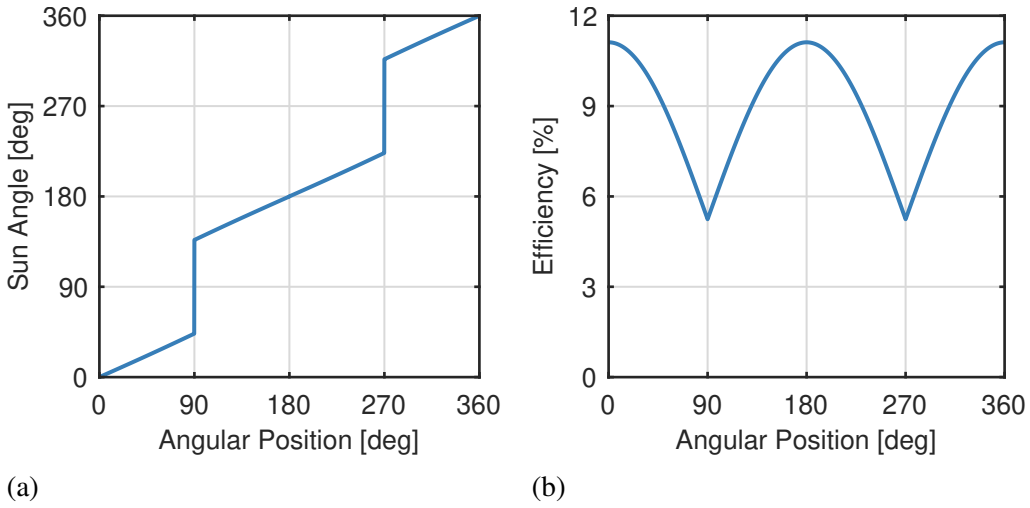

Figure 2.5: Power-optimal guidance for a PV2RF1 power station in GEO: (a) optimal orientation trajectory $\beta^*(\theta)$ and (b) power transmission efficiencies [Eq. (2.4)].

where $\overline{\eta}_t(\beta(\theta))$ is the orbit-averaged power transmission efficiency

$$\overline{\eta}_t = \frac{1}{2\pi} \int_0^{2\pi} \eta_t(\beta(\theta)) \, \mathrm{d}\theta \tag{2.6}$$

and $\eta_t(\beta(\theta))$ is the instantaneous power transmission efficiency [Eq. (2.4)]. Maximizing $\overline{\eta}_t$ maximizes $\eta_t(\beta(\theta))$ and the transmitted power [Eq. (2.3)].

Equation (2.5) is solved for a PV2RF1 power station in GEO using transcription and local optimization, as discussed in [40]. Transcription approximates the integral in Eq. (2.6) as a weighted sum over N discrete angular positions $\theta_k \in [0, 2\pi)$ for $k = 0, \ldots, N-1$ using a quadrature rule (in this case, a left Riemann sum). For each θ_k, the local optimizer then uses a grid search to identify the interval(s) containing the maximizer(s) of η_t, after which a gradient-free optimizer (a golden section search [60]) solves for the sun angle β_k^* that maximizes η_t. The gradient-free optimizer is necessary because η_t does not have continuous first derivatives.

Figures 2.5a and 2.5b depict the optimal orientation trajectory $\beta^*(\theta)$ and the corresponding power transmission efficiencies for the GEO-based power station. The optimal orientation trajectory consists of a single-axis slew maneuver at constant angular velocity punctuated by sharp, approximately 90 deg reorientation maneuvers twice per orbit. These reorientation maneuvers change the sun-pointed PV surface to minimize the local sun and squint angles, thereby maximizing the total transmitted power; see Fig. 2.6. The optimal orbit-averaged power transmission efficiency $\overline{\eta}_t^*$ for this scenario is 8.98%. This is comparable to previously published

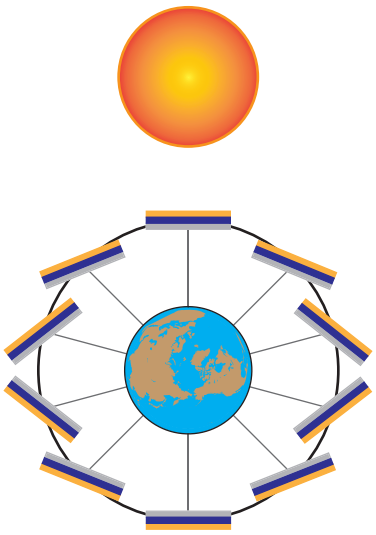

Figure 2.6: Illustration of the optimal orientation trajectory $\beta^*(\theta)$ for a PV2RF1 power station in GEO.

estimates; e.g., with $\eta_{\text{PV}} = 18\%$, a constant RFIC efficiency of 33%, and $\beta = \phi = 0$, [61] estimates that approximately 6% of the incident sunlight is transmitted to the receiving station and 3% is ultimately delivered to the electrical grid.

Ideally, the reorientation maneuvers occur instantaneously. This maximizes the overall system efficiency by minimizing the time spent operating in the vicinities of the local minima in Fig. 2.5b. However, instantaneous slew maneuvers are infeasible for a real system. For this reason, sub-optimal scenarios where the reorientation maneuvers occur over finite lengths of time are also considered. Figure 2.7a compares a sub-optimal orientation trajectory with maneuvers that occur over $\Delta\theta = 45$ deg of angular position (3 hours) with the optimal orientation trajectory from Fig. 2.5a. If an instantaneous reorientation maneuver nominally occurs at $\bar{\theta}$, then the finite duration reorientation maneuvers are obtained by linearly interpolating the optimal orientation trajectory from $\bar{\theta} - \Delta\theta/2$ to $\bar{\theta} + \Delta\theta/2$. Figure 2.7b plots the corresponding power transmission efficiencies.

Reorientation maneuvers occur in the vicinities of the local minima of the power transmission efficiency. For this reason, increasing the durations of the reorientation maneuvers decreases $\overline{\eta}_t$. Figure 2.8 quantifies $\overline{\eta}_t$ as a function of the maneuver duration for reorientation maneuvers that each occur over an angular position $\Delta\theta$. For example, if each maneuver occurs over an angular position of 30 deg, i.e., each maneuver takes 2 hours, then $\overline{\eta}_t$ decreases to 8.59%. This is an approximately

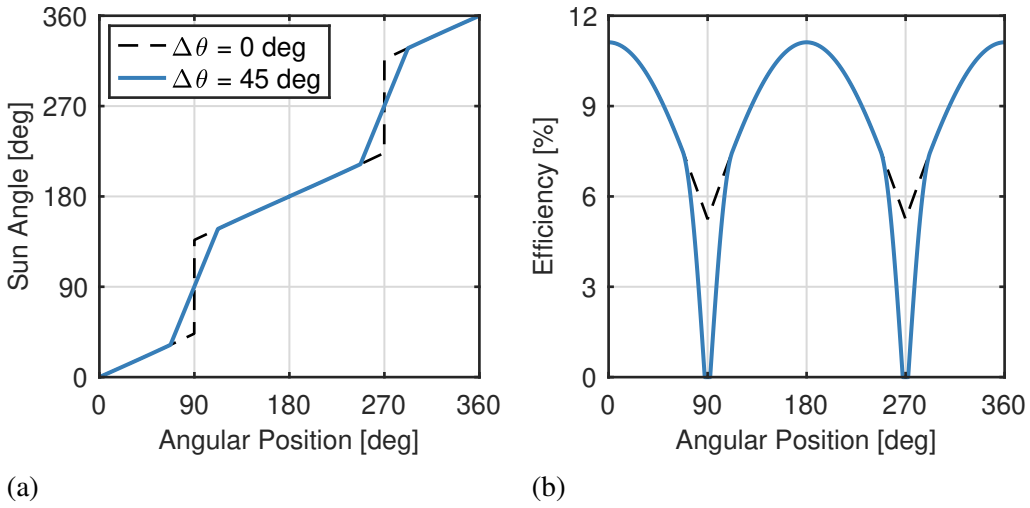

Figure 2.7: (a) sub-optimal orientation trajectory $\beta(\theta)$ and (b) power transmission efficiencies [Eq. (2.4)] for a PV2RF1 power station in GEO.

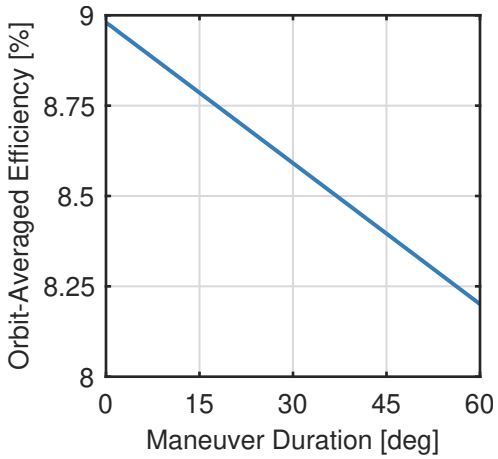

Figure 2.8: Orbit-averaged power transmission efficiency $\overline{\eta}_t$ [Eq. (2.6)] as a function of the reorientation maneuver duration (expressed in terms of the angular position $\Delta\theta$ subtended during each maneuver).

4.3% decrease relative to the case with instantaneous maneuvers. To put this in perspective, the increase in $\overline{\eta}_t$ associated with decreasing the duration of each orientation maneuver from 2 hours to 10 minutes is comparable to increasing the PV cell efficiency from 25% to 26%. In short, the faster the slew maneuvers, the higher the overall system efficiency.

2.4 Discussion

This chapter has described a novel concept for space solar power proposed by the Caltech Space Solar Power Project (SSPP) [13] that requires ultralight flexible

space vehicles with fast slew maneuver capabilities. An idealized power-optimal guidance calculation for a dual-sided PV, single-sided RF space solar power station demonstrates that instantaneous single-axis slew maneuvers maximize the total transmitted power. These maneuvers occur twice per orbit, each of which reorients the power station by approximately 90 deg. The main takeaway is that faster slew maneuvers increase the overall system efficiency, which in turn increases both the power delivered to the electrical grid and the system's economic viability.

The Caltech SSPP architecture is representative of a class of spacecraft structural architectures referred to as bending architectures [24]. Bending architectures encompass spacecraft structural concepts that derive their load carrying capabilities from bending stiffness. This makes them compatible with the integration of functional tiles. While the focus in this chapter is on space solar power, the tile concept can be generalized to other high-performance applications, e.g., high-power communications and radar imaging. For these reasons, the SSPP structural architecture is the focus of the case studies in Chapters 7 and 8. Notably, the baseline 90 deg, single-axis slew maneuver used for the dynamic simulations in Chapter 8 is inspired by the 90 deg, single-axis reorientation maneuvers required to maximize the power transmitted by a space solar power station.

Chapter 3

FLEXIBLE SPACECRAFT SLEW MANEUVER REQUIREMENTS

3.1 Introduction

Many current and future space missions involve increasingly large and flexible spacecraft. These spacecraft sacrifice structural stiffness in order to achieve higher performance (e.g., by increasing the size of solar arrays and antennas) or unlock new capabilities (e.g., solar sailing). As a result, they are envisioned for a variety of applications including planetary [62] and solar system exploration [10]; space science [11]; communications, power transfer, and sensing [12]; and space solar power [13]. Each application requires attitude slew maneuvers, e.g., to reorient sensors and antennas or a thrust vector. Slew maneuvers are required overhead, i.e., they are critical for achieving mission objectives, but are generally time lost in the sense that the spacecraft is not actively performing a useful function (remote sensing, data downlinking, etc.). For this reason, minimizing slew times has significant practical implications for space mission design. In particular, slewing faster leaves more useful time available for executing a spacecraft's intended mission.

Given the proliferation of applications for flexible spacecraft, a common question during mission concept development and preliminary design pertains to how fast these spacecraft can be slewed. In some cases, a rapid slew capability may even be a prerequisite for feasibility. For example, space solar power requires two approximately 90 deg slews per orbit [40]. Here, slew time is tied to economic viability. As demonstrated in Chapter 2, system efficiency decreases as slew time increases, from which it follows that slower slew times result in the transmission of less energy to an electrical grid. Hence, as the trend of fielding increasingly large and flexible spacecraft continues, so too does the importance of slew time as a design driver.

Motivated by the goal of achieving agility despite structural flexibility, this chapter proposes a framework for the prediction of minimum slew times for flexible spacecraft. The framework relies on the canonical model for flexible spacecraft attitude control system (ACS) analysis and design [63, 64], a simple linear system with both a rigid body and a flexible mode. The methods in this chapter are classical and primarily draw from linear systems theory and modal analysis, leading to simple

analytical and quasi-analytical results suitable for concept development and requirements definition. Ultimately, this chapter lays the groundwork for studying the slew maneuver dynamics of ultralight flexible spacecraft in subsequent chapters. While the focus here is on attitude maneuvers, the analysis and results are applicable to both translational and rotational maneuvers.

The remainder of this chapter is organized as follows: Sec. 3.2 introduces the canonical model for flexible spacecraft ACS analysis and design. Sec. 3.3 demonstrates the use of the Craig-Bampton method [30, 31] to reduce an arbitrary flexible spacecraft finite element model into a form analogous to the canonical model from Sec. 3.2. Sec. 3.4 then studies slew maneuver requirements based on both settling times and the peak amplitude of the disturbance due to the flexible dynamics. The former motivates the proposal of a criterion based on the amplitude of the residual elastic velocity for estimating minimum slew times. The chapter concludes with a discussion of the results and their implications in Sec. 3.5.

3.2 Canonical Flexible Spacecraft Model

The classical approach for ACS analysis and design reduces complex flexible spacecraft dynamics into three decoupled, single-axis modal models, one for rotation about each axis [63, 64]. Each model includes a single rigid body mode and one or more dynamically significant elastic modes. Preliminary analysis and design in particular often rely on single-axis modal models with a single retained elastic mode, so-called single-mode models. This is the simplest structural dynamic model that includes both rigid body and flexible modes, and hence, is the canonical model for flexible spacecraft dynamics [63, 64]. The canonical model takes the form of the unrestrained spring-mass-damper system with two degrees of freedom (DOFs) depicted in Fig. 3.1 and applies for either rotational or translational motion.

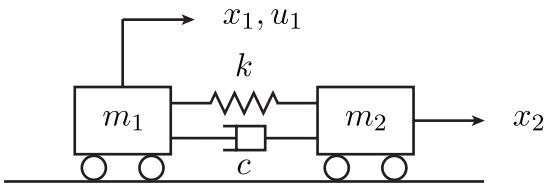

Figure 3.1: The canonical model of a flexible spacecraft is a floating spring-mass-damper system with two degrees of freedom.

The equations of motion for the canonical model in Fig. 3.1 take the form

$$\begin{bmatrix} m_1 & 0 \\ 0 & m_2 \end{bmatrix} \begin{bmatrix} \ddot{x}_1 \\ \ddot{x}_2 \end{bmatrix} + \begin{bmatrix} c & -c \\ -c & c \end{bmatrix} \begin{bmatrix} \dot{x}_1 \\ \dot{x}_2 \end{bmatrix} + \begin{bmatrix} k & -k \\ -k & k \end{bmatrix} \begin{bmatrix} x_1 \\ x_2 \end{bmatrix} = \begin{bmatrix} u_1 \\ 0 \end{bmatrix} \tag{3.1}$$

where m_1 denotes the mass of the spacecraft "bus" with position x_1, m_2 is the mass of the flexible "appendage" with position x_2, k is the spring stiffness, c is the viscous damping coefficient, u_1 is the control input on m_1, and dot notation denotes differentiation with respect to time t. In practice, x_1 is the bus orientation, x_2 is the modal coordinate corresponding to the dominant flexible mode (which is not necessarily the lowest frequency mode), and u_1 is the attitude control torque. The remaining parameters are related to the rigid and flexible body properties of the spacecraft. Sec. 3.3 shows how to reduce arbitrary finite element models into single-axis modal models, and by doing so, derives expressions for these parameters.

The classical ACS analysis and design approach treats flexibility as a disturbance acting on the spacecraft bus. Thus, the parameter of interest for ACS design and analysis is the influence of m_2 on m_1, not the motion of m_2 itself. To eliminate the motion of m_2, the standard approach is to rewrite Eq. (3.1) in the Laplace domain and evaluate the transfer function from u_1 to x_1. Taking the Laplace transform of Eq. (3.1) (with zero initial conditions, as is standard for the evaluation of a transfer function [65, Ch. 4]) gives

$$m_1 s^2 X_1(s) + cs\left(X_1(s) - X_2(s)\right) + k\left(X_1(s) - X_2(s)\right) = U_1(s), \tag{3.2}$$

$$m_2 s^2 X_2(s) + cs\left(X_2(s) - X_1(s)\right) + k\left(X_2(s) - X_1(s)\right) = 0 \tag{3.3}$$

where $X_1(s) = \mathcal{L}(x_1(t))$, $X_2(s) = \mathcal{L}(x_2(t))$, $U_1(s) = \mathcal{L}(u_1(t))$, and $\mathcal{L}(\cdot)$ denotes the Laplace transform that converts a function of time t to a function of the complex frequency s. Rearranging Eq. (3.3) renders the following expression for the transfer function $X_2(s)/X_1(s)$:

$$\frac{X_2(s)}{X_1(s)} = \frac{cs + k}{m_2 s^2 + cs + k}. \tag{3.4}$$

Substituting $X_2(s)/X_1(s)$ into Eq. (3.2), taking a partial fraction expansion, and simplifying then yields

$$\frac{X_1(s)}{U_1'(s)} = \frac{1}{s^2} + \frac{m_2/m_1}{s^2 + 2\left(1 + m_2/m_1\right)\zeta\omega_n s + \left(1 + m_2/m_1\right)\omega_n^2} \tag{3.5}$$

where $\omega_n = \sqrt{k/m_2}$ is the fixed-base natural frequency, $\zeta = c/\left(2\sqrt{km_2}\right)$ is the fixed-base damping ratio (fraction of critical damping), and u_1' is the acceleration input to the system, i.e., $u_1 = (m_1 + m_2)\,u_1'$ [equivalently, $U_1(s) = (m_1 + m_2)\,U_1'(s)$].

Equation (3.5) consists of two terms, the rigid body translation of m_1 and a perturbation due to the motion of m_2, i.e., due to flexibility. To make this more explicit, let $X_1(s) = X_{1,r}(s) + X_{1,f}(s)$ where the subscripts r and f denote the rigid body and flexible terms with corresponding transfer functions

$$\frac{X_{1,r}(s)}{U_1'(s)} = \frac{1}{s^2}, \tag{3.6}$$

$$\frac{X_{1,f}(s)}{U_1'(s)} = \frac{m_2/m_1}{s^2 + 2\left(1 + m_2/m_1\right)\zeta\omega_n s + \left(1 + m_2/m_1\right)\omega_n^2}. \tag{3.7}$$

Taking the inverse Laplace transforms of Eqs. (3.6) and (3.7) then gives

$$\ddot{x}_{1,r} = u_1', \tag{3.8}$$

$$\ddot{x}_{1,f} + 2\left(1 + \frac{m_2}{m_1}\right)\zeta\omega_n\dot{x}_{1,f} + \left(1 + \frac{m_2}{m_1}\right)\omega_n^2 x_{1,f} = \frac{m_2}{m_1}u_1'. \tag{3.9}$$

From Eq. (3.9), the perturbation due to flexibility (i.e., the flexible dynamics) can be modeled as a damped harmonic oscillator with increased natural frequency $\omega_n\sqrt{1 + m_2/m_1}$ and damping ratio $\zeta\sqrt{1 + m_2/m_1}$ relative to the fixed-base case. The shifted natural frequency $\omega_n\sqrt{1 + m_2/m_1}$ corresponds with the free-free natural frequency of Eq. (3.5).

Classical approaches for flexible spacecraft ACS analysis and design are predicated on minimizing the magnitude of any disturbances induced by flexibility, i.e., by making the magnitude of $x_{1,f}$ small. This entails moving the system sufficiently "slowly" to prevent significant excitation of the flexible mode(s). For example, the standard practice for ACS design is to require that the closed-loop bandwidth of the control system is at least an order of magnitude below the system natural frequency $\omega_n\sqrt{1 + m_2/m_1}$ [63].[1] In this case, the control system reacts on a time scale at least an order of magnitude longer than the natural time scale of the system's dynamics. Practically speaking, this means that it is often possible to neglect flexibility altogether in control system design, and instead simply design a control system for the rigid body motion, as is done, e.g., in [66].

A similar philosophy is usually adopted for designing slew maneuvers. A common heuristic is that the duration of a slew maneuver must be an order of magnitude or

[1] In practice, this depends on the spacing of the structural modes. For a system with a few distantly spaced modes, it is possible to achieve higher bandwidth linear control systems by filtering the structural modes (see e.g., [64] and the references therein). However, this becomes difficult, if not impossible for large space structures with many closely spaced modes (see e.g., [66]), in which case the aforementioned requirement on closed-loop bandwidth becomes imperative.

more longer than the system's natural period, although as shown in Sec. 3.4, such a requirement is often misguided. In particular, "slow" is relative, and depends on both the "shape" of the forcing applied to the system and the ratio T/T_n between the slew maneuver duration T and the natural period $T_n = 2\pi/\omega_n$ of the flexible mode. These issues are returned to in Sec. 3.4. In the interim, the discussion turns to the derivation of single-axis modal models from arbitrary finite element models.

3.3 Derivation of Single-Axis Modal Models

Using the canonical model of Sec. 3.2 in practice requires relating its parameters m_1, m_2, and ω_n to a flexible spacecraft finite element model. To that end, this section presents a rigorous derivation based on the Craig-Bampton method [30, 31] of how to transform general unrestrained (free-free) finite element models into single-axis modal models. Along the way, it reinforces that the correct set of vibration modes for ACS analysis and design are the fixed-interface normal modes inherent to the Craig-Bampton method. The Craig-Bampton method generalizes the notion of a "bus" with a flexible "appendage" to an arbitrarily complex flexible spacecraft.

3.3.1 General Modal Models

The derivation of the general modal model starts from the standard equation of motion for a free-free linear finite element model:

$$\mathbf{M}\ddot{\mathbf{x}} + \mathbf{C}\dot{\mathbf{x}} + \mathbf{K}\mathbf{x} = \mathbf{B}\mathbf{u}. \tag{3.10}$$

Here, $\mathbf{x} \in \mathbb{R}^n$ contains the nodal displacement DOFs, $\mathbf{u} \in \mathbb{R}^m$ contains the external forces and moments, $\mathbf{M} \in \mathbb{R}^{n\times n}$ is the symmetric positive definite mass matrix, $\mathbf{C} \in \mathbb{R}^{n\times n}$ is the symmetric positive semi-definite damping matrix, $\mathbf{K} \in \mathbb{R}^{n\times n}$ is the symmetric positive semi-definite stiffness matrix, and $\mathbf{B} \in \mathbb{R}^{n\times m}$ maps the external forces and moments to the nodal DOFs. In general, each node in the finite element model has six DOFs, three translations and three rotations, from which it follows that Eq. (3.10) admits up to six rigid body modes. The damping model (e.g., Rayleigh or modal) determines the rank deficiency of $\mathbf{C}$, whereas the number of rigid body modes corresponds to the rank deficiency of $\mathbf{K}$.

Per the standard procedure for the Craig-Bampton method [30, 31], Eq. (3.10) is partitioned into n_I interior (I) and n_B boundary (B) coordinates, as follows:

$$\begin{bmatrix} \mathbf{M}_{II} & \mathbf{M}_{IB} \\ \mathbf{M}_{BI} & \mathbf{M}_{BB} \end{bmatrix} \begin{bmatrix} \ddot{\mathbf{x}}_I \\ \ddot{\mathbf{x}}_B \end{bmatrix} + \begin{bmatrix} \mathbf{C}_{II} & \mathbf{C}_{IB} \\ \mathbf{C}_{BI} & \mathbf{C}_{BB} \end{bmatrix} \begin{bmatrix} \dot{\mathbf{x}}_I \\ \dot{\mathbf{x}}_B \end{bmatrix} + \begin{bmatrix} \mathbf{K}_{II} & \mathbf{K}_{IB} \\ \mathbf{K}_{BI} & \mathbf{K}_{BB} \end{bmatrix} \begin{bmatrix} \mathbf{x}_I \\ \mathbf{x}_B \end{bmatrix} = \begin{bmatrix} \mathbf{0}_{n_I\times 1} \\ \mathbf{u}_B \end{bmatrix} \tag{3.11}$$

where $n = n_I + n_B$. Typically, the B-set contains DOFs either shared with adjacent components (when the Craig-Bampton substructure is a component of a larger structural dynamic model) or loaded by external forces or moments; the remaining DOFs belong to the I-set [31]. For a flexible spacecraft, the B-set coordinates correspond with the six rigid body DOFs of the bus, and hence, are the generalization of x_1 from the canonical model [Eq. (3.1)]. The I-set coordinates (or the corresponding modal coordinates) are then analogous to x_2 in Eq. (3.1). With the B-set coordinates defined in this way, $\mathbf{K}_{II}$ is the full-rank stiffness matrix corresponding to fixed (clamped) boundary conditions at the bus. $\mathbf{u}_B$ then contains the forces (e.g., due to thrusters) and moments (e.g., due to the ACS) acting on the bus. Equation (3.11) is simply a permutation of the rows and columns of Eq. (3.10).

The partitioned finite element model [Eq. (3.11)] is a special case of the nodal-fixed [67] finite element floating frame of reference (FFR) formulations (see e.g., [68, Ch. 5–6] and [69]) often used in flexible multibody dynamics for simulating structural dynamics with large rigid body motions. This can be shown by substituting the coordinate transformation

$$\begin{bmatrix} \mathbf{x}_I \\ \mathbf{x}_B \end{bmatrix} = \begin{bmatrix} \mathbf{I}_{n_I \times n_I} & -\mathbf{K}_{II}^{-1}\mathbf{K}_{IB} \\ \mathbf{0}_{n_B \times n_I} & \mathbf{I}_{n_B \times n_B} \end{bmatrix} \begin{bmatrix} \overline{\mathbf{x}}_I \\ \mathbf{x}_B \end{bmatrix} \tag{3.12}$$

into Eq. (3.11). Here, $\overline{\mathbf{x}}_I$ contains the elastic displacements of the I-set coordinates relative to the B-set and the last n_B columns of the transformation matrix contain the rigid body modes of $\mathbf{K}$ [31]. In this case, the B-set coordinates correspond with the rigid body translations and rotations of the FFR. With a general FFR formulation, nonlinearities arise due to (i) 3D rotations, (ii) coupling between translations and rotations, (iii) inertia changes due to elastic deformations, and (iv) gyroscopic forces (velocity-squared terms). An expression equivalent to Eq. (3.11) results when (iii) and (iv) are negligible and either the angular displacements are small or the only rigid body motion of the FFR is rotation about a single axis. If the angular displacements are small, Eq. (3.11) can simulate arbitrarily large translations. Likewise, if the only rigid body motion of the FFR is rotation about a single axis, then Eq. (3.11) can simulate arbitrarily large rotations about that axis. Thus, Eq. (3.11) is a useful representation for simulating flexible spacecraft dynamics during, e.g., single-axis slews, fine pointing (attitude stabilization), and propulsive maneuvers.

Following Sec. 3.2, the immediate goal is to derive the transfer function $\mathbf{G}(s)$ that relates a force or moment on the bus (B) to the corresponding translations and rotations, i.e., to find $\mathbf{G}(s)$ such that $\mathbf{G}(s)\mathbf{X}_B(s) = \mathbf{U}_B(s)$ where $\mathbf{X}_B(s) = \mathcal{L}(\mathbf{x}_B(t))$ and

$\mathbf{U}_B(s) = \mathcal{L}(\mathbf{u}_B(t))$. $\mathbf{G}(s)$ is subsequently simplified for the special case of a single-axis slew and inverted to obtain an expression analogous to Eq. (3.5). The derivation of $\mathbf{G}(s)$ closely follows the procedure in [70, Sec. 8.1] for the undamped sinusoidal (steady-state) transfer function $\mathbf{G}(j\omega)$ (referred to as "mechanical impedance" in [70]) where $j^2 = -1$ and ω is the frequency of the harmonic forcing.

The derivation of $\mathbf{G}(s)$ continues by taking the Laplace transform of Eq. (3.11) (again with zero initial conditions) which yields

$$\left(s^2 \begin{bmatrix} \mathbf{M}_{II} & \mathbf{M}_{IB} \\ \mathbf{M}_{BI} & \mathbf{M}_{BB} \end{bmatrix} + s \begin{bmatrix} \mathbf{C}_{II} & \mathbf{C}_{IB} \\ \mathbf{C}_{BI} & \mathbf{C}_{BB} \end{bmatrix} + \begin{bmatrix} \mathbf{K}_{II} & \mathbf{K}_{IB} \\ \mathbf{K}_{BI} & \mathbf{K}_{BB} \end{bmatrix}\right) \begin{bmatrix} \mathbf{X}_I(s) \\ \mathbf{X}_B(s) \end{bmatrix} = \begin{bmatrix} \mathbf{0}_{n_I \times 1} \\ \mathbf{U}_B(s) \end{bmatrix} \tag{3.13}$$

where $\mathbf{X}_I(s) = \mathcal{L}(\mathbf{x}_I(t))$. Eliminating the first equation in Eq. (3.13) then results in the following exact expression relating $\mathbf{X}_I(s)$ and $\mathbf{X}_B(s)$:

$$\mathbf{X}_I(s) = -\left(s^2\mathbf{M}_{II} + s\mathbf{C}_{II} + \mathbf{K}_{II}\right)^{-1}\left(s^2\mathbf{M}_{IB} + s\mathbf{C}_{IB} + \mathbf{K}_{IB}\right)\mathbf{X}_B(s) \tag{3.14}$$

from which it follows that

$$\mathbf{G}(s) = s^2\mathbf{M}_{BB} + s\mathbf{C}_{BB} + \mathbf{K}_{BB} - \mathbf{Z}_{BI}(s)\mathbf{Z}_{II}^{-1}(s)\mathbf{Z}_{IB}(s) \tag{3.15}$$

where $\mathbf{Z}_{kl}(s) = s^2\mathbf{M}_{kl} + s\mathbf{C}_{kl} + \mathbf{K}_{kl}$. While exact, Eq. (3.15) is not always useful because it masks the modal properties of the structure. Hence, Eq. (3.15) is rewritten explicitly in terms of mode shapes and natural frequencies in what follows. Truncating the resulting modal expansion ultimately yields a single-axis modal model.

The fixed-interface normal modes, i.e., the eigenmodes corresponding to a clamped boundary, are the solutions to the following generalized eigenproblem [30, 31]:

$$\mathbf{K}_{II}\boldsymbol{\phi}_i = \omega_i^2\mathbf{M}_{II}\boldsymbol{\phi}_i \tag{3.16}$$

where the fixed-interface normal modes ϕ_i for $i = 1, \ldots, n_I$ are orthogonal to $\mathbf{M}_{II}$ and normalized such that $\boldsymbol{\phi}_i^T\mathbf{M}_{II}\boldsymbol{\phi}_j = \delta_{ij}$.[2] The n_I solutions to Eq. (3.16) can equivalently be written in the form

$$\mathbf{K}_{II}\boldsymbol{\Phi} = \mathbf{M}_{II}\boldsymbol{\Phi}\boldsymbol{\Omega}^2 \tag{3.17}$$

where $\boldsymbol{\Phi} = \left(\boldsymbol{\phi}_1, \ldots, \boldsymbol{\phi}_{n_I}\right)$ is the orthogonal matrix corresponding to the n_I generalized eigenvectors and $\boldsymbol{\Omega}^2 = \operatorname{diag}\left\{\omega_1^2, \ldots, \omega_{n_I}^2\right\}$. It follows that

$$\boldsymbol{\Phi}^T\mathbf{M}_{II}\boldsymbol{\Phi} = \mathbf{I}_{n_I \times n_I}, \tag{3.18}$$

$$\boldsymbol{\Phi}^T\mathbf{K}_{II}\boldsymbol{\Phi} = \boldsymbol{\Omega}^2. \tag{3.19}$$

[2] δ_{ij} is the Kronecker delta symbol defined such that $\delta_{ij} = 1$ for $i = j$ and $\delta_{ij} = 0$ otherwise.

Additionally, subsequent developments assume that

$$\mathbf{\Phi}^T \mathbf{C}_{II} \mathbf{\Phi} = 2\mathbf{Z}\mathbf{\Omega} \tag{3.20}$$

where $\mathbf{Z} = \text{diag}\left\{\zeta_1, \ldots, \zeta_{n_I}\right\}$ is the matrix of modal damping coefficients and $\zeta_i \geq 0$ for all $i = 1, \ldots, n_I$.

The n_I generalized eigenvectors are linearly independent, i.e., $\mathbf{\Phi}$ is invertible. As a result, inverting Eqs. (3.18), (3.19), and (3.20) results in the following identities:

$$\mathbf{M}_{II} = \mathbf{\Phi}^{-T} \mathbf{\Phi}^{-1}, \tag{3.21}$$

$$\mathbf{K}_{II} = \mathbf{\Phi}^{-T} \mathbf{\Omega}^2 \mathbf{\Phi}^{-1}, \tag{3.22}$$

$$\mathbf{C}_{II} = 2\mathbf{\Phi}^{-T} \mathbf{Z}\mathbf{\Omega} \mathbf{\Phi}^{-1}. \tag{3.23}$$

Inverting the expressions for $\mathbf{M}_{II}$ and $\mathbf{K}_{II}$ then yields the following modal expansions [70, Sec. 8.1]:

$$\mathbf{M}_{II}^{-1} = \mathbf{\Phi}\mathbf{\Phi}^T = \sum_{i=1}^{n_I} \boldsymbol{\phi}_i \boldsymbol{\phi}_i^T, \tag{3.24}$$

$$\mathbf{K}_{II}^{-1} = \mathbf{\Phi}\mathbf{\Omega}^{-2}\mathbf{\Phi}^T = \sum_{i=1}^{n_I} \frac{\boldsymbol{\phi}_i \boldsymbol{\phi}_i^T}{\omega_i^2} \tag{3.25}$$

from which it readily follows that

$$\mathbf{K}_{II}^{-1} \mathbf{M}_{II} \mathbf{K}_{II}^{-1} = \mathbf{\Phi}\mathbf{\Omega}^{-4}\mathbf{\Phi}^T = \sum_{i=1}^{n_I} \frac{\boldsymbol{\phi}_i \boldsymbol{\phi}_i^T}{\omega_i^4}. \tag{3.26}$$

By analogy with Eq. (3.26),

$$\mathbf{K}_{II}^{-1} \mathbf{C}_{II} \mathbf{K}_{II}^{-1} = 2\mathbf{\Phi}\mathbf{\Omega}^{-2}\mathbf{Z}\mathbf{\Omega}\mathbf{\Omega}^{-2}\mathbf{\Phi}^T = \sum_{i=1}^{n_I} \frac{\boldsymbol{\phi}_i \left(2\zeta_i \omega_i\right) \boldsymbol{\phi}_i^T}{\omega_i^4}. \tag{3.27}$$

Together, Eqs. (3.21), (3.22), and (3.23) render the identity

$$\mathbf{Z}_{II}^{-1}(s) = \left(s^2 \mathbf{\Phi}^{-T}\mathbf{\Phi}^{-1} + 2s\mathbf{\Phi}^{-T}\mathbf{Z}\mathbf{\Omega}\mathbf{\Phi}^{-1} + \mathbf{\Phi}^{-T}\mathbf{\Omega}^2\mathbf{\Phi}^{-1}\right)^{-1} \tag{3.28}$$

which factorises and simplifies to

$$\mathbf{Z}_{II}^{-1}(s) = \mathbf{\Phi}\left(s^2 \mathbf{I}_{n_I \times n_I} + 2s\mathbf{Z}\mathbf{\Omega} + \mathbf{\Omega}^2\right)^{-1} \mathbf{\Phi}^T = \sum_{i=1}^{n_I} \frac{\boldsymbol{\phi}_i \boldsymbol{\phi}_i^T}{s^2 + 2\zeta_i \omega_i s + \omega_i^2}. \tag{3.29}$$

Further simplifications require the identities [70, Sec. 8.1]

$$\frac{1}{s^2 + \omega_i^2} = \frac{1}{\omega_i^2} - \frac{s^2}{\omega_i^2\left(s^2 + \omega_i^2\right)} = \frac{1}{\omega_i^2} - \frac{s^2}{\omega_i^4} + \frac{s^4}{\omega_i^4\left(s^2 + \omega_i^2\right)} \tag{3.30}$$

and the substitution $s^2 \rightarrow s^2 + 2\zeta_i\omega_i s$. The second identity results from applying the first identity to itself. Using the second part of Eq. (3.30) to expand the denominator in Eq. (3.29) then gives

$$\mathbf{Z}_{II}^{-1}(s) = \sum_{i=1}^{n_I} \left\{ \frac{\boldsymbol{\phi}_i \boldsymbol{\phi}_i^T}{\omega_i^2} - s^2 \frac{\boldsymbol{\phi}_i \boldsymbol{\phi}_i^T}{\omega_i^4} - s \frac{\boldsymbol{\phi}_i \left(2\zeta_i\omega_i\right) \boldsymbol{\phi}_i^T}{\omega_i^4} + \frac{\boldsymbol{\phi}_i \left(s^2 + 2\zeta_i\omega_i s\right)^2 \boldsymbol{\phi}_i^T}{\omega_i^4 \left(s^2 + 2\zeta_i\omega_i s + \omega_i^2\right)} \right\} \tag{3.31}$$

$$= \mathbf{K}_{II}^{-1} - s^2 \mathbf{K}_{II}^{-1} \mathbf{M}_{II} \mathbf{K}_{II}^{-1} - s \mathbf{K}_{II}^{-1} \mathbf{C}_{II} \mathbf{K}_{II}^{-1} + \sum_{i=1}^{n_I} \frac{\boldsymbol{\phi}_i \left(s^2 + 2\zeta_i\omega_i s\right)^2 \boldsymbol{\phi}_i^T}{\omega_i^4 \left(s^2 + 2\zeta_i\omega_i s + \omega_i^2\right)} \tag{3.32}$$

where the last step requires Eqs. (3.25), (3.26), and (3.27).

Substituting Eq. (3.32) into Eq. (3.15) and simplifying ultimately result in the following expression for $\mathbf{G}(s)$:

$$\mathbf{G}(s) = s^2 \mathbf{M}_{BB}^* + s \mathbf{C}_{BB}^* + \mathbf{K}_{BB}^* - s^2 \sum_{i=1}^{n_I} \frac{\left(\mathbf{g}_i + s\mathbf{h}_i\right) \left(\mathbf{g}_i + s\mathbf{h}_i\right)^T}{\omega_i^4 \left(s^2 + 2\zeta_i\omega_i s + \omega_i^2\right)} \tag{3.33}$$

where $\mathbf{g}_i = \left(2\zeta_i\omega_i \mathbf{K}_{BI} - \omega_i^2 \mathbf{C}_{BI}\right) \boldsymbol{\phi}_i$ and $\mathbf{h}_i = \left(\mathbf{K}_{BI} - \omega_i^2 \mathbf{M}_{BI}\right) \boldsymbol{\phi}_i$ are modal vectors and

$$\mathbf{M}_{BB}^* = \mathbf{M}_{BB} - \mathbf{M}_{BI}\mathbf{K}_{II}^{-1}\mathbf{K}_{IB} - \mathbf{K}_{BI}\mathbf{K}_{II}^{-1}\mathbf{M}_{IB} + \mathbf{K}_{BI}\mathbf{K}_{II}^{-1}\mathbf{M}_{II}\mathbf{K}_{II}^{-1}\mathbf{K}_{IB}, \tag{3.34}$$

$$\mathbf{K}_{BB}^* = \mathbf{K}_{BB} - \mathbf{K}_{BI}\mathbf{K}_{II}^{-1}\mathbf{K}_{IB}, \tag{3.35}$$

$$\mathbf{C}_{BB}^* = \mathbf{C}_{BB} - \mathbf{C}_{BI}\mathbf{K}_{II}^{-1}\mathbf{K}_{IB} - \mathbf{K}_{BI}\mathbf{K}_{II}^{-1}\mathbf{C}_{IB} + \mathbf{K}_{BI}\mathbf{K}_{II}^{-1}\mathbf{C}_{II}\mathbf{K}_{II}^{-1}\mathbf{K}_{IB}. \tag{3.36}$$

The derivation of Eq. (3.33) is conceptually straightforward, but the details are involved. It specifically entails (i) substituting Eq. (3.32) into Eq. (3.15) and expanding the product; (ii) identifying the terms that contribute to Eqs. (3.34), (3.35), and (3.36); (iii) expanding the remaining terms using the modal expansions for $\mathbf{K}_{II}^{-1}$, $\mathbf{K}_{II}^{-1}\mathbf{M}_{II}\mathbf{K}_{II}^{-1}$, and $\mathbf{K}_{II}^{-1}\mathbf{C}_{II}\mathbf{K}_{II}^{-1}$ [Eqs. (3.25), (3.26), and (3.27)]; and (iv) combining terms and simplifying. Equation (3.33) is readily verified for simple systems, e.g., the canonical model from Sec. 3.2. In practice, it is advantageous to precompute $\mathbf{g}_i$ and $\mathbf{h}_i$. This avoids unnecessary calculations of computationally expensive matrix-vector products during repeated evaluations of Eq. (3.33).

In Eq. (3.33), $\mathbf{M}_{BB}^*$ and $\mathbf{K}_{BB}^*$ are the statically reduced mass and stiffness matrices [70, Sec. 8.1]. By analogy, $\mathbf{C}_{BB}^*$ is the statically reduced damping matrix. If the structure has n_B rigid body modes and the n_B boundary coordinates fully restrain those modes, then $\mathbf{K}_{BB}^*$ is the projection of the unrestrained stiffness matrix onto

the rigid body modes, i.e., $\mathbf{K}^*_{BB} = \mathbf{0}_{n_B \times n_B}$ (otherwise, $\mathbf{K}^*_{BB}$ is singular but non-zero). The properties of $\mathbf{C}^*_{BB}$ depend on the damping model. For example, with stiffness-proportional damping, $\mathbf{C} = \beta\mathbf{K}$ where $\beta = 2\zeta_1/\omega_1$, ω_1 is the first-mode natural frequency, and ζ_1 is the fraction of critical damping in the first mode. Higher-frequency modes are more heavily damped; specifically, $\zeta_i = \zeta_1(\omega_i/\omega_1)$ for $i = 1, \ldots, n_I$. With these assumptions, $\mathbf{C}^*_{BB} = \mathbf{0}_{n_B \times n_B}$ and $\mathbf{g}_i = \mathbf{0}_{n_B \times 1}$. Thus, Eq. (3.33) reduces to

$$\mathbf{G}(s) = s^2\mathbf{M}^*_{BB} - s^4 \sum_{i=1}^{n_I} \frac{\mathbf{h}_i \mathbf{h}_i^T}{\omega_i^4 \left(s^2 + 2\zeta_i\omega_i s + \omega_i^2\right)}. \tag{3.37}$$

and $\mathbf{M}^*_{BB}$ is the rigid body mass matrix of the unrestrained structure. Assuming the B-set coordinates coincide with a node at the structure's undeformed center of mass and the global finite element reference frame coincides with principal inertial axes, then $\mathbf{M}^*_{BB}$ is diagonal. The modal participation vector $\mathbf{h}_i$ then represents the dynamic reaction of the ith mode on B due to an external force or moment on B [70, Sec. 8.1]. The corresponding modal mass matrix $\mathbf{M}_i = \mathbf{h}_i\mathbf{h}_i^T/\omega_i^4$ determines the flexible body accelerations required to dynamically react an external force or moment on B and how those accelerations are distributed throughout the eigenmodes. Equation (3.37) emphasizes that a force or moment on B induces both rigid body and elastic motions.

3.3.2 Mode Selection Criteria

As outlined in [70, Sec. 8.2], Eq. (3.37) shows how to select "dominant" eigenmodes for reduced-order models, i.e., which modes to retain in a truncated modal expansion. Specifically, $\mathbf{h}_i$ is a measure of the modal participation of mode i [70, Sec. 8.1]. The larger the magnitude of $\mathbf{h}_i$, the larger the dynamic reaction on B, the larger the modal mass, and the more dominant the mode. For this reason, [70, Sec. 8.2] suggests using the following criterion to rank modes from most dominant to least dominant:

$$p_i = ||\mathbf{h}_i/\omega_i^2||_2^2 \tag{3.38}$$

where $||\cdot||_2$ denotes the Euclidean norm and larger values correspond to more dominant modes. Equation (3.38) is the magnitude of the ith term in the modal expansion [Eq. (3.37)] and equals the trace of the modal mass matrix $\mathbf{M}_i$. The ω_i^4 in the denominator implies that dominant modes tend to be lower-frequency modes, but in general, the dominant mode is not necessarily the lowest-frequency mode.

Due to unit discrepancies, Eq. (3.38) is ill-defined for structures with both nodal translational and rotational DOFs. To remedy this, the coordinate partition from [71]

is used to develop a modified mode selection criterion. Specifically, $\mathbf{h}_i$ is partitioned into translational (T) and rotational (R) DOFs such that $\mathbf{h}_i^T = \left(\mathbf{h}_{i,T}^T, \mathbf{h}_{i,R}^T\right)$. Modes are then sorted according to the following criterion:

$$\overline{p}_i = \frac{1}{2}\left(\frac{||\mathbf{h}_{i,T}/\omega_i^2||_2^2}{\sum_{i=1}^{n_I}||\mathbf{h}_{i,T}/\omega_i^2||_2^2} + \frac{||\mathbf{h}_{i,R}/\omega_i^2||_2^2}{\sum_{i=1}^{n_I}||\mathbf{h}_{i,R}/\omega_i^2||_2^2}\right) \tag{3.39}$$

where $\mathbf{h}_{i,T}\mathbf{h}_{i,T}^T/\omega_i^4$ and $\mathbf{h}_{i,R}\mathbf{h}_{i,R}^T/\omega_i^4$ are the translational and rotational blocks of the modal mass matrix $\mathbf{M}_i$ and again larger values correspond to more dominant modes. Equation (3.39) is the average of the translational modal mass (normalized by the total modal mass) and rotational modal inertia (normalized by the total modal inertia). Equivalently, it is a normalized measure of the ith mode's dynamic reaction on B. For finite element models with either translational DOFs or rotational DOFs, but not both, Eq. (3.39) reduces to a normalized version of Eq. (3.38).

Equation (3.39) is equivalent to the effective interface mass introduced by Kammer and Triller [71]. Specifically, $\mathbf{M}_i$ is equivalent to the matrix $[\overline{\mathbf{M}}_i]$ from [71]. This is straightforward to show by expanding $[\overline{\mathbf{M}}_i]$, substituting Eq. (3.25), and using the orthogonality of $\mathbf{\Phi}$ [Eq. (3.18)]. According to [72], effective interface mass, and by extension, Eq. (3.39), also measures the relative controllability and observability [73] of each fixed-interface mode. The higher the value of Eq. (3.39), the more controllable and observable the mode. Moreover, effective interface mass is closely related to the balanced singular values [74] from the balanced truncation method of model reduction [75]. For undamped free vibrations, balanced truncation yields normal vibration modes [76, 77].

Standard eigenproblem solvers used in structural mechanics, particularly those suitable for large-scale problems, only solve for a subset of the eigenmodes [78]. When only a subset of the eigenmodes are available, the denominators in Eq. (3.39) are instead calculated from the cumulative modal mass matrix

$$\sum_{i=1}^{n_I}\mathbf{M}_i = \mathbf{K}_{BI}\mathbf{K}_{II}^{-1}\mathbf{M}_{II}\mathbf{K}_{II}^{-1}\mathbf{K}_{BI}^T - \mathbf{K}_{BI}\mathbf{K}_{II}^{-1}\mathbf{M}_{BI}^T - \mathbf{M}_{BI}\mathbf{K}_{II}^{-1}\mathbf{K}_{BI}^T + \mathbf{M}_{BI}\mathbf{M}_{II}^{-1}\mathbf{M}_{BI}^T \tag{3.40}$$

which is derived from the definition of $\mathbf{M}_i$ and Eqs. (3.24), (3.25), and (3.26). Equation (3.40) is only a function of the finite element mass and stiffness matrices, i.e., it is independent of the computed eigenmodes.

Importantly, both Eqs. (3.38) and (3.39), and hence, the resulting mode sortings, are invariant to reference frame transformations.

For single-axis modal models, the dominant mode is the mode with the maximum modal mass or inertia per axis, i.e., the maximum absolute value in the corresponding DOF in $\mathbf{h}_i$. In general, different modes are dominant for translational and rotational motions about different axes.

Lastly, many flexible spacecraft, including solar sails [9] and the Caltech Space Solar Power Project satellite [13], nominally feature structural symmetries. It is well known that symmetric structures have natural frequencies (eigenvalues) with multiplicities greater than one; the actual multiplicity of a given eigenvalue depends on a structure's specific symmetries [79]. Due to the limitations of floating point computations and the accumulation of round-off errors, it is often difficult to distinguish between symmetric modes with repeated eigenvalues and merely closely spaced modes. Conveniently, the same criteria used to sort modes can also be used to identify repeated eigenvalues. In particular, both the magnitude of the modal participation vector $||\mathbf{h}_i||_2$ and the trace of the modal mass matrix $\mathbf{M}_i$ are invariant to the operations of a symmetry group. Hence, these quantities are both invariant for symmetric modes, meaning symmetric modes have the same values (to within close numerical tolerances) of both Eq. (3.38) and Eq. (3.39). Closely spaced modes, on the other hand, typically have distinct values of both Eq. (3.38) and Eq. (3.39). This has important implications for the development of single-axis modal models for symmetric structures, something discussed further in Sec. 3.3.4.

3.3.3 Single-Axis Modal Models

Several additional simplifying assumptions are required to reduce Eq. (3.37) to an expression analogous to the canonical model [Eq. (3.5)]. Before applying these assumptions, Eq. (3.37) is rewritten by substituting the modal mass matrix $\mathbf{M}_i = \mathbf{h}_i\mathbf{h}_i^T/\omega_i^4$ and expressing the control input as an acceleration, i.e., substituting $\mathbf{u}_B = \mathbf{M}_{BB}^*\mathbf{u}'_B$ [equivalently, $\mathbf{U}_B(s) = \mathbf{M}_{BB}^*\mathbf{U}'_B(s)$], which yields

$$\left(s^2\mathbf{M}_{BB}^* - s^4\sum_{i=1}^{n_I}\frac{\mathbf{M}_i}{s^2+2\zeta_i\omega_i s+\omega_i^2}\right)\mathbf{X}_B(s) = \mathbf{M}_{BB}^*\mathbf{U}'_B(s). \tag{3.41}$$

For a single-axis modal model, the control input on the right side of Eq. (3.41) is restricted to a force or moment about a single axis, in which case

$$\left(s^2\mathbf{M}_{BB}^* - s^4\sum_{i=1}^{n_I}\frac{\mathbf{M}_i}{s^2+2\zeta_i\omega_i s+\omega_i^2}\right)\mathbf{X}_B(s) = \mathbf{M}_{BB}^*\mathbf{e}_j U'_{B,j}(s) \tag{3.42}$$

where $U'_{B,j}(s)$ is the jth scalar control input and $\mathbf{e}_j$ for $j = 1, \ldots, n_B$ is a standard unit basis vector in $\mathbb{R}^{n_B}$. In principle, inverting the transfer function matrix on the left side of Eq. (3.42) immediately results in a single-axis modal model, but this is not analytically tractable in the general case due to couplings between all n_B DOFs.

Subsequent assumptions are aimed at eliminating these couplings. In particular, it is assumed that (i) the B-set coordinates correspond to a node located at the structure's undeformed center of mass, (ii) the global finite element reference frame coincides with principal inertial axes, and (iii) off-diagonal terms in each of the $\mathbf{M}_i$ are negligible. Together, (i) and (ii) diagonalize $\mathbf{M}^*_{BB}$; (iii) then diagonalizes each of the $\mathbf{M}_i$, at least for practical purposes. Moreover, only a small subset of the n_I eigenmodes are typically retained in the modal expansion, in this case, the $n_D \leq n_I$ most dominant eigenmodes. Under these assumptions, the dynamics take the form

$$\left(s^2 M^*_{BB,jj} - s^4 \sum_{i=1}^{n_D} \frac{M_{i,jj}}{s^2 + 2\zeta_i \omega_i s + \omega_i^2} \right) X_{B,j}(s) = M^*_{BB,jj} U'_{B,j}(s) \tag{3.43}$$

where the subscript jj denotes the jth main diagonal entry of the corresponding matrix. Transforming Eq. (3.43) into a form analogous to Eq. (3.5) then entails retaining the most-dominant eigenmode ($n_D = 1$), solving for $X_{B,j}(s)/U'_{B,j}(s)$, and expanding with partial fractions, the result of which is

$$\frac{X_{B,j}(s)}{U'_{B,j}(s)} = \frac{1}{s^2} + \frac{\eta_{jj}}{s^2 + 2\left(1 + \eta_{jj}\right)\zeta_1 \omega_1 + \left(1 + \eta_{jj}\right)\omega_1^2} \tag{3.44}$$

where

$$\eta_{jj} = \frac{M_{1,jj}}{M^*_{BB,jj} - M_{1,jj}} \tag{3.45}$$

is the mass ratio. Comparing Eqs. (3.44) and (3.5) shows that $m_1 = M^*_{BB,jj} - M_{1,jj}$, i.e., the *difference* between the rigid body mass and the modal mass, not the rigid body mass itself; $m_2 = M_{1,jj}$; $\zeta = \zeta_1$; and $\omega_n = \omega_1$. In other words, the parameters in the canonical model are related to the rigid body mass and the dominant fixed-interface mode's modal mass, damping ratio, and natural frequency where "mass" is to be interpreted in the general sense of either translational or rotational inertia.

3.3.4 Single-Axis Modal Models for Symmetric Structures

The derivation of single-axis modal models for flexible spacecraft with structural symmetries requires special considerations when the dominant eigenmode corresponds to a repeated eigenvalue. This is particularly important for flexible spacecraft

with 4-fold symmetric, plate-like structural architectures, like solar sails [9] and the Caltech Space Solar Power Project satellite [13].

When the dominant eigenmode corresponds to a repeated eigenvalue, Eq. (3.44) underpredicts the magnitude of the elastic disturbance on the spacecraft bus. Instead of truncating the modal expansion after the dominant mode, the correct truncation includes both the dominant mode and any associated symmetric modes. In this case, the summation in Eq. (3.43) now includes all n_D modes at the dominant mode frequency ω_1. Assuming these modes also share the same damping ratio ζ_1, then

$$\left(s^2 M^*_{BB,jj} - \frac{s^4}{s^2 + 2\zeta_1\omega_1 s + \omega_1^2} \sum_{i=1}^{n_D} M_{i,jj}\right) X_{B,j}(s) = M^*_{BB,jj} U'_{B,j}(s) \tag{3.46}$$

from which it follows that replacing $M_{1,jj}$ in Eq. (3.44) with $\Sigma M_{jj} = \sum_{i=1}^{n_D} M_{i,jj}$ results in the correct expression for the transfer function:

$$\frac{X_{B,j}(s)}{U'_{B,j}(s)} = \frac{1}{s^2} + \frac{\eta_{jj}}{s^2 + 2\left(1+\eta_{jj}\right)\zeta_1\omega_1 + \left(1+\eta_{jj}\right)\omega_1^2} \tag{3.47}$$

where the mass ratio η_{jj} now takes the form

$$\eta_{jj} = \frac{\Sigma M_{jj}}{M^*_{BB,jj} - \Sigma M_{jj}}. \tag{3.48}$$

Equation (3.47) is equivalent to

$$\frac{X_{B,j}(s)}{U'_{B,j}(s)} = \frac{1}{s^2} + \sum_{i=1}^{n_D} \frac{M_{i,jj}}{M_{1,jj}} \frac{M_{1,jj}}{M^*_{BB,jj} - \Sigma M_{jj}} \left(\frac{1}{s^2 + 2\left(1+\eta_{jj}\right)\zeta_1\omega_1 + \left(1+\eta_{jj}\right)\omega_1^2}\right) \tag{3.49}$$

which shows that the elastic disturbance due to each symmetric mode is proportional to the ratio of its modal mass $M_{i,jj}$ to the dominant mode's modal mass $M_{1,jj}$.

3.4 Slew Maneuver Requirements

The canonical flexible spacecraft model from Sec. 3.2 provides a useful tool for developing quantitative insights into slew maneuver requirements. The emphasis here is on structure-based requirements, specifically requirements on the ratio T/T_n between the slew duration T and the fixed-base natural period T_n as a function of the mass ratio m_2/m_1 from Eq. (3.5).

Using a baseline bang-bang slew maneuver (Sec. 3.4.1), the analysis demonstrates that settling time is a poor metric for determining slew maneuver requirements (Sec. 3.4.2), in large part due to the very low damping of flexible spacecraft.

This motivates an alternate metric for determining slew maneuver requirements (Sec. 3.4.3). A smooth slew maneuver then highlights how tailoring the "shape" of the slew profile can decrease the excitation of the flexible mode relative to the baseline bang-bang case (Sec. 3.4.4). The latter is a fairly well-known result in general (see e.g., [80–84]) and is the premise underlying the use of input shaping for reducing residual vibrations (see e.g., [85–88] and the references therein), but seems less well-known (or at the very least, less well-used) in the definition of flexible spacecraft slew maneuver requirements.

The focus of this section is on attitude slew maneuvers. To emphasize this, the following changes are made to the notation from Sec. 3.2: $x_1 \rightarrow \theta_1$, $x_2 \rightarrow \theta_2$, $u_1 \rightarrow \ddot{\theta}$, $m_1 \rightarrow J_1$, and $m_2 \rightarrow J_2$. θ_1 and θ_2 denote the orientations of the "bus" and flexible "appendage" with rotational inertias J_1 and J_2, respectively, and $\ddot{\theta}$ denotes the angular acceleration input to the system.

3.4.1 Baseline Slew Maneuver

The baseline slew maneuver considered in this section is the bang-bang slew maneuver through an angle $\Delta\theta$ in time T depicted in Fig. 3.2. A bang-bang slew is the time-optimal, rest-to-rest, single-axis reorientation maneuver for a rigid body with angular acceleration (torque) constraints [89]. Each "bang" is a step angular acceleration input of magnitude

$$\ddot{\theta}_{\max} = \frac{4\Delta\theta}{T^2} \tag{3.50}$$

and duration $T/2$, as depicted in Fig. 3.2a. For a rigid body, the initial "bang" linearly accelerates the system from rest to a peak angular velocity of

$$\dot{\theta}_{\max} = \frac{\ddot{\theta}_{\max} T}{2} = \frac{2\Delta\theta}{T} \tag{3.51}$$

at time $t = T/2$. The final "bang" then linearly decelerates the system back to rest; see Fig. 3.2b. The constant magnitude angular acceleration results in the quadratic variation in the slew angle shown in Fig. 3.2c.

Figure 3.2 depicts the response of a rigid spacecraft during a bang-bang slew. To highlight the differences between a rigid spacecraft and a flexible one, Fig. 3.3 depicts several representative responses of an undamped canonical flexible spacecraft [Eq. (3.1)] with $J_1 = J_2$ to a bang-bang slew. The general trend is that the magnitude of the disturbance due to the flexible dynamics decreases as the duration of the slew increases, i.e., as the ratio T/T_n increases. In other words, as T/T_n increases, the response approaches the response of the rigid spacecraft from Fig. 3.2.

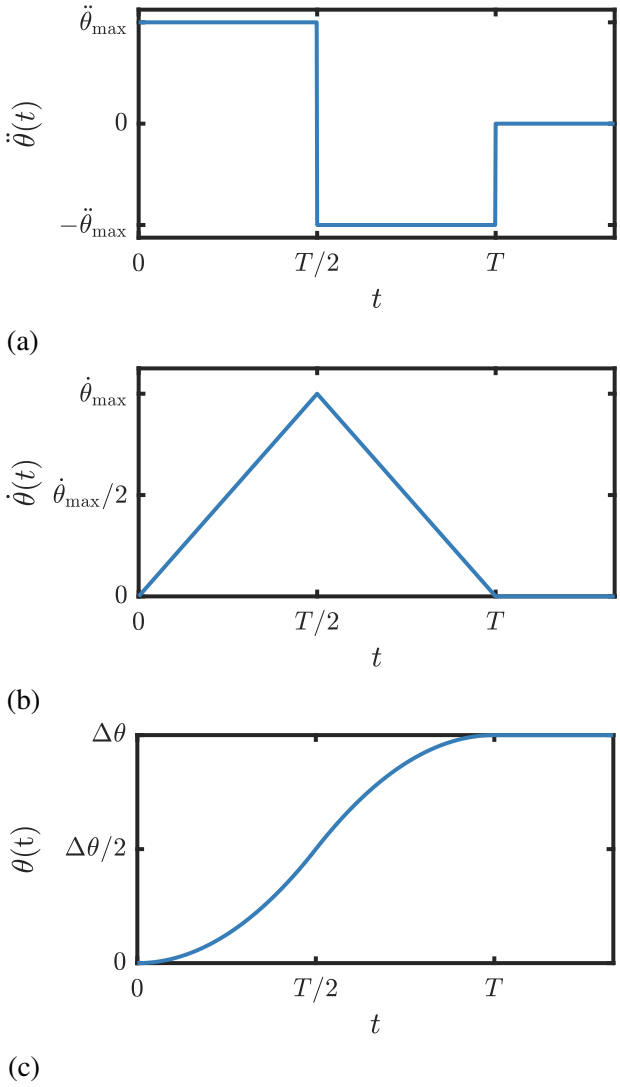

Figure 3.2: Rest-to-rest bang-bang slew maneuver profile for a rigid spacecraft: (a) slew acceleration, (b) slew rate, and (c) slew angle.

Step inputs are broadband, and hence, they lead to the excitation of every flexible mode in the system. As a result, a bang-bang slew is the worst-case from the standpoint of flexible mode excitation. Standard practice usually involves more benign slew maneuvers, e.g., something analogous to a bang-off-bang slew where the intermediate "off" corresponds to a coasting period of significantly longer duration than either "bang". Nevertheless, a bang-bang slew remains useful for preliminary analysis and requirements definition because it leads to simple analytical results.

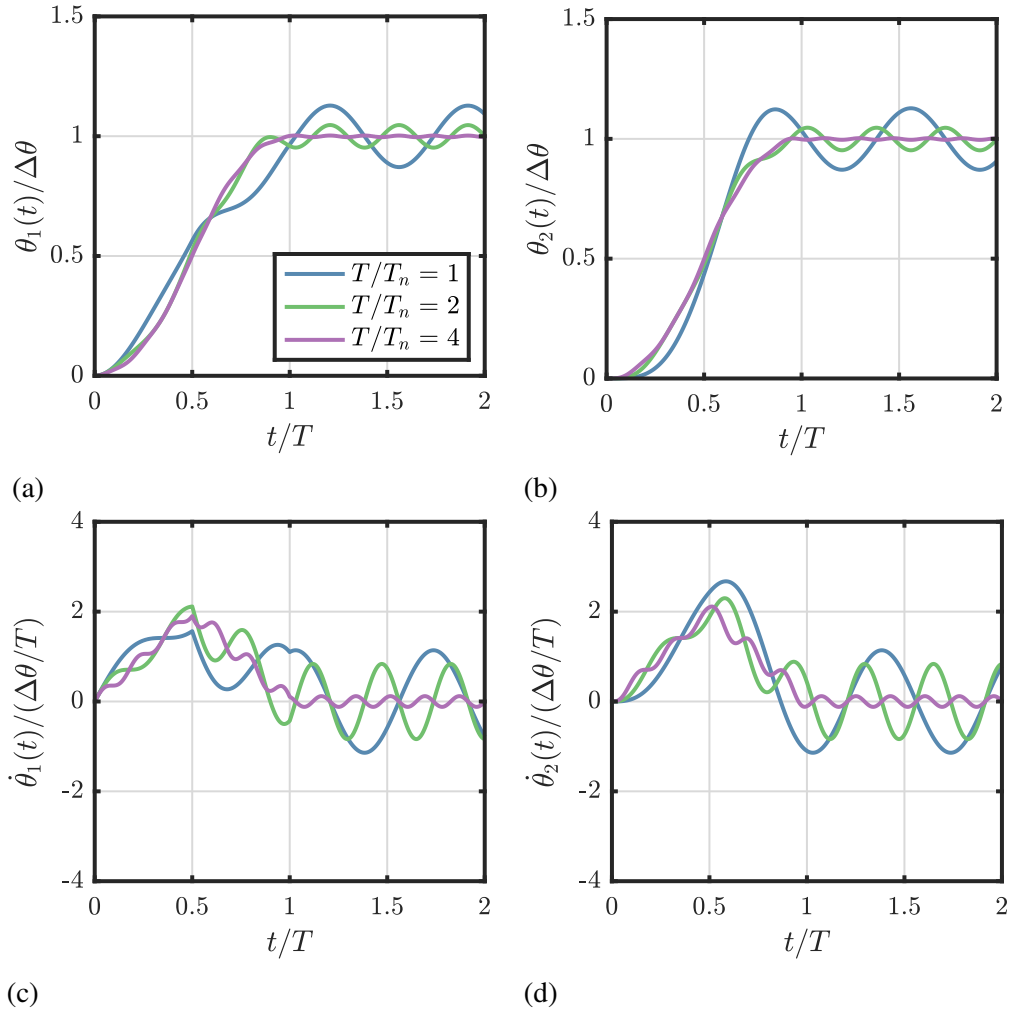

Figure 3.3: Non-dimensionalized transient responses of an undamped canonical flexible spacecraft [Eq. (3.1)] with $J_1 = J_2$ to a bang-bang slew maneuver of duration T. (a) orientation of the spacecraft bus J_1; (b) orientation of the flexible appendage J_2; (c) angular velocity of the spacecraft bus J_1; (d) angular velocity of the flexible appendage J_2.

3.4.2 Slew Maneuver Requirements Based on Settling Times

The settling time, i.e., the time it takes for the amplitude of oscillation to subside below some specified threshold, is a natural way to specify the minimum slew time for a flexible spacecraft. For second-order linear systems, it is common to use either 2% or 5% of the final (steady-state) response to a specified input [65, Ch. 10]. The choice is largely arbitrary, so 2% is used in what follows.

Figure 3.4 plots the 2% settling time T_s versus the damping ratio $\zeta = c/\left(2\sqrt{km}\right)$ for a unit step input applied to the damped 1-DOF harmonic oscillator with natural period $T_n = 2\pi/\sqrt{k/m}$ depicted in Fig. 3.5. The solid blue line is calculated from the

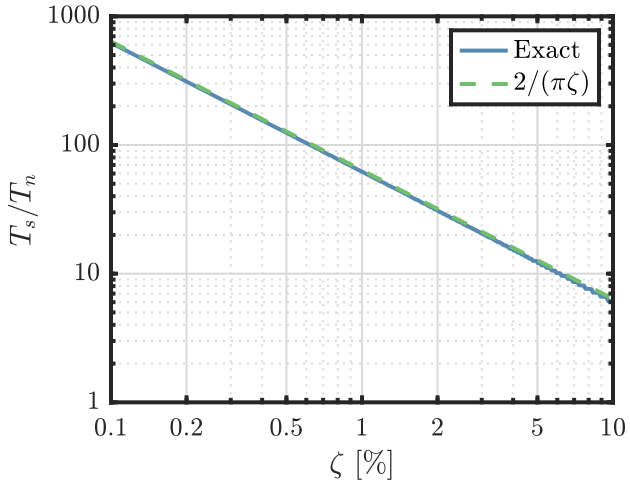

Figure 3.4: 2% settling time T_s for a damped 1-DOF harmonic oscillator with undamped natural period T_n. $2/(\pi\zeta)$ is an upper bound on the 2% settling time.

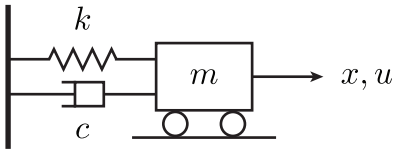

Figure 3.5: Damped harmonic oscillator with mass m, damping coefficient c, stiffness k, and external force u.

analytical response; the dashed green line is an approximation from [65, Ch. 10] that is an upper bound for the range of considered damping ratios. The approximation provides a marginally more conservative and significantly simpler estimate for T_s, and hence, is preferred here. The main takeaways from Fig. 3.4 are that T_s increases inversely proportionally to the damping ratio and that the very low damping ratios ($\zeta \ll 1\%$) characteristic of flexible spacecraft [90] imply settling times that are roughly 100 to 1000 times the natural period.

For a bang-bang slew, the minimum slew time T is twice the settling time T_s, i.e., $T = 2T_s$. In this way, there is sufficient time for the response to settle from both the first "bang" before applying the second "bang" and from the second "bang" before the end of the slew. It follows that the minimum slew time for the canonical flexible spacecraft [Eq. (3.5)] takes the form

$$\frac{T}{T_n} = \frac{4}{\pi\zeta\,(1 + J_2/J_1)} \tag{3.52}$$

where T_n and ζ are again its fixed-base natural period and damping ratio. The deriva-

tion of Eq. (3.52) involves substituting $T = 2T_s$ and the natural period $T_n/\sqrt{1 + J_2/J_1}$ and damping ratio $\zeta\sqrt{1 + J_2/J_1}$ for the canonical flexible spacecraft from Eq. (3.9) into the settling time estimate $T_s/T_n = 2/(\pi\zeta)$ from Fig. 3.4. With a settled response, the spacecraft can immediately resume operations like science data collection post-slew, something with important practical implications for space mission design.

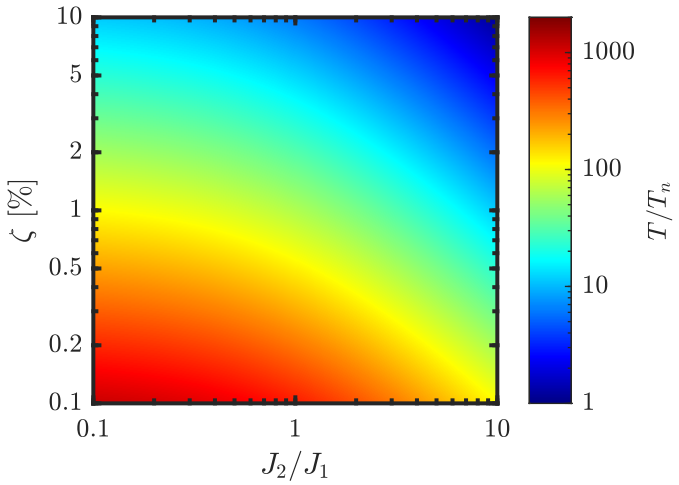

Figure 3.6: Minimum bang-bang slew time T derived from the 2% settling time for the canonical flexible spacecraft [Eq. (3.1)] with fixed-base natural period T_n.

Figure 3.6 plots Eq. (3.52) as a function of both the inertia ratio J_2/J_1 and the damping ratio ζ. The figures shows that minimum slew times are typically on the order of 100 to 1000 times the fixed-base natural period for large flexible spacecraft ($J_2 > J_1$) with low modal damping ($\zeta < 1\%$). For example, with a dominant mode of 0.1 Hz, $J_2 = J_1$, and 0.5% modal damping, the minimum slew time is approximately 22 min, something comparable to the slew maneuver durations for existing exploration-class spacecraft (e.g., Juno or Europa Clipper) and smaller solar sails [91, 92]. The situation, however, progressively deteriorates as flexibility decreases and damping increases. With a dominant mode frequency of 1 mHz (reminiscent of some proposed flexible spacecraft concepts, e.g. [13]), $J_2 = J_1$, and 0.2% modal damping, the minimum slew time from Eq. (3.52) increases to over 88 h! This is obviously not practical. In short, if settling time drives slew maneuver requirements, the spacecraft engineer may be led to believe that slewing very large flexible spacecraft is impossible. This is not the case, as explained next.

3.4.3 Proposed Performance Metric

For a bang-bang slew, the settling time [Eq. (3.52)] is independent of the magnitude of the step inputs. However, in light of Fig. 3.3, the magnitude of the disturbance

due to the flexible dynamics decreases as the slew time increases. As a result, for a sufficiently slow slew, the magnitude of this disturbance can be considered negligible even though Eq. (3.52) predicts a very long slew time. This implies that a more suitable criterion for determining flexible spacecraft slew maneuver requirements is a metric based on the magnitude of the disturbance due to the flexible dynamics. In other words, instead of relying on damping to dissipate the flexible dynamics, it is preferable to slew the spacecraft in a way that maintains the disturbance due to the flexible dynamics at or below a tolerable level. The metric for defining what is tolerable depends on the application. The sequel proposes a metric that prioritizes spacecraft pointing performance, but other metrics may be more suitable for other applications, e.g., ones that prioritize shape accuracy.

A nominally rest-to-rest slew maneuver for a rigid spacecraft leads to residual structural vibrations for a flexible one. In light of Eq. (3.5), the spacecraft bus perceives these structural vibrations as angular position and velocity errors, the magnitudes of which are often included in ACS pointing error budgets (see e.g., [93]) and are a proxy for pointing stability and jitter. Here, jitter refers to the classical definition of unwanted mechanical vibrations, as opposed to more nuanced definitions typically used for space-borne optical systems [94, 95]. A flexible spacecraft ACS with its closed-loop bandwidth set an order of magnitude below the flexible mode frequency is incapable of rejecting jitter. Thus, minimizing jitter is imperative for pointing accuracy and stability. Likewise, an ACS can more easily tolerate angular position errors than angular velocity ones. Unlike angular position errors, even small angular velocity errors can lead to unwanted effects, e.g., smearing in optical sensors, that are difficult to correct a posteriori. With this in mind, the proposed performance metric for determining slew times is the amplitude of the residual angular velocity after a slew from Eq. (3.9). For a given slew profile, specifying a requirement on the maximum amplitude indirectly specifies a minimum slew time. Hedgepeth [96] uses similar arguments to determine a first-mode natural frequency requirement for slewing flexible spacecraft; for additional details, see Appendix A.

Slew maneuver loads are generally impulsive, i.e., they are applied over (relatively) short time scales. A structure's peak, i.e., worst-case, response to an impulsive load is usually reached before damping can dissipate significant energy [97, Ch. 6]. Additionally, spacecraft structures are usually extremely lightly damped to begin with; 0.5% modal damping is typical [90]. For these reasons, it is reasonable to

neglect damping for preliminary slew maneuver analysis (although the same cannot necessarily be said for preliminary ACS analysis and design). The underlying assumption here is that slew times are only going to decrease with damping. Said another way, the undamped response provides a conservative slew time estimate.

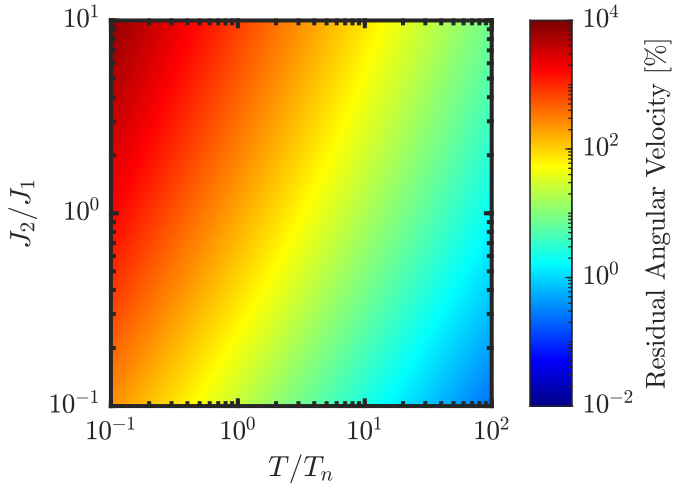

Figure 3.7: Amplitude of the residual angular velocity [Eq. (3.54)] for a bang-bang slew maneuver.

For a bang-bang slew maneuver of the canonical flexible spacecraft, the amplitude of the residual angular velocity is

$$\frac{|\dot{\theta}_{1,f}|}{(\Delta\theta/T)} = \frac{8}{\pi}\frac{J_2/J_1}{\sqrt{1+J_2/J_1}}\left(\frac{T}{T_n}\right)^{-1}\sin^2\left(\frac{\pi}{2}\sqrt{1+J_2/J_1}\left(\frac{T}{T_n}\right)\right) \tag{3.53}$$

with upper bound

$$\frac{|\dot{\theta}_{1,f}|}{(\Delta\theta/T)} \leq \frac{8}{\pi}\frac{J_2/J_1}{\sqrt{1+J_2/J_1}}\left(\frac{T}{T_n}\right)^{-1}. \tag{3.54}$$

Equations (3.53) and (3.54) are straightforward to derive from the forced vibration of Eq. (3.9) using, e.g., the methods in [98, Ch. 2]. Figure 3.7 then plots the upper bound [Eq. (3.54)] as a function of both T/T_n and J_2/J_1. Not surprisingly, lower inertia ratios and higher slew times result in lower residual angular velocities. Figure 3.7 is useful because it charts the design space of possible values for T/T_n and J_2/J_1 that meet a specified requirement on the residual angular velocity. In practice, of course, this requires both a model of the spacecraft (to calculate T_n and J_2/J_1) and the slew angle $\Delta\theta$. Thus, the main utility of Fig. 3.7 is for comparing the flexible excitations due to different slew profiles.

3.4.4 Reducing Flexible Excitation with a Smooth Slew

As previously mentioned, both the "shape" of a slew profile and the ratio T/T_n between the slew maneuver duration T and the natural period T_n determine the disturbance due to the flexible dynamics. To illustrate this, an example smooth slew maneuver is compared to the baseline bang-bang slew maneuver from Sec 3.4.1. The specific smooth slew maneuver discussed here is not necessarily realistic for implementation on an actual spacecraft (e.g., due to the limitations associated with the use of real angular momentum devices [84] or thrusters [99, p. 272–275] for slew actuation). Rather, this discussion is merely intended to demonstrate the advantages of using even a simple smooth slew maneuver to reduce the flexible excitation.

Table 3.1: Non-zero polynomial coefficients for smooth slew maneuver profile

Coefficient	**Value**
a_7	$-20\Delta\theta/T^7$
a_6	$70\Delta\theta/T^6$
a_5	$-84\Delta\theta/T^5$
a_4	$35\Delta\theta/T^4$

Following [80], the smooth slew maneuver considered in this section is based on a higher-order (in this case, 7th-order) polynomial for the slew angle θ:

$$\theta(t) = a_7t^7 + a_6t^6 + a_5t^5 + a_4t^4 + a_3t^3 + a_2t^2 + a_1t + a_0. \tag{3.55}$$

This is the lowest-order polynomial that can simultaneous satisfy boundary conditions on θ and its velocity, acceleration, and jerk (the time derivative of acceleration). Jerk boundary conditions lead to flattening of the acceleration curve in the vicinities of the start and end points. In general, reducing jerk (in this case, via the boundary conditions) reduces the amplitude of the flexible excitations [80–84]. Additionally, momentum control systems are usually jerk-limited [84], and hence, operational considerations may also motivate the use of low-jerk slew trajectories. Table 3.1 lists the non-zero polynomial coefficients derived from these boundary conditions for a slew through an angle $\Delta\theta$ in time T. Figure 3.8 then depicts the corresponding accelerations, velocities, and slew angles as functions of time for a rigid body. All told, the polynomial slew smoothly accelerates and then decelerates a nominally rigid spacecraft from rest-to-rest.

Compared to the baseline bang-bang slew, the polynomial slew requires higher peak angular accelerations to achieve the same total slew angle in the same time. In this

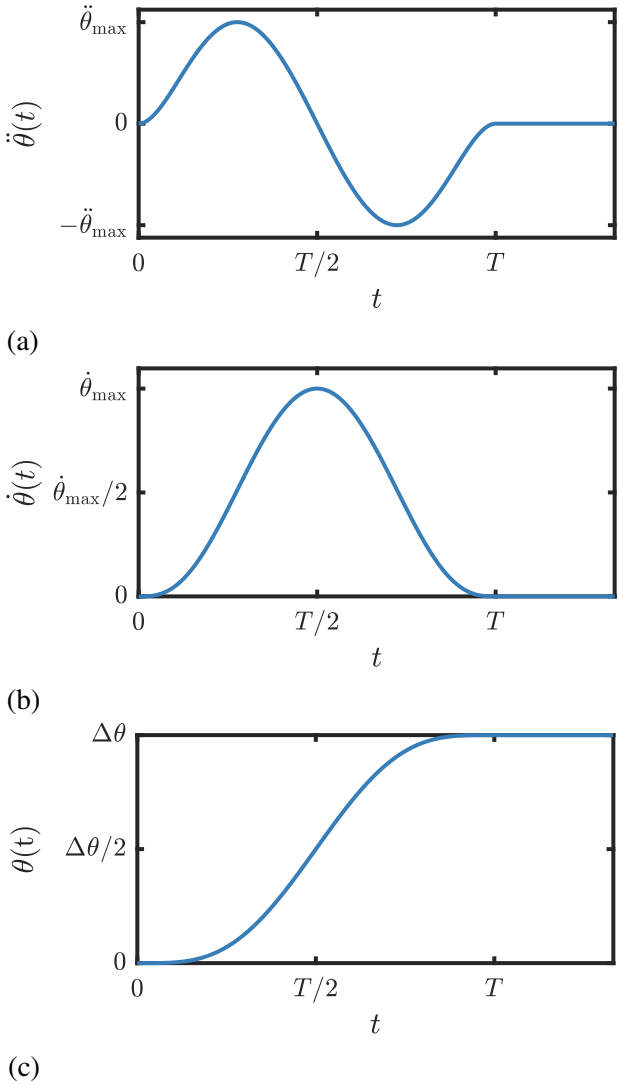

Figure 3.8: Rest-to-rest polynomial slew maneuver profile for a rigid spacecraft: (a) slew acceleration, (b) slew rate, and (c) slew angle.

case, the peak angular acceleration is

$$\ddot{\theta}_{\max} = \frac{84\sqrt{5}\Delta\theta}{25T^2} \tag{3.56}$$

which occurs at times $t = (5 \mp \sqrt{5})T/10$. The peak acceleration is approximately 1.9 times higher than the peak acceleration for the bang-bang slew and leads to proportionally higher peak structural loads. Larger accelerations also lead to larger angular velocities. The peak angular velocity occurs at $t = T/2$ and is given by

$$\dot{\theta}_{\max} = \frac{35\Delta\theta}{16T}. \tag{3.57}$$

This is approximately 1.1 times higher than the peak velocity for the bang-bang slew. Thus, for a given slew time T, the smooth slew also requires a higher average acceleration than the bang-bang slew, which in turn results in proportionally higher average structural loads.

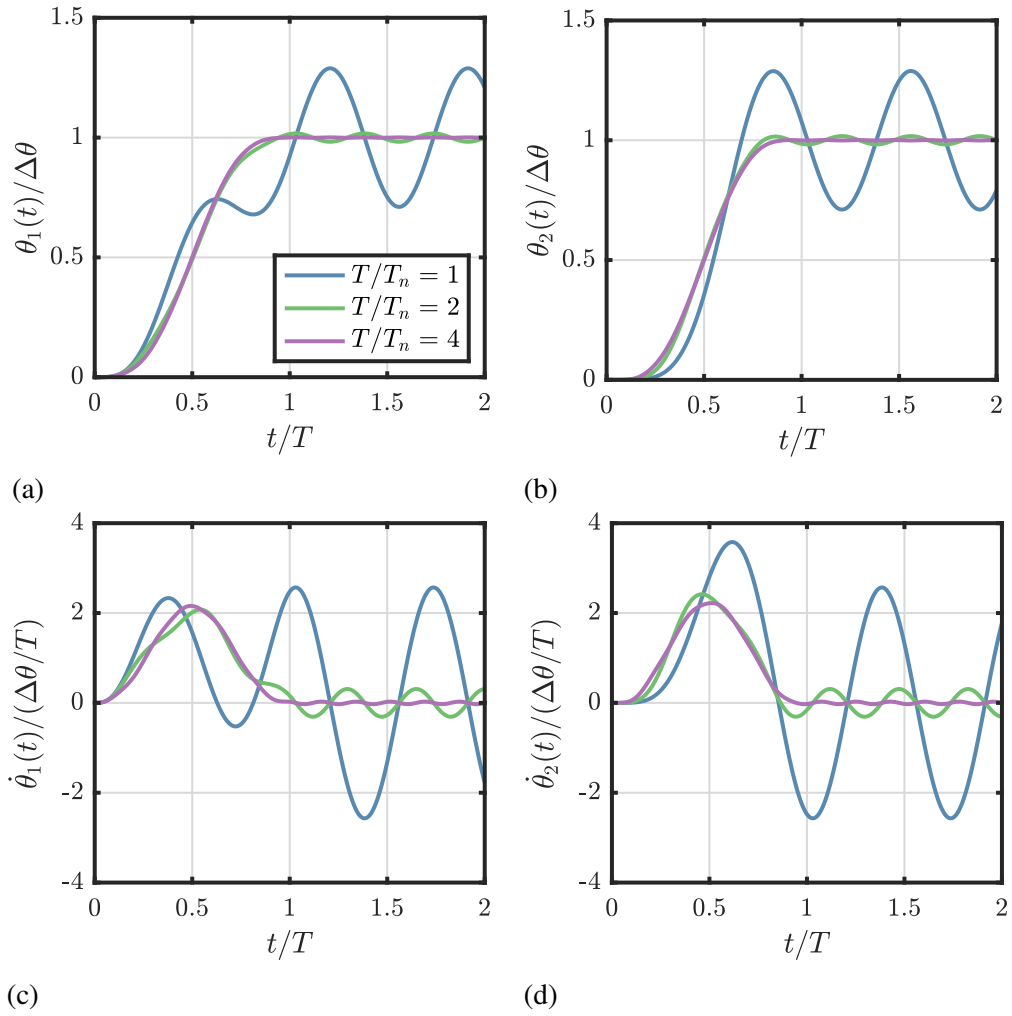

Figure 3.9: Non-dimensionalized transient responses of an undamped canonical flexible spacecraft [Eq. (3.1)] with $J_1 = J_2$ to a polynomial slew maneuver of duration T. (a) orientation of the spacecraft bus J_1; (b) orientation of the flexible appendage J_2; (c) angular velocity of the spacecraft bus J_1; (d) angular velocity of the flexible appendage J_2.

Figure 3.8 depicts the response of a rigid spacecraft during a smooth polynomial slew. To again highlight the differences between a rigid spacecraft and a flexible one, Fig. 3.9 depicts several representative responses of an undamped canonical flexible spacecraft [Eq. (3.1)] with $J_1 = J_2$ to a polynomial slew. Similar to Fig. 3.3, the general trend is that the magnitude of the disturbance due to the flexible

dynamics again decreases as the duration of the slew increases, i.e., as the ratio T/T_n increases. In particular, with $T/T_n = 4$, the response of the flexible spacecraft closely approximates the response of the rigid spacecraft from Fig. 3.8. Compared to the responses to a bang-bang slew from Fig. 3.3, the larger peak accelerations during the polynomial slew result in larger-amplitude transient oscillations for small values of T/T_n, e.g., for $T/T_n = 1$. However, as T/T_n increases, the amplitude of these oscillations decreases faster for the polynomial slew than it does for the bang-bang slew. This implies that there is a critical value of T/T_n beyond which the disturbance due to the flexible dynamics is always smaller for a polynomial slew than it is for a bang-bang slew.

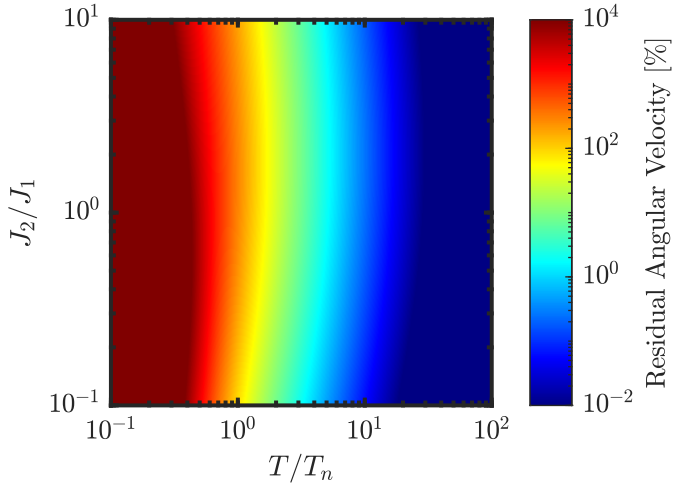

Figure 3.10: Amplitude of the residual angular velocity for the smooth polynomial slew maneuver.

Analogous to Fig. 3.7, Fig. 3.10 plots an upper bound for the quantity $|\dot{\theta}_{1,f}|/(\Delta\theta/T)$ as a function of both T/T_n and J_2/J_1 for the polynomial slew. For $T/T_n > 1$, Fig. 3.10 demonstrates that the polynomial slew often reduces the amplitude of the residual angular velocity by upwards of two orders of magnitude compared to the reference bang-bang slew. In other words, the polynomial slew significantly lowers the excitation of the flexible mode despite its higher peak velocity and acceleration. Thus, for a given requirement on the amplitude of the residual angular velocity, the polynomial slew achieves significantly faster slews than its bang-bang counterpart.

3.5 Discussion

This chapter has described standard modeling approaches for flexible spacecraft, specifically those that pertain to attitude dynamics and control, and the subsequent definition of slew maneuver requirements. The chapter started with a description of

the canonical model for flexible spacecraft attitude dynamics and control, a 2-DOF floating oscillator, and then showed how to rigorously derive the canonical model from an arbitrary finite element model using the Craig-Bampton method. Besides its consistency with the canonical model, the Craig-Bampton method is advantageous because it facilitates the systematic selection of dominant modes for various types of flexible spacecraft dynamics models.

The chapter then analyzed slew maneuver requirements for flexible spacecraft. There are two important results from this analysis. The first is that settling time is a poor metric for quantifying slew times. Instead, a more suitable metric is proposed based on the magnitude of the disturbance due to the flexible dynamics. The second is that the ratio between the slew duration and natural period and the shape of the slew profile together determine the magnitude of this disturbance. To emphasize this, it is shown that a 7th-order polynomial slew maneuver reduces the amplitude of the disturbance due to the flexible dynamics by upwards of two orders of magnitude relative to a baseline bang-bang slew.

The analysis of slew maneuver requirements has demonstrated that flexible spacecraft can achieve significantly faster slew times by using a properly shaped slew maneuver profile. Consequently, there is a significant opportunity to extend modern computational optimal control methods to improve flexible spacecraft slew performance. In particular, modern robust optimal control methods [100–103] can design slew maneuvers that are simultaneously robust to the uncertainties inherent to flexible spacecraft structures, minimize the magnitude of the flexible excitation either during or after the maneuver, and satisfy any constraints on the system, e.g., on maximum angular velocity or torque. The uncertainties are driven, at least in part, by the inability to test these structures in representative 0-g environments before launch [14–18]. Perhaps most importantly, using a tailored slew profile to minimize structural excitations does not necessarily require changes to a spacecraft's attitude control system (ACS). Thus, these maneuvers can be flown using an ACS designed with classical control methods [63, 64], ultimately reducing risk for their eventual flight implementation. This is left to future work.

Chapter 4

REVIEW OF GEOMETRICALLY EXACT BEAM THEORY

4.1 Introduction

Beam theories are widely used for the nonlinear analysis of slender structures in applications ranging from very flexible aircraft wings [104, 105], helicopter rotors [106–108], and wind turbine blades [109, 110] to robotic manipulators [111, 112] (especially soft robotic manipulators [113, 114]), flexible multibody systems [115, 116], and even DNA [117]. Slender structures have a single dominant dimension which makes them *dimensionally reducible*, i.e., they can be accurately and efficiently modeled as 1D. Many ultralight flexible spacecraft, including heliogryos [118], solar sails [9], and space solar power satellites [13], are assembled from slender structural components. As a result, beam theories provide computationally efficient tools for the preliminary design, analysis, and optimization of these spacecraft. In fact, many developments in the history of beam theory have been spurred by problems associated with the modeling (and to some extent, control) of flexible spacecraft and their structural components; see e.g., [119–122]. This trend is likely to continue.

Recent years have seen a proliferation of nonlinear beam theories and their finite element implementations in the literature. Examples include Reissner-Simo geometrically exact beam theory (GEBT) [32–34], the corotational method [123], the absolute nodal coordinate formulation [68, Ch. 7], and the intrinsic formulation [105, 124, 125], among others; for a detailed discussion of the advantages and disadvantages of some of these theories, see e.g., [126–128] and the references therein. Of these, Reissner-Simo GEBT (hereafter referred to as GEBT) is generally regarded as one of the highest performing (and certainly one of the most well-developed) nonlinear beam theories. As a result, GEBT is the nonlinear beam theory of choice in what follows. GEBT is a nonlinear generalization of classical Timoshenko beam theory featuring axial, shearing, bending, and torsional deformation modes. Various authors sometimes refer to GEBT as the Cosserat theory of rods.[1]

[1] In structural mechanics, nonlinear generalizations of linear, small-deflection beam theories are typically referred to as rod theories. Confusingly, however, much of the existing literature on the finite element implementations of these rod theories describes the resulting finite elements as beam finite elements. For this reason, the term "beam" is preferred in this and subsequent chapters, although generally speaking, "beam" and "rod" can be used interchangeably.

What makes a beam theory "geometrically exact"? In the present context, geometrical exactness is interpreted in the sense of Simo [34]. Paraphrasing [34], Crisfield and Jelenić [129] state that a beam theory is considered geometrically exact when

> . . . the relationships between the configuration and the strain measures are consistent with the virtual work principle and the equilibrium equations at a deformed state *regardless of the magnitude of displacements, rotations, and strains*.

In other words, geometrical exactness implies that a beam theory is capable of modeling arbitrarily large elastic deformations, including those associated with finite strains. In practice, however, existing GEBTs are usually limited to linear-elastic deformations by their lack of appropriate finite strain constitutive models [129]. As a result, these theories can typically only model arbitrarily large deformations provided the local stresses/strains at each point in the beam remain linear-elastic. Nonlinearities due to large, linear-elastic deformations are referred to as geometric nonlinearities. In the sequel, geometrical exactness is to be understood in the context of these geometric nonlinearities.

The remainder of this chapter provides the theoretical foundation for the quaternion-based geometrically exact beam finite elements developed in Chapters 5 and 6. To that end, Secs. 4.2 and 4.3 briefly review finite rotations and the quaternion parameterization of rotations. For more exhaustive treatments, see e.g., [70, 130–133]. To avoid any potential ambiguities, Secs. 4.2 and 4.3 also rigorously define the rotation and quaternion conventions used throughout the thesis. A finite rotation parameterization, like the quaternion, describes the orientation of the beam's reference axis in GEBT. Consequently, these results are used extensively throughout Chapters 5 and 6. Sec. 4.4 then reviews the kinematics of Reissner-Simo GEBT. This discussion closely follows [129]. Sec. 4.5 introduces the geometrically exact material strain measures and defines the strain energy. From there, Secs. 4.6 and 4.7 evaluate the kinetic energy and external virtual work. The strain energy, kinetic energy, and external virtual work are the inputs to the variational principle in Sec. 4.8, which in turn is the starting point for the derivations of the continuous-time and discrete-time equations of motion in Chapters 5 and 6, respectively.

4.2 Finite Rotations

Two reference frames are considered: a spatial (inertial) reference frame and a material (body) reference frame. The material frame coincides with the initial (undeformed) configuration of an elastic body and can be considered a local corotational frame. An arbitrary material vector $\mathbf{X} \in \mathbb{R}^3$, i.e., a vector expressed in the material frame, is related to the corresponding spatial vector $\mathbf{x} \in \mathbb{R}^3$ by

$$\mathbf{x} = \mathbf{\Lambda}\mathbf{X} \tag{4.1}$$

where $\mathbf{\Lambda} \in \mathrm{SO}(3)$ is the matrix of the passive rotation (reference frame transformation) from the material frame to the spatial frame. Physically, $\mathbf{\Lambda}$ can also be interpreted as the active rotation that aligns the axes of the spatial frame with those of the material frame, although the passive rotation convention is preferred here. A detailed discussion of the differences between active and passive rotations is outside the scope of this thesis; instead, see [131, 133, 134]. Alternatively, $\mathbf{\Lambda}$ can be understood as the deformation gradient of spherical motion, i.e., the motion of a rigid body about a spatially fixed point. The notation $\mathrm{SO}(3)$ denotes the special orthogonal group, i.e., the 3D rotation group defined such that

$$\mathrm{SO}(3) = \left\{ \mathbf{\Lambda} \in \mathbb{R}^{3\times 3} : \mathbf{\Lambda}^T\mathbf{\Lambda} = \mathbf{\Lambda}\mathbf{\Lambda}^T = \mathbf{I}_{3\times 3},\ \det(\mathbf{\Lambda}) = 1 \right\}. \tag{4.2}$$

The orthogonality condition in Eq. (4.2) implies that $\mathbf{\Lambda}$, and hence, $\mathrm{SO}(3)$, can be parameterized by three independent variables, a so-called three-parameter rotation representation. $\mathrm{SO}(3)$ is a Lie group; for an introduction to Lie groups, see e.g., [135, Secs. 9.1–9.2].

Infinitesimal rotations are required for the variational formulations in Chapters 5 and 6. The remainder of this section derives the infinitesimal material and spatial rotations corresponding to a finite rotation. These developments largely follow [70, Sec. 3.5.1].

From Eq. (4.1), the infinitesimal spatial vector $\delta\mathbf{x}$ can be expressed as

$$\delta\mathbf{x} = \delta\mathbf{\Lambda}\mathbf{X} = \delta\mathbf{\Lambda}\mathbf{\Lambda}^T\mathbf{x} = [\delta\boldsymbol{\theta}]_\times\mathbf{x} \tag{4.3}$$

where $\mathbf{X}$ is assumed to be constant in the material frame, $[\delta\boldsymbol{\theta}]_\times = \delta\mathbf{\Lambda}\mathbf{\Lambda}^T$ is the matrix of infinitesimal spatial rotations, and $[\mathbf{v}]_\times$ denotes the skew-symmetric matrix

$$[\mathbf{v}]_\times = \begin{bmatrix} 0 & -v_3 & v_2 \\ v_3 & 0 & -v_1 \\ -v_2 & v_1 & 0 \end{bmatrix} \tag{4.4}$$

corresponding to an arbitrary vector $\mathbf{v} \in \mathbb{R}^3$. The skew-symmetry of $[\delta\boldsymbol{\theta}]_\times$ follows from the orthogonality of $\boldsymbol{\Lambda}$. The coefficients of the axial vector $\delta\boldsymbol{\theta}$ corresponding to $[\delta\boldsymbol{\theta}]_\times$ are the infinitesimal angular displacements expressed in the spatial frame. Similarly, the infinitesimal material vector $\mathbf{X}$ satisfies the identity $\delta\mathbf{x} = \boldsymbol{\Lambda}\delta\mathbf{X}$, which together with Eq. (4.3) implies that

$$\delta\mathbf{X} = \boldsymbol{\Lambda}^T\delta\boldsymbol{\Lambda}\mathbf{X} = [\delta\boldsymbol{\Theta}]_\times\mathbf{X} \tag{4.5}$$

where $[\delta\boldsymbol{\Theta}]_\times = \boldsymbol{\Lambda}^T\delta\boldsymbol{\Lambda}$ is the matrix of infinitesimal material rotations. The skew-symmetry again follows from the orthogonality of $\boldsymbol{\Lambda}$. The coefficients of the axial vector $\delta\boldsymbol{\Theta}$ corresponding to $[\delta\boldsymbol{\Theta}]_\times$ are the infinitesimal angular displacements expressed in the material frame.

The set of skew-symmetric matrices in $\mathbb{R}^{3\times3}$ forms the Lie algebra of SO(3), denoted $\mathfrak{so}(3)$, which is isomorphic to $\mathbb{R}^3$ via Eq. (4.4). Importantly, $\mathfrak{so}(3)$ is the space tangent to SO(3); $[\delta\boldsymbol{\theta}]_\times$ and $[\delta\boldsymbol{\Theta}]_\times$ are respectively tangent to SO(3) at the current rotation $\boldsymbol{\Lambda}$ and at identity, i.e, in the undeformed configuration. Defining variational principles with respect to infinitesimal spatial and material rotations results in Updated and Total Lagrangian formulations, respectively [121].

From Eqs. (4.3) and (4.5), $[\delta\boldsymbol{\theta}]_\times$ and $[\delta\boldsymbol{\Theta}]_\times$ are related by $\boldsymbol{\Lambda}[\delta\boldsymbol{\Theta}]_\times = [\delta\boldsymbol{\theta}]_\times\boldsymbol{\Lambda}$, from which it follows that the corresponding vectors are related by

$$\delta\boldsymbol{\theta} = \boldsymbol{\Lambda}\delta\boldsymbol{\Theta}. \tag{4.6}$$

Equations (4.3) and (4.5) demonstrate that infinitesimal rotations must be three-dimensional, which is intuitive because any physical rotation can be parameterized by three independent variables. Due to the Lie group structure of SO(3), neither $\delta\boldsymbol{\theta}$ nor $\delta\boldsymbol{\Theta}$ are directly integrable to obtain a suitable three-parameter rotation representation, i.e., $\boldsymbol{\Lambda} \neq \boldsymbol{\Lambda}(\boldsymbol{\theta})$ and $\boldsymbol{\Lambda} \neq \boldsymbol{\Lambda}(\boldsymbol{\Theta})$.

4.3 Unit Quaternions

A quaternion $\mathbf{p} \in \mathbb{H}$ is a linear operator isomorphic to $\mathbb{R}^4$, i.e., a quaternion can be explicitly represented as a vector $\mathbf{p} \in \mathbb{R}^4$. In this thesis, quaternions follow the Hamiltonian convention [133], i.e., they are right-handed (so-called right quaternions [134]) and define a passive rotation (reference frame transformation) from a local (material) frame to a global (spatial) one, with the caveat that the scalar part

of the quaternion appears last.[2] Hence, a quaternion is written as

$$\mathbf{p}^T = \begin{bmatrix} \mathbf{p}_v^T & p_s \end{bmatrix} \tag{4.7}$$

where $\mathbf{p}_v \in \mathbb{R}^3$ and $p_s \in \mathbb{R}$ are respectively referred to as its vector and scalar parts. A detailed discussion of the various quaternion conventions is outside the scope of this thesis; interested readers are instead referred to [133, 136]. In general, a quaternion $\mathbf{p} \in \mathbb{H}$ can have an arbitrary magnitude.

It is well known that the set of unit quaternions

$$\mathbb{H}_1 = \left\{ \mathbf{p} \in \mathbb{H} : \mathbf{p}^T\mathbf{p} - 1 = 0 \right\} \subset \mathbb{H} \tag{4.8}$$

defines a double cover for SO(3); i.e., a unit quaternion defines a four-parameter representation of SO(3) such that both $\mathbf{p}$ and $-\mathbf{p}$ represent the same physical rotation [133]. The double cover can be observed by considering the rotation matrix $\mathbf{\Lambda}(\mathbf{p}) \in \mathrm{SO}(3)$ parameterized by a unit quaternion $\mathbf{p} \in \mathbb{H}_1$ [133]:

$$\mathbf{\Lambda}(\mathbf{p}) = \left(p_s^2 - \mathbf{p}_v^T\mathbf{p}_v\right)\mathbf{I}_{3\times 3} + 2p_s[\mathbf{p}_v]_\times + 2\mathbf{p}_v\mathbf{p}_v^T. \tag{4.9}$$

Since $\mathbf{\Lambda}(\mathbf{p})$ is quadratic in $\mathbf{p}$, $\mathbf{\Lambda}(\mathbf{p}) = \mathbf{\Lambda}(-\mathbf{p})$. Due to the unit norm constraint, $\mathbb{H}_1$ defines the unit three-sphere $\mathbb{S}^3$, i.e., a hypersphere in $\mathbb{R}^4$. Various algorithms exist for extracting quaternions from rotation matrices; see e.g., [137, 138].

In the sequel, the terms quaternion and unit quaternion are used interchangeably, and unless otherwise stated, both terms should be understood to refer to a unit quaternion. Unit quaternions are also variously referred to as Euler-Rodrigues symmetric parameters [131], or more simply, as Euler parameters [70, Ch. 4] in the literature, but again, the term quaternion is preferred here.

4.3.1 Quaternion Algebra

The quaternion product, denoted $\otimes$, is used to implement rotations. Given quaternions $\mathbf{p}_1, \mathbf{p}_2 \in \mathbb{H}_1$, the quaternion product is defined as

$$\mathbf{p}_2 \otimes \mathbf{p}_1 = \mathbf{L}(\mathbf{p}_2)\mathbf{p}_1 = \mathbf{R}(\mathbf{p}_1)\mathbf{p}_2 \tag{4.10}$$

where $\mathbf{L}(\mathbf{p}), \mathbf{R}(\mathbf{p}) \in \mathbb{R}^{4\times 4}$ are the orthogonal matrices

$$\mathbf{L}(\mathbf{p}) = \begin{bmatrix} \mathbf{G}(\mathbf{p}) & \mathbf{p} \end{bmatrix}, \tag{4.11}$$

$$\mathbf{R}(\mathbf{p}) = \begin{bmatrix} \mathbf{H}(\mathbf{p}) & \mathbf{p} \end{bmatrix} \tag{4.12}$$

[2] The quaternions defined herein are mathematically equivalent to quaternions that are right-handed and define the active rotation that aligns the axes of the global (spatial) frame with the local (material) one [133]. This latter interpretation is often preferred in structural mechanics.

with $\mathbf{G}(\mathbf{p}), \mathbf{H}(\mathbf{p}) \in \mathbb{R}^{4\times 3}$ given by

$$\mathbf{G}(\mathbf{p}) = \begin{bmatrix} p_s\mathbf{I}_{3\times 3} + [\mathbf{p}_v]_\times \\ -\mathbf{p}_v^T \end{bmatrix}, \tag{4.13}$$

$$\mathbf{H}(\mathbf{p}) = \begin{bmatrix} p_s\mathbf{I}_{3\times 3} - [\mathbf{p}_v]_\times \\ -\mathbf{p}_v^T \end{bmatrix}. \tag{4.14}$$

The matrices $\mathbf{L}(\mathbf{p})$ and $\mathbf{R}(\mathbf{p})$ are rotation matrices for $\mathbb{H}_1$. However, unlike rotation matrices for $\mathbb{R}^3$, $\mathbf{L}(\mathbf{p})$ and $\mathbf{R}(\mathbf{p})$ commute, i.e., $\mathbf{L}(\mathbf{p}_1)\mathbf{R}(\mathbf{p}_2) = \mathbf{R}(\mathbf{p}_2)\mathbf{L}(\mathbf{p}_1)$ and $\mathbf{L}(\mathbf{p}_1)\mathbf{R}^T(\mathbf{p}_2) = \mathbf{R}^T(\mathbf{p}_2)\mathbf{L}(\mathbf{p}_1)$. It is straightforward to show that $\mathbf{G}(\mathbf{p})$ and $\mathbf{H}(\mathbf{p})$ satisfy the following useful identities:

$$\mathbf{G}(\mathbf{p})^T\mathbf{G}(\mathbf{p}) = \mathbf{H}(\mathbf{p})^T\mathbf{H}(\mathbf{p}) = \mathbf{I}_{3\times 3}, \tag{4.15}$$

$$\mathbf{G}(\mathbf{p})\mathbf{G}^T(\mathbf{p}) = \mathbf{H}(\mathbf{p})\mathbf{H}^T(\mathbf{p}) = \mathbf{I}_{4\times 4} - \mathbf{p}\mathbf{p}^T, \tag{4.16}$$

$$\mathbf{G}^T(\mathbf{p})\mathbf{p} = \mathbf{H}^T(\mathbf{p})\mathbf{p} = \mathbf{0}_{3\times 1}. \tag{4.17}$$

Using Eqs. (4.9) and (4.10), it can then be shown that the quaternion product satisfies the identity

$$\mathbf{\Lambda}(\mathbf{p}_2 \otimes \mathbf{p}_1) = \mathbf{\Lambda}(\mathbf{p}_2)\mathbf{\Lambda}(\mathbf{p}_1). \tag{4.18}$$

Hence, the quaternion product represents successive rotations, meaning it is associative but not commutative.

Every unit quaternion $\mathbf{p}$ has an inverse $\mathbf{p}^{-1}$ equal to its conjugate [133]; i.e., $\mathbf{p}^{-1} = \mathbf{p}^*$. The conjugate $\mathbf{p}^*$ represents the opposite rotation and is obtained by negating the vector part of the quaternion; i.e.,

$$\mathbf{p}^* = \begin{bmatrix} -\mathbf{p}_v \\ p_s \end{bmatrix} = \begin{bmatrix} -\mathbf{I}_{3\times 3} & \mathbf{0}_{3\times 1} \\ \mathbf{0}_{1\times 3} & 1 \end{bmatrix} \begin{bmatrix} \mathbf{p}_v \\ p_s \end{bmatrix} = \mathbf{Z}\mathbf{p}. \tag{4.19}$$

The matrix $\mathbf{Z}$ is referred to as the quaternion conjugator. The conjugate quaternion satisfies the identity

$$\mathbf{p} \otimes \mathbf{p}^* = \mathbf{p}^* \otimes \mathbf{p} = \begin{bmatrix} \mathbf{0}_{3\times 1} \\ 1 \end{bmatrix} = \mathbf{I}_p \tag{4.20}$$

where $\mathbf{I}_p$ is the identity quaternion. Likewise, any vector $\mathbf{v} \in \mathbb{R}^3$ can be expressed as an equivalent (non-unit) quaternion in $\mathbb{H}$ with zero scalar part, as follows:

$$\hat{\mathbf{v}} = \begin{bmatrix} \mathbf{v} \\ 0 \end{bmatrix} = \begin{bmatrix} \mathbf{I}_{3\times 3} \\ \mathbf{0}_{1\times 3} \end{bmatrix} \mathbf{v} = \mathbf{T}\mathbf{v} \tag{4.21}$$

where $\mathbf{T}^T\mathbf{T} = \mathbf{I}_{3\times 3}$. Using Eqs. (4.11) to (4.14), it is straightforward to prove the following identities:

$$\mathbf{L}(\mathbf{Zp}) = \mathbf{L}^T(\mathbf{p}), \tag{4.22}$$

$$\mathbf{R}(\mathbf{Zp}) = \mathbf{R}^T(\mathbf{p}), \tag{4.23}$$

$$\mathbf{L}(\mathbf{p})\mathbf{T} = \mathbf{G}(\mathbf{p}), \tag{4.24}$$

$$\mathbf{R}(\mathbf{p})\mathbf{T} = \mathbf{H}(\mathbf{p}) \tag{4.25}$$

which hold for $\mathbf{p} \in \mathbb{H}$.

Equations (4.19) and (4.21) facilitate the rotation of vectors using the quaternion product. Specifically, the pure rotation $\mathbf{x} = \mathbf{\Lambda}(\mathbf{p})\mathbf{X}$ is equivalent to

$$\mathbf{Tx} = \mathbf{p} \otimes \mathbf{TX} \otimes \mathbf{p}^* \tag{4.26}$$

which can be simplified using Eq. (4.10), the commutativity of $\mathbf{L}(\mathbf{p})$ and $\mathbf{R}(\mathbf{p})$, and Eqs. (4.22) to (4.25) to obtain

$$\mathbf{x} = \mathbf{T}^T\mathbf{L}(\mathbf{p})\mathbf{R}^T(\mathbf{p})\mathbf{TX} = \mathbf{T}^T\mathbf{R}^T(\mathbf{p})\mathbf{L}(\mathbf{p})\mathbf{TX} = \mathbf{H}^T(\mathbf{p})\mathbf{G}(\mathbf{p})\mathbf{X} = \mathbf{\Lambda}(\mathbf{p})\mathbf{X}. \tag{4.27}$$

Equation (4.27) contains several useful quaternion identities.

4.3.2 Infinitesimal Quaternions

Any variational principle involving a quaternion independent variable $\mathbf{p}$ requires an expression for the infinitesimal quaternion $\delta\mathbf{p}$. This requires a mapping from the space tangent to $\mathbb{H}_1$ to $\mathfrak{so}(3)$, which is developed next.

Equation (4.26) provides the starting point for the derivations of the mappings from $\delta\boldsymbol{\theta}$ and $\delta\mathbf{\Theta}$ to $\delta\mathbf{p}$. These relationships are fundamental to understanding the quaternion representation of $\mathrm{SO}(3)$. The derivation requires the identity

$$\delta\mathbf{p}^T\mathbf{p} = 0 \tag{4.28}$$

which follows directly from the unit norm constraint [Eq. (4.8)]. Thus, $\delta\mathbf{p}$ and $\mathbf{p}$ are orthogonal, which implies that $\delta\mathbf{p}$ occupies the 3D hyperplane tangent to $\mathbb{H}_1$ at $\mathbf{p}$.

Using Eq. (4.26), the infinitesimal spatial vector $\delta\mathbf{x}$ can be expressed in terms of the infinitesimal quaternion $\delta\mathbf{p}$ as follows:

$$\mathbf{T}\delta\mathbf{x} = \delta\mathbf{p} \otimes \mathbf{TX} \otimes \mathbf{p}^* + \mathbf{p} \otimes \mathbf{TX} \otimes \delta\mathbf{p}^* \tag{4.29}$$

which is analogous to Eq. (4.3). The definition of the quaternion product [Eq. (4.10)], Eqs. (4.23) through (4.25), and the commutativity of $\mathbf{L}(\mathbf{p})$ and $\mathbf{R}(\mathbf{p})$ are then used

to simplify Eq. (4.29). Substituting $\mathbf{X} = \mathbf{\Lambda}^T(\mathbf{p})\mathbf{x}$ and comparing the resulting expression with Eq. (4.3) reveals that the quaternion representation of $[\delta\boldsymbol{\theta}]_\times$ is

$$[\delta\boldsymbol{\theta}]_\times = \left(\mathbf{H}^T(\delta\mathbf{p})\mathbf{G}(\mathbf{p}) + \mathbf{H}^T(\mathbf{p})\mathbf{G}(\delta\mathbf{p})\right)\mathbf{\Lambda}^T(\mathbf{p}). \tag{4.30}$$

The matrix of infinitesimal material rotations then follows from Eq. (4.6) as

$$[\delta\mathbf{\Theta}]_\times = \mathbf{\Lambda}^T(\mathbf{p})\left(\mathbf{H}^T(\delta\mathbf{p})\mathbf{G}(\mathbf{p}) + \mathbf{H}^T(\mathbf{p})\mathbf{G}(\delta\mathbf{p})\right). \tag{4.31}$$

The corresponding vectors are given by

$$\delta\boldsymbol{\theta} = 2\mathbf{H}^T(\mathbf{p})\delta\mathbf{p}, \tag{4.32}$$

$$\delta\mathbf{\Theta} = 2\mathbf{G}^T(\mathbf{p})\delta\mathbf{p} \tag{4.33}$$

where Eqs. (4.30) and (4.31) are simplified into Eqs. (4.32) and (4.33), respectively, using $\mathbf{p}^T\mathbf{p} = 1$ and Eq. (4.28). Equivalently,

$$\delta\mathbf{p} = \frac{1}{2}\mathbf{H}(\mathbf{p})\delta\boldsymbol{\theta} = \frac{1}{2}\mathbf{G}(\mathbf{p})\delta\mathbf{\Theta} \tag{4.34}$$

which is straightforward to show using Eqs. (4.16) and (4.28).

Based on Eq. (4.34), the matrices $\mathbf{G}(\mathbf{p})$ and $\mathbf{H}(\mathbf{p})$ map infinitesimal rotations in $\mathfrak{so}(3)$ to the 3D hyperplane tangent to $\mathbb{H}_1$. Alternatively, they can be interpreted as rotation Jacobians that allow infinitesimal quaternions to be corrected a posteriori for the Lie group structure of $\mathbb{H}_1$ [139]. In this way, a variational principle can treat a quaternion independent variable $\mathbf{p}$ as a vector in $\mathbb{R}^4$, and then subsequently use Eq. (4.34) to correct for the Lie group structure of $\mathbb{H}_1$. Thus, Eq. (4.34) allows quaternion Lie group formulations to be developed without differential geometry.

While useful for theoretical developments, Eq. (4.34) does not respect the quaternion unit norm constraint. Consequently, using Eq. (4.34) to evaluate the infinitesimal (or incremental) quaternion corresponding to an infinitesimal (or incremental) rotation in practical applications is ill-advised. Following [139], infinitesimal quaternions are instead related to the corresponding infinitesimal rotation by

$$\delta\mathbf{p} = \text{cay}(\delta\boldsymbol{\theta}/2) = \text{cay}(\delta\mathbf{\Theta}/2) \tag{4.35}$$

where the function $\text{cay}(\cdot)$ is known as the Cayley map [131, p. 62]. The Cayley map relates a Rodrigues parameter [131, 132] (also sometimes referred to as a Gibbs vector) $\boldsymbol{\gamma}$ to the corresponding quaternion $\mathbf{p}$, as follows:

$$\mathbf{p} = \text{cay}(\boldsymbol{\gamma}) = \frac{1}{\sqrt{1+\boldsymbol{\gamma}^T\boldsymbol{\gamma}}}\begin{bmatrix}\boldsymbol{\gamma}\\ 1\end{bmatrix} \tag{4.36}$$

which has unit norm and the inverse

$$\boldsymbol{\gamma} = \text{cay}^{-1}(\mathbf{p}) = \frac{\mathbf{p}_v}{p_s}. \tag{4.37}$$

With material (spatial) rotations, Eq. (4.35) right-multiplies (left-multiplies) the corresponding quaternion $\mathbf{p}$.

Rodrigues parameters are a computationally efficient three-parameter rotation representation which projects $\mathbb{H}_1$ onto a 3D plane. To second-order, an infinitesimal rotation is equal to twice the corresponding infinitesimal Rodrigues vector; e.g., for material rotations, $\delta\boldsymbol{\Theta} = 2\delta\boldsymbol{\gamma}$ [132, p. 59]. This property makes the Cayley map useful for updating quaternions.[3]

4.4 Kinematic Description

GEBT uses the kinematic assumptions of Timoshenko beam theory to reduce a slender 3D continuum to a space curve in $\mathbb{R}^3$ with cross-sectional stiffness and inertia properties. With Timoshenko beam kinematics, each cross-section is rigid in its plane, meaning the cross-sections remain plane but not necessarily normal to the beam's deformed reference axis. This implies that the shear stresses and strains are constants over each plane of the cross-section. The space curve coincides with the beam's reference axis. The most convenient choice for the reference axis is the locus of cross-sectional centroids, which for homogeneous, isotropic materials corresponds with both the elastic (neutral) axis and the locus of cross-sectional mass centers. However, in general, other choices are possible, and for non-homogeneous cross-sections, the reference axis may not coincide with either the neutral axis or the locus of cross-sectional mass centers. The space curve is located in an inertial (spatial) reference frame described by the standard unit basis vectors

$$\mathbf{e}_1 = \begin{bmatrix} 1 \\ 0 \\ 0 \end{bmatrix}, \qquad \mathbf{e}_2 = \begin{bmatrix} 0 \\ 1 \\ 0 \end{bmatrix}, \qquad \mathbf{e}_3 = \begin{bmatrix} 0 \\ 0 \\ 1 \end{bmatrix}.$$

Two configurations are considered: an initial (undeformed) configuration and a deformed configuration; see Fig. 4.1. The initial position of the beam's reference axis is described by the space curve $s \longrightarrow \mathbf{x}_0(s) \in \mathbb{R}^3$ of length ℓ which is parameterized

[3] Alternatives to the Cayley map include the quaternion exponential map [133, 140] and Modified Rodrigues parameters [131, 132]. The quaternion exponential map is popular in nonlinear mechanics, although evaluating the requisite trigonometric functions makes it more computationally expensive than the Cayley map. For practical purposes, these three methods are equivalent.

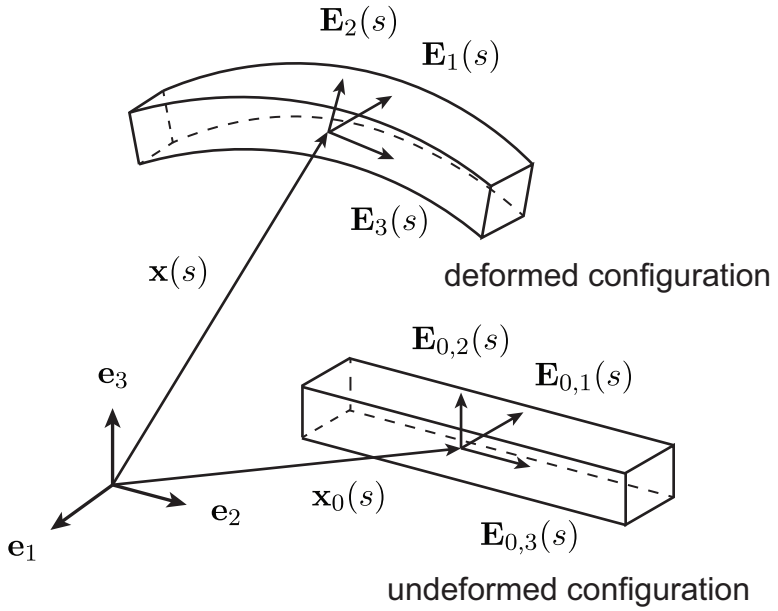

Figure 4.1: Kinematic description of an initially straight Reissner-Simo geometrically exact beam.

by the arc length coordinate $s \in [0, \ell]$. The corresponding cross-sectional orientations are given by the orientations of the local body (material) reference frame with orthonormal unit basis vectors $s \rightarrow \mathbf{E}_{0,1}(s),\ \mathbf{E}_{0,2}(s),\ \mathbf{E}_{0,3}(s) \in \mathbb{R}^3$. These orthonormal basis vectors are commonly referred to as *directors* in the literature; see e.g., [141–143].

Throughout this thesis, the convention is that $\mathbf{E}_{0,1}(s)$ and $\mathbf{E}_{0,2}(s)$ are in the plane of the cross-section at s and $\mathbf{E}_{0,3}(s)$ is tangent to the reference axis, i.e.,

$$\mathbf{E}_{0,3}(s) = \mathbf{x}_0'(s). \tag{4.38}$$

$\mathbf{E}_{0,1}(s)$ and $\mathbf{E}_{0,2}(s)$ are commonly directed parallel to the cross-section's principal axes of inertia, although again, other choices are possible. $\mathbf{E}_{0,1}(s)$, $\mathbf{E}_{0,2}(s)$, and $\mathbf{E}_{0,3}(s)$ define the transformation

$$s \rightarrow \mathbf{\Lambda}_0(s) = \begin{bmatrix} \mathbf{E}_{0,1}(s) & \mathbf{E}_{0,2}(s) & \mathbf{E}_{0,3}(s) \end{bmatrix}^T \in \mathrm{SO}(3) \tag{4.39}$$

from the material reference frame to the spatial one; i.e., $\mathbf{e}_i = \mathbf{\Lambda}_0(s)\mathbf{E}_{0,i}(s)$ for $i = 1,\ 2,\ 3$. The beam's initial configuration is fully described by the position of the reference axis and the corresponding cross-sectional orientation at s. Given some initial configuration $s \rightarrow (\mathbf{x}_0(s), \mathbf{\Lambda}_0(s)) \in \mathbb{R}^3 \times \mathrm{SO}(3)$, known forcing, and initial conditions (if applicable), the goal of GEBT is to determine the beam's subsequent deformed configuration(s).

The beam's deformed configuration is defined analogously. Specifically, the deformed reference axis is described by the space curve $s \to \mathbf{x}(s) \in \mathbb{R}^3$, although in this case, the space curve is not necessarily of length ℓ to allow stretching of the reference axis. Likewise, the cross-sectional orientations are represented by the orthonormal unit basis vectors $s \to \mathbf{E}_1(s),\ \mathbf{E}_2(s),\ \mathbf{E}_3(s) \in \mathbb{R}^3$, which together define the transformation

$$s \to \mathbf{\Lambda}(s) = \begin{bmatrix} \mathbf{E}_1(s) & \mathbf{E}_2(s) & \mathbf{E}_3(s) \end{bmatrix}^T \in \mathrm{SO}(3) \tag{4.40}$$

from the deformed material reference frame to the spatial one; i.e., $\mathbf{e}_i = \mathbf{\Lambda}(s)\mathbf{E}_i(s)$ for $i = 1,\ 2,\ 3$. $\mathbf{E}_1(s)$ and $\mathbf{E}_2(s)$ are again in the plane of the cross-section s. This plane, which is perpendicular to the reference axis in the undeformed configuration, remains undeformed in the deformed configuration, consistent with the assumptions of Timoshenko beam theory. However, in the deformed configuration, $\mathbf{E}_3(s)$ is not necessarily tangent to the reference axis to allow for shearing deformations, i.e., $\mathbf{E}_3(s) \neq \mathbf{x}'(s)$. The beam's deformed configuration $s \to (\mathbf{x}(s), \mathbf{\Lambda}(s)) \in \mathbb{R}^3 \times \mathrm{SO}(3)$ is fully described by the position of the reference axis and the corresponding cross-sectional orientation at s.

The kinematic description of GEBT is independent of the parameterization of the 3D rotation group SO(3). To that end, GEBT has been reformulated using rotation vectors [121, 144], Clifford algebra [145], directors [141–143], quaternions [146–148], and the special Euclidean group SE(3) [149], among others. Quaternions represent the most compact singularity-free parameterization of SO(3) [150]. For this and other reasons discussed in Chapter 5, quaternions are preferred here. Equation (4.9) relates a quaternion $\mathbf{p}(s) \in \mathbb{H}_1$ to the corresponding transformation matrix $\mathbf{\Lambda}(s)$.

4.5 Strain Energy and Strain Measures

This section introduces the geometrically exact strain measures that describe the local changes between the undeformed and deformed configurations.

In GEBT, the material stress resultant $\mathbf{N}$ and material moment resultant $\mathbf{M}$ are respectively work-conjugate to the material translational strain measure $\mathbf{\Gamma}$ and the material rotational strain measure $\mathbf{K}$. The strain energy for an initially straight beam takes the form

$$\mathcal{U} = \int_0^\ell \frac{1}{2}\mathbf{S}^T\mathbf{E}\,\mathrm{d}s \tag{4.41}$$

where $\mathbf{S}^T = \left(\mathbf{N}^T, \mathbf{M}^T\right)$, and $\mathbf{E}^T = \left(\mathbf{\Gamma}^T, \mathbf{K}^T\right)$. Assuming that the beam is isotropic linear-elastic with its reference axis coincident with the neutral axis, then the internal

stress resultants are related to the corresponding strain measures by

$$\mathbf{S} = \mathbf{C}\mathbf{E} \tag{4.42}$$

where $\mathbf{C} = \text{diag}\{GA_1, GA_2, EA, EI_1, EI_2, GJ\}$ is the sectional stiffness matrix that contains the translational and rotational stiffnesses. Specifically,

- GA_1 and GA_2 are the shear stiffnesses along the $\mathbf{e}_1$ and $\mathbf{e}_2$ axes;[4]
- EA is the axial stiffness;
- EI_1 and EI_2 are the bending stiffnesses about the $\mathbf{e}_1$ and $\mathbf{e}_2$ axes; and
- GJ is the torsional stiffness.

These sectional material properties are defined analogously to those in standard Timoshenko beam theory. As an aside, it is straightforward to modify GEBT for composite materials by appropriately redefining $\mathbf{C}$, in which case $\mathbf{C}$ is no longer diagonal.

The geometrically exact material strain measures for an initially straight beam are given by [129]

$$\boldsymbol{\Gamma} = \boldsymbol{\Lambda}^T\mathbf{x}' - \begin{bmatrix} 0 \\ 0 \\ 1 \end{bmatrix} \tag{4.43}$$

$$[\mathbf{K}]_\times = \boldsymbol{\Lambda}^T\boldsymbol{\Lambda}' - \boldsymbol{\Lambda}_0^T\boldsymbol{\Lambda}_0' \tag{4.44}$$

where $[\cdot]_\times$ refers to the skew-symmetric matrix defined by Eq. (4.4), $(\cdot)'$ denotes differentiation with respect to the undeformed arc length coordinate s, and the subscript 0 denotes the initial (undeformed) configuration. $\boldsymbol{\Gamma}$ and $\mathbf{K}$ represent the translational strain and curvature, respectively, between the initial and current configurations. Both strain measures are objective, i.e., they are invariant to superposed rigid body motions [129, 153, 154], from which it follows that $\mathcal{U}$ is also objective. The first two components of $\boldsymbol{\Gamma}$ represent the shear strains in the $\mathbf{e}_1$ and $\mathbf{e}_2$ directions,

[4]The assumption that plane cross-sections remain plane after deformation implies that the shear stresses and strains are constant over each plane of the cross-section. This is an approximation of the actual cross-sectional shear stress and strain distributions. As a result, GA_1 and GA_2 typically include Timoshenko shear correction factors [151, 152] so that the strain energy associated with shearing in the beam equals the strain energy associated with the actual shear stress and strain distributions in the corresponding 3D solid.

respectively. The third component represents the axial strain, i.e., the stretching of the reference axis. Likewise, the first two components of $\mathbf{K}$ represent the bending curvatures about the $\mathbf{e}_1$ and $\mathbf{e}_2$ axes, respectively. The third component represents the twist (torsion) of the cross-section about the $\mathbf{e}_3$ axis.

Strictly speaking, Eqs. (4.43) and (4.44) are also applicable for initially curved beams. In particular, for an initially straight beam, Eq. (4.44) simplifies to

$$[\mathbf{K}]_\times = \mathbf{\Lambda}^T \mathbf{\Lambda}' \tag{4.45}$$

because there are no cross-sectional variations along the beam's axis in the undeformed configuration. However, it has been observed in practice that using Eq. (4.44) instead of Eq. (4.45) in the finite element implementation can reduce the accumulation of round-off errors. Hence, Eq. (4.44) is preferred in what follows.

Subsequent developments require reparameterizing Eqs. (4.43) and (4.44) as functions of the quaternion $\mathbf{p}$ describing the cross-sectional orientation, which is done next. Using Eq. (4.9), $\mathbf{\Gamma}$ can be expressed as

$$\mathbf{\Gamma} = \mathbf{\Lambda}^T(\mathbf{p})\mathbf{x}' - \begin{bmatrix} 0 \\ 0 \\ 1 \end{bmatrix} \tag{4.46}$$

with variation

$$\delta\mathbf{\Gamma} = \mathbf{\Lambda}^T(\mathbf{p})\delta\mathbf{x}' - 2\mathbf{G}^T(\mathbf{p})\mathbf{L}^T(\mathbf{T}\mathbf{x}')\delta\mathbf{p} \tag{4.47}$$

which follows from the identity $\delta(\mathbf{\Lambda}^T(\mathbf{p})\mathbf{v}) = -2\mathbf{G}^T(\mathbf{p})\mathbf{L}^T(\mathbf{T}\mathbf{v})\delta\mathbf{p}$ for a constant vector $\mathbf{v} \in \mathbb{R}^3$. Similarly, starting from Eq. (4.9) and using the identities $\mathbf{p}^T\mathbf{p} = 1$ and $\mathbf{p}^T\mathbf{p}' = 0$ allows $\mathbf{K}$ to be written as

$$\mathbf{K} = 2\left(\mathbf{G}^T(\mathbf{p})\mathbf{p}' - \mathbf{G}^T(\mathbf{p}_0)\mathbf{p}_0'\right). \tag{4.48}$$

For a detailed derivation of Eq. (4.48) and additional discussion, see [147]. The variation of $\mathbf{K}$ requires the identity $\mathbf{G}^T(\mathbf{p})\mathbf{p}' = -\mathbf{G}^T(\mathbf{p}')\mathbf{p}$ and is given by

$$\delta\mathbf{K} = 2\mathbf{G}^T(\mathbf{p})\delta\mathbf{p}' - 2\mathbf{G}^T(\mathbf{p}')\delta\mathbf{p}. \tag{4.49}$$

Together, Eqs. (4.47) and (4.49) can be written in matrix form as

$$\delta\mathbf{E} = \begin{bmatrix} \mathbf{\Lambda}^T(\mathbf{p}) & \mathbf{0}_{3\times4} & -2\mathbf{G}^T(\mathbf{p})\mathbf{L}^T(\mathbf{T}\mathbf{x}') \\ \mathbf{0}_{3\times3} & 2\mathbf{G}^T(\mathbf{p}) & -2\mathbf{G}^T(\mathbf{p}') \end{bmatrix} \begin{bmatrix} \delta\mathbf{x}' \\ \delta\mathbf{p}' \\ \delta\mathbf{p} \end{bmatrix} \tag{4.50}$$

which appears in the finite element formulations in Chapters 5 and 6.

4.6 Kinetic Energy

Due to the in-plane rigidity of the beam's cross-sections, the total kinetic energy is simply the sum of the translational and rotational kinetic energies of the reference axis. Thus,

$$\mathcal{T} = \frac{1}{2}\int_0^\ell \left(\rho A\, \dot{\mathbf{x}}^T\dot{\mathbf{x}} + \boldsymbol{\Omega}^T\mathbf{J}\boldsymbol{\Omega}\right)\, \mathrm{d}s \tag{4.51}$$

where $\boldsymbol{\Omega} \in \mathbb{R}^3 \hookrightarrow [\boldsymbol{\Omega}]_\times \in \mathfrak{so}(3)$ is the material angular velocity, i.e., the angular velocity of the material frame with respect to the spatial frame expressed in the coordinates of the material frame, and is given by

$$[\boldsymbol{\Omega}]_\times = \boldsymbol{\Lambda}^T\dot{\boldsymbol{\Lambda}}. \tag{4.52}$$

Here, ρ is the volumetric mass density, A is the cross-sectional area, and $\mathbf{J} = \rho\,\mathrm{diag}\,\{I_1, I_2, J\}$ is the sectional moment of inertia matrix. I_1 and I_2 are the second moments of area about the $\mathbf{e}_1$ and $\mathbf{e}_2$ axes; $J = I_1 + I_2$ is the polar moment of area. Equation (4.51) assumes that the reference axis is coincident with the cross-sectional mass centers and that the axes $\mathbf{e}_1$ and $\mathbf{e}_2$ are parallel to the cross-sectional principal inertia directions. These assumptions can be relaxed by appropriately redefining the sectional inertia properties to introduce coupling between translations and rotations. Due to the similarities between Eq. (4.44) and Eq. (4.52), the material curvature $\mathbf{K}$ can be considered the spatial analogue of $\boldsymbol{\Omega}$.

The decision to use spatial translations but material rotations in Eq. (4.51) is motivated by the observation that the sectional moment of inertia matrix in the material frame is constant [121]. For spatial rotations, the correct form of the inertia matrix to use in the kinetic energy is $\mathbf{j} = \boldsymbol{\Lambda}\mathbf{J}\boldsymbol{\Lambda}^T$, which is clearly configuration-dependent.

Following Sec. 4.5, Eq. (4.52) is rewritten as a function of the quaternion $\mathbf{p}$ describing the cross-sectional orientation. By analogy with Eq. (4.48), the quaternionic expression for $\boldsymbol{\Omega}$ is

$$\boldsymbol{\Omega} = 2\mathbf{G}^T(\mathbf{p})\dot{\mathbf{p}} \tag{4.53}$$

from which it follows that its variation can be expressed as

$$\delta\boldsymbol{\Omega} = 2\mathbf{G}^T(\mathbf{p})\delta\dot{\mathbf{p}} - 2\mathbf{G}^T(\dot{\mathbf{p}})\delta\mathbf{p}. \tag{4.54}$$

Equation (4.54) is used in the finite element formulation in Chapter 5.

4.7 Virtual Work of External Forces

Following [121], the virtual work done by the external forces is

$$\begin{aligned}\delta\mathcal{W}_{\text{ext}} &= \int_0^\ell \left(\delta\mathbf{x}^T\overline{\mathbf{n}} + \delta\boldsymbol{\theta}^T\overline{\mathbf{m}}\right)\,\mathrm{d}s \\ &= \int_0^\ell \left(\delta\mathbf{x}^T\overline{\mathbf{n}} + \delta\boldsymbol{\Theta}^T\overline{\mathbf{M}}\right)\,\mathrm{d}s\end{aligned} \tag{4.55}$$

where $\overline{\mathbf{n}}$ and $\overline{\mathbf{m}}$ are the external forces and moments per unit length expressed in the spatial frame and $\overline{\mathbf{M}} = \boldsymbol{\Lambda}^T\overline{\mathbf{m}}$ is the corresponding material moment per unit length, i.e., the spatial moment expressed in the coordinates of the material frame. For brevity, Eq. (4.55) only considers a continuous distribution of applied forces and moments. Point forces and moments can be treated within this framework using the sifting property of the Dirac delta function [155, p. 241–243].

No assumptions are made regarding the origins of $\overline{\mathbf{n}}$ and $\overline{\mathbf{m}}$, and hence, they can be considered non-conservative. For finite rotations, constant spatial moments, i.e., moments about fixed spatial axes, are known to be non-conservative, and consequently, conservative moments are necessarily configuration-dependent [156]. In general, conservative moments are moments induced by conservative forces.

For consistency with previous developments, material rotation variables are used in what follows. Expressing the spatial moment in material coordinates yields

$$\delta\mathcal{W}_{\text{ext}} = \int_0^\ell \left(\delta\mathbf{x}^T\overline{\mathbf{n}} + \delta\boldsymbol{\Theta}^T\boldsymbol{\Lambda}^T(\mathbf{p})\overline{\mathbf{m}}\right)\,\mathrm{d}s \tag{4.56}$$

which can be rewritten in terms of the quaternion variation $\delta\mathbf{p}$ using Eqs. (4.27) and (4.33) to obtain

$$\delta\mathcal{W}_{\text{ext}} = \int_0^\ell \left(\delta\mathbf{x}^T\overline{\mathbf{n}} + \delta\mathbf{p}^T\left(2\mathbf{H}(\mathbf{p})\overline{\mathbf{m}}\right)\right)\,\mathrm{d}s. \tag{4.57}$$

The quantity $\overline{\mathbf{m}}_p = 2\mathbf{H}(\mathbf{p})\overline{\mathbf{m}}$ is the spatial representation of the quaternion moment, i.e., the generalized force induced by a spatial moment on the quaternion degrees of freedom. The material quaternion moment $\overline{\mathbf{M}}_p$ is obtained by replacing the spatial moment $\overline{\mathbf{m}}$ with the corresponding material moment $\overline{\mathbf{M}} = \boldsymbol{\Lambda}^T(\mathbf{p})\overline{\mathbf{m}}$ and simplifying; i.e., $\overline{\mathbf{M}}_p = 2\mathbf{G}(\mathbf{p})\overline{\mathbf{M}}$. The quaternion moment is conservative if and only if $\overline{\mathbf{m}}$ is also conservative. Since the quaternion is neither a spatial variable nor a material one, Eq. (4.57) results if either convention is used as a starting point.

Left-multiplying $\overline{\mathbf{m}}_p$ and $\overline{\mathbf{M}}_p$ by $\mathbf{H}^T(\mathbf{p})$ and $\mathbf{G}^T(\mathbf{p})$, respectively, and simplifying then allows the spatial and material moments to be written in terms of the corre-

sponding quaternion moments, i.e.,

$$\overline{\mathbf{m}} = \frac{1}{2}\mathbf{H}^T(\mathbf{p})\overline{\mathbf{m}}_p, \tag{4.58}$$

$$\overline{\mathbf{M}} = \frac{1}{2}\mathbf{G}^T(\mathbf{p})\overline{\mathbf{M}}_p. \tag{4.59}$$

Thus, a non-zero quaternion moment produces zero physical moment provided that the quaternion moment lies in the null space of the corresponding tangent matrix; see Eq. (4.17). Since both tangent matrices share the same null space, zero spatial moment corresponds with zero material moment and vice versa.

4.8 Variational Principle

In GEBT, the nonlinear strain measures are consistent with the force and moment resultant forms of the differential equations of equilibrium [129]. As a result, the resultant forms of the kinetic energy, strain energy, and external virtual work can be inserted directly into a standard variational principle, in this case, the Lagrange-d'Alembert principle, to derive the weak form of the equations of motion. For a geometrically exact beam, the continuous-time Lagrange-d'Alembert principle takes the form [135, Sec. 7.8]:

$$\delta \int_0^T \mathcal{L}(\mathbf{q}, \dot{\mathbf{q}})\, \mathrm{d}t + \int_0^T \delta\mathcal{W}_{\text{ext}}(t, \mathbf{q}, \dot{\mathbf{q}})\, \mathrm{d}t = 0 \tag{4.60}$$

where $\mathcal{L}(\mathbf{q}, \dot{\mathbf{q}}) = \mathcal{T}(\mathbf{q}, \dot{\mathbf{q}}) - \mathcal{U}(\mathbf{q})$ is the Lagrangian, $\mathcal{T}(\mathbf{q}, \dot{\mathbf{q}})$ is the configuration-dependent kinetic energy [Eq. (4.51)], $\mathcal{U}(\mathbf{q})$ is the strain energy [Eq. (4.41)], $\delta\mathcal{W}_{\text{ext}}(t, \mathbf{q}, \dot{\mathbf{q}})$ is the virtual work done by the external and/or non-conservative generalized forces [Eq. (4.57)], $\mathbf{q}$ contains the generalized coordinates (in this case, the translation $\mathbf{x}(s)$ and quaternion $\mathbf{p}(s)$ describing the position and orientation of the reference axis), and T is an arbitrary final time. Equation (4.60), or alternatively, its constrained form (see e.g., [135, Secs. 7.8 and 8.3]), is the starting point for the derivations of the continuous-time and discrete-time finite elements in Chapters 5 and 6, respectively.

Chapter 5

OBJECTIVE QUATERNION-BASED GEOMETRICALLY EXACT BEAM FINITE ELEMENT

5.1 Introduction

This chapter presents a new quaternion-based finite element implementation of the Reissner-Simo geometrically exact beam theory (GEBT) [32–34]. The development and implementation of 3D finite elements based on GEBT are challenging due to the nonlinear structure of the 3D rotation group SO(3). As a result, finite element implementations of GEBT typically use differential geometry to account for the Lie group structure of SO(3), as is done, e.g., in [34, 121, 157, 158]. This chapter takes a different approach, instead leveraging several recent results from quaternion calculus [139] to develop an objective, two-node, quaternion-based beam finite element that is derivable using only standard mathematical tools from vector calculus and linear algebra. For this reason, the proposed beam element is more straightforward to derive than many of the comparable elements in the literature.

The proposed beam element is a quaternion-based reparameterization of the Total Lagrangian beam element originally proposed by Cardona and Géradin [121] (see also [70, Ch. 6]), which itself is a finite element implementation of Simo's original GEBT [34]. Compared to [121], the present formulation replaces rotation vectors with quaternions to describe nodal rotations and uses spherical linear interpolation (slerp) [133, 140] instead of standard linear interpolation to interpolate the nodal rotations along the element's reference axis. Slerp results in an objective finite element discretization, i.e., the discrete strain measures preserve the objectivity of the corresponding 1D continuum-beam strain measures. In this context, objectivity refers to invariance to superposed rigid body motions. Generally speaking, the finite element discretization of an objective continuum strain measure is itself non-objective [129, 153, 154], something known to lead to the accumulation of errors and non-physical path-dependence in the solution process. These problems are exacerbated for coarse meshes and large rigid body motions, like those that occur during the tumbling motions of flexible spacecraft. Unlike some other objective finite element interpolations, slerp guarantees objectivity at every point along the reference axis of the beam, not just at the nodes. Objectivity also eliminates any

requirement to use local element reference frames during the finite element assembly step. This is advantageous because it allows complex models to be assembled in a single global reference frame. Several objective finite element implementations of GEBT are currently available in the literature, including [141–144, 146, 158, 159].

The use of quaternions to describe nodal rotations in GEBT is not new. Many existing formulations are quaternion-based, including [146–148, 159–166], among others. The proliferation of quaternion-based formulations is largely due to their advantages over implementations based on other parameterizations of SO(3), including:

1. Quaternions are the most compact singularity-free parameterization of SO(3) [150]. This leads to many computational benefits. For example, it is simpler and more efficient to guarantee that a quaternion is of unit length than it is to guarantee the orthogonality of a rotation matrix. In fact, quaternions are often used as intermediaries for orthogonalizing rotation matrices; see e.g, [138]. Unlike rotation-vector-based formulations (e.g., [158, 167]), quaternions do not require reparameterizations of SO(3) for rotations in excess of 180 deg.

2. The consistent use of a single singularity-free rotation parameterization simplifies theoretical developments and the subsequent implementation. Many existing formulations are cumbersome because they use multiple rotation parameterizations throughout the solution process. References [144, 158], for example, both employ three parameterizations: the rotation matrix, rotation vector, and quaternion (which appears via Spurrier's algorithm [137] during the extraction of a rotation vector from a rotation matrix). Even some quaternion-based implementations suffer from this problem; e.g., [146] uses rotation vectors to describe nodal rotations, which are then mapped to quaternions for interpolation.

3. Since quaternions lie on the unit three-sphere, they are intuitive to interpolate without destroying their Lie group structure. Specifically, their geodesic interpolation (slerp) traces an arc of a great circle on the unit three-sphere. Hence, slerp can be defined from purely geometrical arguments [133, 140], whereas the equivalent constructs for other parameterizations of SO(3) typically require tools from differential geometry, like the exponential map [133].

Despite their advantages, quaternions are not without their challenges. A major downside is that quaternions are a double cover for SO(3), i.e., two quaternions

describe each rotation in 3D space. In some applications, this can lead to undesirable properties like unwinding, where a solution may start arbitrarily close to its final orientation and yet still traverse large rotations before settling there [168, 169]. For finite elements, however, these concerns are usually unfounded as long as the relative rotations across individual elements are much smaller than 180 deg, something typically required for mesh convergence anyway.

Altogether, the proposed beam finite element represents an incremental improvement over the current state-of-the-art for geometrically exact beam finite elements. Compared to existing quaternion-based elements [146, 147, 159, 160, 163–166], the present formulation has several advantages. References [160] and [164], for example, are vector space formulations that use Lagrange multipliers to explicitly enforce the quaternion unit norm constraint. Despite its conceptual simplicity, this approach is prone to experiencing numerical difficulties due to the interpolation of the Lagrange multipliers. The present work avoids this pitfall with a Lie group formulation that implicitly enforces the quaternion unit norm constraint and results in governing equations of minimal dimension. Many of the remaining formulations, including [146, 147, 159, 166], are limited to statics, making them of no utility for the dynamic problems studied in this thesis. Likewise, the proposed element consistently uses a single singularity-free rotation parameterization throughout the entire solution process, and by doing so, it can accommodate arbitrarily large rotations without switching between rotation parameterizations.

For the purposes of this thesis, the proposed beam element is the continuous-time limit of the discrete-mechanics-based formulation of GEBT subsequently developed in Chapter 6. Both formulations share many of the same mathematical details; e.g., the continuous-time mass matrix developed here relates the discrete generalized momenta in Chapter 6 to the corresponding discrete generalized velocities. Importantly, the element developed in this chapter also provides a reference solution for verifying the variational integrator in Chapter 6.

The remainder of this chapter is organized as follows: Sec. 5.2 starts from the continuous-time Lagrange-d'Alembert principle to derive the weak form of the equations of motion. Sec. 5.3 implements the finite element discretization and obtains expressions for the elemental elastic and inertia forces. This section shares some similarities with [121] and [70, Ch. 6], but replaces rotation vectors with quaternions and employs a structure-preserving spatial discretization. Sec. 5.4 presents several numerical examples. Sec. 5.5 then concludes the chapter.

This chapter assumes familiarity with the material in Chapter 4.

5.2 Variational Principle

The finite element formulation starts from the constrained Lagrange-d'Alembert principle in continuous-time (see e.g., [135, Secs. 7.8 and 8.3]):

$$\delta \int_0^T \left(\mathcal{L}(\mathbf{q}, \dot{\mathbf{q}}) - \mathbf{c}(\mathbf{q}, \boldsymbol{\lambda}) \right) \, \mathrm{d}t + \int_0^T \delta \mathcal{W}_{\text{ext}}(t, \mathbf{q}) \, \mathrm{d}t = 0 \tag{5.1}$$

where $\mathcal{L}(\mathbf{q}, \dot{\mathbf{q}}) = \mathcal{T}(\mathbf{q}, \dot{\mathbf{q}}) - \mathcal{U}(\mathbf{q})$ is the Lagrangian; $\mathcal{T}(\mathbf{q}, \dot{\mathbf{q}})$ is the configuration-dependent kinetic energy; $\mathcal{U}(\mathbf{q})$ is the strain energy; $\delta \mathcal{W}_{\text{ext}}(t, \mathbf{q})$ is the virtual work done by the external and/or non-conservative forces and moments; $\mathbf{q}$ contains the generalized coordinates, in this case, $\mathbf{q}^T = \left(\mathbf{x}^T, \mathbf{p}^T\right)$; and T is an arbitrary final time. The function $\mathbf{c}(\mathbf{q}, \boldsymbol{\lambda})$ contains the constraints conjugated to the independent Lagrange multipliers $\boldsymbol{\lambda}$ and is given by [142, 143, 160, 164]

$$\mathbf{c}(\mathbf{q}, \boldsymbol{\lambda}) = \int_0^\ell \boldsymbol{\phi}^T(\mathbf{q}) \boldsymbol{\lambda} \, \mathrm{d}s \tag{5.2}$$

where $\boldsymbol{\phi}(\mathbf{q})$ is the vector of holonomic constraints. In the general case, Eq. (5.2) can enforce distributed constraints along the beam's reference axis, like the unit norm constraints associated with quaternion vector space [160, 164] or director-based [142, 143] formulations. The Lie group formulation developed here, however, implicitly satisfies the quaternion unit norm constraint. Hence, $\boldsymbol{\phi}(\mathbf{q})$ exclusively enforces external constraints at the finite element nodes, e.g., the joint constraints in flexible multibody systems. This entails the use of Dirac delta functions to interpolate the Lagrange multipliers in the spatial discretization.

Next, expressions for the kinetic energy [Eq. (4.51)], strain energy [Eq. (4.41)], virtual work done by the external forces [Eq. (4.57)], and constraints [Eq. (5.2)] are substituted into Eq. (5.1) to obtain

$$\begin{aligned} \delta \int_0^T \int_0^\ell \frac{1}{2} \left(\rho A \, \dot{\mathbf{x}}^T \dot{\mathbf{x}} + \boldsymbol{\Omega}^T \mathbf{J} \boldsymbol{\Omega} - \mathbf{S}^T \mathbf{E} - 2 \boldsymbol{\phi}^T(\mathbf{q}) \boldsymbol{\lambda} \right) \, \mathrm{d}s \, \mathrm{d}t \\ + \int_0^T \int_0^\ell \left(\delta \mathbf{x}^T \overline{\mathbf{n}} + \delta \mathbf{p}^T \left(2 \mathbf{H}(\mathbf{p}) \overline{\mathbf{m}} \right) \right) \, \mathrm{d}s \, \mathrm{d}t = 0. \end{aligned} \tag{5.3}$$

This is the constrained variational principle for a geometrically exact beam. From here, the finite element formulation entails evaluating the variations in Eq. (5.3), followed by the substitution of an appropriate spatial discretization.

In Eq. (5.3) and what follows, variations with respect to the quaternion $\mathbf{p}$ are intentionally evaluated without explicitly considering the associated unit norm constraint.

In other words, variations with respect to $\mathbf{p}$ assume that its four components are independent. This assumption is corrected to account for the group structure of quaternions using the structure-preserving spatial discretization in Sec. 5.3.

5.2.1 Variation of the Strain Energy

The variation of the strain energy follows directly from Eq. (4.41) as

$$\delta\mathcal{U} = \int_0^\ell \delta\mathbf{E}^T\mathbf{S}\,\mathrm{d}s \tag{5.4}$$

where $\mathbf{S}^T = \left(\mathbf{N}^T, \mathbf{M}^T\right)$ is the vector of internal force and moment resultants and $\delta\mathbf{E}$ is given by Eq. (4.50). Substituting $\delta\mathbf{E}$ and simplifying then gives

$$\delta\mathcal{U} = \int_0^\ell \left[\delta\mathbf{x}'^T\mathbf{\Lambda}(\mathbf{p})\mathbf{N} + 2\delta\mathbf{p}'^T\mathbf{G}(\mathbf{p})\mathbf{M} - 2\delta\mathbf{p}^T\left(\mathbf{L}(\mathbf{T}\mathbf{x}')\mathbf{G}(\mathbf{p})\mathbf{N} + \mathbf{G}(\mathbf{p}')\mathbf{M}\right)\right]\mathrm{d}s \tag{5.5}$$

where $\mathbf{x}'(s)$, $\mathbf{p}'(s)$, and $\mathbf{p}(s)$ are taken as independent variables. The internal force and moment resultants are functions of the generalized strains $\mathbf{\Gamma}$ and $\mathbf{K}$ [Eqs. (4.46) and (4.48)] through the constitutive relation $\mathbf{S} = \mathbf{C}\mathbf{E}$ [Eq. (4.42)]. Equation (5.5) is equal to the virtual work done by the internal elastic forces, i.e, $\delta\mathcal{W}_{\text{int}} = \delta\mathcal{U}$.

5.2.2 Variation of the Kinetic Energy

The variation of the kinetic energy is evaluated from Eq. (4.51), as follows:

$$\delta\mathcal{T} = \int_0^\ell \left(\delta\dot{\mathbf{x}}^T\left(\rho A\dot{\mathbf{x}}\right) + \delta\mathbf{\Omega}^T\mathbf{J}\mathbf{\Omega}\right)\mathrm{d}s \tag{5.6}$$

$$= \int_0^\ell \left[\delta\dot{\mathbf{x}}^T\left(\rho A\dot{\mathbf{x}}\right) + 4\left(\delta\dot{\mathbf{p}}^T\mathbf{G}(\mathbf{p}) - \delta\mathbf{p}^T\mathbf{G}(\dot{\mathbf{p}})\right)\mathbf{J}\mathbf{G}^T(\mathbf{p})\dot{\mathbf{p}}\right]\mathrm{d}s \tag{5.7}$$

where Eqs. (4.53) and (4.54) are used to eliminate the dependencies on $\mathbf{\Omega}$ and $\delta\mathbf{\Omega}$ and $\dot{\mathbf{x}}$, $\dot{\mathbf{p}}$, and $\mathbf{p}$ are taken as independent variables.

From here, the standard procedure is to evaluate the integral $\int_0^T \delta\mathcal{T}\,\mathrm{d}t$ using integration by parts in time with the assumption that $\delta\mathbf{x}$ and $\delta\mathbf{p}$ both vanish at times $t = 0$ and $t = T$, i.e., $\delta\mathbf{x}(0) = \delta\mathbf{x}(T) = \mathbf{0}_{3\times1}$ and $\delta\mathbf{p}(0) = \delta\mathbf{p}(T) = \mathbf{0}_{4\times1}$. This results in the following:

$$\int_0^T \delta\mathcal{T}\,\mathrm{d}t = -\int_0^T \delta\mathcal{W}_{\text{iner}}\,\mathrm{d}t \tag{5.8}$$

where $\delta\mathcal{W}_{\text{iner}}$ is the virtual work of the inertia forces, given by

$$\delta\mathcal{W}_{\text{iner}} = \int_0^\ell \left[\delta\mathbf{x}^T\left(\rho A\ddot{\mathbf{x}}\right) + \delta\mathbf{p}^T\left(4\mathbf{G}(\mathbf{p})\mathbf{J}\mathbf{G}^T(\mathbf{p})\ddot{\mathbf{p}} + 8\mathbf{G}(\dot{\mathbf{p}})\mathbf{J}\mathbf{G}^T(\mathbf{p})\dot{\mathbf{p}}\right)\right]\mathrm{d}s. \tag{5.9}$$

The integration by parts eliminates $\delta\dot{\mathbf{p}}$. The first term in the integrand of Eq. (5.9) contains the configuration-independent translational inertia forces. The second term contains the configuration-dependent rotational inertia forces. The rotational inertia forces share the same form as their counterparts from quaternion-based formulations of rigid body dynamics; see e.g., [170].

5.2.3 Variation of the Constraints

The variation of the constraints is straightforward to evaluate from Eq. (5.2). Taking $\mathbf{q}^T = \left(\mathbf{x}^T, \mathbf{p}^T\right)$ and $\boldsymbol{\lambda}$ as the independent variables in the evaluation of the variation gives

$$\delta\mathbf{c} = \int_0^\ell \left(\delta\boldsymbol{\lambda}^T \boldsymbol{\phi}(\mathbf{q}) + \delta\mathbf{q}^T \left(\frac{\partial \boldsymbol{\phi}}{\partial \mathbf{q}} \right)^T \boldsymbol{\lambda} \right) \mathrm{d}s \tag{5.10}$$

where $\partial\boldsymbol{\phi}/\partial\mathbf{q}$ is the constraint gradient matrix.

5.2.4 Weak Form of the Equations of Motion

To evaluate the weak form of the equations of motion, the variations of the strain energy [Eq. (5.5)], kinetic energy [Eq. (5.8)], and constraints [Eq. (5.10)] are substituted into the constrained variational principle [Eq. (5.3)]. After some rearranging, the constrained variational principle takes the form

$$\int_0^T \left[\delta\mathcal{W}_{\text{iner}} + \delta\mathcal{W}_{\text{int}} + \int_0^\ell \left(\delta\boldsymbol{\lambda}^T \boldsymbol{\phi}(\mathbf{q}) + \delta\mathbf{q}^T \left(\frac{\partial \boldsymbol{\phi}}{\partial \mathbf{q}} \right)^T \boldsymbol{\lambda} \right) \mathrm{d}s - \delta\mathcal{W}_{\text{ext}} \right] \mathrm{d}t = 0 \tag{5.11}$$

where $\delta\mathcal{W}_{\text{iner}}$ is the virtual work of the inertia forces [Eq. (5.9)], $\delta\mathcal{W}_{\text{int}}$ is the virtual work of the internal elastic forces [Eq. (5.5)], and $\delta\mathcal{W}_{\text{ext}}$ is the virtual work done by the external forces [Eq. (4.57)]. The variational principle then implies that

$$\delta\mathcal{W}_{\text{iner}} + \delta\mathcal{W}_{\text{int}} + \int_0^\ell \left(\delta\boldsymbol{\lambda}^T \boldsymbol{\phi}(\mathbf{q}) + \delta\mathbf{q}^T \left(\frac{\partial \boldsymbol{\phi}}{\partial \mathbf{q}} \right)^T \boldsymbol{\lambda} \right) \mathrm{d}s - \delta\mathcal{W}_{\text{ext}} = 0 \tag{5.12}$$

for all admissible variations $\delta\mathbf{x}$, $\delta\mathbf{x}'$, $\delta\mathbf{p}$, and $\delta\mathbf{p}'$. Equation (5.12) is the weak form of the equations of motion. It is subsequently discretized in space using a structure-preserving finite element method.

5.3 Finite Element Discretization

The spatial discretization via the finite element method considers a two-node beam element of length ℓ. Each node has 7 degrees of freedom (DOFs), 3 translations and a quaternion, for a total of 14 DOFs per element. Due to the quaternion unit

norm constraint, only 12 of these are independent. The subscripts 1 and 2 denote the nodes at the left and right ends of the element. The beam element is prismatic, homogeneous, and isotropic linear-elastic with the sectional stiffness matrix $\mathbf{C}$ from Sec. 4.5 and the linear mass density ρA and sectional moment of inertia matrix $\mathbf{J}$ from Sec. 4.6. Following the standard approach for geometrically exact beam finite elements, the spatial discretization assumes independent position and rotation (quaternion) fields.

In the sequel, the derivation considers a single element. The corresponding system-level quantities are then assembled using a standard finite element assembly step. Likewise, the terms interpolated and discretized/discrete are used interchangeably and should be understood as referring to a quantity after spatial discretization via the finite element method. The superscript h denotes an interpolated quantity.

5.3.1 Interpolation of Positions

The spatial discretization linearly interpolates the reference axis position $\mathbf{x}(s)$. Thus, $\mathbf{x}(s)$ is related to the nodal positions $\mathbf{x}_1$ and $\mathbf{x}_2$ by

$$\mathbf{x}(s) \doteq \mathbf{x}^h(s) = M_1(s)\mathbf{x}_1 + M_2(s)\mathbf{x}_2 \tag{5.13}$$

where the symbol $\doteq$ denotes that $\mathbf{x}(s)$ is approximated by the interpolated quantity $\mathbf{x}^h(s)$, $M_1(s) = 1 - s/\ell$, and $M_2(s) = s/\ell$. Linear interpolation of vector space quantities like position is objective [129]. Due to the objectivity of both the strain measures and the finite element interpolation, the spatial discretization can directly interpolate the nodal positions instead of the corresponding nodal displacements.

The discrete translational velocity and acceleration are the first and second time derivatives of Eq. (5.13):

$$\dot{\mathbf{x}}(s) \doteq \dot{\mathbf{x}}^h(s) = M_1(s)\dot{\mathbf{x}}_1 + M_2(s)\dot{\mathbf{x}}_2, \tag{5.14}$$

$$\ddot{\mathbf{x}}(s) \doteq \ddot{\mathbf{x}}^h(s) = M_1(s)\ddot{\mathbf{x}}_1 + M_2(s)\ddot{\mathbf{x}}_2. \tag{5.15}$$

The finite element implementation also requires the first spatial derivative of Eq. (5.13),

$$\mathbf{x}'(s) \doteq \mathbf{x}^{h\prime}(s) = M_1(s)\mathbf{x}'_1 + M_2(s)\mathbf{x}'_2, \tag{5.16}$$

and the discretizations of both $\delta\mathbf{x}$ and $\delta\mathbf{x}'$:

$$\delta\mathbf{x}(s) \doteq \delta\mathbf{x}^h(s) = M_1(s)\delta\mathbf{x}_1 + M_2(s)\delta\mathbf{x}_2, \tag{5.17}$$

$$\delta\mathbf{x}'(s) \doteq \delta\mathbf{x}^{h\prime}(s) = M'_1(s)\delta\mathbf{x}_1 + M'_2(s)\delta\mathbf{x}_2. \tag{5.18}$$

5.3.2 Interpolation of Quaternions

Unlike positions, quaternions are defined on a Lie group: the unit three-sphere $\mathbb{H}_1$. It follows that standard linear interpolation does not preserve their Lie group structure. This is straightforward to show by calculating the length of a quaternion interpolated analogously to Eq. (5.13); the interpolated quaternion only satisfies the unit norm constraint at the two endpoints. As a result, the linear interpolation of quaternions is non-objective, leading to non-objective discrete strain measures.

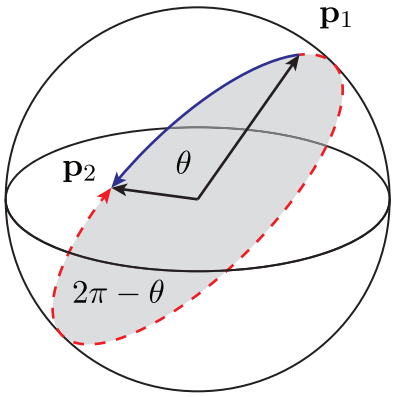

Figure 5.1: Quaternion spherical linear interpolation (slerp) on the 4D unit hypersphere $\mathbb{H}_1$ (the unit three-sphere). The solid arc subtending the angle $\theta = \cos^{-1}\left(\mathbf{p}_1^T\mathbf{p}_2\right) \in [0, \pi]$ in the plane spanned by $\mathbf{p}_1$ and $\mathbf{p}_2$ denotes the shortest path from $\mathbf{p}_1$ to $\mathbf{p}_2$.

Spherical linear interpolation (slerp) [133, 140] is analogous to standard linear interpolation on $\mathbb{H}_1$. Unlike linear interpolation, slerp traces the arc of the great circle on $\mathbb{H}_1$ connecting two quaternions $\mathbf{p}_1$ and $\mathbf{p}_2$; see Fig. 5.1. Hence, slerp is a geodesic interpolation from $\mathbf{p}_1$ to $\mathbf{p}_2$. By construction, the interpolated quaternion belongs to $\mathbb{H}_1$, i.e., slerp preserves the Lie group structure of $\mathbb{H}_1$. Consequently, the substitution of slerp into the nonlinear beam strain measures [Eqs. (4.46) and (4.48)] leads to objective discrete strain measures [146, 154]. As discussed in [154], slerp is the quaternion equivalent of the objective interpolation from [129], with the added advantage that slerp can directly interpolate the total nodal rotations (via the corresponding quaternions) as opposed to the incremental ones [146]. Note that slerp is considered a constant "angular velocity" interpolation because each infinitesimal arc length segment subtends the same infinitesimal angle.

As depicted in Fig. 5.1, there are two paths between any two quaternions on $\mathbb{H}_1$. These paths correspond to the subtended angles $\theta \in [0, \pi]$ and $2\pi - \theta$ where

$$\cos(\theta) = \mathbf{p}_2^T\mathbf{p}_1. \tag{5.19}$$

Physically, the existence of two paths between any two quaternions corresponds to the observation that there are two constant "angular velocity" rotation sequences between any two orientations in 3D space. These two paths are unrelated to the double cover of SO(3). Rather, since two quaternions describe each orientation in 3D space, there are actually eight possible paths on $\mathbb{H}_1$ between any two physical orientations. An additional complication, however, does arise due to the double cover. When $\theta > \pi/2$, the angle between $\mathbf{p}_1$ and the antipode $-\mathbf{p}_2$ is less than $\pi/2$ [133]. In this case, the shortest path corresponds to the interpolation from $\mathbf{p}_1$ to $-\mathbf{p}_2$. In most applications (including finite element ones), the shortest path between the two quaternions is preferred. These issues are not salient for beam finite elements. Because θ measures the angle between the two nodal quaternions, it typically must be small (e.g., less than 15 deg) for mesh convergence. With a sufficiently dense mesh, so long as the two nodal quaternions are close to each other in the initial configuration, they generally remain close in the deformed configuration. Hence, the finite element discretization assumes $\theta < \pi/2$.

The slerp formula is straightforward to derive using vector algebra on $\mathbb{H}_1$. The derivation is omitted for brevity; instead, see [133, 140]. Given two nodal quaternions $\mathbf{p}_1$ and $\mathbf{p}_2$, their slerp is given by

$$\mathbf{p}(s) \doteq \mathbf{p}^h(s) = N_1(s)\mathbf{p}_1 + N_2(s)\mathbf{p}_2 \tag{5.20}$$

where

$$N_1(s) = \sin\left(\left(1 - \frac{s}{\ell}\right)\theta\right)\csc(\theta), \tag{5.21}$$

$$N_2(s) = \sin\left(\frac{s}{\ell}\theta\right)\csc(\theta), \tag{5.22}$$

and θ is the angle between $\mathbf{p}_1$ and $\mathbf{p}_2$ [Eq. (5.19)]. When $\mathbf{p}_1 = \mathbf{p}_2$, i.e., when $\theta = 0$, slerp reduces to standard linear interpolation:

$$\lim_{\theta\to 0} N_i(s) = M_i(s) \tag{5.23}$$

for $i = 1,\ 2$. The limit indicates that the approximate geometric tangent stiffness matrix developed in Sec. 5.3.7 is exact in the inital (undeformed) configuration. Unlike standard finite element interpolations, slerp is a nonlinear function of its endpoints. This complicates the finite element discretization.

The formulation of the internal forces requires the first spatial derivative of $\mathbf{p}^h(s)$:

$$\mathbf{p}'(s) \doteq \mathbf{p}^h(s) = N_1'(s)\mathbf{p}_1 + N_2'(s)\mathbf{p}_2 \tag{5.24}$$

where

$$-N_1'(s) = \frac{\theta}{\ell}\cos\left(\left(1-\frac{s}{\ell}\right)\theta\right)\csc(\theta), \tag{5.25}$$

$$N_2'(s) = \frac{\theta}{\ell}\cos\left(\frac{s}{\ell}\theta\right)\csc(\theta). \tag{5.26}$$

The finite element discretization also requires the first and second temporal derivatives of $\mathbf{p}^h(s)$ (for the formulation of the inertia forces) and the discretizations of both $\delta\mathbf{p}$ and $\delta\mathbf{p}'$. For brevity, only the latter are included here; the remaining terms are listed in Appendix B.

Evaluating the discrete variations $\delta\mathbf{p}^h(s)$ and $\delta\mathbf{p}^{h\prime}(s)$ is more complicated. Assuming that the components of $\mathbf{p}_1$ and $\mathbf{p}_2$ are independent yields the following expressions for $\delta\mathbf{p}^h(s)$ and $\delta\mathbf{p}^{h\prime}(s)$:

$$\delta\mathbf{p}(s) \doteq \delta\mathbf{p}^h(s) = \frac{\partial\mathbf{p}^h(s)}{\partial\mathbf{p}_1}\delta\mathbf{p}_1 + \frac{\partial\mathbf{p}^h(s)}{\partial\mathbf{p}_2}\delta\mathbf{p}_2, \tag{5.27}$$

$$\delta\mathbf{p}'(s) \doteq \delta\mathbf{p}^{h\prime}(s) = \frac{\partial\mathbf{p}^{h\prime}(s)}{\partial\mathbf{p}_1}\delta\mathbf{p}_1 + \frac{\partial\mathbf{p}^{h\prime}(s)}{\partial\mathbf{p}_2}\delta\mathbf{p}_2. \tag{5.28}$$

The Jacobians of $\mathbf{p}^h(s)$ and $\mathbf{p}^{h\prime}(s)$ with respect to $\mathbf{p}_1$ and $\mathbf{p}_2$ are listed in Appendix B. As is, Eqs. (5.27) and (5.28) are not structure-preserving because they are derived without taking into account the group structure of $\mathbb{H}_1$. To rectify this, $\delta\mathbf{p}_1$ and $\delta\mathbf{p}_2$ are projected into their associated material tangent spaces using Eq. (4.34) (reproduced below):

$$\delta\mathbf{p}_i = \frac{1}{2}\mathbf{G}(\mathbf{p}_i)\delta\boldsymbol{\Theta}_i \tag{5.29}$$

which holds for $i = 1, 2$. As discussed in Sec. 4.3.2, Eq. (5.29) a posteriori corrects for the group structure of $\mathbb{H}_1$, analogous to the "conversion factor" approach introduced in [139] that allows standard results from vector calculus and linear algebra to be applied to $\mathbb{H}_1$. Introducing Eq. (5.29) into Eqs. (5.27) and (5.28) then results in the following structure-preserving discretizations for $\delta\mathbf{p}^h(s)$ and $\delta\mathbf{p}^{h\prime}(s)$:

$$\delta\mathbf{p}^h(s) = \frac{1}{2}\left(\frac{\partial\mathbf{p}^h(s)}{\partial\mathbf{p}_1}\mathbf{G}(\mathbf{p}_1)\delta\boldsymbol{\Theta}_1 + \frac{\partial\mathbf{p}^h(s)}{\partial\mathbf{p}_2}\mathbf{G}(\mathbf{p}_2)\delta\boldsymbol{\Theta}_2\right), \tag{5.30}$$

$$\delta\mathbf{p}^{h\prime}(s) = \frac{1}{2}\left(\frac{\partial\mathbf{p}^{h\prime}(s)}{\partial\mathbf{p}_1}\mathbf{G}(\mathbf{p}_1)\delta\boldsymbol{\Theta}_1 + \frac{\partial\mathbf{p}^{h\prime}(s)}{\partial\mathbf{p}_2}\mathbf{G}(\mathbf{p}_2)\delta\boldsymbol{\Theta}_2\right). \tag{5.31}$$

While nontrivial, it can be shown that

$$\delta\mathbf{p}^{hT}(s)\mathbf{p}^h(s) = 0 \tag{5.32}$$

for all $s \in [0, \ell]$, as expected for the variation of a quaternion. Since $\mathbf{G} \in \mathbb{R}^{4\times3}$ [Eq. (4.13)], the elemental elastic and inertia forces derived in Secs. 5.3.3 and 5.3.4, respectively, are of minimal dimension, i.e., they have three forces and moments per node. To simplify the notation, the explicit dependence on s is subsequently dropped.

5.3.3 Elastic Forces

The elemental elastic forces $\mathbf{F}_{\text{int}}$ are derived by substituting expressions for $\delta\mathbf{x}^{h\prime}$, $\delta\mathbf{p}^{h\prime}$, $\delta\mathbf{p}^{h}$, and the appropriate interpolated position and quaternion variables into either Eq. (5.4) or Eq. (5.5). In matrix form, $\delta\mathbf{x}^{h\prime}$, $\delta\mathbf{p}^{h\prime}$, and $\delta\mathbf{p}^{h}$ are related to the variations of the nodal coordinates by

$$\begin{bmatrix} \delta\mathbf{x}^{h\prime} \\ \delta\mathbf{p}^{h\prime} \\ \delta\mathbf{p}^{h} \end{bmatrix} = \mathbf{P}\delta\mathbf{g} \tag{5.33}$$

where $\mathbf{P} \in \mathbb{R}^{11\times12}$ is the shape interpolation matrix

$$\mathbf{P} = \begin{bmatrix} M_1'\mathbf{I}_{3\times3} & \mathbf{0}_{3\times3} & M_2'\mathbf{I}_{3\times3} & \mathbf{0}_{3\times3} \\ \mathbf{0}_{4\times3} & \frac{1}{2}\frac{\partial\mathbf{p}^{h\prime}}{\partial\mathbf{p}_1}\mathbf{G}(\mathbf{p}_1) & \mathbf{0}_{4\times3} & \frac{1}{2}\frac{\partial\mathbf{p}^{h\prime}}{\partial\mathbf{p}_2}\mathbf{G}(\mathbf{p}_2) \\ \mathbf{0}_{4\times3} & \frac{1}{2}\frac{\partial\mathbf{p}^{h}}{\partial\mathbf{p}_1}\mathbf{G}(\mathbf{p}_1) & \mathbf{0}_{4\times3} & \frac{1}{2}\frac{\partial\mathbf{p}^{h}}{\partial\mathbf{p}_2}\mathbf{G}(\mathbf{p}_2) \end{bmatrix} \tag{5.34}$$

assembled from the structure-preserving spatial discretizations from Secs. 5.3.1 and 5.3.2 and

$$\delta\mathbf{g}^T = \begin{bmatrix} \delta\mathbf{x}_1^T & \delta\boldsymbol{\Theta}_1^T & \delta\mathbf{x}_2^T & \delta\boldsymbol{\Theta}_2^T \end{bmatrix}. \tag{5.35}$$

The discrete strain gradient matrix $\mathbf{B} \in \mathbb{R}^{6\times12}$ is then defined such that

$$\delta\mathbf{E}^h = \mathbf{B}\delta\mathbf{g}. \tag{5.36}$$

Using Eqs. (4.50) and Eq. (5.33), it follows that

$$\mathbf{B} = \begin{bmatrix} \boldsymbol{\Lambda}^T(\mathbf{p}^h) & \mathbf{0}_{3\times4} & -2\mathbf{G}^T(\mathbf{p}^h)\mathbf{L}^T(\mathbf{T}\mathbf{x}^{h\prime}) \\ \mathbf{0}_{3\times3} & 2\mathbf{G}^T(\mathbf{p}^h) & -2\mathbf{G}^T(\mathbf{p}^{h\prime}) \end{bmatrix}\mathbf{P}. \tag{5.37}$$

In turn, Eq. (5.5) can be written as

$$\delta\mathcal{W}_{\text{int}} = \delta\mathbf{g}^T\int_0^\ell \mathbf{B}^T\mathbf{S}^h \,\mathrm{d}s = \delta\mathbf{g}^T\mathbf{F}_{\text{int}} \tag{5.38}$$

where $\mathbf{F}_{\text{int}} \in \mathbb{R}^{12}$ is the vector of elemental internal elastic forces, $\mathbf{S}^h = \mathbf{C}\mathbf{E}^h$ contains the interpolated internal force and moment resultants, and $\mathbf{E}^h$ is the interpolated strain vector. The integral in Eq. (5.38) is approximated using a quadrature rule.

The components of the discrete strain vector are evaluated by substituting $\mathbf{x}^{h\prime}$, $\mathbf{p}^{h\prime}$, and $\mathbf{p}^h$ into Eqs. (4.46) and (4.48). With slerp, it can be shown that the discrete material curvature $\mathbf{K}^h$ is a constant for all $s \in [0, \ell]$ given by

$$\mathbf{K} \doteq \mathbf{K}^h = \frac{2}{\ell}\left(\frac{\theta}{\sin(\theta)}\right)\mathbf{G}^T(\mathbf{p}_1)\mathbf{p}_2 \tag{5.39}$$

which is only a function of the relative rotation between the two nodes of the element. Since $\mathbf{K}^h$ is constant with s, one-point Gaussian quadrature (the midpoint rule) is exact for evaluating the corresponding contributions to the strain energy and elemental elastic forces. Likewise, it is expected that the coefficients of $\mathbf{B}$ corresponding to the discrete curvature gradients $\partial\mathbf{K}^h/\partial\mathbf{p}_1$ and $\partial\mathbf{K}^h/\partial\mathbf{p}_2$ are also independent of s. This is in fact the case, but the proof is involved and best left to a symbolic algebra software. Alternatively, these gradients can be directly evaluated from Eq. (5.39).

5.3.4 Inertia Forces

The elemental inertia forces are derived analogously to the elemental elastic ones. Specifically, $\delta\mathbf{x}^h$ and $\delta\mathbf{p}^h$ are expressed in terms of the variations of the nodal coordinates such that

$$\begin{bmatrix} \delta\mathbf{x}^h \\ \delta\mathbf{p}^h \end{bmatrix} = \mathbf{Q}\delta\mathbf{g} \tag{5.40}$$

where $\mathbf{Q} \in \mathbb{R}^{7\times 12}$ is the shape interpolation matrix

$$\mathbf{Q} = \begin{bmatrix} M_1\mathbf{I}_{3\times3} & \mathbf{0}_{3\times3} & M_2\mathbf{I}_{3\times3} & \mathbf{0}_{3\times3} \\ \mathbf{0}_{4\times3} & \dfrac{1}{2}\dfrac{\partial\mathbf{p}^h}{\partial\mathbf{p}_1}\mathbf{G}(\mathbf{p}_1) & \mathbf{0}_{4\times3} & \dfrac{1}{2}\dfrac{\partial\mathbf{p}^h}{\partial\mathbf{p}_2}\mathbf{G}(\mathbf{p}_2) \end{bmatrix}. \tag{5.41}$$

Equation (5.40) is then substituted into Eq. (5.9) along with the appropriate interpolated position and quaternion variables to obtain

$$\delta\mathcal{W}_{\text{iner}} = \delta\mathbf{g}^T\int_0^\ell \mathbf{Q}^T\begin{bmatrix} \rho A\ddot{\mathbf{x}}^h \\ 4\mathbf{G}(\mathbf{p}^h)\mathbf{J}\mathbf{G}^T(\mathbf{p}^h)\ddot{\mathbf{p}}^h + 8\mathbf{G}(\dot{\mathbf{p}}^h)\mathbf{J}\mathbf{G}^T(\mathbf{p}^h)\dot{\mathbf{p}}^h \end{bmatrix}\mathrm{d}s \tag{5.42}$$

from which it follows that

$$\delta\mathcal{W}_{\text{iner}} = \delta\mathbf{g}^T\mathbf{F}_{\text{iner}} \tag{5.43}$$

where $\mathbf{F}_{\text{iner}} \in \mathbb{R}^{12}$ is the vector of elemental inertia forces. The translational inertia forces in Eq. (5.42) are linear functions of the nodal accelerations. Hence, they can be integrated exactly. The rotational inertia forces in Eq. (5.42) are approximated with a quadrature rule.

5.3.5 Constraints

In the absence of internal constraints, the Lagrange multipliers in the weak form [Eq. (5.12)] exclusively enforce external constraints between finite element nodes. Hence, following [142], the Lagrange multipliers and their variations are interpolated using Dirac delta functions $\delta(\cdot)$, as follows:

$$\boldsymbol{\lambda}(s) \doteq \boldsymbol{\lambda}^h(s) = \delta(s/\ell)\boldsymbol{\lambda}_1 + \delta(1 - s/\ell)\boldsymbol{\lambda}_2, \tag{5.44}$$

$$\delta\boldsymbol{\lambda}(s) \doteq \delta\boldsymbol{\lambda}^h(s) = \delta(s/\ell)\delta\boldsymbol{\lambda}_1 + \delta(1 - s/\ell)\delta\boldsymbol{\lambda}_2. \tag{5.45}$$

Substituting Eqs. (5.44) and (5.45) into the variation of the constraints [Eq. (5.10)] and evaluating the integral via the sifting property of the Dirac delta function [155, p. 241–243] gives

$$\delta\mathbf{c} = \delta\boldsymbol{\lambda}_1^T\boldsymbol{\phi}_1(\mathbf{q}_1) + \delta\boldsymbol{\lambda}_2^T\boldsymbol{\phi}_2(\mathbf{q}_2) + \delta\mathbf{q}_1^T\left(\frac{\partial\boldsymbol{\phi}_1}{\partial\mathbf{q}_1}\right)^T\boldsymbol{\lambda}_1 + \delta\mathbf{q}_2^T\left(\frac{\partial\boldsymbol{\phi}_2}{\partial\mathbf{q}_2}\right)^T\boldsymbol{\lambda}_2 \tag{5.46}$$

where $\mathbf{q}_i^T = \left(\mathbf{x}_i^T, \mathbf{p}_i^T\right)$ and $\boldsymbol{\phi}_i \in \mathbb{R}^{n_c^{(i)}}$ contains the $n_c^{(i)}$ constraints at node i, both for $i = 1,\ 2$. Correcting for the Lie group structure of $\mathbb{H}_1$ using Eq. (5.29) then yields

$$\delta\mathbf{c} = \delta\boldsymbol{\lambda}^T\boldsymbol{\Phi}(\mathbf{g}) + \delta\mathbf{g}^T\left(\frac{\partial\boldsymbol{\Phi}}{\partial\mathbf{g}}\right)^T\boldsymbol{\lambda} \tag{5.47}$$

where $\mathbf{g}^T = \left(\mathbf{q}_1^T, \mathbf{q}_2^T\right)$ is the vector of nodal coordinates, $\boldsymbol{\lambda}^T = \left(\boldsymbol{\lambda}_1^T, \boldsymbol{\lambda}_2^T\right)$ is the vector of Lagrange multipliers, $\boldsymbol{\Phi}^T = \left(\boldsymbol{\phi}_1^T, \boldsymbol{\phi}_2^T\right)$ is the constraint function, and

$$\frac{\partial\boldsymbol{\Phi}}{\partial\mathbf{g}} = \begin{bmatrix} \dfrac{\partial\boldsymbol{\phi}_1}{\partial\mathbf{x}_1} & \dfrac{1}{2}\dfrac{\partial\boldsymbol{\phi}_1}{\partial\mathbf{p}_1}\mathbf{G}(\mathbf{p}_1) & \mathbf{0}_{n_c^{(1)}\times 3} & \mathbf{0}_{n_c^{(1)}\times 3} \\ \mathbf{0}_{n_c^{(2)}\times 3} & \mathbf{0}_{n_c^{(2)}\times 3} & \dfrac{\partial\boldsymbol{\phi}_2}{\partial\mathbf{x}_2} & \dfrac{1}{2}\dfrac{\partial\boldsymbol{\phi}_2}{\partial\mathbf{p}_2}\mathbf{G}(\mathbf{p}_2) \end{bmatrix} \tag{5.48}$$

is the constraint gradient matrix for a single element. While a slight abuse of notation, the meaning of $\boldsymbol{\lambda}$ should be clear from its context.

5.3.6 External Forces

The external forces are derived from the external virtual work [Eq. (4.57)] using Eq. (5.40):

$$\delta\mathcal{W}_{\text{ext}} = \delta\mathbf{g}^T\int_0^\ell \mathbf{Q}^T\begin{bmatrix} \overline{\mathbf{n}} \\ 2\mathbf{H}(\mathbf{p}^h)\overline{\mathbf{m}} \end{bmatrix}\mathrm{d}s \tag{5.49}$$

from which it follows that

$$\delta \mathcal{W}_{\text{ext}} = \delta \mathbf{g}^T \mathbf{F}_{\text{ext}} \tag{5.50}$$

where $\mathbf{F}_{\text{ext}} \in \mathbb{R}^{12}$ is the vector of external forces. The integral in Eq. (5.49) is approximated using a quadrature rule. Since rotations are expressed in the material frame, external moments specified in the spatial frame result in configuration-dependent external forces. When external forces and moments are only applied at the nodes, $\mathbf{F}_{\text{ext}}$ simplifies to

$$\mathbf{F}_{\text{ext}} = \begin{bmatrix} \overline{\mathbf{n}}_1 \\ \boldsymbol{\Lambda}^T(\mathbf{p}_1)\overline{\mathbf{m}}_1 \\ \overline{\mathbf{n}}_2 \\ \boldsymbol{\Lambda}^T(\mathbf{p}_2)\overline{\mathbf{m}}_2 \end{bmatrix} \tag{5.51}$$

where $\overline{\mathbf{n}}_i$ and $\overline{\mathbf{m}}_i$ are the external forces and moments, respectively, at nodes $i = 1,\ 2$. This can be derived by writing the distribution of external forces and moments in terms of the Dirac delta function, tantamount to how the Lagrange multipliers are interpolated in Sec. 5.3.5.

5.3.7 Dynamic Equilibrium and Linearization

The spatial discretization of the weak form [Eq. (5.12)] leads to the following holonomically-constrained dynamic equilibrium equations for the beam element:

$$\begin{aligned} \mathbf{F}_{\text{iner}}(\mathbf{g}, \dot{\mathbf{g}}, \ddot{\mathbf{g}}) + \mathbf{F}_{\text{int}}(\mathbf{g}) + \left(\frac{\partial \boldsymbol{\Phi}}{\partial \mathbf{g}}\right)^T \boldsymbol{\lambda} &= \mathbf{F}_{\text{ext}}(\mathbf{g}) \\ \boldsymbol{\Phi}(\mathbf{g}) &= \mathbf{0}_{n_c \times 1} \end{aligned} \tag{5.52}$$

where $n_c = n_c^{(1)} + n_c^{(2)}$ is the total number of holonomic constraints. The dynamic equilibrium equations for $n_e \geq 1$ elements take the same general form after a standard finite element assembly step.

Due to the nodal quaternion DOFs, solving Eq. (5.52) requires a quaternion-based generalization of a Lie group time integrator, e.g., the Lie group generalized-α method [36–38], which is a generalization of the standard generalized-α method [25]. The Lie group generalized-α method includes Lie group generalizations of the HHT-α [171] and Newmark-β [172] methods as special cases.

Implicit solution procedures, including the Lie group generalized-α method, require the linearization of Eq. (5.52) to evaluate the dynamic tangent matrix at each iteration of a Newton-Raphson-type solution scheme. For brevity, only expressions

for the tangent stiffness matrix $\mathbf{K}_T$ and mass matrix $\mathbf{M}$ are developed here. The remaining tangent matrices usually have small contributions to the dynamic tangent matrix, and hence, can generally be neglected [70, Ch. 6], with the caveat that the dynamic tangent matrix should account for the load stiffness [173] associated with any deformation-dependent (follower) forces and/or moments.

The tangent stiffness matrix $\mathbf{K}_T$ is the linearization of the internal forces with respect to the configuration $\mathbf{g}$. Substituting the constitutive relation $\mathbf{S}^h = \mathbf{C}\mathbf{E}^h$ [Eq. (4.42)] into Eq. (5.38) and differentiating with respect to $\mathbf{g}$ results in the following expression for the tangent stiffness matrix:

$$\mathbf{K}_T = \frac{\partial \mathbf{F}_{int}}{\partial \mathbf{g}} = \int_0^\ell \left(\mathbf{B}^T \mathbf{C} \mathbf{B} + \frac{\partial \mathbf{B}^T}{\partial \mathbf{g}} \mathbf{S}^h \right) \mathrm{d}s \tag{5.53}$$

which can be recast in the equivalent form

$$\mathbf{K}_T = \mathbf{K}_M + \mathbf{K}_G \tag{5.54}$$

where $\mathbf{K}_M$ and $\mathbf{K}_G$ are the material and geometric tangent stiffness matrices:

$$\mathbf{K}_M = \int_0^\ell \mathbf{B}^T \mathbf{C} \mathbf{B} \, \mathrm{d}s, \tag{5.55}$$

$$\mathbf{K}_G = \int_0^\ell \frac{\partial \mathbf{B}^T}{\partial \mathbf{g}} \mathbf{S}^h \, \mathrm{d}s. \tag{5.56}$$

An approximation for the geometric tangent stiffness matrix is derived in Appendix C which assumes that the angle θ is constant, i.e., any stiffness due to the nonlinearities in the slerp is negligible compared to the changes in the internal force and moment resultants. The material tangent stiffness matrix is exact.

Lastly, the mass matrix $\mathbf{M}$ is derived from the linearization of the inertia forces [Eq. (5.42)] with respect to the generalized acceleration $\ddot{\mathbf{q}}$, the result of which is

$$\mathbf{M} = \frac{\partial \mathbf{F}_{\text{iner}}}{\partial \ddot{\mathbf{g}}} = \int_0^\ell \mathbf{Q}^T(s) \begin{bmatrix} \rho A \mathbf{I}_{3\times 3} & \mathbf{0}_{3\times 4} \\ \mathbf{0}_{4\times 3} & 4\mathbf{G}(\mathbf{p}^h)\mathbf{J}\mathbf{G}^T(\mathbf{p}^h) \end{bmatrix} \mathbf{Q}(s) \, \mathrm{d}s. \tag{5.57}$$

The mass matrix consists of a constant translational part and a configuration-dependent rotational part.

5.4 Numerical Examples

A MATLAB® implementation of the finite element formulation is used to evaluate several standard benchmark problems from the literature. The example problems

specifically demonstrate the formulation's (i) susceptibility to shear locking and its subsequent correction (Sec. 5.4.1), (ii) path-independence (Sec. 5.4.2), and (iii) objectivity (Sec. 5.4.3). All three examples in this section are static. For completeness, however, this section also details the numerical implementation of the dynamic finite element formulation used in subsequent chapters. Chapter 6 studies several dynamic examples to facilitate comparisons between the Lie group generalized-α method [36–38] and a structure-preserving variational integrator.

MATLAB® is a vectorized programming language. To bypass the use of FOR loops and improve computational efficiency, the MATLAB® implementation features a vectorized finite element assembly step inspired by [174–176] that uses 4D arrays. The first two dimensions represent an elemental vector or matrix quantity, like the elemental elastic forces. The third dimension represents the quadrature points for the numerical integration. The fourth dimension represents the individual elements in the finite element model. Each two-node element has six generalized forces (three forces and three moments) per node. Thus, 4D arrays of dimensions $12 \times 1 \times n_q \times n_e$ and $12 \times 12 \times n_q \times n_e$ represent element force and matrix quantities where n_q and n_e are respectively the number of quadrature points and elements. The computer implementation evaluates the nonlinear element forces and tangent matrices for all elements at each quadrature point simultaneously, and then uses a single summation step (implemented by summing over all the quadrature points, followed by array indexing and the application of the SPARSE function) to assemble the complete finite element model.

The examples in Secs. 5.4.1, 5.4.2, and 5.4.3 are evaluated using a nonlinear static solver based on a quaternion Lie group generalization of the standard Newton-Raphson method [139, 177]. Similarly, the dynamic problems in subsequent chapters use a quaternion-based implementation of the Lie group generalized-α method [36–38]. The Lie group generalized-α method is second-order accurate for unconstrained linear systems and includes numerical dissipation (specified via the spectral radius at infinity) that damps any high-frequency numerical oscillations and stabilizes the weak numerical instabilities associated with any constraints [178]. For improved numerical conditioning, it is implemented using the scaling approach from [179]. Both solution procedures use the Cayley map for updating quaternion DOFs; see Sec. 4.3.2. Additionally, both procedures use the approximate geometric tangent stiffness matrix [Eq. (5.56)] and neglect terms with small contributions to the total tangent matrix, as discussed in Sec. 5.3.7. This results in quasi-Newton

methods with typically less-than-quadratic convergence. The dynamic solution procedure also neglects the tangent gyroscopic damping and stiffness matrices. Finally, both solution procedures use the absolute convergence criterion

$$||\mathbf{r}_\mathbf{g}||_\infty \leq \tau \quad \wedge \quad ||\mathbf{r}_\lambda||_\infty \leq \tau \tag{5.58}$$

where $\mathbf{r}_\mathbf{g}$ is the generalized force residual, $\mathbf{r}_\lambda$ is the constraint residual (if applicable), $||\cdot||_\infty$ denotes the infinity norm, $\wedge$ denotes logical AND, and τ is the convergence tolerance. The infinity norm of a vector is equal to the magnitude of its coefficient with the maximum absolute value. In this chapter, $\tau = 10^{-6}$.

In each example, boundary conditions and any additional constraints are enforced via the method of Lagrange multipliers, as is common in multibody dynamics; see e.g., [180]. The method of Lagrange multipliers does not result in the most computationally efficient constraint enforcement. Instead, its usage here is motivated by its simplicity above all else, although it is also convenient for problems requiring the explicit evaluation of reaction forces and/or moments. Other methods of constraint enforcement, including standard Boolean identification and so-called "master-slave" relationships [181, 182], typically yield more computationally efficient implementations. Due to the implicit satisfaction of the quaternion unit norm constraint, constraints on the rotational DOFs are only applied to the vector part of the quaternion. This guarantees that the tangent matrix is full-rank.

Unless otherwise specified, the examples in this section use 1-point reduced integration for the elastic forces and tangent stiffness matrix.

5.4.1 Example 1: Shear Locking Test

It is well known that certain finite element discretizations of the classical (i.e., linear-elastic, small-deflection) Timoshenko beam theory are prone to shear locking. In particular, initially straight Timoshenko beam finite elements based on the linear interpolation of independent displacement and rotation fields (often referred to as C^0 beam elements) suffer from two types of shear locking. These occur during (i) constant curvature deformation (Type 1 locking) and (ii) linear curvature deformation (Type 2 locking) [183]. The standard approach for eliminating Type 1 locking is reduced integration, specifically 1-point Gaussian quadrature (the midpoint rule), which decouples constant curvature bending from shear [183]. Alleviating Type 2 locking is more nuanced, but for isotropic C^0 beam elements, it can be accomplished by scaling the shear stiffnesses; [183] demonstrates that the correct scale factor for

isotropic C^0 beam elements is MacNeal's residual bending flexibility (RBF) correction [184]. For an isotropic C^0 beam element of length ℓ, the RBF correction scales the shear stiffnesses GA_1 and GA_2, as follows:

$$GA_1 \to \frac{GA_1}{1 + GA_1\ell^2/(12EI_2)}, \tag{5.59}$$

$$GA_2 \to \frac{GA_2}{1 + GA_2\ell^2/(12EI_1)} \tag{5.60}$$

so that the finite element stiffness matrix matches the analytically computed stiffness matrix [183]. Given that GEBT is a large-deformation generalization of Timoshenko beam theory and that slerp is analogous to linear interpolation on $\mathbb{H}_1$, it is natural to expect that the proposed quaternion-based geometrically exact beam finite elements are also prone to both Type 1 and Type 2 locking. This turns out to be the case, as demonstrated next.

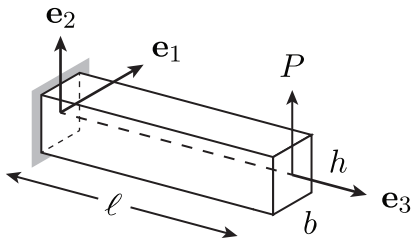

Figure 5.2: Cantilever beam subject to a transverse tip load P in the $\mathbf{e}_2$-direction for shear locking test. The local (material) frame in the initial configuration coincides with the global $\{\mathbf{e}_1, \mathbf{e}_2, \mathbf{e}_3\}$ frame.

Table 5.1: Geometric and material properties from [147] for shear locking test

Parameter	**Value**
b	0.1 m
h	0.1 m – 1 m
E	10 MPa
G	10^7 MPa
ℓ	1 m

To demonstrate the shear locking susceptibility of the proposed beam finite elements, this example studies the simple shear locking test introduced in [147]. The test considers the deflection of an isotropic cantilever beam with length ℓ and rectangular cross-section of breadth b and height h due to a small transverse tip load P

(Fig. 5.2). Table 5.1 lists the corresponding geometric and material properties. Since increasing the shear modulus G exacerbates shear locking, the test intentionally uses a large (and non-physical) value for G. Likewise, decreasing the slenderness ratio (i.e., increasing h) and the number of elements both exacerbate shear locking. Consequently, the test varies h from 0.1 m to 10 m and considers finite element discretizations with between 1 and 20 elements. Despite the use of non-physical properties to emphasize shear locking, shear locking (especially Type 1 locking) is often problematic in finite element models of real systems. Note that the computed shear stiffnesses use a Timoshenko shear correction factor of $5/6$ [151].

To overcome numerical ill-conditioning of the tangent stiffness matrix due to extrapolation locking [185, 186] for $h > 1$ m, the nonlinear static solver uses a quaternion-based Lie group implementation of the mixed integration point (MIP) Newton-Raphson method [187]. Extrapolation locking occurs due to large mismatches between terms in the tangent stiffness matrix, like those that occur in geometrically exact beam formulations due to their stiffer (axial, shearing) and softer (bending, torsional) DOFs. It is worse for larger stiffness mismatches.

The shear locking test limits the deflections to the geometrically linear regime in order to compare the tip deflection $u_2(\ell)$ with the corresponding analytical solution from classical Timoshenko beam theory:

$$u_{2,\text{ref}}(\ell) = P\left(\frac{\ell^3}{3EI_1} + \frac{\ell}{GA_2}\right). \tag{5.61}$$

Shear locking decreases as $u_2(\ell)/u_{2,\text{ref}}(\ell) \to 1$. Figures 5.3a, 5.3b, and 5.3c plot $u_2(\ell)/u_{2,\text{ref}}(\ell)$ as a function of $G\ell^2/Eh^2$ where the elastic forces are evaluated using 5-point Gaussian quadrature (as a substitute for full integration), 1-point reduced integration, and 1-point reduced integration with MacNeal's RBF correction. For an isotropic beam with a rectangular cross-section, $G\ell^2/Eh^2$ is proportional to the ratio of $\ell^3/3EI_1$ to ℓ/GA_2, i.e., the ratio of the tip deflection due to bending and the tip deflection due to shear. Hence, $G\ell^2/Eh^2$ is a proxy for slenderness. Decreasing values of $G\ell^2/Eh^2$ correspond to increasing values of h; $\log_{10}(G\ell^2/Eh^2) = 8$ and $\log_{10}(G\ell^2/Eh^2) = 4$ respectively correspond to $h = 0.1$ m and $h = 10$ m.

The main takeaway from Figs. 5.3a and 5.3b is that shear locking occurs using both 5-point Gaussian quadrature and 1-point reduced integration, indicating that reduced integration alone is insufficient to fully alleviate shear locking in the present formulation. However, 1-point reduced integration with a sufficiently dense mesh mitigates the dominant locking effect. Additionally, it is apparent from Fig. 5.3a that

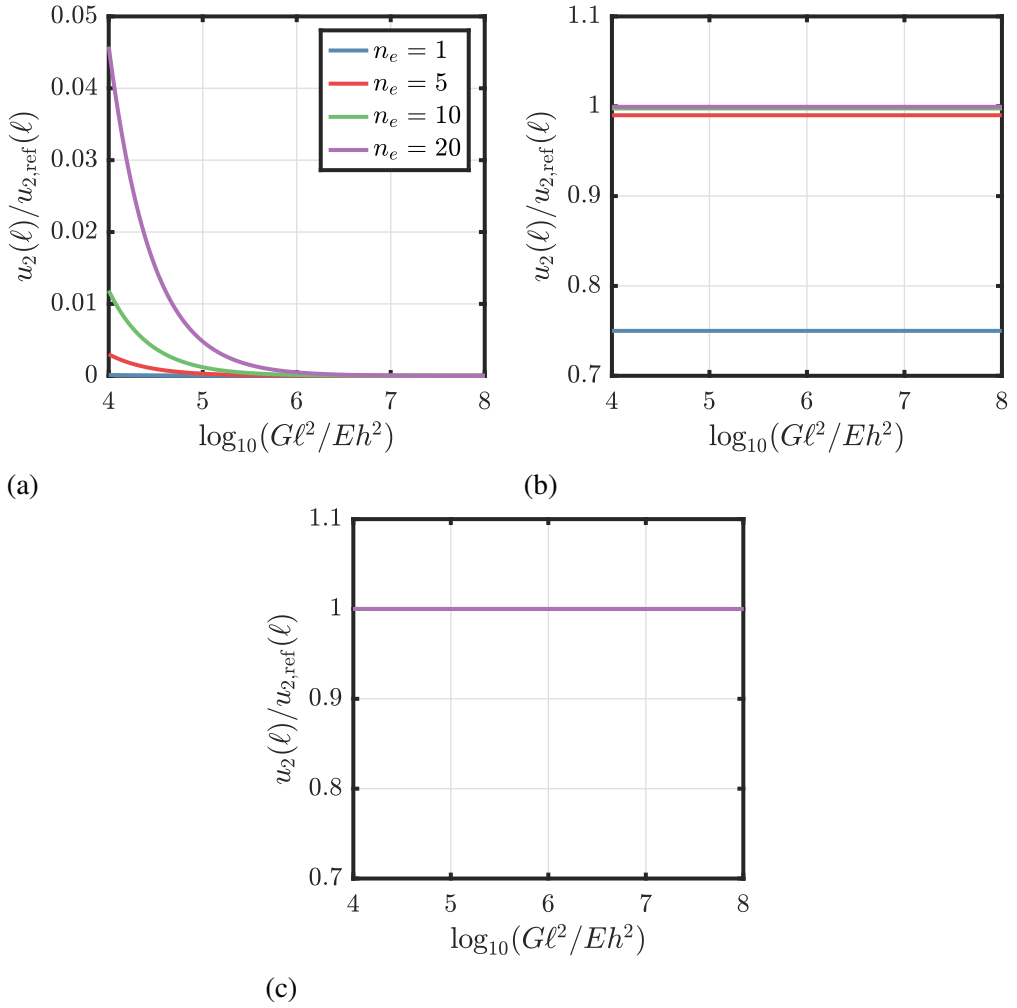

Figure 5.3: Normalized tip displacements in the $\mathbf{e}_2$-direction using (a) 5-point Gaussian quadrature, (b) 1-point reduced integration (the midpoint rule), and (c) 1-point reduced integration with MacNeal's residual bending flexibility (RBF) correction. Shear locking decreases as $u_2(\ell)/u_{2,\mathrm{ref}}(\ell) \to 1$.

locking increases as slenderness decreases, i.e., as h increases (moving left on the horizontal axis), as expected. Figures 5.3a and 5.3b likewise show that increasing the number of elements decreases locking, again as expected. The application of MacNeal's RBF correction then fully corrects for shear locking; see Fig. 5.3c. For a cantilever beam loaded by a transverse tip force, Fig. 5.3c demonstrates that the tip displacements calculated with the combination of 1-point reduced integration and the RBF correction are independent of the mesh density.

By analogy with the C^0 element case, it is apparent that the proposed slerp-based geometrically exact beam finite elements suffer from both Type 1 and Type 2 locking. This has ramifications for many of the existing geometrically exact beam finite

elements formulations in the literature. Specifically, many of these formulations are based on either linear interpolation of translations and rotations (see e.g, [121]) or an analogous Lie group interpolation (see e.g., the objective interpolations from [144] and [146]). As a result, these formulations are also likely prone to both types of locking. Many existing formulations, including [121, 141, 143, 158], exclusively address Type 1 locking; the consideration of Type 2 locking is absent from much of the existing literature, with limited exceptions (see e.g, [70, Ch. 6]). Importantly, this discussion only applies to *initially straight* beam finite elements; locking in *initially curved* elements is more complicated and discussed elsewhere (see e.g., [188]).

A final note of caution: MacNeal's RBF correction is not generally applicable to arbitrary (i.e., anisotropic) C^0 beam elements. It is straightforward to show, for example, that the application of the RBF correction to the linear analysis of an anisotropic C^0 beam element can lead to a negative (semi-) definite stiffness matrix. To the author's knowledge, a generalization of MacNeal's RBF correction for anisotropic beams does not currently exist in the literature. As a result, the requisite numerical tools for eliminating Type 2 locking in anisotropic geometrically exact beam finite elements based on either linear interpolation or analogous interpolations for $\mathrm{SO}(3)$ also do not currently exist. This is a possible area for future research.

5.4.2 Example 2: Path-Independence Test

This example uses the 45 deg cantilever bend from [189] to demonstrate the path-independence of the proposed finite element formulation under different load incrementation schemes. Path-independence requires that the final deformed configuration is independent of the load incrementation scheme. Since its introduction in [189], the 45 deg cantilever bend has become a standard test problem for geometrically exact beam finite elements because it combines axial, shearing, torsional, and bending deformations; representative references include [121, 141, 142, 144, 146, 153, 157, 158], among others. References [142, 144, 146, 153] specifically use it to investigate path-independence.

The 45 deg cantilever bend consists of an initially curved beam of radius R that subtends an angle of 45 deg along a circular arc and is loaded by a vertical force P at its free end; see Fig. 5.4a. The present finite element formulation assumes initially straight beam finite elements. As a result, the finite element implementation approximates the initially curved beam with a series of straight line segments.

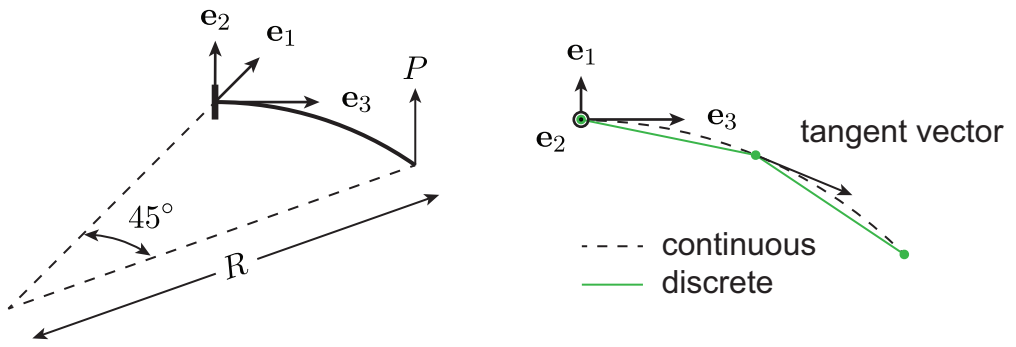

(a) (b)

Figure 5.4: (a) Initially curved cantilever beam subject to a transverse tip load P in the $\mathbf{e}_2$-direction. (b) Top view of discretization using $n_e = 2$ initially straight geometrically exact beam finite elements. In both (a) and (b), the local (material) frame in the initial (undeformed) configuration is defined such that $\mathbf{E}_3$ is tangent to the beam's axis, $\mathbf{E}_2 = \mathbf{e}_2$, and $\mathbf{E}_1 = \mathbf{E}_2 \times \mathbf{E}_3$.

Figure 5.4b illustrates this discretization using a coarse mesh with $n_e = 2$ initially straight beam finite elements, but following [189] and others, the beam is discretized using $n_e = 8$ elements in what follows. Due to the discretization, the material frames for adjacent elements do not coincide. This leads to quaternion constraints at the nodes connecting adjacent elements of the form

$$\mathbf{G}^T(\mathbf{p}_1^{(i+1)})\mathbf{L}(\mathbf{p}_2^{(i)})\Delta\mathbf{p}^{(i)} = \mathbf{0}_{3\times 1} \tag{5.62}$$

where the subscripts 1 and 2 denote each element's first and second node (the second node on element i overlaps the first node on element $i+1$) and $\Delta\mathbf{p}^{(i)} = \mathbf{L}^T(\mathbf{p}_0^{(i)})\mathbf{p}_0^{(i+1)}$ for $i = 1, \ldots, n_e - 1$ is the quaternion describing the orientation of the material frame of element $i+1$ relative to the material frame of element i in the beam's initial configuration.

Table 5.2: Geometric and material properties in the local (material) frame from [144] for 45 deg cantilever bend

Parameter	**Value**
GA_1, GA_2	5×10^6 N
EA	10^7 N
EI_1, EI_2, GJ	$10^7/12$ N m^2
R	100 m

Table 5.2 lists the geometric and material properties from [144] for the 45 deg cantilever bend. The finite element implementation applies MacNeal's RBF correction [184] to the shear stiffnesses (see the discussion in Sec. 5.4.1), but numerical experiments show that neglecting the RBF correction in this example has a negligible effect on the computed deflections.

Four load incrementation schemes are considered: (i) a single load increment, (ii) 3 equal load increments, (iii) 3 unequal load increments, and (iv) 100 equal load increments. Case (iii) specifically considers the load increments $P/2$, $P/4$, and $P/4$, in that order. Case (iv) provides a reference solution.

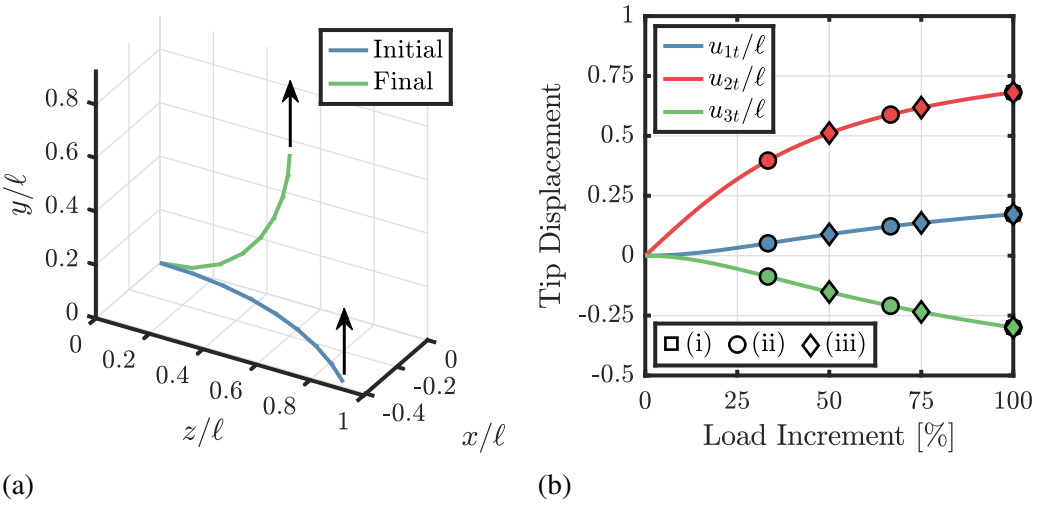

Figure 5.5: 45 deg cantilever bend: comparisons of (a) initial (undeformed) and final (deformed) configurations and (b) tip displacements as a function of load increment from 4 different load incrementation schemes. In (a), the arrows denote the direction of the load and there is no magnification of the deformation. In (b), $\ell = 25\pi$ m.

Figure 5.5a compares the initial and final configurations of the cantilever to emphasize the 3D nature of the deformation. Figure 5.5b then plots the components of the tip displacement as a function of the load increment for cases (i)–(iii); the continuous lines depict case (iv). Figure 5.5b depicts the expected result, namely that the tip displacements converge to the same final values irrespective of the load incrementation scheme. This confirms the path-independence. To further emphasize the path-independence, Table 5.3 compares the final tip displacements from cases (i)–(iv); in each case, the results are numerically identical to engineering accuracy. The table also lists two reference solutions from the literature to demonstrate that these results are in good agreement with those from other geometrically exact beam finite element formulations.

Table 5.3: Comparison of tip displacements from 45 deg cantilever bend (Fig. 5.4a) using 4 different load incrementation schemes. The tip displacements are compared to those from the path-independent formulations from [144] and [153]

Formulation	**Tip Displacements, m**		
	u_{1t}	u_{2t}	u_{3t}
Present (i)	13.5739	53.5248	−23.5338
Present (ii)	13.5739	53.5248	−23.5338
Present (iii)	13.5739	53.5248	−23.5338
Present (iv)	13.5739	53.5248	−23.5338
Total Lagrangian [144]	13.4834	53.3712	−23.4791
Incremental rotation vector [153]	13.490	53.370	−23.477

5.4.3 Example 3: Objectivity Test

This final example studies the objectivity of the proposed finite element formulation using the right-angle cantilever beam introduced in [144]. This problem has subsequently become a standard objectivity test for geometrically exact beam finite elements; see e.g., [146, 153, 159]. In practice, objectivity means that rigid body rotations of a deformed configuration do not result in the accumulation of errors, i.e., the errors remain below the convergence tolerance of the Newton-Raphson solver. Thus, to test objectivity, successive rotations can be applied to the deformed configuration of a structure, and after each complete rotation, the current configuration can be compared with the initial deformed configuration, as is done next.

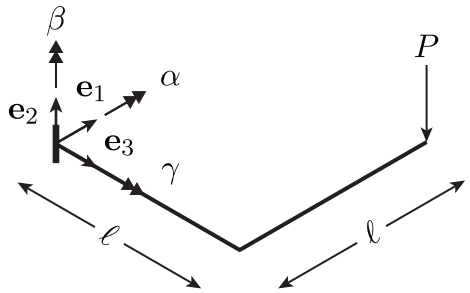

Figure 5.6: Right-angle cantilever beam subject to an out-of-plane force P at its tip and prescribed base rotation (α, β, or γ) introduced in [144] for objectivity test. The local (material) frame in the initial (undeformed) configuration is defined such that $\mathbf{E}_3$ is tangent to the beam's axis, $\mathbf{E}_2 = \mathbf{e}_2$, and $\mathbf{E}_1 = \mathbf{E}_2 \times \mathbf{E}_3$.

The right-angle cantilever beam is depicted in Fig. 5.6 and consists of two initially straight beam segments of length ℓ connected at a right angle and clamped at the

Table 5.4: Geometric and material properties in the local (material) frame for right-angle cantilever beam in objectivity test

Parameter	**Value**
GA_1, GA_2, EA	10^6 N
EI_1, EI_2, GJ	10^3 N m^2
ℓ	10 m

root. Its geometric and material properties are listed in Table 5.4. Unless otherwise specified, each segment is discretized with 5 equal-length beam elements.

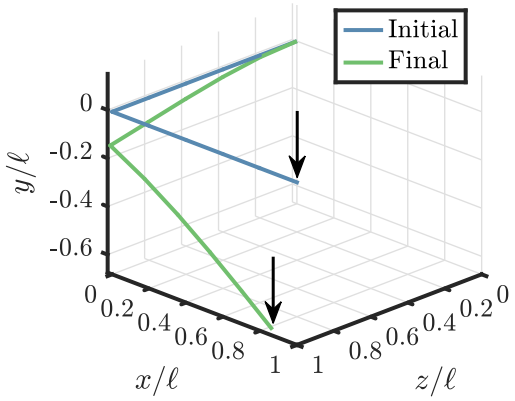

Figure 5.7: Comparison of initial (undeformed) configuration with deformed configuration after application of out-of-plane force at the beam's tip. The arrows denote the direction of the load. There is no magnification of the deformation.

Table 5.5: Tip displacements for right-angle cantilever beam subject to free-end out-of-plane force $P = 5$ N (Fig. 5.6)

Formulation	**Tip Displacements, m**		
	u_{1t}	u_{2t}	u_{3t}
Present (1 element/segment)	−1.6325	−6.2159	−0.2926
Present (5 elements/segment)	−1.7463	−6.7468	−0.4211
Present (20 elements/segment)	−1.7509	−6.7671	−0.4265
2-node orthogonal tensor [153]	−1.7368	−6.7329	−0.43081
3-node orthogonal tensor [153]	−1.4618	−6.2755	−0.44565
Rotation vector [153]	−1.7367	−6.7330	−0.43080
[146] (5 elements/segment)	−1.7511	−6.7468	−0.4126
[146] (20 elements/segment)	−1.7512	−6.7671	−0.4259

The cantilever is loaded by a vertical force $P = 5$ N at its free end and prescribed base rotations α, β, and γ about the spatially fixed $\mathbf{e}_1$, $\mathbf{e}_2$, and $\mathbf{e}_3$ axes, respectively. The direction of the vertical force is constant with respect to the global $\{\mathbf{e}_1, \mathbf{e}_2, \mathbf{e}_3\}$ frame. The objectivity test consists of two nonlinear static steps. In step (1), the vertical force is applied using five uniform load increments. This results in the deformed configuration depicted in Fig. 5.7. As a check, Table 5.5 compares the tip displacements obtained using 1, 5, and 20 elements per segment with published results. Based on the table, the present results obtained with 5 or more elements per segment are in good agreement with those from the literature. In steps (2a) through (2d), the following successive prescribed base rotations are then applied: (2a) rotation about the $\mathbf{e}_1$ axis through an angle α; (2b) rotation about the $\mathbf{e}_2$ axis through an angle β; (2c) rotation about the $\mathbf{e}_3$ axis through an angle γ; and (2d) rotation about the $\mathbf{e}_3 - \mathbf{e}_1$ axis through an angle δ (not shown in Fig. 5.6). (2d) is used to demonstrate that objectivity is independent of the choice of the rotation axis.

For each of steps (2a) through (2d), the cantilever is rotated through 100 complete turns about the corresponding axis using 4000 rotation increments, each through an angle of 9 deg. Objectivity (or lack thereof) is ascertained from the accumulation of errors after each complete turn. Nominally, the deformed configurations after each complete turn should exactly match the reference deformed configuration obtained after step (1).

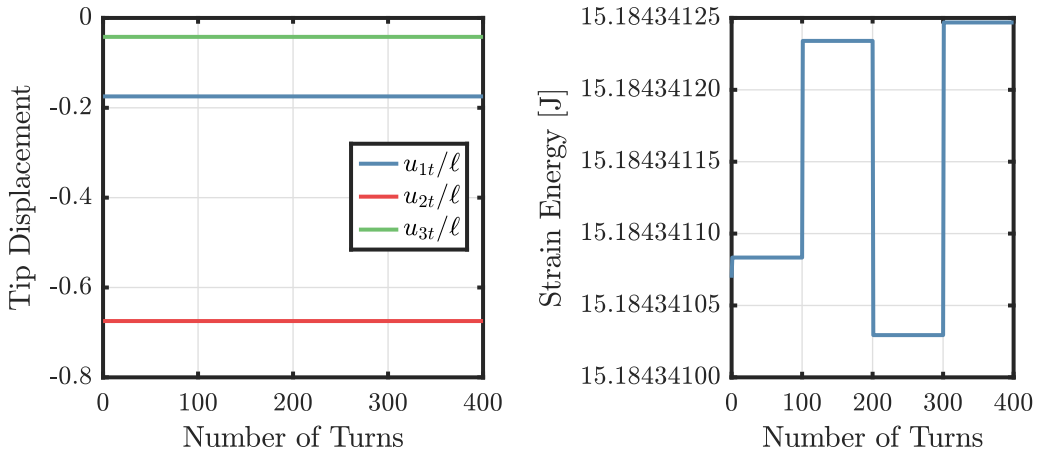

Figure 5.8: (a) Tip displacements and (b) strain energy as a function of the number of complete turns for steps (2a) through (2d). Turn 0 corresponds to the deformed configuration after step (1), turns 1-100 correspond to step (2a), turns 101-200 correspond to step (2b), and so on.

Figure 5.8a plots the three components of the tip displacement after each complete turn from steps (2a) through (2d). The figure demonstrates that the tip displacements are constant, irrespective of the number of turns or the choice of the rotation axis. In other words, there is no appreciable error accumulation in the computed tip displacement, as expected for an objective finite element formulation.

Figure 5.8b then uses the strain energy evaluated after each complete turn as a global configuration error metric. The figure depicts "jumps" in the strain energy between each step. Each jump corresponds to the re-equilibration of the resultant forces and moments after a change of the rotation axis; subsequent rotations about a single axis otherwise show no change in the strain energy. The maximum absolute strain energy error $|\mathcal{U} - \mathcal{U}_{\text{ref}}|$ between the current configuration with strain energy $\mathcal{U}$ and the configuration obtained from step (1) with strain energy $\mathcal{U}_1$ is on the order of 10^{-8} J, i.e., the absolute errors are approximately two orders of magnitude below the convergence tolerance of the Newton-Raphson solver. Thus, the jumps in the strain energy are consistent with the finite element formulation's objectivity.

Table 5.6: Tip displacements and relative displacement errors for right-angle cantilever beam subject to free-end out-of-plane force $P = 5$ N (Fig. 5.6). Relative errors are calculated with respect to the corresponding tip displacements from Table 5.5

Elements/	**Tip Displacements, m**			**Relative Errors, %**		
Segment	u_{1t}	u_{2t}	u_{3t}	u_{1t}	u_{2t}	u_{3t}
1	0.6660	−5.3456	−1.4042	−140.80	−14.001	379.84
5	−1.7498	−6.7531	−0.4219	0.1962	0.0926	0.1887
20	−1.7511	−6.7675	−0.4265	0.0123	0.0058	0.0118

Lastly, to quantify the numerical advantages of the objective finite element formulation, the objectivity test is re-evaluated using a non-objective formulation that replaces slerp with standard linear (vector space) interpolation of the nodal quaternions. Table 5.6 lists the tip displacements computed during step (1) with 1, 5, and 20 elements per segment and evaluates the relative displacement errors with respect to those from the objective formulation in Table 5.5. The table demonstrates that the non-objective formulation exhibits very poor accuracy with a coarse mesh (1 element per segment) and that the relative errors decrease as the mesh density increases. Intuitively, the discretization errors due to non-objectivity are related to the relative rotations across each element. For a given load, the relative rotations decrease as the mesh density increases, which in turn decreases the discretization

errors [144]. Physically, the discretization errors are at least in part due to the underprediction of the elemental curvatures. This results in a phenomenon analogous to locking. For a deformed element of length ℓ with nodal quaternions $\mathbf{p}_1$ and $\mathbf{p}_2$,

$$\frac{\left\|\mathbf{K}_l^h\right\|_2}{\left\|\mathbf{K}^h\right\|_2} = \frac{\sin(\theta)}{\theta} \leq 1 \tag{5.63}$$

where $\mathbf{K}_l^h = (2/\ell)\mathbf{G}^T(\mathbf{p}_1)\mathbf{p}_2$ is the discrete material curvature obtained using linear interpolation; $\mathbf{K}^h$ is the discrete material curvature evaluated with slerp [Eq. (5.39)]; $||\cdot||_2$ denotes the Euclidean norm; $\theta \in [0, \pi]$ [Eq. (5.19)]; and the equality only occurs in the limit as $\theta \to 0$, i.e., in the undeformed configuration. Based on Eq. (5.63), since θ decreases as the relative rotation across the element decreases, so too does the error between $\mathbf{K}_l^h$ and $\mathbf{K}^h$.

In step (1), the equilibrium iterations for each load increment converge despite the lack of objectivity. The same cannot be said in step (2). In particular, with the same rotation increment size (9 deg per increment), the non-objective formulation only convergences for the first 22 rotation increments (198 deg of rotation) in step (2a). The accumulation of discretization errors due to non-objectivity culminates in a numerical instability associated with ill-conditioning of the tangent stiffness matrix. Halving the rotation increment size merely postpones the onset of this instability. In this case, the equilibrium iterations stop converging in step (2c). Conversely, the objective formulation does not experience any numerical problems, i.e., it can use larger load (or rotation) increments and is more numerically stable for problems with large rotations. Altogether, the objective formulation achieves faster spatial convergence and exhibits both improved numerical stability and accuracy relative to the non-objective one.

5.5 Discussion

The main contribution of this chapter is the development of a new quaternion-based geometrically exact beam finite element in the Total Lagrangian description using only standard mathematical tools from vector calculus and linear algebra. Conventional geometrically exact beam finite elements rely on the mathematical machinery of differential geometry to account for the nonlinear structure of the 3D rotation group SO(3). Here, the quaternion-based approach achieves an equivalent end result from a significantly simpler conceptual framework. The new element is based on a Lie group formulation that implicitly enforces the quaternion unit norm constraint and uses spherical linear interpolation (slerp) to preserve the rigid body invariance

(i.e., the objectivity) of the 1D continuum strain measures. It likewise remedies several cumbersome characteristics of comparable elements from the literature. In particular, it uses a single rotation parameterization throughout the computer implementation and does not require switching between rotation parameterizations to handle large rotations.

Several numerical examples then illustrated salient aspects of the new element, including its susceptibility to shear locking and its subsequent correction, its path independence, and its objectivity. The objectivity test also demonstrated that slerp results in a formulation that is more numerically stable and achieves faster spatial convergence than an analogous formulation with linear interpolation of the nodal quaternions. All three numerical examples were static. Numerical examples for dynamics appear as reference solutions for the discrete-mechanics-based formulation of geometrically exact beam theory developed in Chapter 6.

Chapter 6

QUATERNION VARIATIONAL INTEGRATOR FOR SPATIAL BEAM DYNAMICS

6.1 Introduction

The goal of this chapter is to apply discrete mechanics to flexible multibody systems described by geometrically exact beams using a quaternion parameterization of the rotational degrees of freedom (DOFs). This results in a quaternion-based Lie group variational integrator for simulating the dynamics of holonomically constrained geometrically exact beams.

Traditionally, continuous-time (differential) equations of motion for mechanical systems are derived from continuous-time variational principles and then discretized in time using standard integrators; see e.g., [70]. Discrete mechanics [28, 29] inverts this paradigm, instead discretizing the governing variational principle in time before evaluating any variations. The resulting discrete-time (algebraic) equations of motion are referred to as a variational integrator. Discrete mechanics provides a systematic framework for deriving variational integrators of arbitrary accuracy for mechanical systems [28, 29].

Most standard integrators do not preserve the structure of the underlying physical system. As a consequence, these integrators can exhibit pathological, i.e., non-physical, behaviors that lead to spurious solutions, regardless of the spatial or temporal grid sizes used to discretize the physical system [190]. For example, standard integrators for mechanical systems, like the generalized-α method [25], introduce numerical dissipation to annihilate the high-frequency oscillations that can arise in the solution of numerically stiff differential equations. Excessive numerical dissipation, however, can spill over into the low-frequency dynamics, leading to non-physical energy decay. In general, these integrators neither preserve the structure nor any other invariants (e.g., energy or momentum) of the physical system.

Variational integrators, on the other hand, have several characteristics that make them particularly advantageous for simulating mechanical systems. In particular, they are symplectic, inherit the structure of the underlying physical system (including their stability characteristics), conserve momentum, and exhibit excellent energy stability, even for exponentially long simulation times. “Symplecticity” is a

conserved property of the solutions of Hamiltonian systems, a detailed discussion of which is outside the scope of this chapter; interested readers are instead referred to [191, 192] for concise introductions and [135] for a rigorous exposition. With that being said, some intuition into the notion of symplecticity can be developed by way of a simple example: the free vibration of a simple harmonic oscillator.[1] The practical significance of symplecticity is that unlike standard integrators, variational integrators converge to the exact continuous-time equations of motion as the time step size approaches zero. Variational integrators and other symplectic-momentum conserving integrators, however, have a significant disadvantage: they are prone to numerical instabilities driven by temporally unresolved high-frequency oscillations that can appear in the simulation of numerically stiff dynamical systems [193–198]. These instabilities are exacerbated for large time steps and highlight how structure preservation alone does not guarantee integration accuracy.

The standard structure-preserving alternative to symplectic-momentum integrators are energy-momentum ones. Fixed time step structure-preserving integrators are either symplectic-momentum conserving or energy-momentum conserving, not both [27]. Compared to symplectic-momentum methods, energy-momentum methods are advantageous because they are immune to instabilities associated with unresolved high-frequency oscillations [194, 196]. As a result, they are potentially more robust (but not necessarily more accurate) than symplectic-momentum methods for

[1]The free vibration of a simple harmonic oscillator with natural frequency ω_n is the solution to the differential equation

$$\ddot{x}(t) + \omega_n^2 x(t) = 0 \tag{6.1}$$

with initial conditions $x(0) = x_0$ and $\dot{x}(0) = \dot{x}_0$. In position-momentum form, the solution to Eq. (6.1) can be written as

$$\mathbf{z}(t) = \boldsymbol{\Xi}(t)\mathbf{z}_0 \tag{6.2}$$

where $\mathbf{z}^T(t) = (x(t), p(t))$ is the state vector with momentum $p(t) = \dot{x}(t)$ and

$$\boldsymbol{\Xi}(t) = \begin{bmatrix} \cos(\omega_n t) & \sin(\omega_n t)/\omega_n \\ -\omega_n \sin(\omega_n t) & \cos(\omega_n t) \end{bmatrix}. \tag{6.3}$$

Following [191, 192], the map $\boldsymbol{\Xi}(t)$ is then said to be symplectic because

$$\boldsymbol{\Xi}^T(t)\boldsymbol{\Sigma}\boldsymbol{\Xi}(t) = \boldsymbol{\Sigma} \tag{6.4}$$

for all $t \geq 0$ where $\boldsymbol{\Sigma}$ is the skew-symmetric symplectic matrix

$$\boldsymbol{\Sigma} = \begin{bmatrix} 0 & 1 \\ -1 & 0 \end{bmatrix}. \tag{6.5}$$

The symplectic form [Eq. (6.4)] is a conserved property of the solutions to Eq. (6.1) and implies that $\boldsymbol{\Xi}(t)$ is an area-preserving transformation for all $t \geq 0$ [191, 192]. This area is also a conserved quantity. An integrator is symplectic when it conserves a symplectic form analogous to Eq. (6.4).

simulating complex nonlinear phenomena in mechanical systems. However, as discussed in [199], energy-momentum methods may poorly approximate low-frequency oscillations for systems with multiple temporal scales, i.e., natural frequencies. This can lead to incorrect distributions of energy across the modes of a system. Likewise, for symplectic-momentum methods, non-conservation of energy is an obvious red flag indicative of poor solution accuracy [199]. In other words, energy conservation implies accuracy, even in the nonlinear setting. The same is not necessarily true for energy-momentum methods. In particular, it is well known that energy conservation alone is insufficient to guarantee either accuracy or stability [200]. Symplectic-energy-momentum preserving methods (see e.g., [201, 202]) based on time step adaptation may circumvent some or all of these shortcomings, but compared to fixed time step methods, these methods are still in their infancies [26]. For these reasons, a fixed time step, symplectic-momentum method for simulating the dynamics of geometrically exact beams is preferred here.

The beam formulation in this chapter uses the quaternion-based parameterization of the Reissner-Simo geometrically exact beam theory (GEBT) [32–34] from Chapter 5. To preserve the Lie group structure of GEBT, the temporal discretization of the variational principle uses a quaternion-based Lie group generalization of the standard midpoint rule. Here, quaternions are advantageous because they result in an intuitive geometric derivation of the midpoint quaternion based on vector algebra on the unit three-sphere. The subsequent spatial discretization via the finite element method then proceeds analogously to Chapter 5 using spherical linear interpolation (slerp) [133, 140] to interpolate the nodal quaternions along the reference axis of the beam. Unlike standard linear interpolation, slerp preserves the geometric structure of the 1D continuum strain measures. Thus, the spatial discretization is objective [129, 153, 154], meaning the discrete strain measures inherit their invariance to superposed rigid body motions from their continuum counterparts. Non-objective formulations lead to the accumulation of errors and solutions with non-physical path-dependence. Discretizing in time, then space leads to simpler algebraic equations of motion that reuse several key results from Chapter 5. Importantly, the initial temporal discretization circumvents any requirement to interpolate quaternion rates and accelerations using temporal derivatives of slerp. The resulting Lie group variational integrator implicitly satisfies the quaternion unit norm constraint using a conceptually straightforward quaternion-based approach rooted in vector calculus and linear algebra [139], as opposed to more classical approaches developed with differential geometry. The discrete mechanics framework used to derive the varia-

tional integrator is largely based on the theory of discrete mechanics for constrained mechanical systems from [197].

Structure-preserving integrators in general and variational integrators in particular are becoming increasingly common for numerical simulations in a range of applications; see [26] and the references therein. However, to the author's knowledge, there are only two contemporary applications of discrete mechanics to geometrically exact beam dynamics in the literature [203, 204]. In both cases, the variational principle is discretized in space, then time before evaluating any variations. The opposite is done here. Both [203, 204] likewise use the trapezoidal rule for the temporal discretization of the variational principle. This results in hybrid implicit-explicit integration schemes: an implicit step for updating the nodal rotations, followed by an explicit step for updating the nodal translations. In contrast, the scheme developed here uses a temporal midpoint discretization of the variational principle that requires a fully implicit solution scheme. Each iteration in the fully implicit scheme has a higher computational cost than the hybrid one. However, the fully implicit scheme may benefit from a larger minimum stable time increment to offset its higher computational cost.

In the context of this thesis, the quaternion Lie group variational integrator developed in this chapter is a discrete-time analog of the continuous-time beam element presented in Chapter 5. The variational integrator provides a structure-preserving numerical method for simulating the slew maneuver dynamics of an ultralight flexible spacecraft in Chapter 8.

This chapter is organized as follows: Sec. 6.2 derives a quaternion Lie group variational integrator for a free rigid body using a Lie group generalization of the standard midpoint rule. Due to the similarities between rigid body dynamics and GEBT, these results are directly applicable to the subsequent derivation of the variational integrator for geometrically exact beams. Sec. 6.3 uses the temporal discretization from Sec. 6.2 and a structure-preserving finite element discretization to derive the variational integrator for geometrically exact beams. Sec. 6.4 then applies the variational integrator from Sec. 6.3 to several benchmark problems that illustrate its excellent long-duration energy stability. Finally, Sec. 6.5 discusses the chapter's conclusions.

Like the preceding chapter, this chapter assumes familiarity with the material in Chapter 4. Additionally, it reuses several results from Chapter 5, particularly those related to the spatial discretization via the finite element method.

6.2 Quaternion Variational Integrator for a Free Rigid Body

The quaternion variational integrator for geometrically exact beams is based on a temporal midpoint discretization of the continuous-time variational principle. Due to the parallels between GEBT and rigid body dynamics [121], a quaternion variational integrator for the unforced motion of a free rigid body is derived to provide insights into the temporal midpoint discretization. Manchester and Peck [205] present a similar derivation based on a temporal discretization with the rectangle rule (specifically, a left Riemann sum), which results in a first-order accurate implicit variational integrator. In contrast, the midpoint rule used here results in a second-order accurate implicit variational integrator. Symmetric quadrature rules like the midpoint rule always result in variational integrators of even order [28, 29].

6.2.1 Discrete Variational Principle

Following [205], the derivation starts from the continuous-time variational principle, in this case Hamilton's principle. For the unforced motion of a free rigid body, the Lagrangian is simply the kinetic energy. Thus, Hamilton's principle takes the form

$$\delta \int_0^T \frac{1}{2} \boldsymbol{\Omega}^T \mathbf{J} \boldsymbol{\Omega} \, \mathrm{d}t = 0 \tag{6.6}$$

where $\boldsymbol{\Omega} \in \mathbb{R}^3 \hookrightarrow [\boldsymbol{\Omega}]_\times \in \mathfrak{so}(3)$ is the material angular velocity, i.e., the angular velocity of the material frame with respect to the spatial frame; $\mathbf{J} \in \mathbb{R}^{3\times 3}$ is the moment of inertia matrix about the center of mass; and T is an arbitrary final time. Both $\boldsymbol{\Omega}$ and $\mathbf{J}$ are expressed in the material frame. Next, the integral in Eq. (6.6) is divided into $N-1$ time steps of length h such that

$$\delta \sum_{k=0}^{N-1} \int_{t_k}^{t_{k+1}} \frac{1}{2} \boldsymbol{\Omega}^T \mathbf{J} \boldsymbol{\Omega} \, \mathrm{d}t = 0 \tag{6.7}$$

where $N = T/h + 1$; $t_0 = 0$; $t_N = T$; and $t_{k+1} = t_k + h$. Up until this point, no approximations have been introduced, i.e., Eq. (6.7) is exact.

From here, the standard procedure for deriving a variational integrator is to approximate the integral in Eq. (6.7) using a quadrature rule [28, 29]. However, since the set of quaternions $\mathbb{H}_1$ defines a Lie group, standard quadrature rules like the midpoint rule used here must be modified to account for the group properties. This is done next. For a more general discussion of Lie group midpoint rules in the context of variational integrators, see [206].

For the 3D rotation group SO(3), the midpoint orientation $\mathbf{\Lambda}_{k+1/2} \in \mathrm{SO}(3)$ halfway between two orientations $\mathbf{\Lambda}_k, \mathbf{\Lambda}_{k+1} \in \mathrm{SO}(3)$ is defined as [70, p. 309–311]

$$\mathbf{\Lambda}_{k+1/2} = \mathbf{\Lambda}_k \mathbf{F}_k = \mathbf{\Lambda}_{k+1} \mathbf{F}_k^T \tag{6.8}$$

where $\mathbf{F}_k \in \mathrm{SO}(3)$ is the incremental rotation. From Eq. (6.8), $\mathbf{F}_k$ satisfies

$$\mathbf{\Lambda}_{k+1} = \mathbf{\Lambda}_k \mathbf{F}_k^2. \tag{6.9}$$

Thus, the rotation from $\mathbf{\Lambda}_k$ to $\mathbf{\Lambda}_{k+1}$ is equivalent to two successive rotations by $\mathbf{F}_k$. Per Euler's theorem, any rotation can be described as a rotation about some axis fixed in space. The two successive rotations by $\mathbf{F}_k$ both occur about the same axis.

Analogous to Eq. (6.8), the midpoint quaternion halfway between $\mathbf{p}_k \in \mathbb{H}_1$ and $\mathbf{p}_{k+1} \in \mathbb{H}_1$ is

$$\mathbf{p}_{k+1/2} = \mathbf{L}(\mathbf{p}_k)\mathbf{f}_k = \mathbf{L}(\mathbf{p}_{k+1})\mathbf{f}_k^* \tag{6.10}$$

where $\mathbf{f}_k \in \mathbb{H}_1$ is the incremental quaternion describing the successive rotations from $\mathbf{p}_k$ to $\mathbf{p}_{k+1/2}$ and from $\mathbf{p}_{k+1/2}$ to $\mathbf{p}_{k+1}$, i.e.,

$$\mathbf{p}_{k+1} = \mathbf{L}(\mathbf{p}_k)\mathbf{L}(\mathbf{f}_k)\mathbf{f}_k. \tag{6.11}$$

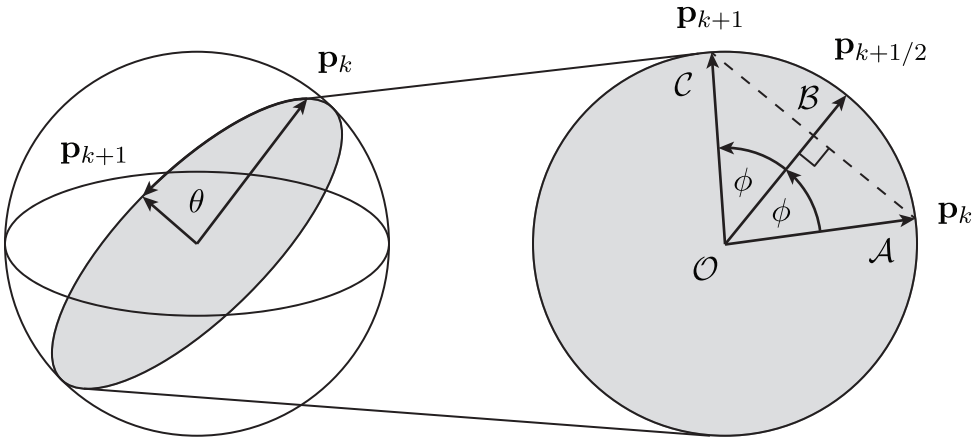

Figure 6.1: Geometric interpretation of the mid-quaternion $\mathbf{p}_{k+1/2}$ on the 4D unit hypersphere (the unit three-sphere) $\mathbb{H}_1$. The incremental quaternion $\mathbf{f}_k$ defines the incremental rotations from $\mathbf{p}_k$ to $\mathbf{p}_{k+1/2}$ and from $\mathbf{p}_{k+1/2}$ to $\mathbf{p}_{k+1}$, both through the angle $\phi = \theta/2$ where $\theta = \cos^{-1}\left(\mathbf{p}_k^T \mathbf{p}_{k+1}\right)$.

It is straightforward to develop an expression for $\mathbf{f}_k$ by considering the geometry of $\mathbb{H}_1$, the unit hypersphere in $\mathbb{R}^4$; see Fig. 6.1. Since the two successive rotations $\mathbf{f}_k$ occur about the same axis, $\mathbf{p}_{k+1/2}$ must lie in the plane spanned by $\mathbf{p}_k$ and $\mathbf{p}_{k+1}$. Thus, $\mathbf{p}_{k+1/2}$ is the unit vector in this plane that bisects $\mathbf{p}_k$ and $\mathbf{p}_{k+1}$, meaning it is

the unit vector parallel to line segment $\mathcal{OB}$ in Fig. 6.1. The vectors parallel to line segments $\mathcal{AC}$ and $\mathcal{AB}$ in Fig. 6.1 are $\mathbf{p}_{k+1} - \mathbf{p}_k$ and $(\mathbf{p}_{k+1} - \mathbf{p}_k)/2$, respectively. Thus, the vector parallel to $\mathcal{OB}$ is $(\mathbf{p}_k + \mathbf{p}_{k+1})/2$, which is normalized to obtain the following expression for $\mathbf{p}_{k+1/2}$:

$$\mathbf{p}_{k+1/2} = \frac{\mathbf{p}_k + \mathbf{p}_{k+1}}{\sqrt{2\left(1 + \mathbf{p}_k^T \mathbf{p}_{k+1}\right)}}. \tag{6.12}$$

By substituting Eq. (6.12) into Eq. (6.10) and rearranging, it follows that

$$\mathbf{f}_k = \frac{\mathbf{I}_\mathbf{p} + \mathbf{L}^T(\mathbf{p}_k)\mathbf{p}_{k+1}}{\sqrt{2\left(1 + \mathbf{p}_k^T \mathbf{p}_{k+1}\right)}}. \tag{6.13}$$

Equation (6.12) is not unique; equivalent expressions can be developed, e.g., using slerp [133, 140]. However, the geometric interpretation given by Eq. (6.12) is advantageous because it avoids the use of trigonometric functions, thereby simplifying subsequent theoretical developments. Likewise, the geometric interpretation simplifies the numerical implementation since $\mathbf{p}_{k+1/2}$ can be evaluated by simply normalizing the sum $\mathbf{p}_k + \mathbf{p}_{k+1}$. $\mathbf{f}_k$ can then be evaluated directly from Eq. (6.10).

The incremental quaternion $\mathbf{f}_k$ appears in the discrete midpoint approximation of the material angular velocity $\boldsymbol{\Omega}$. If $\mathbf{p} \in \mathbb{H}_1$ is the quaternion describing the orientation of the rigid body (the material frame) with respect to the spatial frame, then $\boldsymbol{\Omega}$ is given by the well-known kinematic relationship [133]

$$\boldsymbol{\Omega} = 2\mathbf{G}^T(\mathbf{p})\dot{\mathbf{p}} \tag{6.14}$$

where $\dot{\mathbf{p}}$ is the time derivative of $\mathbf{p}$. To approximate Eq. (6.14) at the midpoint, i.e., to evaluate $\boldsymbol{\Omega}_{k+1/2}$, $\mathbf{p}$ is replaced with $\mathbf{p}_{k+1/2}$ and $\dot{\mathbf{p}}$ is approximated with a finite difference over the interval $t_{k+1} = t_k + h$ to obtain

$$\boldsymbol{\Omega}_{k+1/2} = 2\mathbf{G}^T(\mathbf{p}_{k+1/2})\left(\frac{\mathbf{p}_{k+1} - \mathbf{p}_k}{h}\right). \tag{6.15}$$

Since $\dot{\mathbf{p}}$ is an element of the vector space tangent to $\mathbb{H}_1$, i.e., the Lie algebra of $\mathbb{H}_1$, not the Lie group $\mathbb{H}_1$, its finite difference can be defined in the standard way. Substituting Eq. (6.12) and using Eq. (4.24) and the identity $\mathbf{G}^T(\mathbf{p}_1)\mathbf{p}_2 + \mathbf{G}^T(\mathbf{p}_2)\mathbf{p}_1 = \mathbf{0}_{3\times 1}$ for $\mathbf{p}_1, \mathbf{p}_2 \in \mathbb{H}_1$ then yields the remarkably simple relationship

$$\boldsymbol{\Omega}_{k+1/2} = \frac{4}{h}\mathbf{T}^T\mathbf{f}_k. \tag{6.16}$$

Thus, the angular velocity $\mathbf{\Omega}_{k+1/2}$ at the midpoint is only a function of the incremental quaternion $\mathbf{f}_k$. Using Eq. (6.16), the midpoint approximation of the continuous-time variational principle [Eq. (6.7)] takes the form

$$\delta S = \delta \sum_{k=0}^{N-1} \frac{8}{h} \mathbf{f}_k^T \mathbf{T}\mathbf{J}\mathbf{T}^T \mathbf{f}_k = 0. \tag{6.17}$$

This is the discrete variational principle for a free rigid body.

6.2.2 Quaternion Variational Integrator

The quaternion variational integrator for a free rigid body is derived by evaluating the discrete variational principle [Eq. (6.17)]. Taking the variation of the discrete action sum, i.e., evaluating the variation of the summation in Eq. (6.17), yields

$$\begin{aligned} \delta S &= \sum_{k=0}^{N-1} \frac{16}{h} \left[\delta \mathbf{p}_k^T \left(\frac{\partial \mathbf{f}_k}{\partial \mathbf{p}_k} \right)^T \mathbf{T}\mathbf{J}\mathbf{T}^T \mathbf{f}_k + \delta \mathbf{p}_{k+1}^T \left(\frac{\partial \mathbf{f}_k}{\partial \mathbf{p}_{k+1}} \right)^T \mathbf{T}\mathbf{J}\mathbf{T}^T \mathbf{f}_k \right] \\ &= \sum_{k=1}^{N-1} \frac{16}{h} \delta \mathbf{p}_k^T \left[\left(\frac{\partial \mathbf{f}_{k-1}}{\partial \mathbf{p}_k} \right)^T \mathbf{T}\mathbf{J}\mathbf{T}^T \mathbf{f}_{k-1} + \left(\frac{\partial \mathbf{f}_k}{\partial \mathbf{p}_k} \right)^T \mathbf{T}\mathbf{J}\mathbf{T}^T \mathbf{f}_k \right] \end{aligned} \tag{6.18}$$

where $\delta \mathbf{f}_k = (\partial \mathbf{f}_k / \partial \mathbf{p}_k)\, \delta \mathbf{p}_k + (\partial \mathbf{f}_k / \partial \mathbf{p}_{k+1})\, \delta \mathbf{p}_{k+1}$. The second equality follows from discrete integration by parts (summation by parts) with $\delta \mathbf{p}_0 = \delta \mathbf{p}_N = \mathbf{0}_{4\times 1}$ (since $\mathbf{p}_0$ and $\mathbf{p}_N$ are assumed to be fixed).

Thus far, the evaluation of Eq. (6.17) neglects the group structure of $\mathbb{H}_1$. To account for this, $\delta \mathbf{p}_k$ is referenced to the material tangent space using Eq. (4.34) to obtain

$$\delta S = \sum_{k=1}^{N-1} \frac{8}{h} \delta \mathbf{\Theta}_k^T \mathbf{G}^T(\mathbf{p}_k) \left[\left(\frac{\partial \mathbf{f}_{k-1}}{\partial \mathbf{p}_k} \right)^T \mathbf{T}\mathbf{J}\mathbf{T}^T \mathbf{f}_{k-1} + \left(\frac{\partial \mathbf{f}_k}{\partial \mathbf{p}_k} \right)^T \mathbf{T}\mathbf{J}\mathbf{T}^T \mathbf{f}_k \right]. \tag{6.19}$$

This is analogous to the "conversion factor" approach introduced in [139] that allows standard results from vector calculus and linear algebra to be applied to $\mathbb{H}_1$. Per the standard procedure [28, 29], the variation of the discrete action sum δS is then required to be zero for any $\delta \mathbf{\Theta}_k$. This yields the discrete Euler-Lagrange equations:

$$\frac{8}{h} \mathbf{G}^T(\mathbf{p}_k) \left(\frac{\partial \mathbf{f}_{k-1}}{\partial \mathbf{p}_k} \right)^T \mathbf{T}\mathbf{J}\mathbf{T}^T \mathbf{f}_{k-1} + \frac{8}{h} \mathbf{G}^T(\mathbf{p}_k) \left(\frac{\partial \mathbf{f}_k}{\partial \mathbf{p}_k} \right)^T \mathbf{T}\mathbf{J}\mathbf{T}^T \mathbf{f}_k = \mathbf{0}_{3\times 1} \tag{6.20}$$

which must hold for any k. The discrete Euler-Lagrange equations are commonly referred to as a variational integrator. Given $\mathbf{p}_{k-1}$ and $\mathbf{p}_k$, Eq. (6.20) is a nonlinear implicit equation for $\mathbf{p}_{k+1}$. Equation (6.20) is the discrete-time analogue of Euler's equations for the dynamics of a free rigid body.

The two terms in Eq. (6.20) are equivalent expressions for the discrete angular momentum $\mathbf{h}_k$ at time step k [28, 29]; i.e.,

$$\mathbf{h}_k = \frac{8}{h}\mathbf{G}^T(\mathbf{p}_k)\left(\frac{\partial \mathbf{f}_{k-1}}{\partial \mathbf{p}_k}\right)^T \mathbf{T}\mathbf{J}\mathbf{T}^T\mathbf{f}_{k-1} = -\frac{8}{h}\mathbf{G}^T(\mathbf{p}_k)\left(\frac{\partial \mathbf{f}_k}{\partial \mathbf{p}_k}\right)^T \mathbf{T}\mathbf{J}\mathbf{T}^T\mathbf{f}_k. \tag{6.21}$$

It follows that Eq. (6.20) can be written in the equivalent position-momentum form

$$\mathbf{h}_k = -\frac{8}{h}\mathbf{G}^T(\mathbf{p}_k)\left(\frac{\partial \mathbf{f}_k}{\partial \mathbf{p}_k}\right)^T \mathbf{T}\mathbf{J}\mathbf{T}^T\mathbf{f}_k, \tag{6.22}$$

$$\mathbf{h}_{k+1} = \frac{8}{h}\mathbf{G}^T(\mathbf{p}_{k+1})\left(\frac{\partial \mathbf{f}_k}{\partial \mathbf{p}_{k+1}}\right)^T \mathbf{T}\mathbf{J}\mathbf{T}^T\mathbf{f}_k. \tag{6.23}$$

Hence, Eq. (6.20) can be interpreted as a discrete momentum balance between adjacent time steps. Additionally, since $\mathbf{h}_k = \mathbf{J}\boldsymbol{\Omega}_k$, Eq. (6.21) can be used to initialize the integrator (if $\mathbf{p}_0$ and $\boldsymbol{\Omega}_0$ are known) or to solve for $\boldsymbol{\Omega}_k$ (if either $\mathbf{p}_{k-1}$ and $\mathbf{p}_k$ or $\mathbf{p}_k$ and $\mathbf{p}_{k+1}$ are known) [205]. Similar expressions appear in the variational integrator for geometrically exact beams developed in Sec. 6.3.

The linearization of Eq. (6.20) [or equivalently, Eq. (6.22)] results in an equation for the incremental material rotation $\Delta\boldsymbol{\Theta}_{k+1}$ that advances the solution from $\mathbf{p}_k$ to $\mathbf{p}_{k+1}$, not $\mathbf{p}_{k+1}$ itself. As a result, solving Eq. (6.20) requires a Lie group solver, like the Lie group generalization of the Newton-Raphson method [139, 177], with an appropriate quaternion update (like the Cayley map described in Sec. 4.3.2) to determine $\mathbf{p}_{k+1}$ from $\mathbf{p}_k$ and $\Delta\boldsymbol{\Theta}_{k+1}$. The solution algorithm for Eq. (6.20) using a quaternion-based Lie group generalization of the Newton-Raphson method is described in Algorithm 1. In Algorithm 1, the second argument in the function $\text{norm}(\cdot,\cdot)$ specifies the type of norm, either 2 for the Euclidean norm or ∞ for the infinity norm.

Initializing Algorithm 1 requires the quaternion $\mathbf{p}_0 \in \mathbb{H}_1$ corresponding to the initial orientation $\boldsymbol{\Lambda}_0 \in \text{SO}(3)$ and the material angular velocity $\boldsymbol{\Omega}_0$, both at $t = 0$. The initial angular momentum then follows from $\mathbf{h}_0 = \mathbf{J}\boldsymbol{\Omega}_0$. The time step h, the maximum number of iterations per time step $i_{\max}$, and the convergence tolerance τ must also be specified.

Implementing the Newton-Raphson method in Algorithm 1 requires an expression for the Jacobian matrix. The analytical expression for the Jacobian matrix is involved, and hence, omitted here for brevity. It can be obtained by differentiating Eq. (6.20) (or equivalently, $\mathbf{h}_k$) with respect to $\mathbf{p}_{k+1}$, and then right-multiplying by $\mathbf{G}(\mathbf{p}_{k+1})/2$, in accordance with Eq. (4.34). This replaces the infinitesimal quantities

Algorithm 1 $[\mathbf{p}_{k+1}, \mathbf{h}_{k+1}] = \text{rigidBodyStep}(\mathbf{p}_k, \mathbf{h}_k)$

$\Delta\boldsymbol{\Theta}_{k+1} \coloneqq \mathbf{0}_{3\times 1}$
for $i = 1$ to $i_{\max}$ **do**
  $\mathbf{p}_{k+1} \coloneqq \mathbf{L}(\mathbf{p}_k)\,\text{cay}(\Delta\boldsymbol{\Theta}_{k+1}/2)$ [see Eqs. (4.35) and (4.36)]
  $\mathbf{p}_{k+1/2} \coloneqq (\mathbf{p}_k + \mathbf{p}_{k+1})\,/\text{norm}\,(\mathbf{p}_k + \mathbf{p}_{k+1}, 2)$
  $\mathbf{f}_k \coloneqq \mathbf{L}^T(\mathbf{p}_k)\mathbf{p}_{k+1/2}$
  $\mathbf{h}_k^{(i)} \coloneqq -(8/h)\mathbf{G}^T(\mathbf{p}_k)\,(\partial\mathbf{f}_k/\partial\mathbf{p}_k)^T\,\mathbf{TJT}^T\mathbf{f}_k$
  $\mathbf{r} \coloneqq \mathbf{h}_k^{(i)} - \mathbf{h}_k$
  if $\text{norm}\,(\mathbf{r}, \infty) \leq \tau$ **then**
    break
  end if
  $\Delta\boldsymbol{\Theta}_{k+1} \coloneqq \Delta\boldsymbol{\Theta}_{k+1} - \left[\left(\partial\mathbf{h}_k^{(i)}/\partial\mathbf{p}_{k+1}\right)\mathbf{G}(\mathbf{p}_{k+1})/2\right]^{-1}\mathbf{r}$
end for
$\mathbf{h}_{k+1} \coloneqq (8/h)\mathbf{G}^T(\mathbf{p}_{k+1})\,(\partial\mathbf{f}_k/\partial\mathbf{p}_{k+1})^T\,\mathbf{TJT}^T\mathbf{f}_k$

in Eq. (4.34) with the corresponding small (incremental) quantities so that each Newton-Raphson iteration solves for the incremental material rotation $\Delta\boldsymbol{\Theta}_{k+1}$.

6.3 Quaternion Variational Integrator for Geometrically Exact Beams

The derivation of the quaternion variational integrator for geometrically exact beams mirrors that of the quaternion variational integrator for the free rigid body from Sec. 6.2, but with additional complications due to the finite element discretization.

Like the beam element developed in Chapter 5, the derivation starts from the constrained Lagrange-d'Alembert principle in continuous-time (see e.g., [135, Secs. 7.8 and 8.3]):

$$\delta\int_0^T \left(\mathcal{L}(\mathbf{q},\dot{\mathbf{q}}) - \mathbf{c}(\mathbf{q},\boldsymbol{\lambda})\right)\,\mathrm{d}t + \int_0^T \delta\mathcal{W}_{\text{ext}}(t,\mathbf{q})\,\mathrm{d}t = 0 \tag{6.24}$$

where $\mathcal{L}(\mathbf{q},\dot{\mathbf{q}}) = \mathcal{T}(\mathbf{q},\dot{\mathbf{q}}) - \mathcal{U}(\mathbf{q})$ is the Lagrangian; $\mathcal{T}(\mathbf{q},\dot{\mathbf{q}})$ is the configuration-dependent kinetic energy; $\mathcal{U}(\mathbf{q})$ is the strain energy; $\delta\mathcal{W}_{\text{ext}}(t,\mathbf{q})$ is the virtual work done by the external and/or non-conservative forces and moments; $\mathbf{q}^T = \left(\mathbf{x}^T, \mathbf{p}^T\right)$ contains the generalized coordinates; and T is an arbitrary final time. The function $\mathbf{c}(\mathbf{q},\boldsymbol{\lambda})$ conjugates the constraints to the independent Lagrange multipliers $\boldsymbol{\lambda}$ and is given by [142, 143, 160, 164]

$$\mathbf{c}(\mathbf{q},\boldsymbol{\lambda}) = \int_0^\ell \boldsymbol{\phi}^T(\mathbf{q})\boldsymbol{\lambda}\,\mathrm{d}s \tag{6.25}$$

where $\boldsymbol{\phi}(\mathbf{q})$ is the vector of holonomic constraints. Equation (6.25) can enforce distributed constraints along the beam's reference axis, like the unit norm constraints

associated with quaternion vector space [160, 164] or director-based [142, 143] formulations. However, since the Lie group formulation developed here implicitly satisfies the quaternion unit norm constraint, $\boldsymbol{\phi}(\mathbf{q})$ is exclusively used to enforce external constraints at the finite element nodes, e.g., the joint constraints in flexible multibody systems. This entails the use of Dirac delta functions to interpolate the Lagrange multipliers in the spatial discretization. From here, the derivation diverges from that of the continuous-time beam element presented in Chapter 5.

Following Sec. 6.2.1, the integrals with respect to time in Eq. (6.24) are subdivided into $N-1$ time steps, each of length h, which gives

$$\delta \sum_{k=0}^{N-1} \int_{t_k}^{t_{k+1}} \left(\mathcal{L}(\mathbf{q}, \dot{\mathbf{q}}) - \mathbf{c}(\mathbf{q}, \boldsymbol{\lambda})\right) \, \mathrm{d}t + \sum_{k=0}^{N-1} \int_{t_k}^{t_{k+1}} \delta \mathcal{W}_{\text{ext}}(t, \mathbf{q}) \, \mathrm{d}t = 0 \tag{6.26}$$

where $N = T/h+1$; $t_0 = 0$; $t_N = T$; and $t_{k+1} = t_k + h$. Like Eq. (6.7), Eq. (6.26) is exact. Next, expressions for the kinetic energy [Eq. (4.51)], strain energy [Eq. (4.41)], virtual work done by the external forces [Eq. (4.57)], and constraints [Eq. (6.25)] are substituted into Eq. (6.26) to obtain

$$\begin{aligned} \delta \sum_{k=0}^{N-1} \int_{t_k}^{t_{k+1}} \int_0^{\ell} \frac{1}{2} \left(\rho A \, \dot{\mathbf{x}}^T \dot{\mathbf{x}} + \boldsymbol{\Omega}^T \mathbf{J} \boldsymbol{\Omega} - \mathbf{S}^T \mathbf{E} - 2\boldsymbol{\phi}^T(\mathbf{q}) \boldsymbol{\lambda}\right) \, \mathrm{d}s \, \mathrm{d}t \\ + \sum_{k=0}^{N-1} \int_{t_k}^{t_{k+1}} \int_0^{\ell} \left(\delta \mathbf{x}^T \overline{\mathbf{n}} + \delta \mathbf{p}^T \left(2\mathbf{H}(\mathbf{p}) \overline{\mathbf{m}}\right)\right) \, \mathrm{d}s \, \mathrm{d}t = 0. \end{aligned} \tag{6.27}$$

Energy and work per unit length are both integrable, and consequently, Fubini's theorem implies that the integrals in Eq. (6.27) can be evaluated in any order. This suggests two options for deriving the variational integrator. Specifically, Eq. (6.27) can either be discretized in time and then interpolated in space, or vice versa. Discretization and interpolation are not commutative, but both options converge to the continuous-time case as $h \to 0$. In continuum mechanics, the standard approach is spatial discretization followed by temporal discretization. This results in a system of ordinary differential equations that are often amenable to temporal discretizations (at least in the finite element case) using standard integrators like the generalized-α method [25]. Not surprisingly, this is also a common approach for deriving variational integrators in continuum mechanics; see e.g., [29, 203, 204, 207]. Here, however, the converse approach of discretizing in time, then interpolating in space is adopted because it results in simpler equations of motion. While not especially common, this approach is used elsewhere in mechanics, e.g., in [128, 144].

Like Chapter 5, variations with respect to the quaternion $\mathbf{p}$ initially assume that its four components are independent, in violation of the unit norm constraint. This assumption is subsequently corrected to account for the group structure of $\mathbb{H}_1$ using the structure-preserving spatial discretization in Sec. 6.3.2.

6.3.1 Discrete Variational Principle

After exchanging the order of integration in Eq. (6.27), the temporal discretization of the variational principle [Eq. (6.27)] involves defining finite differences for the velocities and applying quadrature rules to approximate the temporal integrals. The following approximations are specifically introduced:

- $\dot{\mathbf{x}}$ and $\boldsymbol{\Omega}$ are approximated by $\dot{\mathbf{x}} \approx (\mathbf{x}_{k+1} - \mathbf{x}_k)/h$ and Eq. (6.16), respectively;
- the kinetic and strain energy integrals are approximated using the appropriate midpoint rules, i.e., $\mathbf{x}_{k+1/2}$ and $\mathbf{p}_{k+1/2}$ are approximated by $\mathbf{x}_{k+1/2} \approx (\mathbf{x}_k + \mathbf{x}_{k+1})/2$ and Eq. (6.12), respectively;
- the constraint integral is approximated using the trapezoid rule [197], i.e.,

$$\int_{t_k}^{t_{k+1}} \int_0^{\ell} \boldsymbol{\phi}^T(\mathbf{q})\boldsymbol{\lambda} \, \mathrm{d}s \, \mathrm{d}t \approx \frac{h}{2} \int_0^{\ell} \left(\boldsymbol{\phi}_k^T \boldsymbol{\lambda}_k + \boldsymbol{\phi}_{k+1}^T \boldsymbol{\lambda}_{k+1} \right) \mathrm{d}s \tag{6.28}$$

  where $\boldsymbol{\phi}_k = \boldsymbol{\phi}(\mathbf{q}_k)$; and

- the virtual work integral is replaced by left and right discrete forces [28, 29] approximated using the trapezoid rule, i.e.,

$$\begin{aligned} &\int_{t_k}^{t_{k+1}} \int_0^{\ell} \left(\delta\mathbf{x}^T \overline{\mathbf{n}} + \delta\mathbf{p}^T \left(2\mathbf{H}(\mathbf{p})\overline{\mathbf{m}} \right) \right) \mathrm{d}s \, \mathrm{d}t \\ &\qquad \approx \frac{h}{4} \int_0^{\ell} \begin{bmatrix} \delta\mathbf{x}_k + \delta\mathbf{x}_{k+1} \\ \delta\mathbf{p}_k + \delta\mathbf{p}_{k+1} \end{bmatrix}^T \begin{bmatrix} \overline{\mathbf{n}}_k + \overline{\mathbf{n}}_{k+1} \\ 2\mathbf{H}_k\overline{\mathbf{m}}_k + 2\mathbf{H}_{k+1}\overline{\mathbf{m}}_{k+1} \end{bmatrix} \mathrm{d}s \end{aligned} \tag{6.29}$$

  where $\mathbf{H}_k = \mathbf{H}(\mathbf{p}_k)$.

These approximations result in the discrete variational principle

$$\delta \left(S_{\text{iner}} - S_{\text{int}} - S_{\text{con}} \right) + \delta S_{\text{ext}} = 0 \tag{6.30}$$

where S_{iner}, S_{int}, S_{con}, and δS_{ext} are the discrete action sums associated with the kinetic energy, the strain energy, the constraints, and the external virtual work:

$$S_{\text{iner}} = \sum_{k=0}^{N-1} \int_0^{\ell} \frac{1}{2} \left(\frac{\rho A}{h} \left(\mathbf{x}_{k+1} - \mathbf{x}_k \right)^T \left(\mathbf{x}_{k+1} - \mathbf{x}_k \right) + \frac{16}{h} \mathbf{f}_k^T \mathbf{T} \mathbf{J} \mathbf{T}^T \mathbf{f}_k \right) \mathrm{d}s, \tag{6.31}$$

$$S_{\text{int}} = \sum_{k=0}^{N-1} \frac{h}{2} \int_0^{\ell} \mathbf{S}_{k+1/2}^T \mathbf{E}_{k+1/2} \, \mathrm{d}s, \tag{6.32}$$

$$S_{\text{con}} = \sum_{k=0}^{N-1} \frac{h}{2} \int_0^{\ell} \left(\boldsymbol{\phi}_k^T \boldsymbol{\lambda}_k + \boldsymbol{\phi}_{k+1}^T \boldsymbol{\lambda}_{k+1} \right) \mathrm{d}s, \tag{6.33}$$

$$\delta S_{\text{ext}} = \sum_{k=0}^{N-1} \frac{h}{4} \int_0^{\ell} \begin{bmatrix} \delta \mathbf{x}_k + \delta \mathbf{x}_{k+1} \\ \delta \mathbf{p}_k + \delta \mathbf{p}_{k+1} \end{bmatrix}^T \begin{bmatrix} \overline{\mathbf{n}}_k + \overline{\mathbf{n}}_{k+1} \\ 2\mathbf{H}_k \overline{\mathbf{m}}_k + 2\mathbf{H}_{k+1} \overline{\mathbf{m}}_{k+1} \end{bmatrix} \mathrm{d}s. \tag{6.34}$$

The trapezoidal approximations simplify the resulting discrete-time propagation equations by eliminating midpoint evaluations of the forces and constraints. Additionally, the trapezoidal approximation of the constraint term yields discrete Lagrange multipliers consistent with their continuous-time counterparts [197].

6.3.2 Quaternion Variational Integrator

Following [28, 29], the variational integrator is derived by taking the variations of the discrete action sums [Eqs. (6.31) to (6.33)] with fixed boundary conditions ($\delta \mathbf{x}_0 = \delta \mathbf{x}_N = \mathbf{0}_{3\times 1}$ and $\delta \mathbf{p}_0 = \delta \mathbf{p}_N = \mathbf{0}_{4\times 1}$) and then applying discrete integration by parts (summation by parts) to the discrete variational principle [Eq. (6.30)]. The structure-preserving spatial discretization follows using the methods from Sec. 5.3. The spatial discretization assumes that the position and rotation (quaternion) fields in the element are independent, as is standard for geometrically exact beam finite elements. Like Sec. 5.3, it considers a single two-node beam element of length ℓ with 7 DOFs per node, three translations and a quaternion, for a total of 14 DOFs per element. Of these, only 12 are independent due to the quaternion unit norm constraint. In what follows, the superscripts (1) and (2) denote the nodes at the left and right ends of the element. The superscript h likewise denotes an interpolated quantity in the spatial discretization. The complete finite element model is ultimately assembled using a standard finite element step.

The steps outlined above are carried out individually for Eqs. (6.31) to (6.34) next, and the results are subsequently aggregated into the discrete Euler-Lagrange equations for the geometrically exact beam.

Discrete Inertia Forces

The discrete inertia forces are derived by evaluating the variation of S_{iner} [Eq. (6.31)], using discrete integration by parts, and discretizing in space. Evaluating the variation of S_{iner} gives

$$\delta S_{\text{iner}} = \sum_{k=0}^{N-1} \int_0^{\ell} \left[\frac{\rho A}{h} \left(\delta \mathbf{x}_{k+1}^T \left(\mathbf{x}_{k+1} - \mathbf{x}_k \right) - \delta \mathbf{x}_k^T \left(\mathbf{x}_{k+1} - \mathbf{x}_k \right) \right) + \frac{16}{h} \left(\delta \mathbf{p}_k^T \left(\frac{\partial \mathbf{f}_k}{\partial \mathbf{p}_k} \right)^T \mathbf{T}\mathbf{J}\mathbf{T}^T \mathbf{f}_k + \delta \mathbf{p}_{k+1}^T \left(\frac{\partial \mathbf{f}_k}{\partial \mathbf{p}_{k+1}} \right)^T \mathbf{T}\mathbf{J}\mathbf{T}^T \mathbf{f}_k \right) \right] \mathrm{d}s. \quad (6.35)$$

Discrete integration by parts with $\delta \mathbf{x}_0 = \delta \mathbf{x}_N = \mathbf{0}_{3\times 1}$ and $\delta \mathbf{p}_0 = \delta \mathbf{p}_N = \mathbf{0}_{4\times 1}$ then yields

$$\delta S_{\text{iner}} = \sum_{k=1}^{N-1} \int_0^{\ell} \left[-\frac{\rho A}{h} \delta \mathbf{x}_k^T \left(\mathbf{x}_{k+1} - 2\mathbf{x}_k + \mathbf{x}_{k-1} \right) + \frac{16}{h} \delta \mathbf{p}_k^T \left(\left(\frac{\partial \mathbf{f}_{k-1}}{\partial \mathbf{p}_k} \right)^T \mathbf{T}\mathbf{J}\mathbf{T}^T \mathbf{f}_{k-1} + \left(\frac{\partial \mathbf{f}_k}{\partial \mathbf{p}_k} \right)^T \mathbf{T}\mathbf{J}\mathbf{T}^T \mathbf{f}_k \right) \right] \mathrm{d}s \quad (6.36)$$

which simply manipulates the indices in the summation. Due to the assumption that plane cross-sections of a geometrically exact beam remain plane and undeformed, the quaternion terms in Eqs. (6.35) and (6.36) are analogous to those for the free rigid body; see Eq. (6.18).

The structure-preserving spatial discretization approximates the configurations at times t_{k-1}, t_k, and t_{k+1} using linear interpolation [Eq. (5.13)] and slerp [Eq. (5.20)] for the position and orientation of the reference axis. The discretization likewise replaces $\delta \mathbf{x}_k$ and $\delta \mathbf{p}_k$ with their spatial approximations, Eqs. (5.17) and (5.30). Using Eqs. (5.17) and (5.30), $\delta \mathbf{x}_k$ and $\delta \mathbf{p}_k$ are written in terms of the shape interpolation matrix $\mathbf{Q}_k \in \mathbb{R}^{7\times 12}$ [Eq. (5.41)] defined such that

$$\begin{bmatrix} \delta \mathbf{x}_k^h \\ \delta \mathbf{p}_k^h \end{bmatrix} = \mathbf{Q}_k \delta \mathbf{g}_k \quad (6.37)$$

where $\delta \mathbf{g}_k^T = \left(\delta \mathbf{x}_k^{(1)T}, \delta \mathbf{\Theta}_k^{(1)T}, \delta \mathbf{x}_k^{(2)T}, \delta \mathbf{\Theta}_k^{(2)T} \right)$ is the variation of the element's nodal coordinates. The spatial discretization results in the following expression for the variation of the discrete action sum:

$$\delta S_{\text{iner}} = \sum_{k=1}^{N-1} \delta \mathbf{g}_k^T \int_0^{\ell} \mathbf{Q}_k^T \begin{bmatrix} -\frac{\rho A}{h} \left(\mathbf{x}_{k+1}^h - 2\mathbf{x}_k^h + \mathbf{x}_{k-1}^h \right) \\ \frac{16}{h} \left(\left(\frac{\partial \mathbf{f}_{k-1}}{\partial \mathbf{p}_k} \right)^{hT} \mathbf{T}\mathbf{J}\mathbf{T}^T \mathbf{f}_{k-1}^h + \left(\frac{\partial \mathbf{f}_k}{\partial \mathbf{p}_k} \right)^{hT} \mathbf{T}\mathbf{J}\mathbf{T}^T \mathbf{f}_k^h \right) \end{bmatrix} \mathrm{d}s \quad (6.38)$$

which can equivalently be written as

$$\delta S_{\text{iner}} = -\sum_{k=1}^{N-1} \delta \mathbf{g}_k^T \left(\overline{\mathbf{h}}_k^{\,(+)} - \overline{\mathbf{h}}_k^{\,(-)} \right) \tag{6.39}$$

where $\overline{\mathbf{h}}_k^{\,(-)}$ and $\overline{\mathbf{h}}_k^{\,(+)}$ are left and right discrete "momenta-like" quantities given by

$$\overline{\mathbf{h}}_k^{\,(-)} = \frac{1}{h} \int_0^{\ell} \mathbf{Q}_k^T \begin{bmatrix} \rho A \left(\mathbf{x}_k^h - \mathbf{x}_{k-1}^h \right) \\ 16 \left(\dfrac{\partial \mathbf{f}_{k-1}}{\partial \mathbf{p}_k} \right)^{hT} \mathbf{T}\mathbf{J}\mathbf{T}^T \mathbf{f}_{k-1}^h \end{bmatrix} \mathrm{d}s, \tag{6.40}$$

$$\overline{\mathbf{h}}_k^{\,(+)} = \frac{1}{h} \int_0^{\ell} \mathbf{Q}_k^T \begin{bmatrix} \rho A \left(\mathbf{x}_{k+1}^h - \mathbf{x}_k^h \right) \\ -16 \left(\dfrac{\partial \mathbf{f}_k}{\partial \mathbf{p}_k} \right)^{hT} \mathbf{T}\mathbf{J}\mathbf{T}^T \mathbf{f}_k^h \end{bmatrix} \mathrm{d}s. \tag{6.41}$$

In the absence of strain energy, constraints, and external forcing, $\overline{\mathbf{h}}_k^{\,(-)}$ and $\overline{\mathbf{h}}_k^{\,(+)}$ are equivalent expressions for the discrete generalized momenta $\mathbf{h}_k$ at time step t_k. For practical purposes, $\overline{\mathbf{h}}_k^{\,(-)}$ and $\overline{\mathbf{h}}_k^{\,(+)}$ can be considered discrete inertia forces associated with the time intervals from t_{k-1} to t_k and from t_k to t_{k+1}. Since the translational terms in $\overline{\mathbf{h}}_k^{\,(-)}$ and $\overline{\mathbf{h}}_k^{\,(+)}$ are linear functions of the nodal translations, they can be integrated exactly.

Discrete Elastic Forces

Unlike the discrete inertia forces, the discrete elastic forces are derived by evaluating the variation of S_{int} [Eq. (6.32)] and then discretizing in space before discretely integrating by parts. Taking the variation of S_{int} gives

$$\delta S_{\text{int}} = \sum_{k=0}^{N-1} h \int_0^{\ell} \delta \mathbf{E}_{k+1/2}^T \mathbf{S}_{k+1/2} \, \mathrm{d}s \tag{6.42}$$

where $\delta \mathbf{E}_{k+1/2}$ is the variation of the material strain measures [Eq. (4.50), reproduced below]

$$\delta \mathbf{E} = \begin{bmatrix} \mathbf{\Lambda}^T(\mathbf{p}) & \mathbf{0}_{3\times 4} & -2\mathbf{G}^T(\mathbf{p})\mathbf{L}^T(\mathbf{T}\mathbf{x}') \\ \mathbf{0}_{3\times 3} & 2\mathbf{G}^T(\mathbf{p}) & -2\mathbf{G}^T(\mathbf{p}') \end{bmatrix} \begin{bmatrix} \delta \mathbf{x}' \\ \delta \mathbf{p}' \\ \delta \mathbf{p} \end{bmatrix} \tag{6.43}$$

evaluated at time $t_{k+1/2}$. The spatial discretization then relates $\delta \mathbf{x}'$, $\delta \mathbf{p}'$, and $\delta \mathbf{p}$ to the variations of the nodal coordinates as follows:

$$\begin{bmatrix} \delta \mathbf{x}^{h\prime} \\ \delta \mathbf{p}^{h\prime} \\ \delta \mathbf{p}^{h} \end{bmatrix} = \mathbf{P} \delta \bar{\mathbf{g}} \tag{6.44}$$

where $\mathbf{P} \in \mathbb{R}^{11\times 12}$ is the shape interpolation matrix

$$\mathbf{P} = \begin{bmatrix} M_1'\mathbf{I}_{3\times 3} & \mathbf{0}_{3\times 4} & M_2'\mathbf{I}_{3\times 3} & \mathbf{0}_{3\times 4} \\ \mathbf{0}_{4\times 3} & \dfrac{\partial \mathbf{p}^{h\prime}}{\partial \mathbf{p}_1} & \mathbf{0}_{4\times 3} & \dfrac{\partial \mathbf{p}^{h\prime}}{\partial \mathbf{p}_2} \\ \mathbf{0}_{4\times 3} & \dfrac{\partial \mathbf{p}^{h}}{\partial \mathbf{p}_1} & \mathbf{0}_{4\times 3} & \dfrac{\partial \mathbf{p}^{h}}{\partial \mathbf{p}_2} \end{bmatrix} \tag{6.45}$$

and $\delta\bar{\mathbf{g}}^T = \left(\delta\mathbf{x}^{(1)T}, \delta\mathbf{p}^{(1)T}, \delta\mathbf{x}^{(2)T}, \delta\mathbf{p}^{(2)T}\right)$ is the variation of the independent nodal coordinates (i.e., the definition of $\delta\bar{\mathbf{g}}$ assumes that the quaternion components are independent). In turn, a discrete strain gradient matrix $\mathbf{B} \in \mathbb{R}^{6\times 14}$ can be defined as

$$\delta\mathbf{E}^h = \mathbf{B}\delta\bar{\mathbf{g}}, \tag{6.46}$$

from which it follows that

$$\mathbf{B} = \begin{bmatrix} \boldsymbol{\Lambda}^T(\mathbf{p}^h) & \mathbf{0}_{3\times 4} & -2\mathbf{G}^T(\mathbf{p}^h)\mathbf{L}^T(\mathbf{T}\mathbf{x}^{h\prime}) \\ \mathbf{0}_{3\times 3} & 2\mathbf{G}^T(\mathbf{p}^h) & -2\mathbf{G}^T(\mathbf{p}^{h\prime}) \end{bmatrix} \mathbf{P}. \tag{6.47}$$

Thus, the spatial discretization of δS_{int} can be written as

$$\delta S_{\text{int}} = \sum_{k=0}^{N-1} h\left(\delta\bar{\mathbf{g}}_{k+1/2}^T \mathbf{F}_{\text{int}}(\mathbf{g}_{k+1/2})\right) \tag{6.48}$$

where $\mathbf{g}^T = \left(\mathbf{x}^{(1)T}, \mathbf{p}^{(1)T}, \mathbf{x}^{(2)T}, \mathbf{p}^{(2)T}\right)$ is the vector of nodal coordinates and

$$\mathbf{F}_{\text{int}}(\mathbf{g}) = \int_0^\ell \mathbf{B}^T\mathbf{S}^h \, \mathrm{d}s. \tag{6.49}$$

Importantly, $\mathbf{F}_{\text{int}}(\mathbf{g}) \in \mathbb{R}^{14}$ because it has not been corrected for the Lie group structure of $\mathbb{H}_1$. Hence, the moments in $\mathbf{F}_{\text{int}}(\mathbf{g})$ correspond to 4D quaternion moments, as opposed to 3D physical ones; for additional details, see Sec. (4.7).

Evaluating the discrete variational principle requires rewriting $\delta\bar{\mathbf{g}}_{k+1/2}$ in Eq. (6.48) as a function of $\delta\mathbf{g}_k$ and $\delta\mathbf{g}_{k+1}$. Since the midpoint quaternion $\mathbf{p}_{k+1/2}$ is a function of both $\mathbf{p}_k$ and $\mathbf{p}_{k+1}$,

$$\delta\mathbf{p}_{k+1/2} = \frac{\partial \mathbf{p}_{k+1/2}}{\partial \mathbf{p}_k}\delta\mathbf{p}_k + \frac{\partial \mathbf{p}_{k+1/2}}{\partial \mathbf{p}_{k+1}}\delta\mathbf{p}_{k+1} \tag{6.50}$$

$$= \frac{1}{2}\frac{\partial \mathbf{p}_{k+1/2}}{\partial \mathbf{p}_k}\mathbf{G}(\mathbf{p}_k)\delta\boldsymbol{\Theta}_k + \frac{1}{2}\frac{\partial \mathbf{p}_{k+1/2}}{\partial \mathbf{p}_{k+1}}\mathbf{G}(\mathbf{p}_{k+1})\delta\boldsymbol{\Theta}_{k+1} \tag{6.51}$$

where the second equality results from projecting $\delta\mathbf{p}_k$ and $\delta\mathbf{p}_{k+1}$ into their associated material tangent spaces using Eq. (4.34). This corrects for the Lie group structure of $\mathbb{H}_1$ [139] so that $\delta\mathbf{p}_{k+1/2}^T\mathbf{p}_{k+1/2} = 0$. In turn, $\delta\bar{\mathbf{g}}_{k+1/2}$ can be written as

$$\delta\bar{\mathbf{g}}_{k+1/2} = \boldsymbol{\mathcal{A}}_k\delta\mathbf{g}_k + \boldsymbol{\mathcal{B}}_k\delta\mathbf{g}_{k+1} \tag{6.52}$$

where $\mathcal{A}_k, \mathcal{B}_k \in \mathbb{R}^{14\times 12}$ are defined as

$$\mathcal{A}_k = \frac{1}{2}\,\mathrm{diag}\left\{\mathbf{I}_{3\times 3}, \frac{\partial \mathbf{p}_{k+1/2}^{(1)}}{\partial \mathbf{p}_k^{(1)}}\mathbf{G}\left(\mathbf{p}_k^{(1)}\right), \mathbf{I}_{3\times 3}, \frac{\partial \mathbf{p}_{k+1/2}^{(2)}}{\partial \mathbf{p}_k^{(2)}}\mathbf{G}\left(\mathbf{p}_k^{(2)}\right)\right\}, \tag{6.53}$$

$$\mathcal{B}_k = \frac{1}{2}\,\mathrm{diag}\left\{\mathbf{I}_{3\times 3}, \frac{\partial \mathbf{p}_{k+1/2}^{(1)}}{\partial \mathbf{p}_{k+1}^{(1)}}\mathbf{G}\left(\mathbf{p}_{k+1}^{(1)}\right), \mathbf{I}_{3\times 3}, \frac{\partial \mathbf{p}_{k+1/2}^{(2)}}{\partial \mathbf{p}_{k+1}^{(2)}}\mathbf{G}\left(\mathbf{p}_{k+1}^{(2)}\right)\right\}. \tag{6.54}$$

By substituting $\delta\bar{\mathbf{g}}_{k+1/2}$ into Eq. (6.48), it readily follows that

$$\delta S_{\mathrm{int}} = \sum_{k=0}^{N-1} h\left(\delta\mathbf{g}_k^T\mathcal{A}_k^T + \delta\mathbf{g}_{k+1}^T\mathcal{B}_k^T\right)\mathbf{F}_{\mathrm{int}}(\mathbf{g}_{k+1/2}). \tag{6.55}$$

The subsequent application of discrete integration by parts with $\delta\mathbf{g}_0 = \delta\mathbf{g}_N = \mathbf{0}_{12\times 1}$ (which is a consequence of $\delta\mathbf{x}_0 = \delta\mathbf{x}_N = \mathbf{0}_{3\times 1}$ and $\delta\mathbf{p}_0 = \delta\mathbf{p}_N = \mathbf{0}_{4\times 1}$) then results in the following expression for the variation of the discrete action sum:

$$\delta S_{\mathrm{int}} = \sum_{k=1}^{N-1} \delta\mathbf{g}_k^T\left(h\mathcal{A}_k^T\mathbf{F}_{\mathrm{int}}(\mathbf{g}_{k+1/2}) + h\mathcal{B}_{k-1}^T\mathbf{F}_{\mathrm{int}}(\mathbf{g}_{k-1/2})\right) \tag{6.56}$$

where $h\mathcal{B}_{k-1}^T\mathbf{F}_{\mathrm{int}}(\mathbf{g}_{k-1/2})$ and $h\mathcal{A}_k^T\mathbf{F}_{\mathrm{int}}(\mathbf{g}_{k+1/2})$ are the left and right discrete elastic forces associated with the time intervals from t_{k-1} to t_k and from t_k to t_{k+1}.

Discrete Constraint Forces

Evaluating the variation of the discrete action sum S_{con} [Eq. (6.33)] is straightforward and yields

$$\delta S_{\mathrm{con}} = \sum_{k=0}^{N-1}\frac{h}{2}\int_0^\ell \left(\delta\mathbf{q}_k^T\left(\frac{\partial\boldsymbol{\phi}_k}{\partial\mathbf{q}_k}\right)^T\boldsymbol{\lambda}_k + \delta\boldsymbol{\lambda}_k^T\boldsymbol{\phi}_k + \delta\mathbf{q}_{k+1}^T\left(\frac{\partial\boldsymbol{\phi}_{k+1}}{\partial\mathbf{q}_{k+1}}\right)^T\boldsymbol{\lambda}_{k+1} + \delta\boldsymbol{\lambda}_{k+1}^T\boldsymbol{\phi}_{k+1}\right)\mathrm{d}s. \tag{6.57}$$

Discrete integration by parts with $\delta\mathbf{q}_k$ and $\delta\boldsymbol{\lambda}_k$ equal to zero at the endpoints t_0 and t_N then gives

$$\delta S_{\mathrm{con}} = \sum_{k=1}^{N-1} h\int_0^\ell \left(\delta\mathbf{q}_k^T\left(\frac{\partial\boldsymbol{\phi}_k}{\partial\mathbf{q}_k}\right)^T\boldsymbol{\lambda}_k + \delta\boldsymbol{\lambda}_k^T\boldsymbol{\phi}_k\right)\mathrm{d}s. \tag{6.58}$$

In the absence of internal constraints along the element's reference axis, the Lagrange multipliers exclusively enforce constraints between finite element nodes. To reflect

this, $\boldsymbol{\lambda}_k$ and $\delta\boldsymbol{\lambda}_k$ are discretized using Dirac delta functions. Specifically, $\boldsymbol{\lambda}_k$ and $\delta\boldsymbol{\lambda}_k$ are approximated using Eqs. (5.44) and (5.45); for additional details, see Sec. 5.3.5 and [142]. After discretizing $\boldsymbol{\lambda}_k$ and $\delta\boldsymbol{\lambda}_k$, the integral is evaluated using the sifting property of the Dirac delta function [155, p. 241–243], the result of which is

$$\delta S_{\text{con}} = \sum_{k=1}^{N-1} h \Bigg(\delta \mathbf{q}_k^{(1)T} \left(\frac{\partial \boldsymbol{\phi}_k^{(1)}}{\partial \mathbf{q}_k^{(1)}} \right)^T \boldsymbol{\lambda}_k^{(1)} + \delta \mathbf{q}_k^{(2)T} \left(\frac{\partial \boldsymbol{\phi}_k^{(2)}}{\partial \mathbf{q}_k^{(2)}} \right)^T \boldsymbol{\lambda}_k^{(2)} + \delta \boldsymbol{\lambda}_k^{(1)T} \boldsymbol{\phi}_k^{(1)} + \delta \boldsymbol{\lambda}_k^{(2)T} \boldsymbol{\phi}_k^{(2)} \Bigg) \tag{6.59}$$

where $\mathbf{q}^{(i)T} = \left(\mathbf{x}^{(i)T}, \mathbf{p}^{(i)T} \right)$ and $\boldsymbol{\phi}^{(i)} \in \mathbb{R}^{n_c^{(i)}}$ contains the $n_c^{(i)}$ constraints at node i, both for $i = 1,\ 2$. By correcting for the Lie group structure of $\mathbb{H}_1$ using Eq. (4.34) [139], defining the vector of Lagrange multipliers $\boldsymbol{\lambda}^T = \left(\boldsymbol{\lambda}^{(1)T}, \boldsymbol{\lambda}^{(2)T} \right)$, and defining the constraint function $\boldsymbol{\Phi}^T = \left(\boldsymbol{\phi}^{(1)T}, \boldsymbol{\phi}^{(2)T} \right)$, δS_{con} can then be written as

$$\delta S_{\text{con}} = \sum_{k=1}^{N-1} h \left(\delta \mathbf{g}_k^T \left(\frac{\partial \boldsymbol{\Phi}_k}{\partial \mathbf{g}_k} \right)^T \boldsymbol{\lambda}_k + \delta \boldsymbol{\lambda}_k^T \boldsymbol{\Phi}_k \right) \tag{6.60}$$

where the product $h \left(\partial \boldsymbol{\Phi}_k / \partial \mathbf{g}_k \right)^T \boldsymbol{\lambda}_k$ is the discrete generalized force due to the constraints and $\partial \boldsymbol{\Phi} / \partial \mathbf{g}$ is the constraint gradient matrix [Eq. (5.48)]. While a slight abuse of notation, subsequent uses of $\boldsymbol{\lambda}$ are to be understood as referring to the definition $\boldsymbol{\lambda}^T = \left(\boldsymbol{\lambda}^{(1)T}, \boldsymbol{\lambda}^{(2)T} \right)$.

Discrete External Forces

The discrete generalized forces are derived by discretely integrating δS_{ext} by parts [Eq. (6.34)] with $\delta \mathbf{x}_k$ and $\delta \mathbf{p}_k$ set to zero at the endpoints t_0 and t_N, the result of which is

$$\delta S_{\text{ext}} = \sum_{k=1}^{N-1} \frac{h}{4} \int_0^\ell \begin{bmatrix} \delta \mathbf{x}_k \\ \delta \mathbf{p}_k \end{bmatrix}^T \begin{bmatrix} \overline{\mathbf{n}}_{k-1} + 2\overline{\mathbf{n}}_k + \overline{\mathbf{n}}_{k+1} \\ 2\mathbf{H}_{k-1}\overline{\mathbf{m}}_{k-1} + 4\mathbf{H}_k\overline{\mathbf{m}}_k + 2\mathbf{H}_{k+1}\overline{\mathbf{m}}_{k+1} \end{bmatrix} \mathrm{d}s. \tag{6.61}$$

Substituting the shape interpolation matrix $\mathbf{Q}_k$ defined by Eq. (6.37) into this expression and defining $\mathbf{H}_k^h = \mathbf{H}(\mathbf{p}_k^h)$ then yields

$$\delta S_{\text{ext}} = \sum_{k=1}^{N-1} \delta \mathbf{g}_k^T \left(\mathbf{F}_{k-1} + 2\mathbf{F}_k + \mathbf{F}_{k+1} \right) \tag{6.62}$$

where $\mathbf{F}_{k-1}$, $\mathbf{F}_k$, and $\mathbf{F}_{k+1}$ are the discrete generalized forces

$$\mathbf{F}_{k-1} = \frac{h}{4}\int_0^\ell \mathbf{Q}_k^T \begin{bmatrix} \overline{\mathbf{n}}_{k-1} \\ 2\mathbf{H}_{k-1}^h \overline{\mathbf{m}}_{k-1} \end{bmatrix} \mathrm{d}s, \tag{6.63}$$

$$\mathbf{F}_k = \frac{h}{4}\int_0^\ell \mathbf{Q}_k^T \begin{bmatrix} \overline{\mathbf{n}}_{k} \\ 2\mathbf{H}_{k}^h \overline{\mathbf{m}}_{k} \end{bmatrix} \mathrm{d}s, \tag{6.64}$$

$$\mathbf{F}_{k+1} = \frac{h}{4}\int_0^\ell \mathbf{Q}_k^T \begin{bmatrix} \overline{\mathbf{n}}_{k+1} \\ 2\mathbf{H}_{k+1}^h \overline{\mathbf{m}}_{k+1} \end{bmatrix} \mathrm{d}s. \tag{6.65}$$

Discrete Euler-Lagrange Equations

The discrete Euler-Lagrange equations for the geometrically exact beam are derived by substituting the variations of the spatially discretized discrete action sums associated with the kinetic energy [Eq. (6.39)], strain energy [Eq. (6.56)], constraints [Eq. (6.60)], and external virtual work [Eq. (6.62)] into the discrete variational principle [Eq. (6.30)] to obtain:

$$\sum_{k=1}^{N-1}\Bigg\{\delta\mathbf{g}_k^T\Bigg[\left(\overline{\mathbf{h}}_k^{\,(+)} - \overline{\mathbf{h}}_k^{\,(-)}\right) + h\left(\mathcal{A}_k^T\mathbf{F}_{\mathrm{int}}(\mathbf{g}_{k+1/2}) + \mathcal{B}_{k-1}^T\mathbf{F}_{\mathrm{int}}(\mathbf{g}_{k-1/2})\right) + h\left(\frac{\partial\mathbf{\Phi}_k}{\partial\mathbf{g}_k}\right)^T\boldsymbol{\lambda}_k - (\mathbf{F}_{k-1} + 2\mathbf{F}_k + \mathbf{F}_{k+1})\Bigg] + h\delta\boldsymbol{\lambda}_k^T\mathbf{\Phi}_k\Bigg\} = 0. \tag{6.66}$$

Equation (6.66) must hold for all admissible variations $\delta\mathbf{g}_k$ and $\delta\boldsymbol{\lambda}_k$. This results in the following discrete Euler-Lagrange equations:

$$\begin{aligned}\overline{\mathbf{h}}_k^{\,(+)} - \overline{\mathbf{h}}_k^{\,(-)} + h\left(\mathcal{A}_k^T\mathbf{F}_{\mathrm{int}}(\mathbf{g}_{k+1/2}) + \mathcal{B}_{k-1}^T\mathbf{F}_{\mathrm{int}}(\mathbf{g}_{k-1/2}) + \left(\frac{\partial\mathbf{\Phi}_k}{\partial\mathbf{g}_k}\right)^T\boldsymbol{\lambda}_k\right) \\ = \mathbf{F}_{k-1} + 2\mathbf{F}_k + \mathbf{F}_{k+1},\end{aligned} \tag{6.67}$$

$$\mathbf{\Phi}_{k+1} = \mathbf{0}_{n_c\times 1} \tag{6.68}$$

where $\mathbf{\Phi}_{k+1} = \mathbf{\Phi}(\mathbf{g}_{k+1})$ and $n_c = n_c^{(1)} + n_c^{(2)}$ is the total number of holonomic constraints. Equations (6.67) and (6.68) define the variational integrator. Given the configurations $\mathbf{g}_{k-1}$ and $\mathbf{g}_k$, Eqs. (6.67) and (6.68) are a set of nonlinear implicit equations for $\mathbf{g}_{k+1}$ and $\boldsymbol{\lambda}_k$. Since the time-stepping scheme requires that $\mathbf{g}_{k-1}$ and $\mathbf{g}_k$ satisfy the constraints, the variational integrator evaluates the constraints corresponding to the unknown configuration $\mathbf{g}_{k+1}$. These discrete Euler-Lagrange equations are analogous to the continuous-time finite element equations from Sec. 5.3.7.

The discrete Euler-Lagrange equations propagate the dynamics of a single element. For systems discretized with $n_e \geq 1$ elements, a standard finite element assembly step results in similar discrete-time propagation equations for the complete model.

Equation (6.67) can be interpreted as a balance of discrete generalized momenta between adjacent time steps [28, 29], i.e.,

$$\begin{aligned}\mathbf{h}_k &= \overline{\mathbf{h}}_k^{(-)} - h\boldsymbol{\mathcal{B}}_{k-1}^T \mathbf{F}_{\text{int}}(\mathbf{g}_{k-1/2}) - \frac{h}{2}\left(\frac{\partial \boldsymbol{\Phi}_k}{\partial \mathbf{g}_k}\right)^T \boldsymbol{\lambda}_k + \mathbf{F}_{k-1} + \mathbf{F}_k \\ &= \overline{\mathbf{h}}_k^{(+)} + h\boldsymbol{\mathcal{A}}_k^T \mathbf{F}_{\text{int}}(\mathbf{g}_{k+1/2}) + \frac{h}{2}\left(\frac{\partial \boldsymbol{\Phi}_k}{\partial \mathbf{g}_k}\right)^T \boldsymbol{\lambda}_k - \mathbf{F}_{k+1} - \mathbf{F}_k\end{aligned} \tag{6.69}$$

where $\mathbf{h}_k$ is the discrete generalized momenta at time step t_k. This results in the following equivalent position-momentum form:

$$\mathbf{h}_k = \overline{\mathbf{h}}_k^{(+)} + h\boldsymbol{\mathcal{A}}_k^T \mathbf{F}_{\text{int}}(\mathbf{g}_{k+1/2}) + \frac{h}{2}\left(\frac{\partial \boldsymbol{\Phi}_k}{\partial \mathbf{g}_k}\right)^T \boldsymbol{\lambda}_k - \mathbf{F}_{k+1} - \mathbf{F}_k, \tag{6.70}$$

$$\mathbf{h}_{k+1} = \overline{\mathbf{h}}_{k+1}^{(-)} - h\boldsymbol{\mathcal{B}}_k^T \mathbf{F}_{\text{int}}(\mathbf{g}_{k+1/2}) - \frac{h}{2}\left(\frac{\partial \boldsymbol{\Phi}_{k+1}}{\partial \mathbf{g}_{k+1}}\right)^T \boldsymbol{\lambda}_{k+1} + \mathbf{F}_k + \mathbf{F}_{k+1}. \tag{6.71}$$

These are the discrete Legendre transforms for the system. In the absence of constraints, Eqs. (6.70) and (6.71) provide a recipe for updating the configuration of the system. Given $\mathbf{g}_k$ and $\mathbf{h}_k$, Eq. (6.70) is solved for $\mathbf{g}_{k+1}$, which is then substituted into Eq. (6.71) to calculate $\mathbf{h}_{k+1}$. This process can be repeated indefinitely.

For constrained systems, however, the generalized momenta $\mathbf{h}_{k+1}$ cannot be calculated directly due to the term $(\partial \boldsymbol{\Phi}_{k+1}/\partial \mathbf{g}_{k+1})^T \boldsymbol{\lambda}_{k+1}$ in the discrete Legendre transform. Even though Eqs. (6.68) and (6.70) can be solved simultaneously for $\mathbf{g}_{k+1}$ and $\boldsymbol{\lambda}_k$, $\boldsymbol{\lambda}_{k+1}$ remains unknown until the next time step. To remedy this, a modified position-momentum form is proposed for the numerical solution procedure. In particular, the balance of discrete generalized momenta [Eq. (6.69)] is rewritten as

$$\begin{aligned}\mathbf{h}_k^* &= \overline{\mathbf{h}}_k^{(-)} - h\boldsymbol{\mathcal{B}}_{k-1}^T \mathbf{F}_{\text{int}}(\mathbf{g}_{k-1/2}) + \mathbf{F}_{k-1} + \mathbf{F}_k \\ &= \overline{\mathbf{h}}_k^{(+)} + h\boldsymbol{\mathcal{A}}_k^T \mathbf{F}_{\text{int}}(\mathbf{g}_{k+1/2}) + h\left(\frac{\partial \boldsymbol{\Phi}_k}{\partial \mathbf{g}_k}\right)^T \boldsymbol{\lambda}_k - \mathbf{F}_{k+1} - \mathbf{F}_k\end{aligned} \tag{6.72}$$

where the generalized momenta $\mathbf{h}_k$ and $\mathbf{h}_{k+1}$ are replaced by the "pseudo-momenta" $\mathbf{h}_k^*$ and $\mathbf{h}_{k+1}^*$. This pseudo-momenta balance implies the following modified position-momentum form for updating the configuration of the system:

$$\mathbf{h}_k^* = \overline{\mathbf{h}}_k^{(+)} + h\boldsymbol{\mathcal{A}}_k^T \mathbf{F}_{\text{int}}(\mathbf{g}_{k+1/2}) + h\left(\frac{\partial \boldsymbol{\Phi}_k}{\partial \mathbf{g}_k}\right)^T \boldsymbol{\lambda}_k - \mathbf{F}_{k+1} - \mathbf{F}_k, \tag{6.73}$$

$$\mathbf{h}_{k+1}^* = \overline{\mathbf{h}}_{k+1}^{(-)} - h\boldsymbol{\mathcal{B}}_k^T \mathbf{F}_{\text{int}}(\mathbf{g}_{k+1/2}) + \mathbf{F}_k + \mathbf{F}_{k+1}. \tag{6.74}$$

Equations (6.68) and (6.73) can now be used to calculate $\mathbf{g}_{k+1}$ and $\boldsymbol{\lambda}_k$, which can then be substituted into Eq. (6.74) to calculate $\mathbf{h}^*_{k+1}$ before proceeding to the next time step. A post-processing step is required to convert the pseudo-momenta to the corresponding discrete generalized momenta.

When paired with a Lie group solver (e.g., the Lie group generalization of the Newton-Raphson method [139, 177]) and an appropriate quaternion update (e.g., the Cayley map described in Sec. 4.3.2), Eqs. (6.68), (6.73), and (6.74) result in a discrete time-stepping algorithm for propagating the dynamics of a geometrically exact beam. Pseudo-code for this algorithm is included in Algorithm 2. Implementing the algorithm requires the specification of the time step h, the maximum number of Newton iterations per time step $i_{\max}$, and the convergence tolerance τ.

Algorithm 2 $[\mathbf{g}_{k+1}, \mathbf{h}^*_{k+1}, \mathbf{h}_k, \boldsymbol{\lambda}_k] = \text{beamStep}(\mathbf{g}_k, \mathbf{h}^*_k)$

$\mathbf{g}_{k+1} \coloneqq \mathbf{g}_k$
$\Delta\boldsymbol{\Theta}_{k+1} \coloneqq \mathbf{0}_{3\times 1}$
$\boldsymbol{\lambda}_k \coloneqq \mathbf{0}_{n_c\times 1}$
for $i = 1$ to $i_{\max}$ **do**
  $\mathbf{g}_{k+1} \coloneqq \text{groupUpdate}(\mathbf{g}_{k+1}, \Delta\boldsymbol{\Theta}_{k+1})$
  $\mathbf{g}_{k+1/2} \coloneqq \text{groupMidpoint}(\mathbf{g}_k, \mathbf{g}_{k+1})$
  $\mathbf{h}^{(i)}_k \coloneqq \overline{\mathbf{h}}^{\,(+)}_k + h\boldsymbol{\mathcal{A}}^T_k\mathbf{F}_{\text{int}}(\mathbf{g}_{k+1/2}) + h\left(\dfrac{\partial\boldsymbol{\Phi}_k}{\partial\mathbf{g}_k}\right)^T\boldsymbol{\lambda}_k - \mathbf{F}_{k+1} - \mathbf{F}_k$
  $\mathbf{r}_{\mathbf{g}} \coloneqq \mathbf{h}^{(i)}_k - \mathbf{h}^*_k$
  $\mathbf{r}_{\boldsymbol{\lambda}} \coloneqq \boldsymbol{\Phi}(\mathbf{g}_{k+1})$
  if $\text{norm}\left(\mathbf{r}_{\mathbf{g}}, \infty\right) \leq \tau$ and $\text{norm}\left(\mathbf{r}_{\boldsymbol{\lambda}}, \infty\right) \leq \tau$ **then**
    break
  end if
  $\mathbf{K} \coloneqq \begin{bmatrix} h\partial\left(\overline{\mathbf{h}}^{(+)}_k + h\boldsymbol{\mathcal{A}}^T_k\mathbf{F}_{\text{int}}(\mathbf{g}_{k+1/2})\right)/\partial\mathbf{g}_{k+1} & h^2\left(\partial\boldsymbol{\Phi}_k/\partial\mathbf{g}_k\right)^T \\ \partial\boldsymbol{\Phi}_{k+1}/\partial\mathbf{g}_{k+1} & \mathbf{0}_{n_c\times n_c} \end{bmatrix}$
  $\begin{bmatrix} \Delta\boldsymbol{\Theta}_{k+1} \\ \Delta\boldsymbol{\lambda}_k \end{bmatrix} \coloneqq -\mathbf{K}^{-1}\begin{bmatrix} h\mathbf{r}_{\mathbf{g}} \\ \mathbf{r}_{\boldsymbol{\lambda}} \end{bmatrix}$
  $\boldsymbol{\lambda}_k \coloneqq \boldsymbol{\lambda}_k + \Delta\boldsymbol{\lambda}_k$
end for
$\mathbf{h}^*_{k+1} \coloneqq \overline{\mathbf{h}}^{\,(-)}_{k+1} - h\boldsymbol{\mathcal{B}}^T_k\mathbf{F}_{\text{int}}(\mathbf{g}_{k+1/2}) + \mathbf{F}_k + \mathbf{F}_{k+1}$
$\mathbf{h}_k \coloneqq \mathbf{h}^*_k - \dfrac{h}{2}\left(\dfrac{\partial\boldsymbol{\Phi}_k}{\partial\mathbf{g}_k}\right)^T\boldsymbol{\lambda}_k$

In Algorithm 2, note the following:

- the function groupUpdate additively and multiplicatively updates the translational and quaternion DOFs, respectively (see Algorithm 3, which describes the generalized coordinate updating procedure for a single element);
- the function groupMidpoint calculates the temporal midpoint for the translational and quaternion DOFs using $\mathbf{x}_{k+1/2} = (\mathbf{x}_k + \mathbf{x}_{k+1})\,2/$ and Eq. (6.12), respectively;
- the calculation of the tangent matrix $h\partial\left(\overline{\mathbf{h}}_k^{(+)} + h\mathcal{A}_k^T\mathbf{F}_{\text{int}}(\mathbf{g}_{k+1/2})\right)/\partial\mathbf{g}_{k+1}$ involves post-multiplications by Eq. (4.34) to correct for the Lie group structure of the quaternion DOFs; and
- the algorithm is initialized with the configuration $\mathbf{g}_0$ and generalized momenta $\mathbf{h}_0$. $\mathbf{h}_0$ is calculated from the nodal velocities at time t_0 using the configuration-dependent mass matrix $\mathbf{M}(\mathbf{g})$ [Eq. (5.57)].

The derivation of the tangent matrix $h\partial\left(\overline{\mathbf{h}}_k^{(+)} + h\mathcal{A}_k^T\mathbf{F}_{\text{int}}(\mathbf{g}_{k+1/2})\right)/\partial\mathbf{g}_{k+1}$ is involved, and hence, omitted for brevity.

Algorithm 3 $[\mathbf{g}]$ = groupUpdate$(\mathbf{g}, \Delta\boldsymbol{\Theta})$

$\mathbf{g}(1:3) \coloneqq \mathbf{g}(1:3) + \Delta\boldsymbol{\Theta}(1:3)$
$\mathbf{g}(8:11) \coloneqq \mathbf{g}(8:11) + \Delta\boldsymbol{\Theta}(7:9)$
$\mathbf{g}(4:7) \coloneqq \mathbf{L}(\mathbf{g}(4:7))\,\text{cay}(\Delta\boldsymbol{\Theta}(4:6)/2)$
$\mathbf{g}(4:7) \coloneqq \mathbf{g}(4:7)/\text{norm}(\mathbf{g}(4:7), 2)$
$\mathbf{g}(11:14) \coloneqq \mathbf{L}(\mathbf{g}(11:14))\,\text{cay}(\Delta\boldsymbol{\Theta}(4:6)/2)$
$\mathbf{g}(11:14) \coloneqq \mathbf{g}(11:14)/\text{norm}(\mathbf{g}(11:14), 2)$

6.4 Numerical Examples

Results for several standard benchmark problems demonstrate the application of the variational integrator from Sec. 6.3 to problems with (i) large overall motions and large elastic deformations (Sec. 6.4.1); (ii) large amplitude, geometrically nonlinear vibrations (Sec. 6.4.2); and (iii) viscoelastic damping (Sec. 6.4.3). Each example compares the variational integrator with a more traditional structural dynamics integrator, the Lie group generalized-α method [36–38], paired with the continuous-time geometrically exact beam finite elements from Chapter 5. These finite elements are the continuous-time limit of the variational integrator, and hence, provide relevant reference solutions. The first two examples specifically highlight the variational

integrator's excellent long-duration energy behavior. The defining features of all three examples are present in the slew maneuver simulations in Chapter 8.

Each example is solved using MATLAB® implementations of the variational integrator and the Lie group generalized-α method. For computational efficiency, these implementations use a vectorized finite element assembly step inspired by [174–176] to assemble the complete finite element model, as opposed to more standard approaches based on FOR loops; for additional details, see Sec. 5.4. Additionally, both procedures use approximate geometric tangent stiffness matrices and neglect terms with small contributions to their total tangent matrices, resulting in quasi-Newton methods with typically less-than-quadratic convergence. Finally, both procedures use an absolute convergence criterion [Eq. (5.58)] with tolerance $\tau = 10^{-8}$.

For improved numerical conditioning, the generalized-α method uses the scaling approach from [179]. In each example, its spectral radius at infinity is set to 0.7. This results in a low-to-moderate amount of high-frequency numerical dissipation.

The boundary conditions and joints for examples (ii) and (iii) are implemented as constraints via the method of Lagrange multipliers. Due to the implicit satisfaction of the quaternion unit norm constraint, constraints on rotational DOFs are only applied to the vector part of the quaternion to guarantee that the tangent matrix in the Newton-Raphson scheme is full-rank. The discrete null space method [208–210] is then used to eliminate the constraint forces in the variational integrator and reduce the size of the system. The null space matrices are evaluated numerically at each time step from the constraint gradient matrix. In addition to the size reduction, the discrete null space method is known to alleviate numerical conditioning problems in the time-integration of constrained mechanical systems [208].

The variational integrator's kinetic energy at time step t_k is calculated from the corresponding discrete generalized momenta $\mathbf{h}_k$ using $\mathcal{T}_k = \mathbf{h}_k^T \mathbf{M}^{-1}(\mathbf{g}_k)\mathbf{h}_k/2$ where $\mathbf{M}(\mathbf{g})$ is the configuration-dependent mass matrix [Eq. (5.57)].

All three examples use full integration for the translational inertia forces, 5-point Gaussian quadrature for the rotational inertia forces, and 1-point reduced integration for the elastic forces. The latter alleviates shear locking during constant curvature deformations, as discussed in Sec. 5.4.1.

6.4.1 Example 1: Free-Free Flexible Beam

This example studies the free-free flexible beam originally introduced in [211] to demonstrate the variational integrator's excellent long-duration energy behavior

despite large overall motions and large elastic deformations. The free-free flexible beam has since become a standard problem for comparing numerical methods for geometrically exact beams; see e.g., [163, 165, 195, 212], among others.

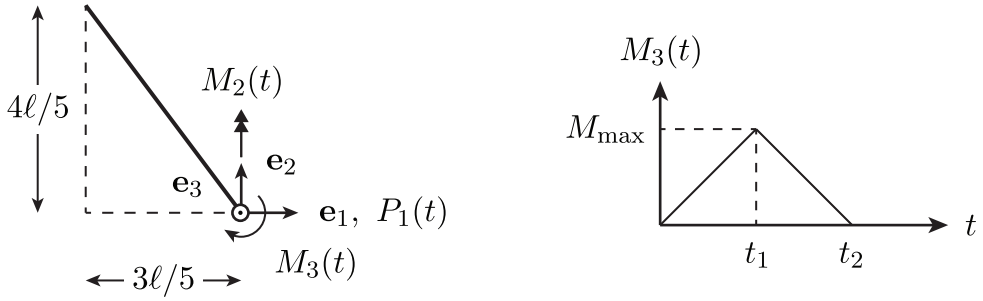

(a) (b)

Figure 6.2: (a) Free-free flexible beam subject to external force $P_1(t)$ and moments $M_2(t)$, $M_3(t)$ and (b) corresponding load history $M_3(t)$. The local (material) frame in the initial (undeformed) configuration is defined such that $\mathbf{E}_2 = \mathbf{e}_3$, $\mathbf{E}_3 = 4\mathbf{e}_2/5 - 3\mathbf{e}_1/5$, and $\mathbf{E}_1 = \mathbf{E}_2 \times \mathbf{E}_3$.

Table 6.1: Geometric and material properties in the local (material) frame for free-free flexible beam

Parameter	**Value**
ρA	1 kg m^{-1}
ρI_1, ρI_2, ρJ	10 kg m^2
GA_1, GA_2, EA	10^4 N
EI_1, EI_2, GJ	500 N m^2
ℓ	10 m

The free-free flexible beam of length ℓ is initially at rest and inclined relative to the spatial $\{\mathbf{e}_1, \mathbf{e}_2, \mathbf{e}_3\}$ reference frame, as depicted in Fig. 6.2a. The beam is loaded by a force $P_1\mathbf{e}_1$ and spatially fixed moments M_2 and M_3 about the $\mathbf{e}_2$ and $\mathbf{e}_3$ axes, respectively. The load history for M_3 is depicted in Fig. 6.2b where $M_{\max} = 200$ N m, $t_1 = t_2/2$, and $t_2 = 5$ s. The external force P_1 and moment M_2 are then given by

$$P_1(t) = M_3(t)/10 \text{ m}, \tag{6.75}$$

$$M_2(t) = M_3(t)/2. \tag{6.76}$$

The spatially fixed moments must be mapped from the spatial frame to the local (material) frame, resulting in configuration-dependent external generalized forces.

The force causes the beam to translate in the $\mathbf{e}_1$ direction. Similarly, the moments induce large rotations about the $\mathbf{e}_2$ and $\mathbf{e}_3$ axes, resulting in complex 3D motion. Since there are no external forces in the $\mathbf{e}_2$ or $\mathbf{e}_3$ directions and no external moment about the $\mathbf{e}_1$ axis, the corresponding linear and angular momenta integrated over the length of the beam are zero for all time. Likewise, after the external force and moments revert to zero at $t_2 = 5$ s, the total mechanical (kinetic plus strain) energy, total linear momenta, and total angular momenta are conserved. The beam is discretized using 10 geometrically exact beam finite elements with the geometric and material properties from Table 6.1.

To compare the long-duration energy behavior of the two integrators, the motion is simulated for 60 min using a time step size of 0.01 s. At each time step, the total mechanical energy, total linear momenta, and total angular momenta are evaluated.

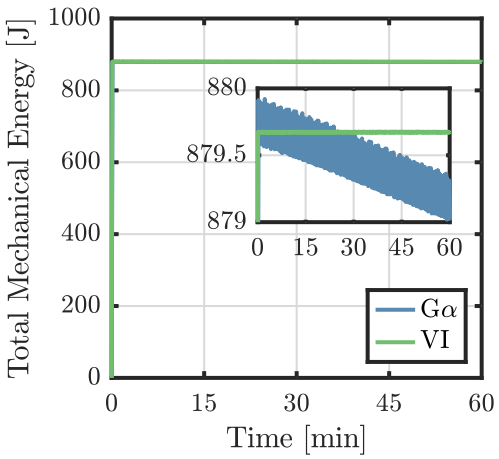

Figure 6.3: Total mechanical (kinetic plus strain) energy for free-free flexible beam. The inset highlights the decay in the total mechanical energy due to the numerical dissipation in the generalized-α method.

Figure 6.3 compares the total mechanical energies for the variational integrator (labeled "VI") and the generalized-α method (labeled "Gα"). The initial ramps in the energy coincide with the presence of the external forces in the first 5 s of the simulations, after which the beam is unforced (and undamped). Hence, the total mechanical energy should be constant for $t > 5$ s, as is the case for the variational integrator. In contrast, the total mechanical energy from the generalized-α method decreases linearly with time due to its numerical dissipation. This behavior is non-physical. Even though the magnitude of this energy decrease is small, small energy errors are subsequently shown to result in significant configuration errors relative to the variational integrator.

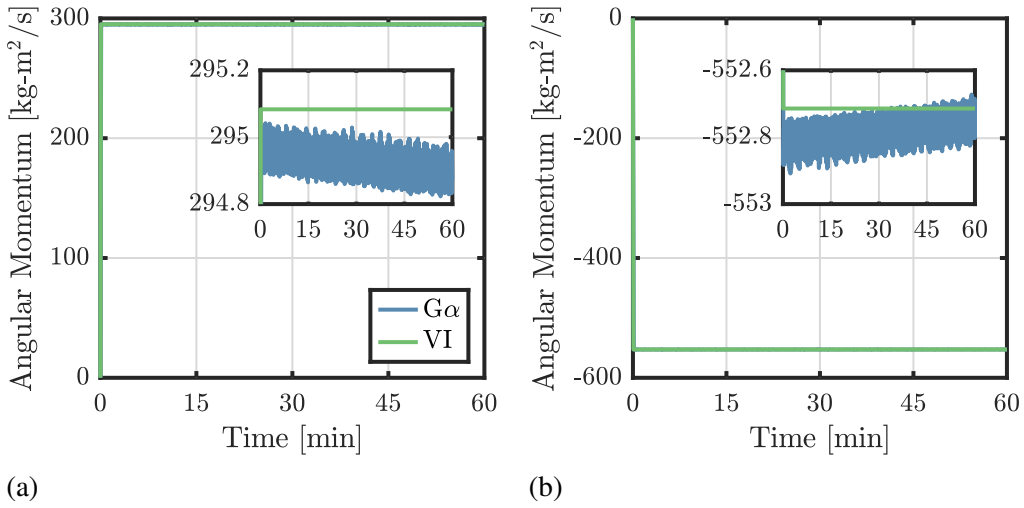

Figure 6.4: Total angular momentum in the spatial frame for directions (a) $\mathbf{e}_2$ and (b) $\mathbf{e}_3$. The angular momentum in direction $\mathbf{e}_1$ is negligible. The insets highlight the decay in the magnitude of the angular momentum due to the numerical dissipation in the generalized-α method.

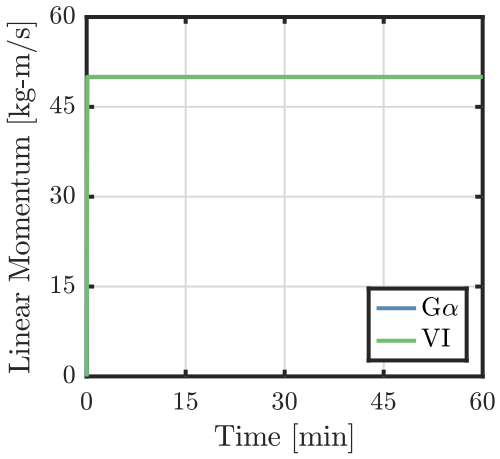

Figure 6.5: Total linear momentum in the $\mathbf{e}_1$ direction for free-free flexible beam. The other linear momentum components are zero.

The total angular momentum behaves similarly. Figures 6.4a and 6.4b compare the non-zero components of the angular momentum about the $\mathbf{e}_2$ and $\mathbf{e}_3$ axes computed relative to the origin of the spatial frame. Like the total mechanical energy, the numerical dissipation in the generalized-α method results in non-physical behavior whereby the magnitude of the angular momentum decreases linearly with time, i.e., the components of the angular momentum approach zero. Small angular momentum errors are likewise shown to correspond to significant configuration errors relative to the variational integrator. Interestingly, however, both integrators actually show

nearly perfect conservation of linear momentum in the $\mathbf{e}_1$ direction; see Fig. 6.5. The reason for this is not entirely clear.

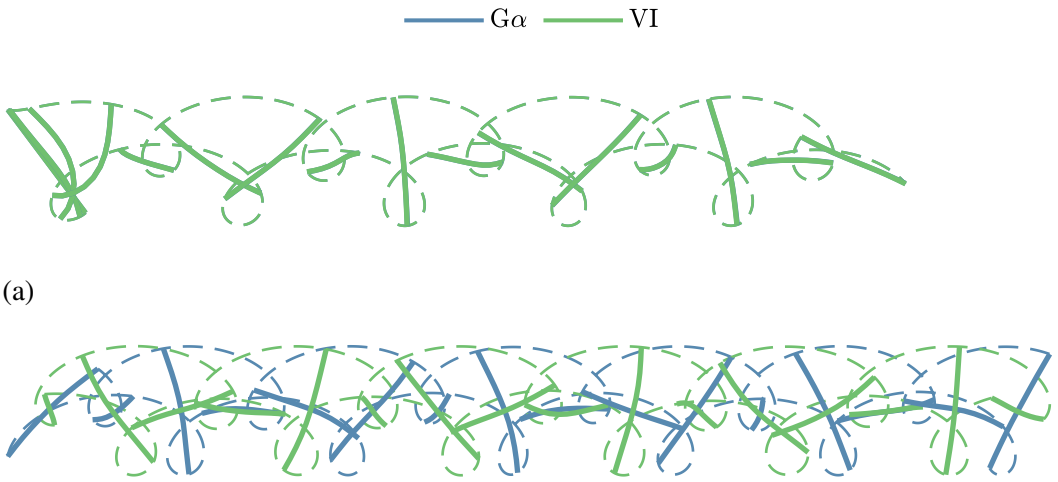

(a)

(b)

Figure 6.6: Deformed configurations plotted in 1 s intervals during (a) initial 15 s and (b) final 15 s of a 60 min simulation of the dynamics of the free-free flexible beam. Initially, the deformed configurations from the generalized-α method and variational integrator are indistinguishable, but the deformed configurations diverge as the simulations progress.

To emphasize that even small energy and momentum errors can lead to significant configuration errors, Figs. 6.6a and 6.6b compare snapshots of the deformed configurations from the variational integrator and generalized-α method at 1 s intervals during the first 15 s (Fig. 6.6a) and the last 15 s of the 60 min-long simulations. The dashed lines trace the motions of the ends of the beams. Figure 6.6a is in excellent agreement with results published elsewhere, e.g., [211]. During the first 15 s, Fig. 6.6a shows that the responses are nearly indistinguishable, but as time increases, so do the configuration errors. By the end of the simulations, Fig. 6.6b depicts significant discrepancies between the deformed configurations. These configuration errors coincide with the non-physical decreases in both the total mechanical energy and angular momentum. Altogether, these results demonstrate the importance of structure preservation for accurately predicting the response of finite element models during long-duration simulations.

6.4.2 Example 2: Right-Angle Cantilever

The right-angle cantilever is a standard dynamic test problem for geometrically exact beam finite elements that has been extensively studied in the literature, e.g., in [144,

149, 158, 163, 165, 211], among others. Here, it provides an additional example that demonstrates the long-duration energy stability of the variational integrator.

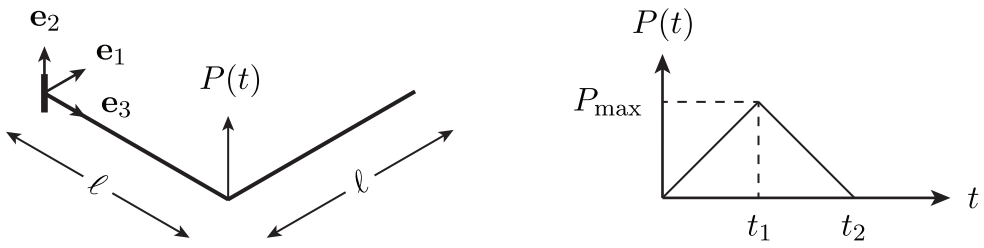

(a) (b)

Figure 6.7: (a) Right-angle cantilever beam subject to an out-of-plane force $P(t)$ and (b) corresponding load history $P(t)$. The local (material) frame in the initial (undeformed) configuration is defined such that $\mathbf{E}_3$ is tangent to the beam's axis, $\mathbf{E}_2 = \mathbf{e}_2$, and $\mathbf{E}_1 = \mathbf{E}_2 \times \mathbf{E}_3$.

Table 6.2: Geometric and material properties in the local (material) frame for right-angle cantilever beam

Parameter	**Value**
ρA	1 kg m^{-1}
ρI_1, ρI_2	10 kg m^2
ρJ	20 kg m^2
GA_1, GA_2, EA	10^6 N
EI_1, EI_2, GJ	10^3 N m^2
ℓ	10 m

The right-angle cantilever beam consists of two initially straight beam segments, both of length ℓ, connected at a right angle (the "elbow") and clamped at the root, as depicted in Fig. 6.7a. At $t = 0$, a triangular pulse $P(t)$ in the $\mathbf{e}_2$ direction with peak magnitude $P_{\max} = 50$ N is applied at the elbow. The load history is plotted in Fig. 6.7b where $t_1 = t_2/2$ and $t_2 = 2$ s. For $t \geq 2$ s, the cantilever undergoes free vibrations, and hence, its total mechanical (kinetic plus strain) energy is conserved. Each beam segment is discretized using 10 geometrically exact beam finite elements with the geometric and material properties from Table 6.2.

The response is simulated with each integrator for $t_f = 60$ min using a time step size of 0.02 s. Due to its exaggerated cross-sectional inertia properties, the response consists of large amplitude deformations with coupled bending and torsion. At each

time step, the total mechanical energy is calculated, along with the displacements in the $\mathbf{e}_2$ direction at both the elbow and tip.

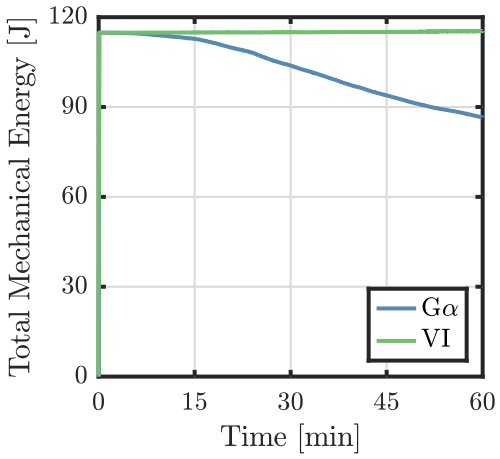

Figure 6.8: Right-angle cantilever beam: total mechanical (kinetic plus strain) energy.

To evaluate the variational integrator's long-duration energy stability, Fig. 6.8 compares its total mechanical energy (labeled "VI") with the total mechanical energy from the generalized-α method (labeled "Gα"). After removing the external force, i.e., for $t \geq t_2$, the variational integrator demonstrates near-perfect conservation of energy. In contrast, the numerical dissipation in the generalized-α method leads to a stark non-physical decrease in the total mechanical energy. Specifically, the relative change in the total mechanical energy from time t_2 to time t_f is 0.48% for the variational integrator and -24.61% for the generalized-α method. Like the previous example, these non-physical energy errors are subsequently shown to result in significant configuration errors relative to the variational integrator.

As proxies for the global configuration errors, Figs. 6.9 and 6.10 compare the elbow and tip displacements in the $\mathbf{e}_2$ direction during the first and last 30 s of the 60 min-long simulations. Both Figs. 6.9a and 6.10a are in excellent agreement with results published elsewhere, e.g., [149, 163, 165, 211]. Like the previous example, both the variational integrator and the generalized-α method predict the same displacements during the first 30 s of motion. However, as the energy errors accumulate, so do the configuration errors. This leads to markedly different responses during the final 30 s of the motion, as depicted in Figs. 6.9b and 6.10b. These results again highlight the importance of structure preservation for achieving accuracy in long-duration finite element simulations.

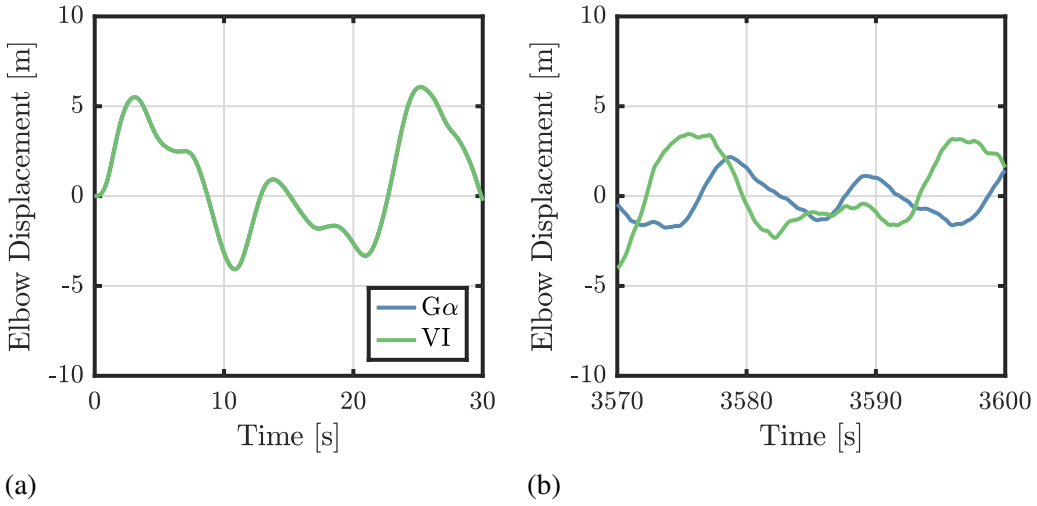

Figure 6.9: Right-angle cantilever beam: elbow displacements along direction $\mathbf{e}_2$ in time intervals (a) $t \in [0, 30]$ s and (b) $t \in [3570, 3600]$ s.

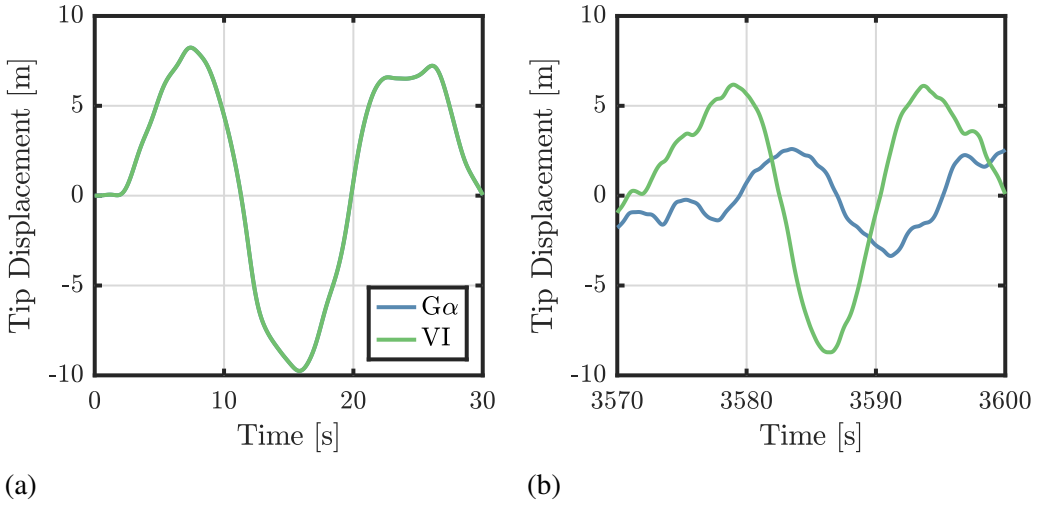

Figure 6.10: Right-angle cantilever beam: tip displacements along direction $\mathbf{e}_2$ in time intervals (a) $t \in [0, 30]$ s and (b) $t \in [3570, 3600]$ s.

6.4.3 Example 3: Swinging Flexible Pendulum

This final example studies the swinging flexible pendulum from [148] to demonstrate the use of a viscoelastic, Kelvin-Voigt-type damping formulation in the variational integrator. Viscoelastic damping can be used for either numerical or physical damping [148, 213]; in this example, it is used for both. More than critically damping the axial and shear DOFs is analogous to numerical damping of the associated high-frequency oscillations. Lightly damping the remaining DOFs then slowly dissipates the transverse (bending) oscillations excited during the pendulum's motion. In both cases, adding damping helps stabilize the simulation and improve its convergence.

Figure 6.11: Initial (undeformed) configuration of swinging flexible pendulum. The local (material) frame in the initial configuration coincides with the global $\{\mathbf{e}_1, \mathbf{e}_2, \mathbf{e}_3\}$ frame. The gravitational field applied at $t = 0$ acts in the $-\mathbf{e}_1$ direction.

The pendulum is initially straight in its undeformed configuration with its reference axis aligned with the $\mathbf{e}_3$ axis and a revolute joint at its left end; see Fig. 6.11. The pendulum is modeled as a prismatic, homogeneous, and isotropic linear-elastic beam with a circular cross-section of radius $r = 5$ mm and length $\ell = 1$ m. It is discretized using 10 geometrically exact beam finite elements. At $t = 0$, a uniform gravitational force with acceleration 9.81 m/s^2 in the $-\mathbf{e}_1$ direction is applied to the pendulum.

Following [148], the Kelvin-Voigt damping model introduces viscoelastic dissipation that is linearly proportional to the generalized strain rates. It specifically incorporates viscoelastic dissipation by modifying the internal force resultant $\mathbf{N}$ and moment resultant $\mathbf{M}$ for a geometrically exact beam as follows:

$$\mathbf{S} = \mathbf{C}\mathbf{E} + \mathbf{D}\dot{\mathbf{E}} \tag{6.77}$$

where $\mathbf{S}^T = \left(\mathbf{N}^T, \mathbf{M}^T\right)$; $\mathbf{E}^T = \left(\boldsymbol{\Gamma}^T, \mathbf{K}^T\right)$; $\dot{\boldsymbol{\Gamma}}$ and $\dot{\mathbf{K}}$ are the strain and curvature rates corresponding to the time derivatives of Eqs. (4.46) and (4.48); $\mathbf{C}$ is the sectional stiffness matrix; and $\mathbf{D} = \text{diag}\{D_{11}, D_{22}, D_{33}, D_{44}, D_{55}, D_{66}\}$ is the matrix of viscoelastic damping coefficients. Here, D_{11}, D_{22}, D_{33} are the damping coefficients for the two shear and the axial DOFs. Likewise, D_{44}, D_{55}, D_{66} are the damping coefficients for the two bending and the torsional DOFs. Unlike more classical damping models, e.g., Rayleigh damping, the Kelvin-Voigt model is introduced at an element level. When coupled with a structure-preserving spatial discretization, it results in a damping formulation that is invariant to superposed rigid body motions. This means that rigid body translations and rotations do not result in the dissipation of energy, i.e., only the elastic motion is damped. The same cannot generally be said about more classical damping formulations.

The viscoelastic damping model is incorporated into the geometrically exact beam finite elements from Chapter 5 and the variational integrator by replacing the internal

force and moment resultants in each element with Eq. (6.77). The subsequent linearization involves modifications to the tangent stiffness matrix and introduces a tangent damping matrix. The variational integrator approximates the quaternion rates in $\dot{\mathbf{\Gamma}}$ and $\dot{\mathbf{K}}$ via finite differences before the spatial discretization.

Table 6.3: Geometric and material properties in the local (material) frame from [148] for swinging flexible pendulum

Parameter	**Value**
r	5.0×10^{-3} m
E	5.0×10^{6} N/m^2
ν	0.5
G	$E/(2(1+\nu))$
ρ	1.1×10^{3} kg/m^3
κ_1, κ_2	1
ℓ	1.0 m
D_{11}, D_{22}	2.0×10^{-1} kg m
D_{33}	4.0×10^{2} kg m
D_{44}, D_{55}	4.0×10^{-4} kg m^3
D_{66}	1.6×10^{-5} kg m^3

The pendulum is made out of rubber with the geometric and material properties from Table 6.3. The shear stiffnesses $\kappa G A_1$ and $\kappa G A_2$ where $A = \pi r^2$ are scaled using MacNeal's residual bending flexibility correction [184] to avoid shear locking during linear curvature deformations; see Sec. 5.4.1. The damping coefficients D_{11} and D_{22} for shearing and D_{33} for extension are chosen to overdamp the corresponding oscillations [148]. Thus, the transient oscillations in the response are primarily due to bending. Note that the damping coefficients in Table 6.3 differ from those in [148] by a factor of 2 due to the different conventions used to define the internal force and moment resultants.

The pendulum's dynamics are simulated using both integrators for 20 s with 1 ms time steps. Snapshots of the deformations at 0.1 s intervals are compared in Figs. 6.12a and 6.12b. These snapshots show excellent agreement with both each other and the results from [148]. The total mechanical (kinetic plus strain plus gravitational potential) energy and the work done by the viscoelastic dissipation for each simulation are then compared in Figs. 6.13a and 6.13b. Unsurprisingly, the total mechanical energies steadily decrease due to the viscoelastic dissipation. Moreover,

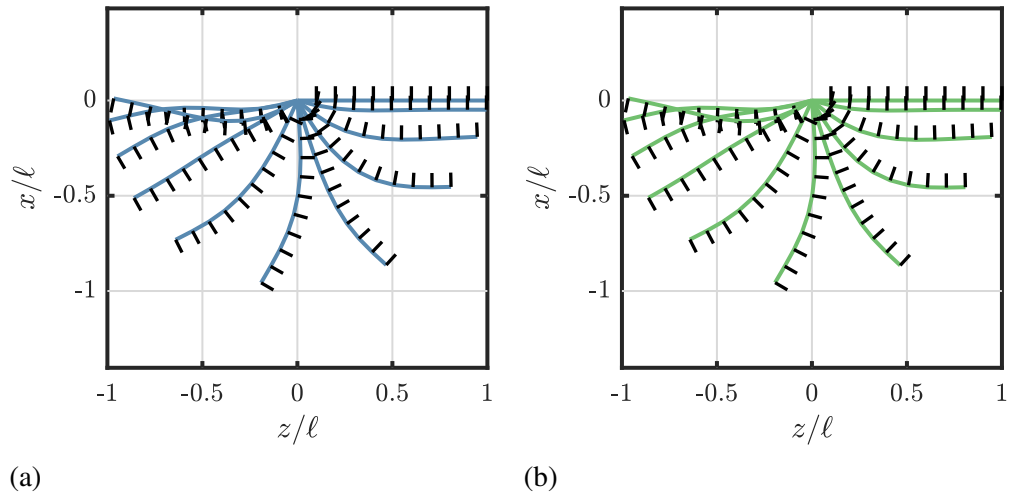

Figure 6.12: Snapshots of the initial (undeformed) configuration and first 10 deformed configurations of swinging flexible pendulum at 0.1 s intervals using (a) the generalized-α method and (b) the variational integrator. The black lines denote the orientations of the $\mathbf{E}_1$ unit vectors in the plane of the cross-section at each node. Configurations are undistorted.

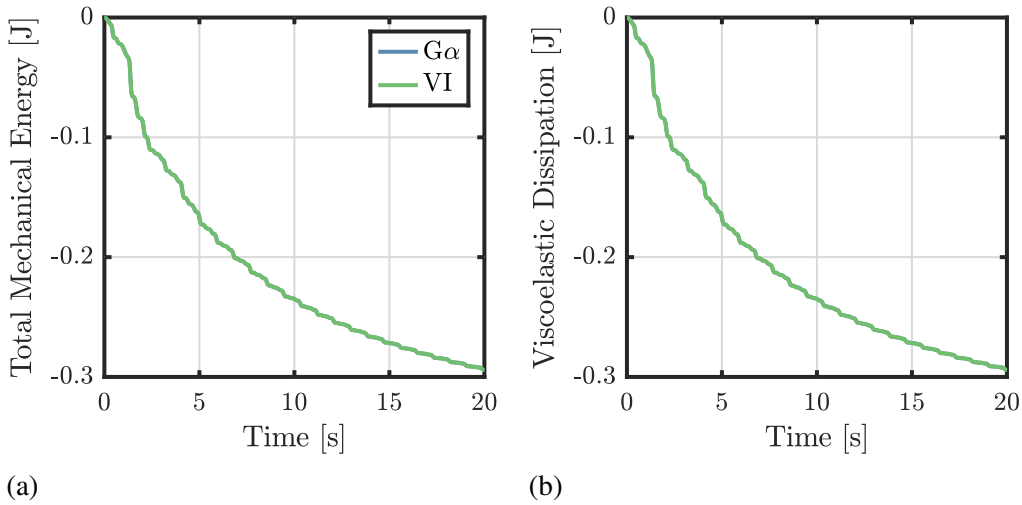

Figure 6.13: Swinging flexible pendulum: (a) total mechanical (kinetic plus strain plus gravitational potential) energy and (b) work done by viscoelastic dissipation.

since the total viscoelastic dissipation is proportional to the strain rate, the energy decay rate also gradually decreases as the kinetic energy decreases. Both integrators have essentially the same energy behaviors for the short time scales considered here.

6.5 Discussion

This chapter has presented a second-order accurate quaternion variational integrator for simulating the dynamics of Reissner-Simo geometrically exact beams in

flexible multibody systems. The discrete mechanics framework used to derive the variational integrator employs a temporal discretization of the variational principle based on a quaternion Lie group generalization of the standard midpoint rule and a structure-preserving finite element discretization based on spherical linear interpolation (slerp). This temporal discretization is general, and consequently, can be applied to develop quaternion-based Lie group variational integrators for other applications, e.g., plate or shell finite elements. The quaternion parameterization of rotations leads to a Lie group formulation of minimal dimension that implicitly enforces the quaternion unit norm constraint. Modified internal force and moment resultants account for viscoelastic damping via a Kelvin-Voigt formulation.

The variational integrator was subsequently applied to several standard benchmark problems: a free-free flexible beam, a right-angle cantilever, and a swinging flexible pendulum with Kelvin-Voigt damping. In each case, comparisons were made between a more traditional structural dynamics integrator, the Lie group generalized-α method, and the variational integrator. In the first two examples, the variational integrator showed nearly perfect energy behavior, even for very long simulation durations, whereas the numerical dissipation in the generalized-α method led to non-physical energy behavior. The two integrators performed nearly identically in the third example, perhaps due to either the short time scales involved or the viscoelastic damping masking the effects of the numerical dissipation. Altogether, the performance of the variational integrator appears advantageous for simulating more complex flexible multibody systems, like the finite element model of an ultralight flexible spacecraft studied in Chapter 8.

Chapter 7

PARAMETRIC MODAL ANALYSIS OF A PLATE-LIKE FLEXIBLE SPACECRAFT

7.1 Introduction

A recent paradigm in spacecraft design trades deployed structural rigidity against packaging efficiency to build higher-performing, lighter-weight, and lower-cost spacecraft with larger deployed apertures that can still stow within the confines of existing launch vehicles. Tightly packaging large apertures into small volumes typically necessitates the use of plate-like (planar) structural architectures, examples of which include solar sails [9], deployable reflectarray antennas [214], and space solar power satellites [13]. As the size of these structures increases, it becomes increasingly difficult to characterize their dynamic properties via ground tests, particularly those in a representative, i.e., gravity-offloaded environment, and to extrapolate the dynamic properties of small-scale test articles to full-scale flight systems. Thus, every step of the design process requires computational models to characterize these structures' dynamic properties.

In 2016, the Caltech Space Solar Power Project (SSPP) proposed a novel ultralight, packageable, and self-deployable spacecraft structural architecture for space solar power applications [13]; see Fig. 7.1. In the years since, a significant research enterprise has focused on understanding the complex behavior of the SSPP architecture's constituent structural components [35, 215–217] and on demonstrating the reliability, repeatability, and robustness of its deployment scheme [7, 8], all in support of an in-space deployment demonstration planned for 2022 or 2023 [218].

The SSPP architecture and its derivatives (see e.g., [214]) are representative of a class of spacecraft structures referred to as bending architectures [24], i.e., structural concepts that derive their load carrying capabilities from bending stiffness. Hence, the SSPP concept occupies a middle ground in terms of stiffness and areal density between membrane-based deployable structures concepts, e.g., solar sails [9], and more traditional spacecraft with deployable solar arrays and antennas. Bending stiffness facilitates the integration of the multi-functional elements [12, 48, 49] that transform the passive structure into a lightweight photovoltaic-powered phased array capable of beaming solar energy to Earth.

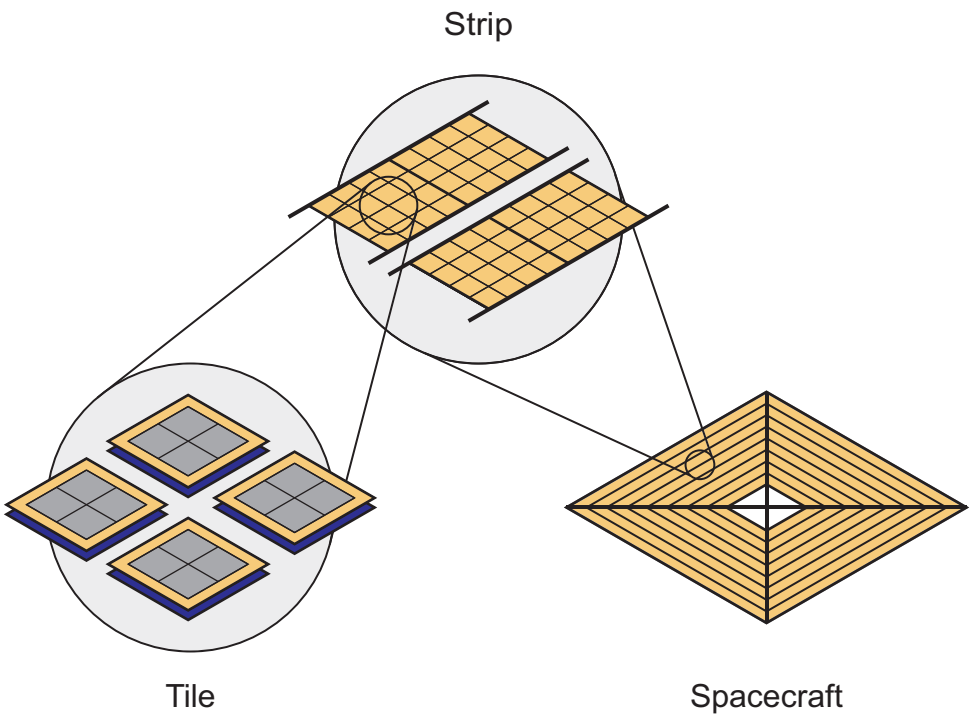

Figure 7.1: Caltech Space Solar Power Project spacecraft structural architecture originally introduced in [13].

The SSPP in-space deployment demonstration [218] uses an approximately 1.7 m $\times$ 1.7 m structure assembled from components (specifically longerons [7]) sized for a nominally 60 m $\times$ 60 m spacecraft. This results in an overly stiff structure compared to the full-scale flight system, i.e., the dynamic properties of this structure are not representative of those of a larger system. As a result, understanding the dynamic properties of these structures requires computational tools capable of exploring their design tradeoffs and sensitivities. With this in mind, this chapter develops and implements a nonlinear flexible multibody dynamics finite element model of an SSPP-like spacecraft suitable for preliminary design and analysis. In particular, the model is useful for modal analyses and calculating static and dynamic responses in both the linear and geometrically nonlinear regimes. To make the simulation of large SSPP-like spacecraft more computationally tractable, the model replaces the slender, thin-shell "strip" structures [35] from Fig. 7.1 with equivalent beam models derived using an energy-equivalence principle [219, Ch. 4]. This limits the model to the simulation of macroscale structural dynamic phenomena. Chapter 8 uses this model to simulate slew maneuver dynamics.

Besides the finite element model, the main contribution of this chapter is a parametric

modal analysis that explores the sensitivities of the dynamic properties of an SSPP-like spacecraft to boom stiffness, strip areal density, and size in order to develop useful insights into their design and dynamics.

This chapter is organized as follows: Sec. 7.2 reviews the Caltech SSPP structural architecture and discusses the simplifying assumptions inherent to the numerical model. Sec. 7.3 derives an equivalent Timoshenko beam model for the strips in the SSPP architecture. Sec. 7.4 describes the implementation of the flexible multibody dynamics finite element model. Sec. 7.5 designs booms for the expected slew maneuver loads and determines an empirical scaling relationship for their radius as a function of spacecraft size. Sec. 7.6 uses a parametric modal analysis to study the relationship between boom stiffness, areal density, and the structure's vibration characteristics. Sec. 7.7 summarizes the chapter's results and implications.

7.2 Spacecraft Structural Architecture

The spacecraft structural architecture considered here is a derivative of the ultralight, packageable, and self-deployable architecture originally proposed by the Caltech SSPP for space solar power satellites in [13] and depicted in Fig. 7.1. The structural architecture is planar to facilitate packaging and deployment using a kirigami-inspired folding scheme and is designed to be both modular and scalable, allowing the same basic structural components to be used for spacecraft designed for different applications at different length scales.

The smallest modular unit in the SSPP architecture is referred to as a tile. Each tile is a multi-layer and multi-functional flexible sandwich structure with typical maximum dimensions on the order of 10 cm. Tiles are flattenable to facilitate efficient packaging. For space solar power, each tile integrates photovoltaics, DC-RF converters, and microwave radiators capable of collecting incident solar power and transmitting it to a receiving station [12, 48, 49]. To-date, several research groups have developed and demonstrated integrated tiles for space solar power [12, 48, 49, 220, 221]. However, the modularity of the tile concept is general. Hence, tiles can be conceived for other applications, including power generation; direct-drive solar-electric propulsion [222–225]; and communications, power transfer, and remote sensing [12]. For simplicity, the stiffness properties of the tiles are neglected. Their mass properties are modeled using a uniform areal density added to the strips.

Tiles are mounted on slender thin-ply composite structures called strips [35]. The strips are ultralight, ladder-like structures assembled from two longerons connected

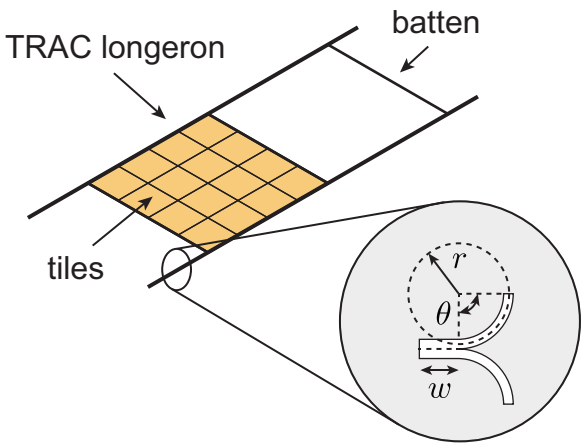

Figure 7.2: Strip architecture and cross-sectional geometry of a TRAC longeron parameterized by the web width w, flange radius r, and flange opening angle θ.

by transverse battens; see Fig. 7.2. Each longeron is a triangular rollable and collapsible (TRAC) boom [226, 227] with cross-sectional geometry parameterized by its web width w, flange radius r, and flange opening angle θ. The longerons contribute bending and shear stiffnesses to the strip. Each batten is then modeled as an isotropic beam with a rectangular cross-section of breadth b and height h, as is done in [6, 24]. The battens contribute lateral bending stiffness and support the tiles. The strips are stiff in torsion due to the combination of longerons and battens.

Table 7.1: Non-zero coefficients of experimentally determined flange and web **ABD** matrices from [215]

Coefficient	**Units**	**Flange**	**Web**
A_{11}	$\mathrm{N\,m^{-1}}$	5432×10^3	11369×10^3
A_{12}	$\mathrm{N\,m^{-1}}$	619×10^3	1512×10^3
A_{22}	$\mathrm{N\,m^{-1}}$	942×10^3	2269×10^3
A_{33}	$\mathrm{N\,m^{-1}}$	737×10^3	1727×10^3
D_{11}	N m	1.076×10^{-3}	28.20×10^{-3}
D_{12}	N m	0.482×10^{-3}	4.32×10^{-3}
D_{22}	N m	0.781×10^{-3}	7.44×10^{-3}
D_{33}	N m	0.459×10^{-3}	4.93×10^{-3}

For simplicity, the material and geometric properties for the strips are taken from the numerical model used in a recent study of their deployment dynamics [6], which in turn is based on a recent experimental characterization of the TRAC longerons [215]. The strips from [6] trace their heritage back to the original Caltech

SSPP design study [13] and are sized for the expected solar radiation pressure (SRP) load on a 60 m × 60 m spacecraft. Like [6], the longerons use the nominal cross-sectional geometry studied in [215]: web width w = 8.0 mm, flange radius r = 12.7 mm, and flange opening angle θ = 90 deg. The flange and web material properties are based on measurements of coupons with $[\pm 45_{\mathrm{GFPW}}/0_{\mathrm{CF}}/\pm 45_{\mathrm{GFPW}}]$ and $[\pm 45_{\mathrm{GFPW}}/0_{\mathrm{CF}}/\pm 45_{3,\mathrm{GFPW}}/0_{\mathrm{CF}}/\pm 45_{\mathrm{GFPW}}]$ laminates, respectively, where GFPW and CF refer to glass fiber plain-weave and carbon fiber. The web laminate consists of the laminates for the two flanges plus an extra $[\pm 45_{\mathrm{GFPW}}]$ ply for the bond. The experimentally determined flange and web **ABD** matrices are listed in Table 7.1; $\mathbf{B} = \mathbf{0}_{3\times 3}$ for both laminates because they are symmetric. Each flange has a nominal thickness t_f = 80 μm and density ρ_f = 1381 kg/m^3. The web has a nominal thickness t_w = 185 μm and density ρ_w = 1396 kg/m^3. The densities ρ_f and ρ_w are calculated from the densities and thicknesses of the plies of GFPW and CF.

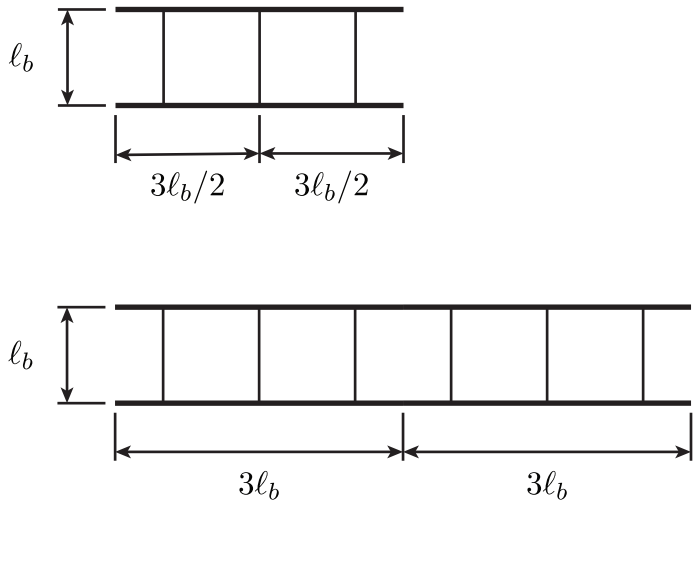

Figure 7.3: Batten spacings for strips of length (a) $3\ell_b$ and (b) $6\ell_b$ where ℓ_b = 1 length unit.

The battens are modeled as isotropic beams of length ℓ_b = 1 m with rectangular cross-sections of breadth b = 3 mm (in the plane of the strip), height h = 0.6 mm (normal to the plane of the strip), elastic modulus E_b = 137 GPa, Poisson's ratio ν_b = 0.3, and density ρ_b = 1610 kg/m^3. These material properties correspond to pultruded carbon fiber (which is anisotropic). The battens are spaced 1 m apart, starting from either the center of the strip or points 0.5 m from the center of the strip, depending on whether the strip has a length that rounds to an odd or even

integer; see Fig. 7.3. A batten of length $\ell_b = 1$ m leads to an overall strip width of $\ell_b + 2(w + r) = 1.0414$ m. To simplify subsequent developments, the overall strip width is rounded down to 1 m in numerical calculations. By doing so, an integer length outer dimension can produce a fully-filled aperture with no spacing between adjacent strips. The only remaining parameter required to fully specify the properties of a strip is its length ℓ_s, which depends on the deployed aperture size and its location in the aperture.

In the original SSPP concept [13], each strip is attached to cords running parallel to the four deployable booms to facilitate deployment [7, 8, 13]. The booms tension the cords in the deployed configuration. To simplify the structural architecture, however, the numerical model eliminates the cords by directly fastening each strip to two diagonal booms via revolute (hinge) joints [180] with axes of rotation parallel to the booms. Importantly, attaching the strips directly to the booms prohibits deployment, something deemed acceptable here due to the emphasis on simulating the deployed spacecraft's macroscale structural dynamics. The amount of tension determines the effects of the cords on the macroscale structural dynamics. As discussed in [13], there is an optimal pre-tension that maximizes the structure's stiffness; too much pre-tension ultimately softens the structure. Assuming the pre-tension is optimal (or nearly so), then eliminating the cords is expected to decrease the structure's stiffness and lower its first-mode frequency. Eliminating the cords likewise removes the associated vibration modes, including any due to cord-strip interactions, and decreases the damping in the system (the cord dynamics provide an additional mechanism for dissipating energy). Despite all this, eliminating the cords is not expected to significantly affect the spacecraft's macroscale structural dynamics, although evaluating this assumption is outside the scope of this thesis and left to future work. Due to this simplification, the spacecraft studied here is often referred to as *SSPP-like*. Note that there are no direct connections between any two strips, i.e., the strips can only interact through the booms.

Four booms, each of length $\ell_B = \ell_n/\sqrt{2}$, are arranged with angular spacings of 90 deg. The areas between two adjacent booms define identical quadrants, each of which contains n rectangular strips of equal width ℓ_b uniformly spaced $\Delta\ell_b$ apart; see Fig. 7.4. Together, the length of the outermost strip ℓ_n and ℓ_b determine the geometry of the quadrant. Specifically, the number of strips is

$$n = \left\lfloor \frac{(\ell_n/2)}{\ell_b} \right\rfloor \tag{7.1}$$

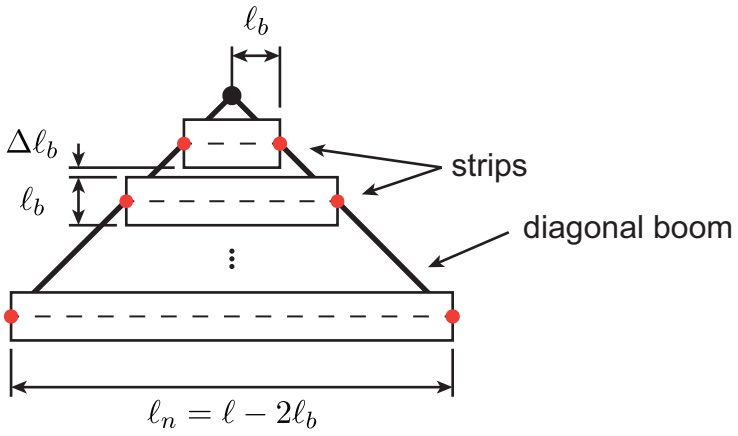

Figure 7.4: Geometry of a quadrant of a complete SSPP-like spacecraft. The corners of each rectangular strip overlap the strips in adjacent quadrants.

where $\lfloor \cdot \rfloor$ denotes rounding down to the nearest integer. Equation (7.1) assumes that the distance from the center of the aperture to the edge of the innermost strip is $\ell_b/2$ and that the outermost strip is attached to the ends of the corresponding booms. The spacing $\Delta\ell_b$ between the strips and the length ℓ_i of the ith strip (for $i = 1, \ldots, n$) then follow as

$$\Delta\ell_b = (\ell_n/2 - n\ell_b)\,/(n-1) \tag{7.2}$$

$$\ell_i = 2\,(i\ell_b + (i-1)\Delta\ell_b) \tag{7.3}$$

where $i = 1$ and $i = n$ denote the innermost and outermost strips, respectively. In accordance with [24], the innermost strip is of length $\ell_1 = 2\ell_b$, leaving a square hole of dimensions $\ell_b \times \ell_b$ at the center of the aperture for the spacecraft bus and deployment mechanism. Due to overlap between the corners of strips in adjacent quadrants, an outermost strip of length ℓ_n simulates an aperture of size $\ell \times \ell$, i.e., $\ell_n = \ell - 2\ell_b$. In the numerical model, each strip is idealized as a beam with its reference axis coincident with its centerline; Fig. 7.4 denotes each centerline by a dashed line.

Following [24], the trapezoidal strips in the SSPP architecture [7, 13] are replaced with rectangles ones. This simplifies the derivation of an equivalent beam model in Sec. 7.3. Specifically, rectangular strips are prismatic, i.e., they have symmetric cross-sections along their lengths. In contrast, a trapezoidal strip is non-prismatic due to the variations of the cross-section in the vicinities of the ends.

Like [24], the diagonal booms are modeled as hollow, thin-walled cylindrical tubes of radius R and thickness t with elastic modulus $E_B = 70$ GPa, Poisson's ratio $\nu_B = 0.3$,

shear modulus $G_B = E_B/(2(1+\nu_B))$, and density $\rho_B = 1610\,\mathrm{kg/m^3}$. The resulting sectional shear stiffnesses are rescaled using the Timoshenko shear correction factor for a hollow circular cross-section from [152] linearized for the case when $t/R \ll 1$. The thin-walled circular cross-section and isotropic material properties are intended to approximate the expected stiffness properties of the deployable, closed cross-section composite booms likely to be used on an actual spacecraft. The optimal boom size is a function of the loading, spacecraft size, structural limits (e.g., due to buckling), and deflection limits [24], i.e., the proportion of the deflection in the strips versus the booms. For a given loading and deflection limit, the general trend is that the boom size increases as the spacecraft size increases. Reference [24], however, only considers uniform transverse pressure loads, like those due to SRP. Slew maneuvers, on the other hand, generate linearly-varying transverse loads due to Euler acceleration. For this reason, Sec. 7.5 uses a parametric analysis to determine a relationship between boom size (specifically, the radius r and thickness t) and spacecraft size for this loading condition.

The combination of the tiles, strips, booms, and central hub constitute the spacecraft. The central hub includes the deployment mechanism and spacecraft bus, the latter of which provides the requisite spacecraft functions like attitude determination and control, command and data handling, propulsion, and communications. The deployment mechanism is modeled as a lumped mass of 40.4 kg at the central hub. This estimate is based on scaling the measured mass plus contingencies of the engineering model of the DOLCE deployment mechanism [218] which is designed for an SSPP structure with 0.2 m-wide strips. As an initial approximation, scaling the mechanism entails simply increasing its height to accommodate 1 m-wide strips. In turn, the masses of the individual components in the as-built mechanism scale accordingly, in this case linearly or nearly linearly with increasing height. The scaling assumes that no additional mechanism structure is required to support wider strips or larger apertures during stowage or deployment. Since the DOLCE deployment mechanism is not mass-optimized, the total mass is then decreased by a factor of 40% to account for future mass optimization, resulting in the estimated mechanism mass of 40.4 kg. Following [228], the spacecraft bus is modeled as a lumped mass of 80 kg. This is an estimate based on state-of-the-art small satellite technology. In reality, the bus mass may vary widely depending on the specifics of a given mission and the masses of the attitude control actuators, propulsion system, etc. Additionally, the bus moments of inertia are expected to be small compared to the moments of inertia of the deployed structure, and hence, are neglected.

7.3 Equivalent Beam Model for a Strip

Both individual TRAC booms [215, 227] and assembled strips [24, 217] are susceptible to localized buckling and folding due to geometrically nonlinear effects associated with cross-sectional deformations. Capturing localized geometrically nonlinear effects requires high-fidelity finite element models with very fine meshes, making the dynamic analysis of SSPP-like spacecraft at best impractical and at worst computationally intractable. However, in the absence of localized geometrical nonlinearities, long strips behave similarly to beams; their internal bending moments predict the onset of localization and buckling [217]. Provided these internal bending moments do not exceed some critical bending moment, it is reasonable to replace the thin-shell strips with equivalent beams to model macro-scale structural deformations, as is done, e.g., in [24].

The flexible multibody dynamics model developed in Sec. 7.4 discretizes the booms and strips using the geometrically exact beam finite elements from Chapter 5. Geometrically exact beam finite elements, in turn, require sectional inertia and stiffness matrices (denoted by $\mathbf{J}$[1] and $\mathbf{C}$, respectively). Since the booms are thin-walled cylindrical tubes, these matrices are straightforward to derive from standard beam theory. The strips, on the other hand, are complex thin-shell structures, motivating the use of a numerical approach for calculating $\mathbf{J}$ and $\mathbf{C}$. The resulting numerical estimates for $\mathbf{J}$ and $\mathbf{C}$ are variously referred to as either *equivalent* or *homogenized* beam models.

Geometrically exact beam theory is a nonlinear generalization of Timoshenko beam theory. Hence, the equivalent sectional stiffness matrix includes axial, shear, torsional, and bending terms. Shear forces induce both bending and shear deformations that can complicate the development of equivalent beam models [229], especially compared to approaches based on Euler-Bernoulli beam assumptions. Since rectangular strips have both geometrically and materially symmetric cross-sections, the appropriate equivalent beam model is a prismatic, homogeneous, and isotropic Timoshenko beam with its reference axis coincident with the centerline of the strip.

The equivalent beam modeling approach described in the sequel primarily draws inspiration from the "stick" modeling approach pervasive in the aeroelasticity literature; see e.g., [230–234] and the references therein. Stick models approximate

[1] In previous chapters, $\mathbf{J}$ refers to the 3×3 sectional moment of inertia matrix used to calculate the rotational kinetic energy per unit length; see Sec. 4.6. Here, $\mathbf{J}$ instead refers to the 6×6 sectional inertia matrix used to calculate the total kinetic energy per unit length.

complex slender structures like aircraft wings [230, 232, 234] and complete aircraft configurations [231, 233] with skeletal frames modeled as beams to make nonlinear aeroelastic analyses more computationally tractable. Similar approaches are commonly used elsewhere, including for modeling wind turbine blades [235] and complex, slender spacecraft structures [236–239]. Existing methods typically compute equivalent beam elements from high-fidelity finite element models, and then as necessary use a post-processing step to extract the equivalent sectional inertia and stiffness matrices [235]. To simplify the homogenization procedure, the present approach directly computes the sectional inertia and stiffness matrices from high-fidelity finite element models.

There is some debate over the best approach for homogenizing complex slender structures. Reference [240], for instance, highlights difficulties with finite-element-based homogenization methods, including boundary layer effects near the applied load(s), the determination of the elastic axis, and potentially the size of the unit cell. For these reasons, [240] instead argues in favor of cross-sectional analysis tools like Variational Asymptotic Beam Sectional Analysis (VABS) [241, 242], as opposed to finite-element-based methods [230, 232, 234, 235]. However, finite-element-based methods are advantageous because they can account for 3D effects like cross-sectional tapering and warping in the resulting 1D beam properties [235]. They can even be extended to capture nonlinear effects, although this is outside the scope of the present work. Additionally, it is not immediately clear how to directly apply a cross-sectional homogenization method like VABS to a ladder-like strip. As a result, a finite-element-based homogenization method is preferred here.

Likewise, there is a question about what part or parts of the structure to homogenize. The approach taken here is global in the sense that each strip is homogenized into a single equivalent beam. This significantly reduces the number of elements required to model each strip, but it also limits both the number and types of admissible deformation modes. For these reasons, a more local homogenization approach may be advantageous for applications requiring higher (but still not full) fidelity. As an example, such an approach can instead homogenize the segments of the TRAC longerons located between the battens into equivalent beams either analytically (e.g., using classical lamination and thin-walled beam theories) or numerically (e.g., using VABS). Unsurprisingly, however, more local homogenization approaches increase the number of modeled degrees of freedom (DOFs). This leads to a commensurate increase in computational cost and is deemed prohibitive for the long-duration time-

domain simulations subsequently studied in Chapter 8.

The homogenization method developed in what follows is similar to [235], at least as far as the equivalent stiffness properties are concerned, but uses a displacement-based approach instead of a force-based one for improved numerical conditioning. The end cross-sections of the strip are rigidly constrained to simplify the application of the external loads and the specification of the equivalent beam's reference axis. The determination of the equivalent inertia properties then uses a convex-optimization-based approach inspired by [243].

The equivalent beam model is developed using two steps, one each for the sectional inertia matrix **J** and the sectional stiffness matrix **C**. Both steps are based on the idea of energy equivalence commonly used to determine inertia and stiffness properties of discrete structural elements from continua; see e.g., [219, Ch. 4]. Here, energy equivalence relates the kinetic and strain energies of a high-fidelity model of an appropriate unit cell, the full-order model (FOM), with those of the equivalent Timoshenko beam model, the reduced-order model (ROM), to solve for **J** and **C**. In general, both **J** and **C** are sensitive to the length of the unit cell [240].

7.3.1 Equivalent Inertia Properties

The equivalent sectional inertia matrix **J** is determined from the solution to a convex-optimization problem that minimizes the kinetic energy error between the FOM and the equivalent Timoshenko beam model. Following [243], the optimization problem explicitly enforces physics-based constraints on **J**. An optimization-based approach is necessary because the sectional inertia properties of a prismatic, homogeneous, and isotropic Timoshenko beam cannot exactly match the mass and inertia distributions of arbitrary structures.

Rigid Body Model

The kinetic energy of the FOM of a strip unit cell is calculated using a simple finite element model based on linear C^0 beam elements and implemented in MATLAB®. Figure 7.5 depicts a representative FOM. C^0 beam elements are linear, small-deflection 3D Timoshenko beam finite elements with linear interpolation of displacements and rotations [183] that exactly model the rigid body inertia of initially straight beams, independent of the number of elements. Since the FOM is effectively composed of two types of beam segments, TRAC longerons and battens, the finite element model exactly models the rigid body inertia so long as its sectional

inertia properties are correctly specified. Longerons and battens are both meshed using two elements per meter. This places a node at the center of each batten.

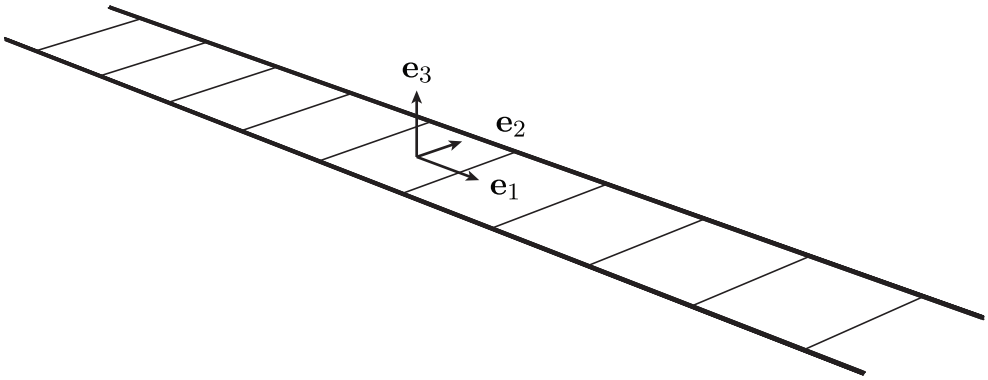

Figure 7.5: Representative full-order model, in this case, of a 10 m-long strip with 1 m-long battens spaced 1 m apart, used for determining equivalent sectional inertia properties. The origin of the reference frame is at the strip's center of mass.

Table 7.2: Non-zero coefficients of sectional inertia matrices for a TRAC longeron and batten calculated with VABS [241, 242]

Coefficient	**Units**	**TRAC Longeron**	**Batten**
J_{11}, J_{22}, J_{33}	$\mathrm{kg\,m^{-1}}$	6.232×10^{-3}	2.898×10^{-3}
J_{15}	kg	-1.327×10^{-12}	–
J_{16}	kg	4.848×10^{-5}	–
J_{24}	kg	1.327×10^{-12}	–
J_{34}	kg	-4.848×10^{-5}	–
J_{44}	kg m	7.701×10^{-7}	2.260×10^{-9}
J_{55}	kg m	1.379×10^{-7}	8.694×10^{-11}
J_{56}	kg m	-5.310×10^{-15}	–
J_{66}	kg m	6.322×10^{-7}	2.174×10^{-9}

The sectional inertia properties for both the TRAC longerons and battens are evaluated using VABS [241, 242] with the PreVABS input processor and the geometrical and material properties from Sec. 7.2. Table 7.2 lists the resulting sectional inertia matrices for the cross-sectional axes defined in Fig. 7.6. The sectional inertia matrix for the TRAC longeron is evaluated about the geometric center of the web, not the centroid. The geometric center defines the location of the attachment point between the TRAC longerons and battens in the finite element model. Since most of the inertia is due to the mass of the longerons, the exact location of the attachment point has a negligible effect on the total inertia.

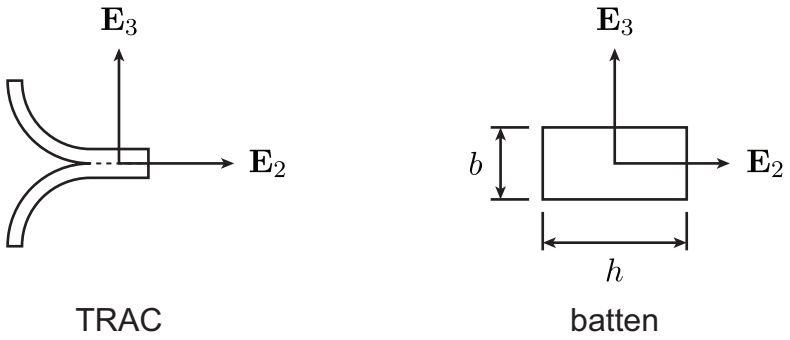

Figure 7.6: Definitions of cross-sectional axes for TRAC longeron and batten. $\mathbf{E}_1$ points out of the page.

Equivalent Beam Sectional Inertia Matrix and Kinetic Energy

The sectional inertia matrix relates the velocities at each point along the reference axis of a beam to the kinetic energy per unit length. Its structure determines the physics-based constraints enforced in the optimization problem that evaluates the equivalent beam model. A derivation of the sectional inertia matrix is provided to highlight this structure.

Consider a Timoshenko beam of length ℓ with volumetric mass density ρ, a cross-section of arbitrary shape, and a reference axis non-collocated with the cross-sectional mass centroid. Since each cross-section is assumed rigid in its own plane, the velocity of any material point in the cross-section is simply

$$\mathbf{v} = \mathbf{v}_{\text{ref}} + \boldsymbol{\omega} \times \mathbf{r} \tag{7.4}$$

where $\mathbf{v}_{\text{ref}}$ is the velocity of the reference axis, $\boldsymbol{\omega}$ is the angular velocity of the cross-section, and $\mathbf{r}^T = (0, x_2, x_3)$. The kinetic energy per unit volume is $\rho\left(\dot{\mathbf{v}}^T\mathbf{v}\right)/2$, from which it follows that the total kinetic energy is

$$\mathcal{T} = \frac{1}{2}\int_0^\ell \int_A \rho\left(\dot{\mathbf{v}}^T\mathbf{v}\right)\,\mathrm{d}A\,\mathrm{d}x \tag{7.5}$$

where A denotes integration over the cross-sectional area. Equation (7.5) can then be written in the equivalent form

$$\mathcal{T} = \frac{1}{2}\int_0^\ell \dot{\mathbf{u}}^T\mathbf{J}\dot{\mathbf{u}}\,\mathrm{d}x \tag{7.6}$$

where $\mathbf{u}^T = \left(\mathbf{v}_{\text{ref}}^T, \boldsymbol{\omega}^T\right)$ and $\mathbf{J}$ is the sectional inertia matrix

$$\mathbf{J} = \begin{bmatrix} \rho A & 0 & 0 & 0 & \rho A\overline{x}_3 & -\rho A\overline{x}_2 \\ & \rho A & 0 & -\rho A\overline{x}_3 & 0 & 0 \\ & & \rho A & \rho A\overline{x}_2 & 0 & 0 \\ & & & \rho I_2 + \rho I_3 & 0 & 0 \\ & & & & \rho I_2 & \rho I_{23} \\ \text{sym} & & & & & \rho I_3 \end{bmatrix}. \tag{7.7}$$

The integrand of Eq. (7.6) is the kinetic energy per unit length. In Eq. (7.7), ρA is the mass per unit length; $\rho I_2 = \int_A \rho x_3^2 \, \mathrm{d}A$ and $\rho I_3 = \int_A \rho x_2^2 \, \mathrm{d}A$ are the cross-sectional area moments of inertia; $\rho I_{23} = -\int_A \rho x_2 x_3 \, \mathrm{d}A$ is the cross-sectional product of inertia; $\rho I_2 + \rho I_3$ is the polar area moment of inertia; and $\rho A\overline{x}_2 = \int_A \rho x_2 \, \mathrm{d}A$ and $\rho A\overline{x}_3 = \int_A \rho x_3 \, \mathrm{d}A$ are the mass-weighted centroidal coordinates. When the mass density over the cross-section is uniform, $\overline{x}_2$ and $\overline{x}_3$ denote the location of the geometric centroid. For a beam with a geometrically and materially symmetric cross-section and a reference axis collocated with its centroid, $\mathbf{J}$ is diagonal. In general, $\mathbf{J}$ is a function of position along the reference axis of the beam, but it is constant for prismatic and homogeneous beams.

The structure of the sectional inertia matrix refers to both the sparsity pattern (i.e., zeros) and properties of Eq. (7.7). Since the kinetic energy per unit length is strictly positive for non-zero $\dot{\mathbf{u}}$, $\mathbf{J}$ is a symmetric positive definite matrix, i.e., $\mathbf{J} > 0$. Additionally, the coefficients of $\mathbf{J}$ must satisfy the following identities:

$$J_{11} = J_{22} = J_{33}, \tag{7.8}$$

$$J_{44} = J_{55} + J_{66}, \tag{7.9}$$

$$J_{15} = -J_{24}, \tag{7.10}$$

$$J_{16} = -J_{34}, \tag{7.11}$$

$$J_{12} = J_{13} = J_{14} = J_{23} = J_{25} = J_{26} = J_{35} = J_{36} = J_{45} = J_{46} = 0. \tag{7.12}$$

Optimization Problem

The kinetic energy [Eq. (7.6)] can be evaluated in closed-form if $\dot{\mathbf{u}}$ is known along the length of the beam. This implies a method for determining the equivalent sectional inertia properties. Specifically, if the same velocity distribution is applied to both the FOM and the equivalent beam, then coefficients of $\mathbf{J}$ can be determined that minimize the error between the two corresponding kinetic energies.

When $\mathbf{J}$ is diagonal, at least four equations are required to solve for the four unknown sectional inertia coefficients. This requires at least four independent velocity distributions. These velocity distributions are not unique. A simple choice is a set of velocity distributions that span each structure's rigid body modes. For the strip depicted in Fig. 7.5, these correspond to a pure translation in either the $\mathbf{e}_1$, $\mathbf{e}_2$, or $\mathbf{e}_3$ directions plus rotations about these three axes. In practice, it is preferable to specify pure translations in all three directions to allow the same computer implementation to be reused for cases when $\mathbf{J}$ is non-diagonal.

When $\mathbf{J}$ is non-diagonal, additional independent velocity distributions are required. Again, these velocity distributions are not unique, but a possible choice is the set that spans the combinations of any two independent rigid body modes.

Given N independent velocity distributions, the corresponding kinetic energies for the FOM and equivalent beam model can be stacked in the vectors

$$\mathbf{b} = \begin{bmatrix} \mathcal{T}_1^{(\mathrm{FE})} & \dots & \mathcal{T}_i^{(\mathrm{FE})} & \dots & \mathcal{T}_N^{(\mathrm{FE})} \end{bmatrix}^T, \tag{7.13}$$

$$\mathbf{A}\mathbf{j} = \begin{bmatrix} \mathcal{T}_1^{(\mathrm{eq})} & \dots & \mathcal{T}_i^{(\mathrm{eq})} & \dots & \mathcal{T}_N^{(\mathrm{eq})} \end{bmatrix}^T \tag{7.14}$$

where $i = 1, \dots, N$ and the superscripts FE and eq denote the full-order finite element and equivalent beam models, respectively. The kinetic energy for the equivalent beam [Eq. (7.6)] is a quadratic function of $\dot{\mathbf{u}}$ but a linear function of $\mathbf{J}$. As a result, the vector of equivalent beam kinetic energies can be written as the product $\mathbf{A}\mathbf{j}$ where $\mathbf{A} \in \mathbb{R}^{N\times 21}$ is a velocity-dependent coefficient matrix and $\mathbf{j} \in \mathbb{R}^{21}$ is the vectorization of the upper-triangular block of $\mathbf{J}$.

The equivalent sectional inertia matrix is then obtained from the solution to the following optimization problem:

$$\underset{\mathbf{j}}{\text{minimize}} \quad \|\mathbf{A}\mathbf{j} - \mathbf{b}\|_2 \tag{7.15}$$

subject to $\mathbf{J} - \epsilon\mathbf{I}_{6\times 6} \geq 0$ and Eqs. (7.8) to (7.12). The notation $\|\cdot\|_2$ and $\geq$ denote the Euclidean norm and positive semidefiniteness, respectively. The small positive constant $\epsilon \ll 1$ guarantees that $\mathbf{J}$ is strictly positive definite. Equation 7.15 is a convex program with a single linear matrix inequality constraint and 15 linear equality constraints with a unique, globally optimal solution. The optimization problem is solved using CVX [244, 245] with the SDPT3 solver [246, 247]. Note that when $\mathbf{J}$ is diagonal, additional constraints are required in Eq. (7.15) to set the off-diagonal entries to zero.

Results

To demonstrate the homogenization approach, equivalent sectional inertia properties are evaluated from Eq. (7.15) for strips with integer lengths between 5 m and 50 m. For each strip, the equivalent beam model is a prismatic, homogeneous, and isotropic Timoshenko beam with its reference axis aligned with the strip's centerline. Hence, the equivalent sectional inertia matrices for the strips are diagonal.

To assess the accuracy of the equivalent beam models, their masses and moments of inertia are compared to the actual masses and moments of inertia calculated from the corresponding FOMs of the strips. Moments of inertia for each equivalent beam and strip are evaluated relative to the appropriate centers of mass. In terms of the coefficients of the equivalent sectional inertia matrix **J**, the mass and moments of inertia of the equivalent beam are

$$m^{(\mathrm{eq})} = J_{11}\ell, \tag{7.16}$$

$$I_{11}^{(\mathrm{eq})} = J_{44}\ell, \tag{7.17}$$

$$I_{22}^{(\mathrm{eq})} = J_{55}\ell + J_{33}\ell^3/12, \tag{7.18}$$

$$I_{33}^{(\mathrm{eq})} = J_{66}\ell + J_{22}\ell^3/12. \tag{7.19}$$

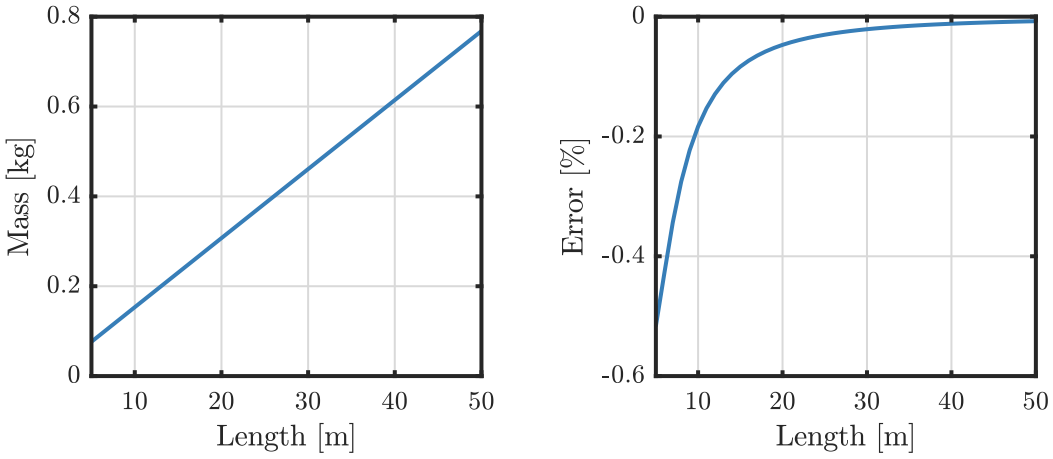

(a) (b)

Figure 7.7: (a) mass calculated from equivalent sectional inertia properties [Eq. (7.16)]. (b) error relative to FOM.

Figure 7.7a plots the equivalent beam's mass [Eq. (7.16)] as a function of strip length. Unsurprisingly, the mass increases linearly with length, reflecting that the linear mass density calculated from Eq. (7.16) is independent of length. Figure 7.7b then plots the relative error $\left(m^{\mathrm{eq}} - m^{\mathrm{FE}}\right)/m^{\mathrm{FE}}$ between the equivalent beam's mass

and the FOM's mass. The general trend is that the errors decrease as length increases, although even for short (5 m-long) strips, the errors are acceptable for preliminary analysis and design. The discrepancies between the equivalent beam model and the FOM reflect that the equivalent beam cannot exactly model the mass and inertia distributions of the strips.

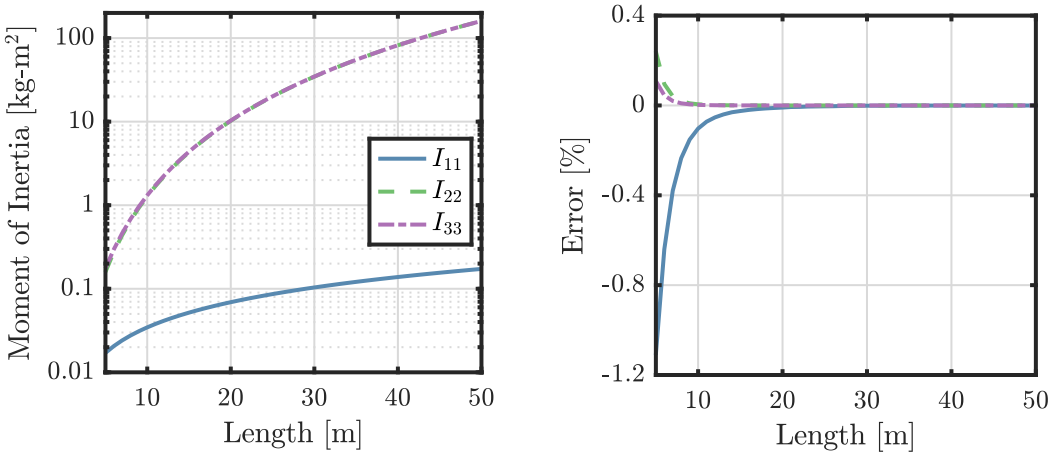

Figure 7.8: (a) moments of inertia calculated from equivalent sectional inertia properties [Eqs. (7.17), (7.18), and (7.19)]. (b) errors relative to FOM.

Figure 7.8a plots the equivalent beam's moments of inertia [Eqs. (7.17), (7.18), and (7.19)] as a function of strip length. Figure 7.8b then plots the corresponding relative errors $\left(I^{\text{eq}} - I^{\text{FE}}\right)/I^{\text{FE}}$ between the moments of inertia for the equivalent beam and the FOM. Again, the general trend is that the errors decrease as length increases, indicating that the inertia properties of the strips become progressively more "beam-like" as their lengths increase. Altogether, even though the equivalent beams cannot exactly model the mass and inertia distributions of the strips, Figs. 7.7b and Fig. 7.8b demonstrate that they still accurately approximate each strip's mass and inertia properties.

7.3.2 Equivalent Stiffness Properties

The equivalent sectional stiffness matrix $\mathbf{C}$ is determined from a system of equations that relate the strain energies of the FOM and the equivalent Timoshenko beam model due to a set of prescribed displacements. Since the sectional stiffness properties are properties of the cross-section, they are independent of the boundary conditions applied to the equivalent beam. As a result, the homogenization can use any boundary conditions that eliminate the equivalent beam's rigid body DOFs and uniquely

define its displacement field. For simplicity, the homogenization uses clamped-free boundary conditions with the displacements $\mathbf{\Delta}^T = (u_1, u_2, u_3, \theta_1, \theta_2, \theta_3)$ prescribed at the free end, as depicted in Fig. 7.9.

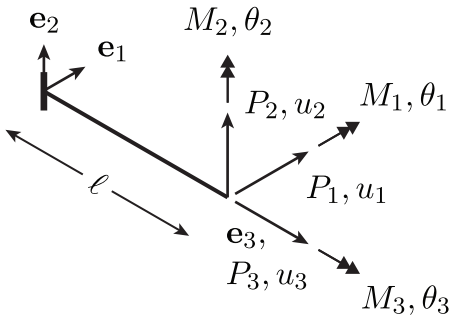

Figure 7.9: Prescribed displacements $\mathbf{\Delta}^T = (u_1, u_2, u_3, \theta_1, \theta_2, \theta_3)$ and corresponding external forces and moments $\mathbf{P}^T = (P_1, P_2, P_3, M_1, M_2, M_3)$ at the free end of the clamped-free equivalent beam.

High-Fidelity Finite Element Model

The FOM of a strip used in the stiffness homogenization is adapted from the Simulia Abaqus 2020 finite element model developed in [6]. An example finite element model of a 10 m-long strip with ten 1 m-long battens spaced 1 m apart is depicted in Fig. 7.10. The main changes from [6] are the removal of the membrane (used as a surrogate for the tiles) and the suspension system. Each TRAC longeron is modeled using reduced-integration general-purpose shell elements with hourglass control and finite membrane strains (S4R elements). Their stiffness properties are defined via the flange and web **ABD** matrices from Table 7.1. The battens are modeled using B31 linear beam elements with rectangular cross-sections and isotropic material properties, as discussed in Sec. 7.2. The longeron-batten connectors are modeled as kinematic coupling constraints between the batten end nodes and a small area of the longeron web. Each longeron is uniformly meshed using approximately 2 mm $\times$ 2 mm elements, resulting in approximately 12000 elements/meter. Each 1 m-long batten is meshed using 500 elements. The model is fully parametric to facilitate the simulation of strips with arbitrary geometry (batten length, batten spacing, and longeron length) and TRAC booms of arbitrary cross-section (web width, flange radius, and flange opening angle).

To replicate the boundary conditions on the equivalent beam (Fig. 7.9), kinematic coupling constraints are used to rigidize the cross-sections at both ends of the strip.

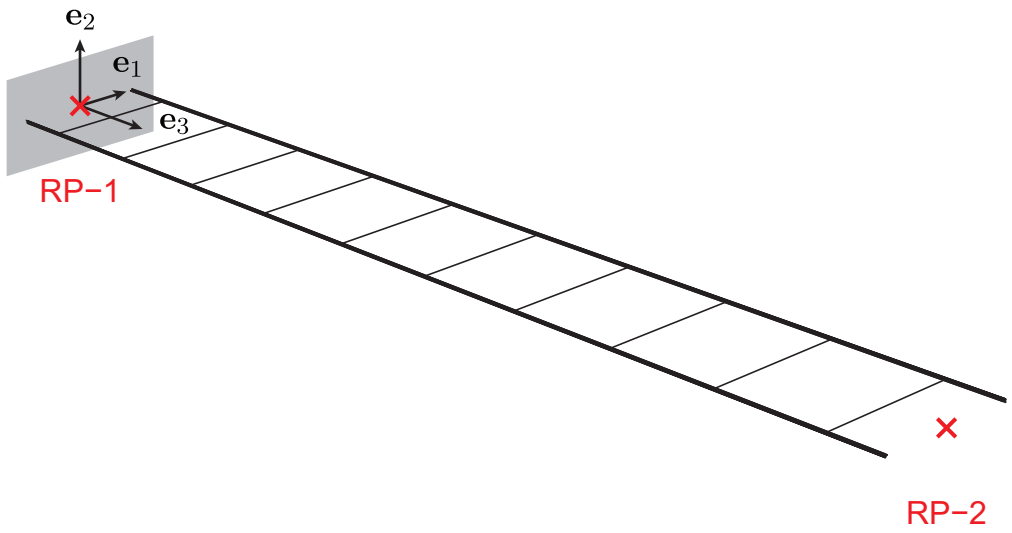

Figure 7.10: Simulia Abaqus 2020 finite element model of a 10 m-long strip with 1 m-long battens spaced 1 m apart. RP-1 and RP-2 are reference points along the strip's centerline in the plane of the end cross-sections.

As a result, there is no cross-sectional deformation at the ends. Two references points, RP-1 and RP-2, are embedded along the strip's centerline in the planes of the end cross-sections. RP-1 is clamped; the prescribed displacements for the homogenization are then applied at RP-2.

Strain Energy for Equivalent Beam

Evaluating the equivalent Timoshenko beam model requires writing the strain energy $\mathcal{U}$ in terms of the to-be-determined equivalent sectional stiffness matrix $\mathbf{C} = \text{diag}\,\{C_{11}, C_{22}, C_{33}, C_{44}, C_{55}, C_{66}\}$ and the prescribed free-end displacements $\mathbf{\Delta}^T = (u_1, u_2, u_3, \theta_1, \theta_2, \theta_3)$. Here, C_{11} and C_{22} are the shear stiffnesses; C_{33} is the axial stiffness; C_{44} and C_{55} are the bending stiffnesses about the $\mathbf{e}_1$ and $\mathbf{e}_2$ axes; and C_{66} is the torsional stiffness. The strain energy for the isotropic clamped-free beam depicted in Fig. 7.9 is

$$\mathcal{U} = \frac{1}{2}\mathbf{\Delta}^T\mathbf{K}\mathbf{\Delta} \tag{7.20}$$

where $\mathbf{K} \in \mathbb{R}^{6\times6}$ is the stiffness matrix [219, Ch. 5]

$$\mathbf{K} = \begin{bmatrix} \frac{C_{11}}{\ell} & 0 & 0 & 0 & 0 & 0 \\ & \frac{12C_{22}C_{66}}{C_{22}\ell^3+12C_{66}\ell} & 0 & 0 & 0 & -\frac{6C_{22}C_{66}}{C_{22}\ell^2+12C_{66}} \\ & & \frac{12C_{33}C_{55}}{C_{33}\ell^3+12C_{55}\ell} & 0 & \frac{6C_{33}C_{55}}{C_{33}\ell^2+12C_{55}} & 0 \\ & & & \frac{C_{44}}{\ell} & 0 & 0 \\ & & & & \frac{4C_{55}\left(C_{33}\ell^2+3C_{55}\right)}{C_{33}\ell^3+12C_{55}\ell} & 0 \\ \text{sym} & & & & & \frac{4C_{66}\left(C_{22}\ell^2+3C_{66}\right)}{C_{22}\ell^3+12C_{66}\ell} \end{bmatrix} \tag{7.21}$$

that relates the free-end displacements and rotations to the corresponding free-end forces and moments. If the equivalent beam model is instead chosen to be anisotropic, an analogous expression for $\mathbf{K}$ can be derived by inverting the flexibility matrix that relates the free-end forces and moments to the corresponding free-end displacements and rotations. This flexibility matrix can be calculated in closed-form using Castigliano's Second Theorem [219, Ch. 3].

Solution Procedure

To calculate the six coefficients of the sectional stiffness matrix $\mathbf{C}$, the strain energies of both the FOM and the equivalent beam model [Eq. (7.20)] are evaluated for six independent prescribed displacements $\mathbf{\Delta}_i$ for $i = 1, \ldots, 6$. Here, the prescribed displacements are displacements and rotations proportional to the six standard unit basis vectors in $\mathbb{R}^6$. The sectional stiffness coefficients are then obtained from the solution to the nonlinear system of equations

$$\mathbf{y} = \mathbf{F}(\mathbf{c}) \tag{7.22}$$

where $\mathbf{c}^T = (C_{11}, C_{22}, C_{33}, C_{44}, C_{55}, C_{66})$ is the main diagonal of $\mathbf{C}$ and

$$\mathbf{y}^T = \begin{bmatrix} \mathcal{U}_1^{(\mathrm{FE})} & \ldots & \mathcal{U}_6^{(\mathrm{FE})} \end{bmatrix}, \tag{7.23}$$

$$\mathbf{F}^T(\mathbf{c}) = \begin{bmatrix} \mathcal{U}_1^{(\mathrm{eq})} & \ldots & \mathcal{U}_6^{(\mathrm{eq})} \end{bmatrix}. \tag{7.24}$$

In Eqs. (7.23) and (7.24), the superscripts FE and eq denote the full-order finite element and equivalent beam models, respectively. For the given independent prescribed displacements, Eq. (7.22) can be solved in closed-form.

For an anisotropic beam, i.e., when $\mathbf{C}$ is non-diagonal, additional prescribed displacements are required. These can be obtained from linear combinations of any two of the six original prescribed displacements.

Results

Figure 7.11 plots the homogenized sectional stiffness coefficients from Eq. (7.22) for strips with integer lengths between 1 m and 50 m. Based on Fig. 7.11, the axial stiffness (C_{33}) and bending stiffnesses (C_{44} and C_{55}) are constant with length. C_{33} and C_{44} in particular are almost exactly equal to twice the corresponding stiffnesses of a single TRAC longeron. The shear stiffnesses (C_{11} and C_{22}) and torsional stiffness (C_{66}), on the other hand, exhibit length-dependencies due to shear-warping. The boundary conditions in the FOM restrain warping, leading to shear boundary layers in the vicinities of the ends of the strips. C_{11}, C_{22}, and C_{66} are therefore effective sectional stiffness terms that include contributions from shear warping.

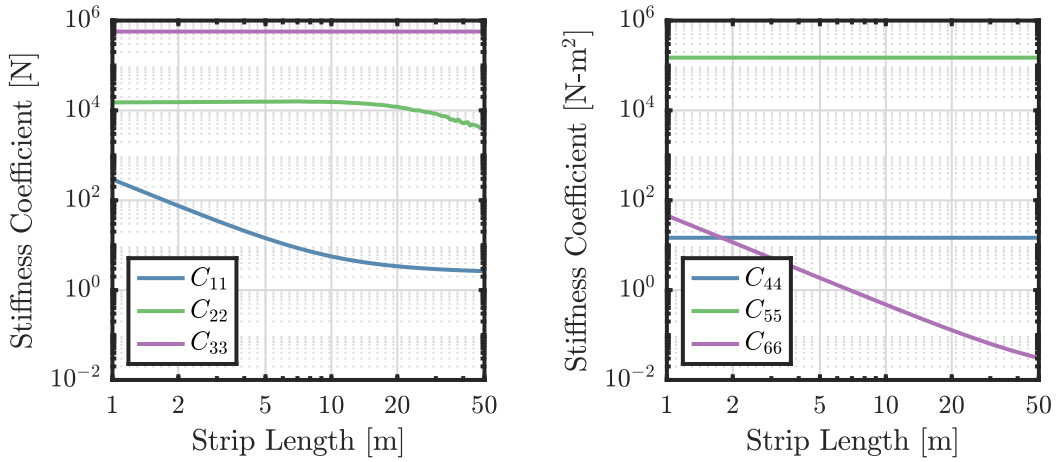

Figure 7.11: Sectional stiffness coefficients for (a) shearing (C_{11} and C_{22}) and axial (C_{33}) DOFs and (b) bending (C_{44} and C_{55}) and torsional (C_{66}) DOFs.

7.4 Flexible Multibody Dynamics Model

The flexible multibody dynamics finite element model of the Caltech SSPP-like spacecraft is implemented in MATLAB® using the equivalent beam models from Sec. 7.3 to define the sectional inertia and stiffness properties of the strips. A uniform areal density is then added to the strips to account for the mass of the tiles. The booms and strips are meshed using the geometrically exact beam finite elements from Chapter 5. The translational and rotational inertia forces are respectively integrated using full integration and 5-point Gaussian quadrature. To alleviate shear locking (see Sec. 5.4.1), the sectional shear stiffnesses are modified using MacNeal's residual bending flexibility correction [184] and the elastic forces are evaluated with 1-point reduced integration. Boom-strip interfaces are modeled using revolute joints

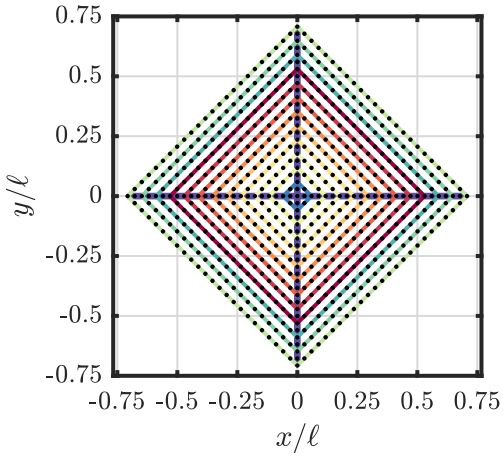

Figure 7.12: Representative finite element mesh of an SSPP-like spacecraft with 24 m-long outermost strips and 12 strips per quadrant. Black dots denote finite element nodes. Different colors denote strips of different lengths with different stiffness properties.

with rotation axes parallel to the booms. Mathematically, the flexible multibody dynamics model is a system of nonlinear differential algebraic equations (DAEs) with holonomic constraints [68, 70].

This chapter only considers spacecraft with integer-length outermost strips. If the length ℓ_n of the outermost strip is even, there are $n = \ell_n/2$ strips per quadrant and no spaces between adjacent strips. However, if ℓ_n is odd, there are $n = (\ell_n - 1)/2$ strips per quadrant which leads to spaces between adjacent strips.

Two parameters define the mesh density in the model: (i) the minimum number of elements per boom n_b and (ii) the number of elements per outermost strip n_s. Elements are added to the booms as needed to place nodes at the locations of the boom-strip interfaces. As a result, booms are typically meshed with more than n_b elements. Interior strips are meshed with elements of approximately the same length as those of the outermost strips. Strips are always meshed using an even number of elements to place a node at their midpoints. A representative mesh for a 24 m$\times$24 m spacecraft with $n = 12$ strips per quadrant and $n_s = n_b = 24$ is depicted in Fig. 7.12.

With 1-point reduced integration, the internal forces and moments in each element are constant. This leads to internal force and moment discontinuities between elements. Mesh convergence requires a reasonably smooth variation in the internal force and moment distributions across the structure. To quantify the required mesh density, a mesh convergence study calculated the natural frequencies of the first 50 modes of a linearized model of the structure as a function of the seed size

$s = n_b = n_s$ and the length ℓ_n. The natural frequencies are a proxy for strain energy, which itself is a cumulative measure of the internal forces and moments in the structure. Convergence occurs when increasing the mesh size negligibly changes the strain energy. The results of this analysis indicated that convergence occurs with maximum element lengths on the order of 1 m, irrespective of the size of the structure. Hence, in subsequent analyses it was assumed that $n_b = n_s = \ell_n$.

7.5 Boom Design

Unlike the strips, there is no generally agreed upon design for the booms. For mass-efficiency, the booms must not be overly stiff, i.e., they must be sized for the expected loads. The inertial loads induced by slew maneuvers increase as spacecraft size increases, leading to a general requirement for stiffer booms on larger spacecraft. The optimal boom size depends on the loading, spacecraft size, structural limits, and deflection limits [24], i.e., the proportion of the maximum deflection carried by the booms and strips. With this in mind, this section uses linear static finite element analyses to estimate boom and strip deflections during a representative slew maneuver as a function of boom radius and spacecraft size. The imposition of deflection limits then results in relationships that scale the size of representative "stiff" and "soft" booms with spacecraft size. Since the emphasis in this chapter is on developing insights into the dynamic behavior of SSPP-like spacecraft, this analysis does not account for structural limits on either the booms (e.g., due to Euler or shell buckling [24]) or the strips (e.g., due to localization and folding [24, 217]); for additional details on possible failure modes, see [24].

As discussed in Sec. 7.2, the booms are hollow, thin-walled cylindrical tubes of radius R and thickness t with isotropic material properties (elastic modulus E_B = 70 GPa, Poisson's ratio $\nu_B = 0.3$, shear modulus $G_B = E_B/(2(1+\nu_B))$, and density $\rho_B = 1610$ kg/m^3). To constrain the design space, the thickness-to-radius ratio t/R is set to 0.03. This represents a reasonable lower limit for manufacturable booms. Additionally, the analysis uses a single-axis slew maneuver, in this case, the 7th order polynomial slew maneuver from Chapter 3 (Fig. 3.8), and a slew angle of 90 deg to define the peak inertial loading (angular acceleration) as a function of slew time. However, the choice of the slew maneuver profile here is arbitrary; different slew maneuvers simply result in different slew times for a given peak angular acceleration. A 90 deg, single-axis slew maneuver is representative of the expected pitch axis maneuvers for a Caltech SSPP space solar power satellite [39, 40].

7.5.1 Inertial Loads due to Slew Maneuvers

In general, slew maneuvers induce inertial loads on a structure due to centripetal acceleration, Euler acceleration, and Coriolis acceleration. Coriolis acceleration is velocity-dependent, i.e., zero for a static analysis. For a plate-like spacecraft, the centripetal and Euler accelerations induce in-plane and out-of-plane (normal) "pressure" loads, respectively. Since the deflections due to the in-plane inertial pressure are expected to be negligible for the SSPP-like spacecraft, the normal pressure is the design load case.

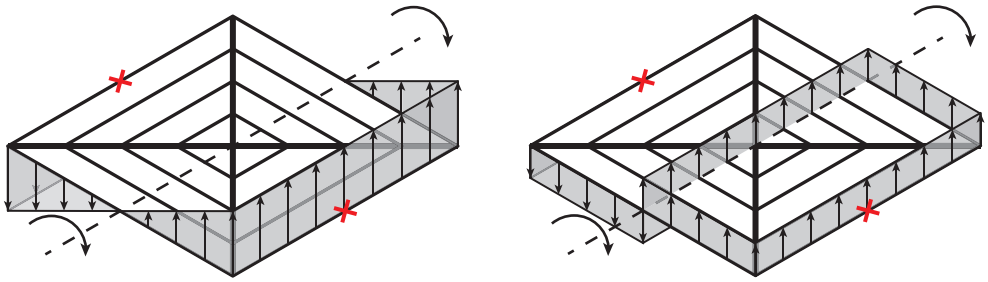

(a) (b)

Figure 7.13: (a) normal and (b) average normal pressures exerted by inertial loads during a single-axis slew maneuver. The normal pressure varies linearly from the rotation axis. The dashed line and curved arrows denote the rotation axis and direction of the angular acceleration.

Figure 7.13a depicts the normal pressure

$$P_{\perp} = \rho_A \ddot{\theta}_{\max} d \tag{7.25}$$

exerted by the Euler acceleration on a square plate-like spacecraft during a single-axis slew maneuver. Here, ρ_A is the areal density, $\ddot{\theta}_{\max}$ is the maximum angular acceleration, and d is the perpendicular distance from the rotation axis (d changes sign at the rotation axis). The magnitude of $P_{\perp}$ increases linearly from the rotation axis. For an SSPP-like spacecraft, this implies that the peak bending deflections occur at the midpoints of the outermost strips (denoted by a red $\times$ in Fig. 7.13). Due to symmetry, these deflections have equal magnitudes and opposite directions on opposite sides of the spacecraft. There is zero deflection along the rotation axis.

To develop some intuition into the magnitude of the slew maneuver loads, Fig. 7.14 plots the average normal pressure on a square plate-like spacecraft with an areal density of 100 g/m^2 as functions of length and slew time. The average normal

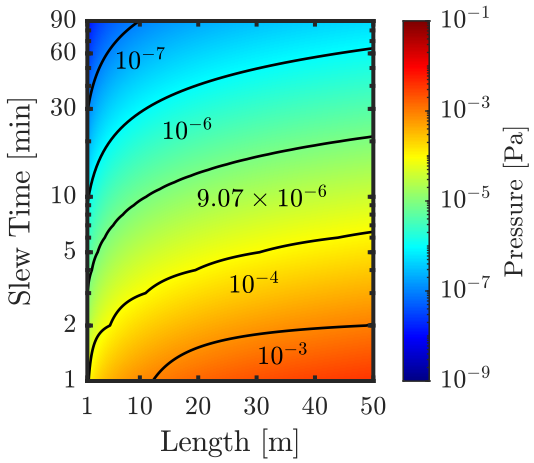

Figure 7.14: Average normal pressure exerted by inertial loads during a single-axis slew maneuver as a function of length and slew time. The black lines are lines of constant pressure. Assumes an areal density of 100 g/m^2.

pressure is depicted in Fig. 7.13b and given by

$$P_{\perp,\text{avg}} = \frac{1}{4}\rho_A \ddot{\theta}_{\max} L \tag{7.26}$$

where L is the side length and $A = L^2$ is the total area. The average normal pressure is the average value of Eq. (7.25) over the area of the plate to one side side of the rotation axis. The peak normal pressure is twice the average normal pressure.

In Fig. 7.14, the black lines are isobars, i.e., lines of constant normal pressure. 9.07×10^{-6} Pa is the magnitude of the SRP on a perfectly reflecting surface at 1 AU (1361 W/m^2 incident solar flux). This corresponds to the worst-case SRP load. For fast slew maneuvers (slew times less than approximately 10 min) and large length scales, the inertial loads dominate the SRP load. Outside of low Earth orbit, the SRP load is the dominant environmental load [13]. Thus, the inertial loads are the critical load case during fast slews and the design load case for the booms.

7.5.2 Analysis and Results

The boom design process uses linear static finite element analyses to evaluate the boom tip and strip midpoint deflections due to the slew maneuver load depicted in Fig. 7.13a as a function of boom radii between 3.33 mm and 100 mm. The minimum boom radius corresponds to a minimum wall thickness of 0.1 mm. The resulting deflection versus radii curves lead to boom designs that meet deflection specifications. For a linear analysis, the fractions of the deflections due to the contributions of the booms and strips are independent of the magnitude of the load.

Thus, the boom design that meets a given deflection specification is also independent of the magnitude of the load.

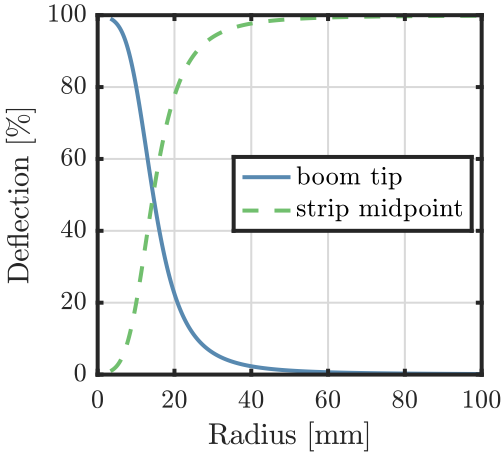

Figure 7.15: Percentage of maximum deflection carried by booms and outermost strips as a function of boom radius for a 24 m × 24 m SSPP-like spacecraft with an areal density of 100 g/m^2.

Figure 7.15 plots a representative deflection versus radii curve for a 24 m × 24 m spacecraft with an areal density of 100 g/m^2. In the figure, the solid blue and dashed green lines respectively denote the percentages of the maximum deflection at the boom tips and the midpoints of the outermost strips. The latter are the locations of the maximum deflections on the structure. Due to symmetry, all four booms have the same deflections. Likewise, strips on opposite sides of the structure have deflections equal in magnitude but opposite in direction. Since the boom stiffness increases as radius increases, the contribution of the outermost strip to the maximum deflection also increases as the radius increases. The strip midpoint deflections are calculated relative to the boom tips; hence, the total deflection for each radius equals 100%.

The deflection versus radii curves in Fig. 7.15 provide a methodology for design. For example, if the booms are to be designed such that both the booms and strips are responsible for 50% of the maximum deflection, then Fig. 7.15 shows that the correct boom radius is 14.46 mm. Two reference boom designs are used for subsequent analyses: "stiff" booms responsible for 10% of the maximum deflection, and "soft" booms responsible for 40%. From Fig. 7.15, the corresponding boom radii are 25.85 mm and 16.07 mm. This analysis is then repeated for spacecraft with dimensions between 5 m and 50 m and strip areal densities of 100 g/m^2 and 1 kg/m^2. Figures 7.16, 7.17, and 7.18 respectively plot the resulting boom radii, linear mass densities, and bending stiffnesses as a function of spacecraft size.

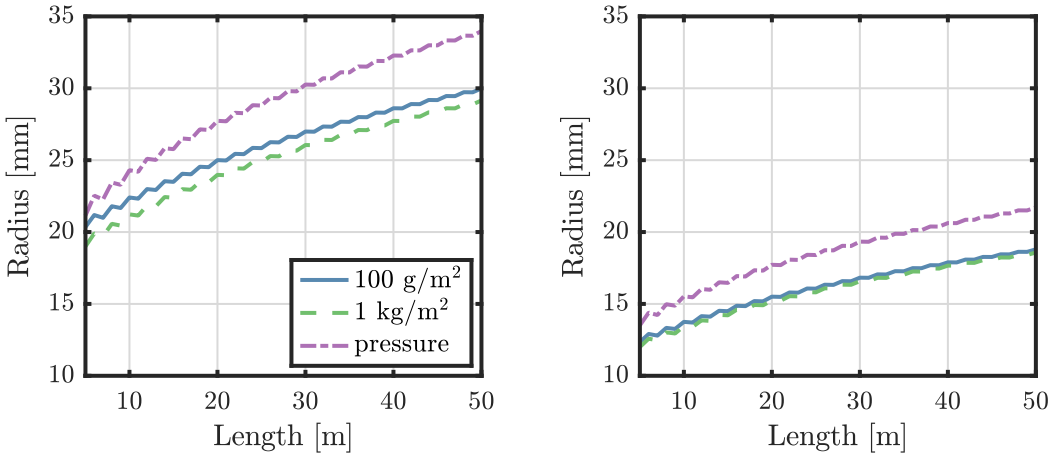

Figure 7.16: Radii for (a) stiff and (b) soft booms.

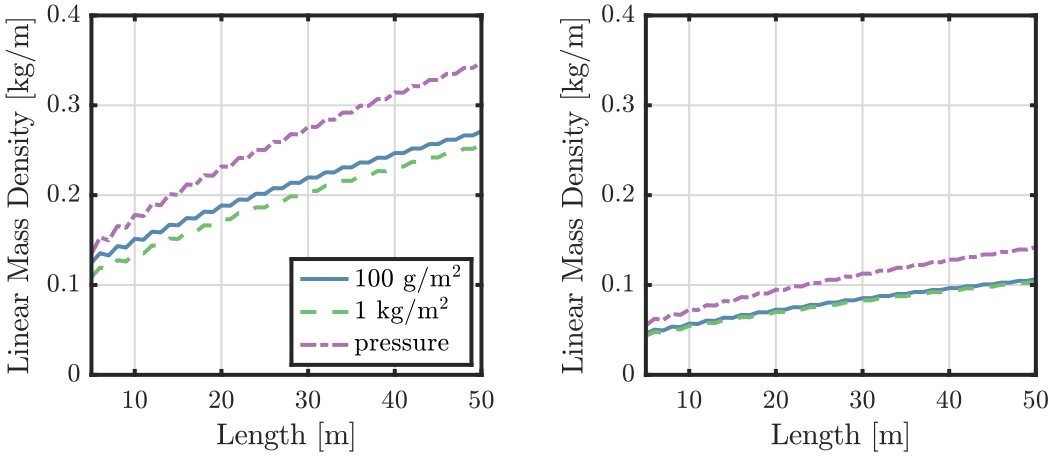

Figure 7.17: Linear mass densities for (a) stiff and (b) soft booms.

Each boom design is compared to a boom designed to meet the same deflection specifications under a uniform pressure loading. In every case, the uniform pressure load results in stiffer, more massive booms. The calculated boom radii, linear mass densities, and bending stiffnesses are comparable to those from other large flexible spacecraft concepts; see e.g., [248, 249]. Note that the "scalloping" in the figures is an artifact of the modeling assumptions. Specifically, with 1 m-wide strips, a spacecraft with odd integer side lengths has large gaps between strips. This has the effect of decreasing the spacecraft's average areal density, which in turn decreases the slew maneuver loads on the structure.

The boom design procedure does not mention the magnitude of the slew maneuver

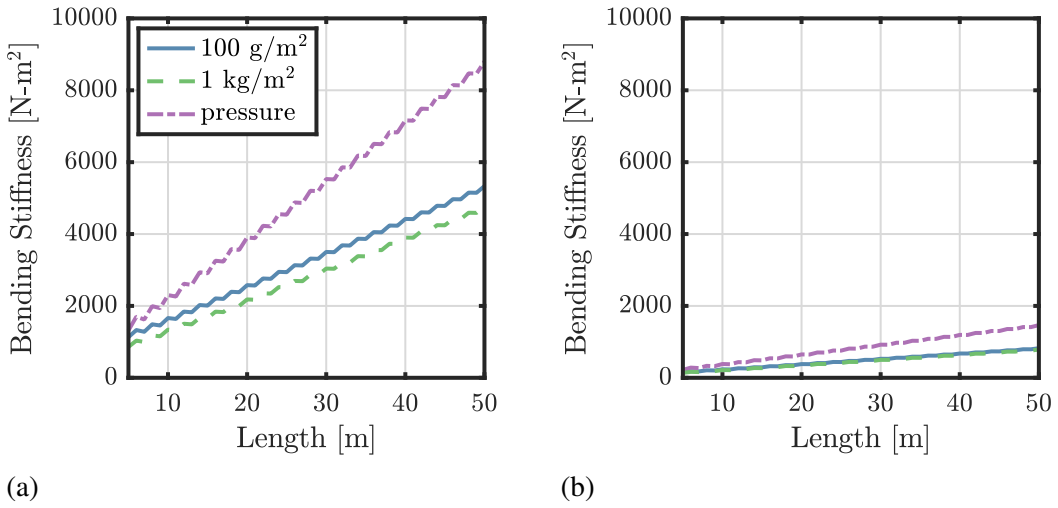

Figure 7.18: Bending stiffnesses for (a) stiff and (b) soft booms with thin-walled circular cross-sections.

deflections. To remedy this, Figs. 7.19 and 7.20 plot the boom tip and strip midpoint deflections as a function of spacecraft size and slew time for areal densities of 100 g/m^2 and 1 kg/m^2. In each figure, the boom tip and strip midpoint deflections are normalized by the appropriate boom and strip lengths. Deflections greater than 10% are assumed to violate the linearity assumption, and hence, are discarded. The figures highlight the rationale behind the design of the soft booms; in particular, the normalized deflections in the booms and strips are approximately equal, leading to mass-efficient boom designs. A comparison of Figs. 7.19 and 7.20 then illustrates the unsurprising result that increasing the areal density increases the inertial loads on the structure, and hence, the deflections. Thus, all else being equal, higher areal densities results in higher slew times.

In practice, the maximum dynamic deflections are a more useful performance metric than the maximum static ones. Therefore, it is useful to study the dynamic amplification of the static deflections from Figs. 7.19 and 7.20. The dynamic load factor (DLF) is the ratio between the maximum dynamic deflection and the static deflection corresponding to the maximum magnitude dynamic load [98, Ch. 2]. For preliminary analysis and design, the DLF can be evaluated from the response of a forced harmonic oscillator (Fig. 7.21) to the inertial loads induced by the slew maneuver. The resulting DLFs are plotted as a function of the ratio between the slew time T and natural period $T_n = 2\pi/\sqrt{k/m}$ in Fig. 7.22. In the absence of modal data, there are two important takeaways from Fig. 7.22: (i) the worst-case DLF is approximately 3.2, and (ii) when $T/T_n > 8$, the dynamic deflections are effectively

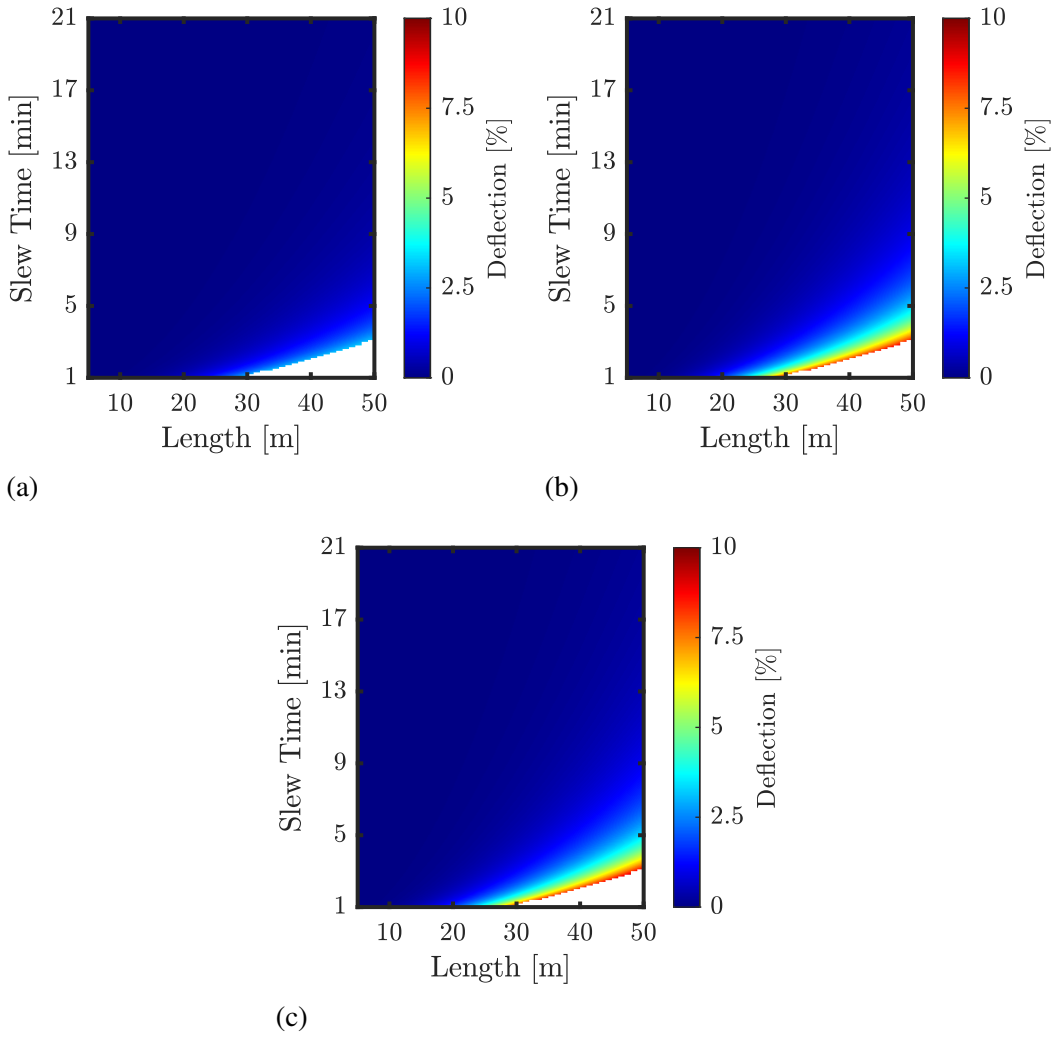

Figure 7.19: Static boom tip and strip midpoint deflections (relative to boom tip) due to maximum slew maneuver loads with a 100 g/m^2 areal density. (a) boom tip deflections with stiff booms. (b) boom tip deflections with soft booms. (c) strip midpoint deflections. Strip midpoint are independent of boom stiffness.

the same as the static ones. Slew times for flexible spacecraft are typically ten or more times longer than their first-mode periods, i.e., $T/T_n > 10$. Hence, assuming the linearity assumption is valid, Figs. 7.19 and 7.20 are likely reasonable estimates of the dynamic deflections during slew maneuvers.

7.6 Parametric Modal Analysis

A parametric modal analysis investigates how boom stiffness and strip areal density affect the dynamic properties of the SSPP-like spacecraft at different length scales.

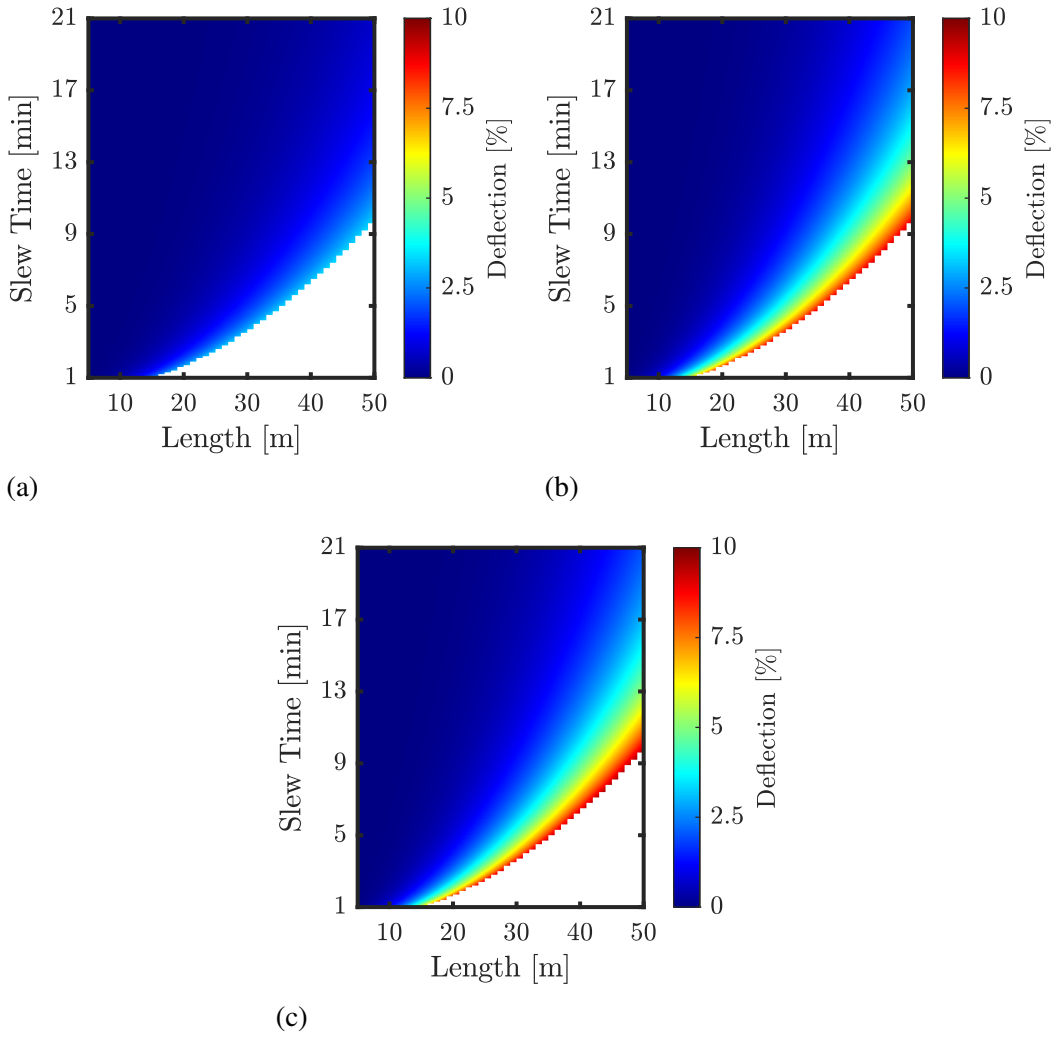

Figure 7.20: Static boom tip and strip midpoint deflections (relative to boom tip) due to maximum slew maneuver loads with a 1 kg/m^2 areal density. (a) boom tip deflections with stiff booms. (b) boom tip deflections with soft booms. (c) strip midpoint deflections. Strip deflections are independent of boom stiffness.

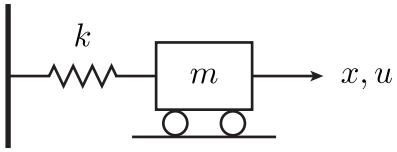

Figure 7.21: Harmonic oscillator with mass m, stiffness k, and external force u.

7.6.1 Preliminaries

A standard modal analysis requires a linear structural model, not the system of nonlinear DAEs describing the flexible multibody dynamics model of the SSPP-like

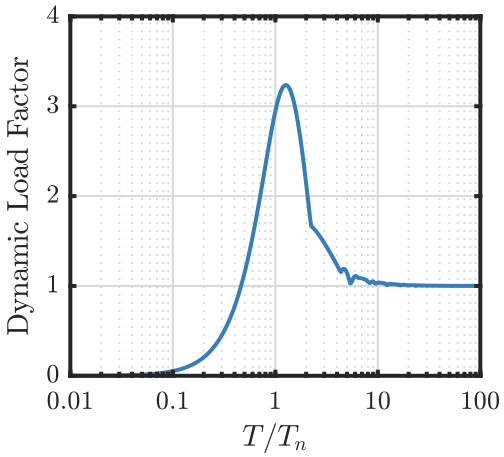

Figure 7.22: Dynamic load factor as a function of the ratio between the slew time T and natural period T_n for the polynomial slew maneuver from Fig. 3.8.

spacecraft. DAEs are not directly amenable to modal analysis [250–253] and hence, require a conversion to a more suitable form. For a nonlinear flexible multibody dynamics model with holonomic constraints, this involves some combination of linearization and either constraint elimination [250, 253] or augmentation [252] (sometimes followed by elimination [251]). The preferred approach here is linearization followed by constraint elimination using a null space projection, i.e., a Galerkin projection of the equations of motion onto the null space of the constraint gradient matrix. This results in linearized mass and stiffness matrices of reduced dimensions (due to the elimination of the redundant DOFs associated with the constraints via the null space projection) that are compatible with any standard modal analysis procedure. The dimension of the reduced mass and stiffness matrices are equal to the number of independent DOFs in the original flexible multibody dynamics model.

The null space of the constraint gradient matrix is generally not unique. Thus, the independent DOFs associated with the reduced mass and stiffness matrices do not necessarily correspond directly to the independent physical DOFs in the flexible multibody dynamics model. Instead, they are linear combinations of the independent physical DOFs. As a result, an additional linear transformation is often required to map these DOFs to the independent physical DOFs. This is necessary, for example, to apply boundary conditions to the reduced model, as is done in the Craig-Bampton method (see Sec. 3.3.1).

Ordinarily, the reduced mass and stiffness matrices can be directly input into any standard generalized eigensolver [78] to obtain the natural frequencies and vibra-

tion modes of the structure. The Caltech SSPP structure, however, features 4-fold symmetry, and hence, symmetric modes with repeated eigenvalues, i.e., natural frequencies with multiplicities greater than one. This introduces numerical challenges for standard eigensolvers. Specifically, due to the limits of machine precision and the accumulation of round-off errors, it is often difficult to distinguish between closely spaced eigenvalues and repeated eigenvalues (although as discussed in Sec. 3.3.2, modal participation can often be used to categorize closely spaced eigenvalues). Eigenvalue errors correspond to errors in the calculated eigenmodes and vice versa. These errors are generally exacerbated by eigensolvers that convert the generalized eigenproblem to standard form, e.g., using the inverse of the Cholesky decomposition. Evaluating the inverse amplifies small numerical errors and can lead to significantly degraded solution accuracy [254, Ch. 10]. As a result, even if the modes can be correctly categorized into symmetric modes with repeated eigenvalues and otherwise, the calculated eigenmodes are not necessarily accurate.

The difficulties associated with eigenanalyses of symmetric structures motivate the use of a two-step eigensolution scheme. In the first step, a standard generalized eigensolver (in this case, the EIGS function in MATLAB®) calculates the eigenmodes corresponding to a perturbed mass matrix and an unperturbed stiffness matrix. The number of calculated eigenmodes depends on the number of desired eigenmodes at the end of the second step. Specifically, to calculate the first p eigenmodes, the first step must at least calculate the first $q = \max\{2p, p + 8\}$ perturbed eigenmodes [255]. There are two requirements on the mass matrix perturbation: (i) it must preserve the mass matrix's symmetric positive-definiteness, and (ii) it must break the structure's (in this case, 4-fold) symmetry. Here, the mass matrix is perturbed by adding a small fraction of the translational entries on the main diagonal to themselves (before the null space projection). The small fraction is a uniformly distributed random number in the interval from 0 to 0.01. The second step then uses the perturbed eigenmodes from the first step to initialize the subspace iteration algorithm [78] with the unperturbed mass and stiffness matrices. Each subspace iteration requires the solution of a low-dimensional generalized eigenproblem, which in this case is solved using the generalized Jacobi method [78]. In essence, the subspace iteration algorithm corrects the perturbed eigenmodes to obtain accurate eigenvalues and eigenmodes for the symmetric structure.

7.6.2 Results

The parametric modal analysis evaluates the first 100 modes of the SSPP-like spacecraft at integer length scales between 5 m and 50 m using the "stiff" and "soft" booms from Fig. 7.16. The stiff (resp. soft) booms are designed to contribute 10% (resp. 40%) of the maximum bending deflection during slew maneuvers. Moreover, the analysis considers two areal densities, 1 $\mathrm{kg/m^2}$ and 100 $\mathrm{g/m^2}$, which are representative of current and future states-of-the-art for strips with integrated power collection and transmission systems for space solar power.

The modal analysis calculates the structure's fixed-interface modes, i.e., the modes corresponding to a fully restrained node at the central hub. Dominant modes are then identified by sorting the modes in descending order according to their modal participation factors [Eq. (3.39)]. The dominant mode provides the highest average dynamic reaction forces and moments on the central bus.

Figure 7.23 plots the natural frequencies of the first 100 modes for the SSPP-like spacecraft at length scales of $\ell = 10$ m, $\ell = 24$ m, and $\ell = 50$ m. The figure illustrates two expected results, namely that natural frequencies decrease as both size and areal density increase. Due to the structure's 4-fold symmetry, it features many very closely spaced or repeated eigenvalues; these correspond to line segments that appear horizontal or nearly so. A comparison of either Figs. 7.23a and 7.23c or Figs. 7.23b and 7.23d then demonstrates that the boom stiffness has a very small effect on the computed natural frequencies. However, the boom stiffness turns out to have a significant effect on modal participation. This is explored more in what follows. Despite the large number of low-frequency modes, a small number of modes (typically less than 10) contain the overwhelmingly majority of the modal participation [Eq. (3.39)]; see Fig. 7.24. For this reason, the remainder of this section focuses on only the lowest frequency and most dominant modes.

Figure 7.25 depicts the natural frequencies for the first (lowest frequency) mode and most dominant mode as a function of the spacecraft's size, boom stiffness, and areal density. For completeness, Fig. 7.26 then plots the corresponding natural periods. At the most relevant length scales (20 m plus), the first-mode periods are typically on the order of 1 to 10 min. In both figures, the first mode and dominant mode are compared to the first bending mode of a pinned-pinned beam with the same bending stiffness as the outermost strip. With stiff booms, the first pinned-pinned beam mode is an excellent approximation for the first natural frequency, but the accuracy of this approximation deteriorates as the boom stiffness decreases.

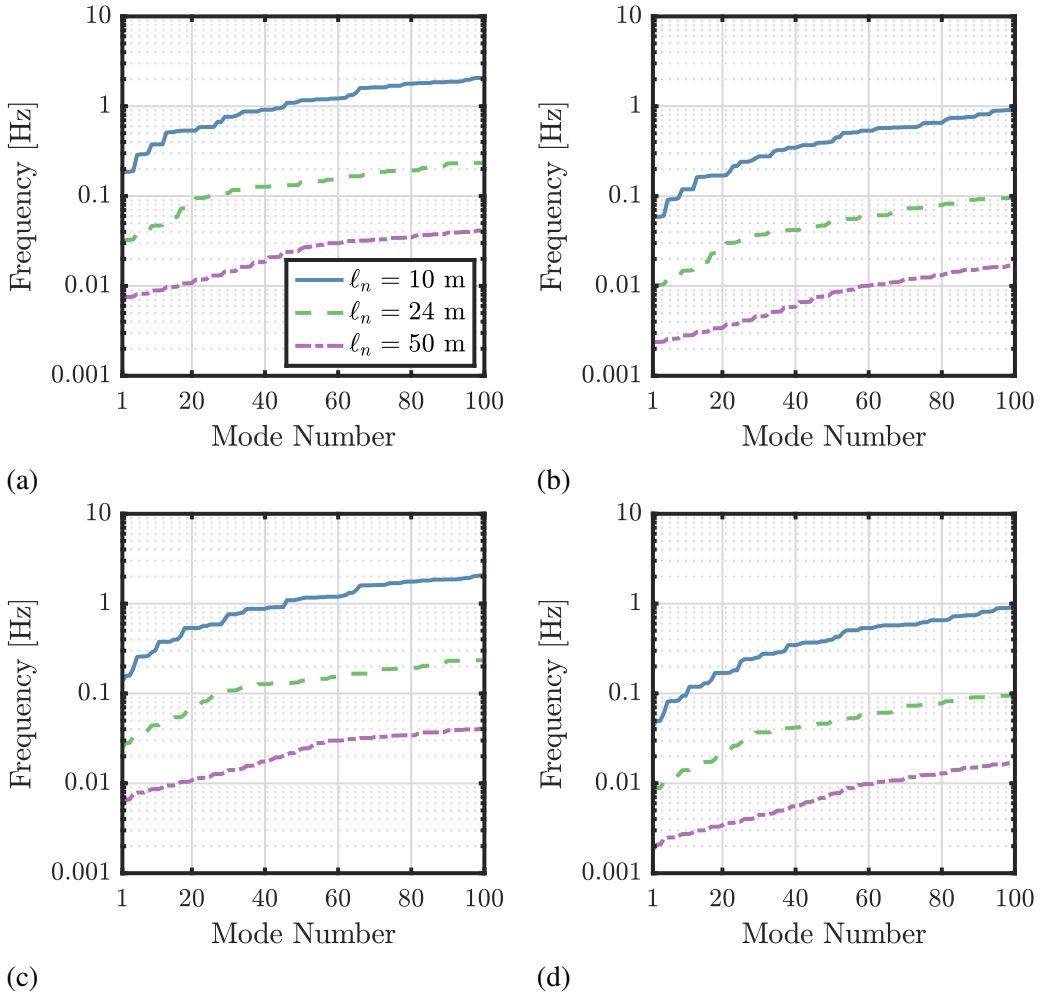

Figure 7.23: Comparisons of 1st 100 natural frequencies at various length scales with (a) 100 g/m^2 areal density, stiff booms; (b) 1 kg/m^2 areal density, stiff booms; (c) 100 g/m^2 areal density, soft booms; and (d) 1 kg/m^2 areal density, soft booms.

To gain some intuition into why the first mode of a pinned-pinned beam accurately approximates the spacecraft's first natural frequency, Fig. 7.27 depicts the first modes for representative 24 m $\times$ 24 m spacecraft with both stiff (Fig. 7.27a) and soft (Fig. 7.27b) booms. Qualitatively, the first mode shows little sensitivity to the areal density. Hence, Fig. 7.27 only depicts modes for spacecraft with areal densities of 100 g/m^2. The first mode primarily consists of strip bending. With stiff booms, the vibrations of the outermost strips are decoupled from the vibrations of the booms and interior strips. Softer booms introduce more coupling between the booms and strips which decreases the accuracy of the pinned-pinned beam approximation and increases the effective modal mass in the first mode.

Whereas the first mode is characterized by bending vibrations of the outermost

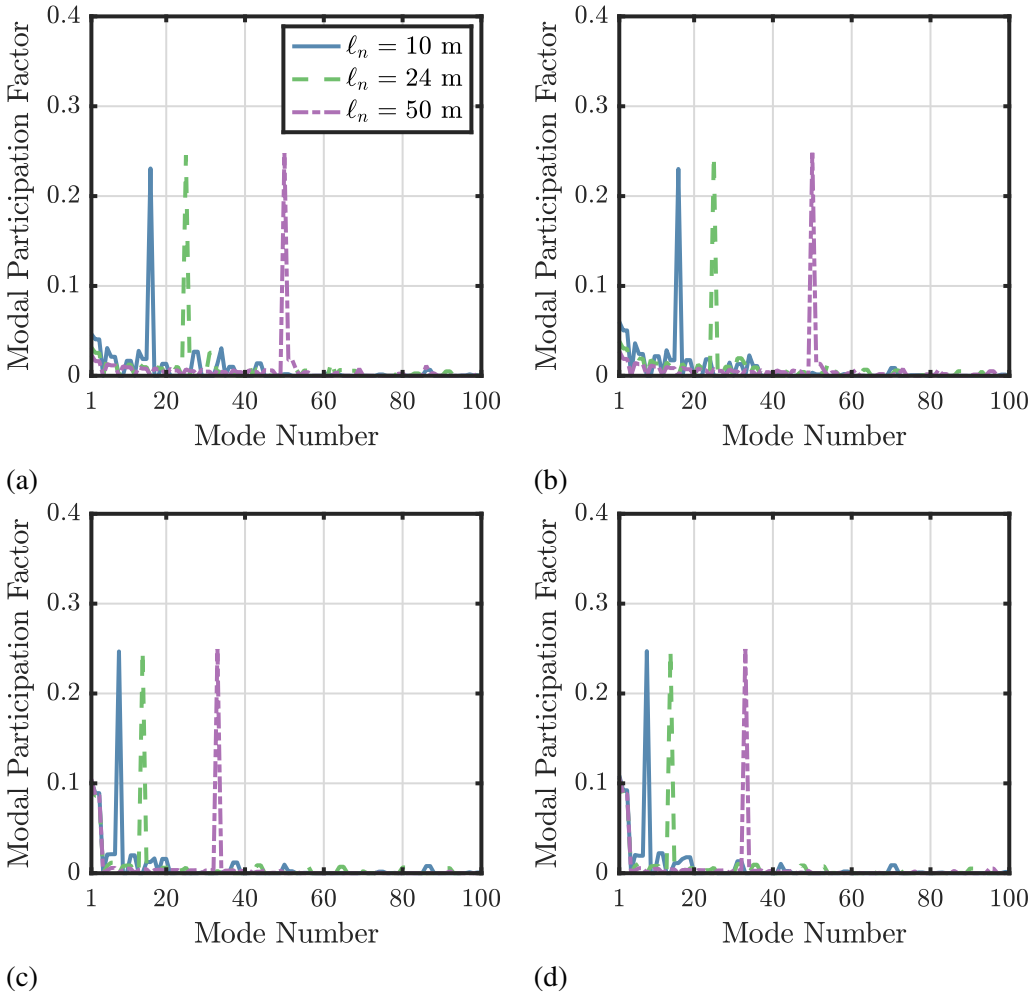

Figure 7.24: Comparisons of modal participation factors [Eq. (3.39)] for 1st 100 modes at various length scales with (a) 100 g/m^2 areal density, stiff booms; (b) 1 kg/m^2 areal density, stiff booms; (c) 100 g/m^2 areal density, soft booms; and (d) 1 kg/m^2 areal density, soft booms.

strips, the dominant mode is characterized by in-plane boom bending; see Fig. 7.28. In-plane boom bending leads to the excitation of every strip in the structure and a correspondingly high modal participation. This type of mode is normally referred to as a "pinwheel" mode, and like the lowest frequency mode, it is qualitatively insensitive to the areal density. Hence, it is sufficient to only consider modes corresponding to a single areal density in Fig. 7.28. Unlike the first mode, though, the dominant mode exhibits the same behavior irrespective of the boom stiffness. The mode number of the first pinwheel mode depends on the boom stiffness and the spacecraft size. At small length scales, the pinwheel mode appears in the interval from modes 5 to 10, but at larger scales, it may be past mode 30.

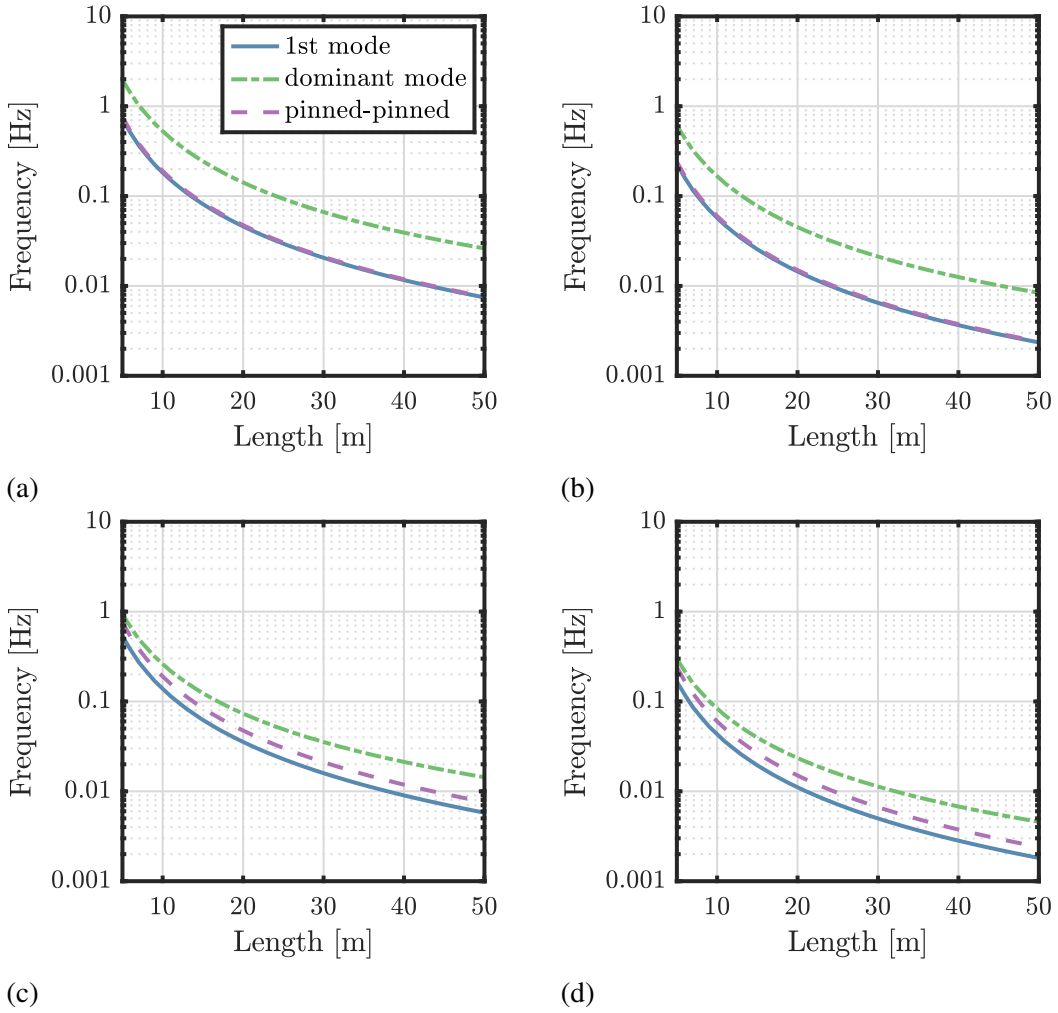

Figure 7.25: Comparisons of 1st mode, dominant mode, and 1st pinned-pinned beam mode frequencies with (a) 100 g/m^2 areal density, stiff booms; (b) 1 kg/m^2 areal density, stiff booms; (c) 100 g/m^2 areal density, soft booms; and (d) 1 kg/m^2 areal density, soft booms.

Altogether, these results highlight an important design trade-off. In particular, while softer booms are lighter, and hence, more mass efficient (see Fig. 7.17), they also more tightly couple the dynamics of the booms and strips. This has significant ramifications for spacecraft design and dynamics. For example, softer booms lead to higher effective modal mass in the lowest frequency modes, which in turn leads to larger reaction forces and moments on the spacecraft bus. Softer booms likewise lead to less precise structures and may locally increase the stresses on any functional elements integrated into the strips. For these reasons, more fully understanding how the boom stiffness influences the spacecraft's design and dynamics is an important area for future research.

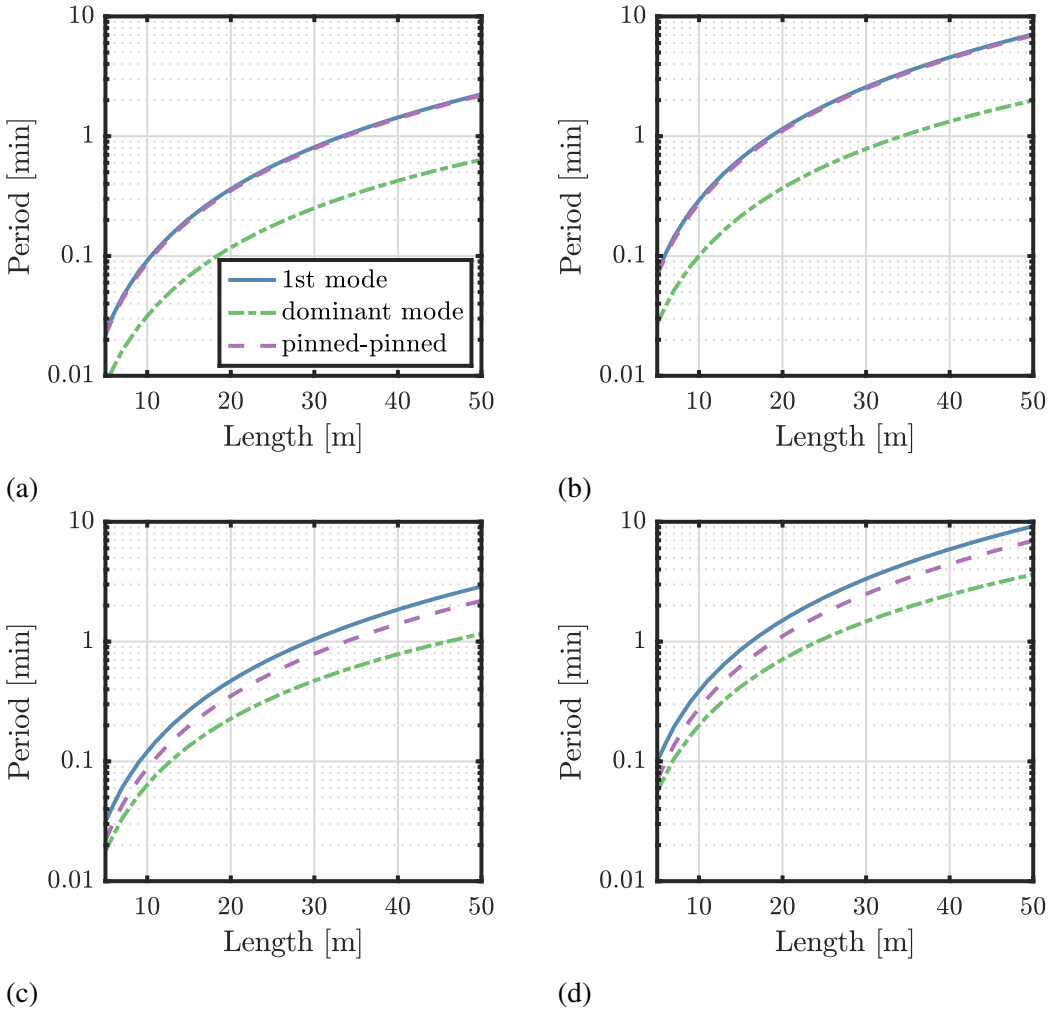

Figure 7.26: Comparisons of 1st mode, dominant mode, and 1st pinned-pinned beam mode periods with (a) 100 g/m^2 areal density, stiff booms; (b) 1 kg/m^2 areal density, stiff booms; (c) 100 g/m^2 areal density, soft booms; and (d) 1 kg/m^2 areal density, soft booms.

7.7 Discussion

This chapter has described the development and implementation of a parametric flexible multibody dynamics finite element model for an SSPP-like ultralight flexible spacecraft. The numerical model eliminates the cords that attach the strips to the booms in the baseline Caltech SSPP structural architecture [13]. Instead, revolute joints were used connect the strips to the booms. The implicit assumption here is that the cords are not significant contributors to the spacecraft's macroscale structural dynamics. Relaxing this assumption is left to future work.

The flexible multibody dynamics model discretizes both the booms and strips in the Caltech SSPP architecture with geometrically exact beam finite elements. This

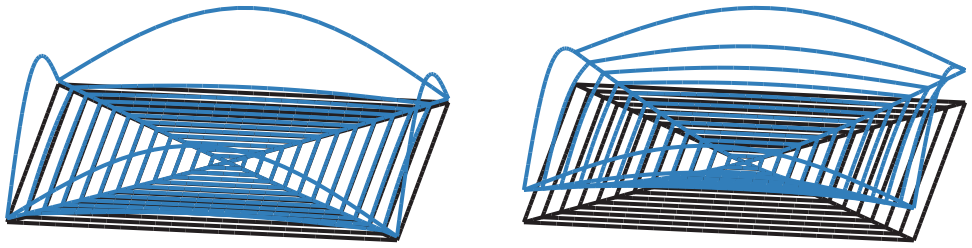

(a) (b)

Figure 7.27: 1st modes for a 24 m $\times$ 24 m SSPP-like spacecraft with an areal density of 100 g/m^2 and (a) stiff booms and (b) soft booms.

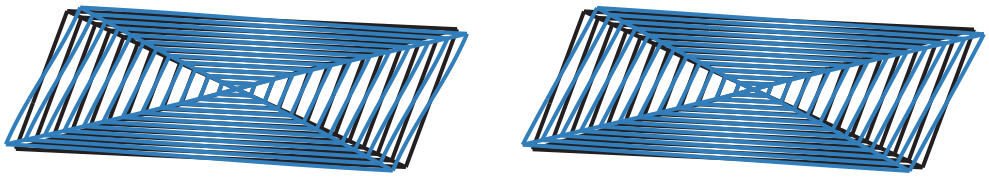

(a) (b)

Figure 7.28: Dominant modes for a 24 m $\times$ 24 m SSPP-like spacecraft with an areal density of 100 g/m^2 and (a) stiff booms (mode 25) and (b) soft booms (mode 14). For clarity, each figure only depicts the in-plane modal deformations.

requires equivalent beam models for the thin-shell strips. These equivalent beam models take the form of sectional inertia and stiffness matrices derived using energy-equivalence-based approaches. The equivalent sectional inertia matrices accurately model each strip's inertia properties. The equivalent sectional stiffness properties are more difficult to validate. The sectional axial and bending stiffnesses are in excellent agreement with estimates from standard beam theory, and accordingly, are effectively independent of the length of the strip. The sectional shear and torsional stiffnesses, however, show significant variations with length. These variations are due to shear warping effects introduced by the rigidly constrained end cross-sections in the high-fidelity finite element model. The equivalent beam models are inherently limited to the regime where the internal bending moments do not exceed the corresponding strip's critical bending moment that marks the onset of localization and buckling. As a result, quantifying the maximum internal bending moments

during slew maneuvers is an important objective of the dynamic analyses in Chapter 8. These maximum internal bending moments impose a structural limit on the minimum feasible slew time.

For a given slew maneuver, the dynamic loads increase as spacecraft size increases. As a result, larger SSPP-like spacecraft require stiffer booms. Linear static analyses calculated the deflection of the booms and outermost strips as a function of boom radius and spacecraft size under a worst-case slew maneuver load. The subsequent modal analysis studied the dynamic characteristics of the spacecraft as a function of its size and areal density with two boom designs: a "stiff" boom designed to contribute 10% of the maximum deflection, and a more mass-efficient "soft" boom designed to contribute 40%. The modal analysis shows that a small number of modes, typically less than 10, are responsible for the majority of the modal participation, i.e., they dominate the dynamic reaction forces and moments on the bus. The modal analysis also emphasizes that the boom stiffness determines the spacecraft's dynamic characteristics. In particular, as the boom stiffness decreases, the vibrations of the booms and strips become more tightly coupled, which in turn increases the effective modal mass in the lowest frequency modes.

Chapter 8

SLEW MANEUVER DYNAMICS

8.1 Introduction

This final chapter studies the slew maneuver dynamics of ultralight flexible spacecraft. Its goals are threefold: (i) to predict slew times using the reduced-order modal models and the slew performance metric proposed in Chapter 3; (ii) to demonstrate the use of geometrically nonlinear finite element models for simulating flexible spacecraft attitude dynamics during slew maneuvers; and (iii) to compare a more traditional structural dynamics integrator with the variational integrator from Chapter 6 for simulating flexible spacecraft slew maneuvers.

Slew time predictions are important for establishing the feasibility of slewing ultralight flexible spacecraft during the early stages of space mission design. Verification and validation then require higher-fidelity analysis tools, like geometrically nonlinear finite element simulations. Even though there are examples of these types of simulations in the open literature (see e.g., [256, 257]), these tools are by no means standard for simulating flexible spacecraft dynamics. As a result, the geometrically nonlinear finite element simulations in this chapter are both useful for developing insights into the slew maneuver dynamics of ultralight flexible spacecraft and as a proof-of-concept for promoting their more widespread adoption in spacecraft engineering practice.

Due to the long durations involved in simulating flexible spacecraft slew maneuvers, there is a question about the accuracy and stability of traditional time integrators. Traditional time integrators, like the generalized-α method [25], often use numerical dissipation to improve their stability, something which can potentially introduce non-physical behaviors into simulations. Variational integrators are a type of symplectic-momentum conserving integrator which usually exhibit excellent long-duration energy behavior [28, 29] and achieve stability without numerical dissipation. For these reasons, they may be advantageous for simulating slew maneuver dynamics. To that end, this chapter compares the variational integrator from Chapter 6 with a Lie group implementation of the generalized-α method [36–38] in order to assess the efficacy of using variational integrators for slew maneuver simulations.

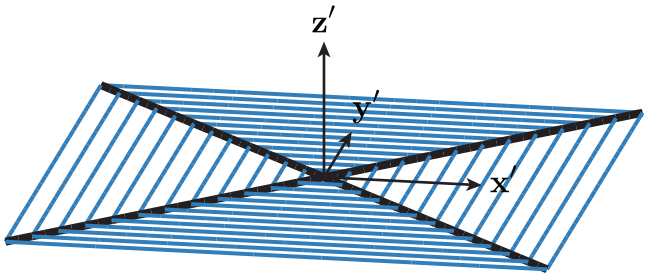

Figure 8.1: Rotation axes for slew maneuver about $\mathbf{y}'$ axis. The $\{\mathbf{x}, \mathbf{y}, \mathbf{z}\}$ reference frame results from a 45 deg counterclockwise rotation about the $\mathbf{z} = \mathbf{z}'$ axis.

Like Chapter 7, this chapter studies a representative ultralight flexible spacecraft based on the Caltech Space Solar Power Project (SSPP) architecture [13] with integer length scales between 5 m and 50 m. However, much of the focus of this chapter is on a 24 m $\times$ 24 m spacecraft. Such a spacecraft has significant flexible dynamics, especially compared to smaller length scales (on the order of 10 m or less), but is less complex and lower risk to design, build, and fly than a full-scale flight system. As a result, a 24 m $\times$ 24 m spacecraft is envisioned as an intermediate step for demonstrating the requisite attitude dynamics and control technologies prior to launching a full-scale flight system. The chapter models each spacecraft using the flexible multibody dynamics finite element model with the "soft" booms developed in Chapter 7 and assumes that the strips have an areal density of 100 g/m^2. Moreover, the chapter baselines a 90 deg, single-axis slew maneuver about the $\mathbf{y}'$ axis depicted in Fig. 8.1 with the "smooth" slew profile from Chapter 3 (Fig. 3.8). The maneuver rotates the spacecraft about the $\mathbf{y}'$ axis from an initial orientation of 0 deg to a final one of 90 deg.

This chapter is organized as follows: Sec. 8.2 derives a reduced-order modal model for the reference spacecraft and uses it to estimate minimum slew times for the baseline slew maneuver. Sec. 8.3 presents an optimization-based approach for determining viscoelastic Kelvin-Voigt damping coefficients for geometrically exact finite element models. Determining appropriate damping coefficients is important for replicating the very low modal damping characteristic of large space structures [90] in the ensuing slew maneuver simulations. Sec. 8.4 describes the results of the slew maneuver simulations obtained using the full finite element model with the Lie group generalized-α method. These results validate the reduced-order model and the slew time predictions from Sec. 8.2. Sec. 8.5 compares the efficacies of the Lie group generalized-α method and the variational integrator from Chapter 6 for slew

maneuver simulations. Sec. 8.6 discusses the important findings from the chapter.

This chapter assumes familiarity with the material in Chapter 3.

8.2 Minimum Slew Times

This section initially derives reduced-order modal models of the SSPP-like spacecraft at integer length scales between 5 m and 50 m. It subsequently uses these reduced-order models to predict minimum slew times using the residual angular velocity slew performance metric proposed in Chapter 3.

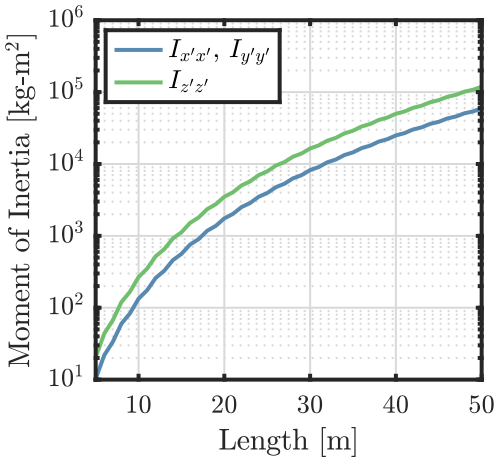

Figure 8.2: Principal moments of inertia for Caltech SSPP-like spacecraft versus size. Due to symmetry, $I_{x'x'} = I_{y'y'}$.

Evaluating the slew performance metric requires reducing the full finite element model (linearized at rest in its undeformed configuration) into the canonical flexible spacecraft model from Chapter 3 (Fig. 3.1). The canonical model nominally retains a single rigid body mode and a single flexible mode, making it the simplest modal representation of a flexible spacecraft. As discussed in Sec. 3.3, the canonical model requires three inputs: the rigid body moment of inertia about the slew axis, the dominant-mode frequency, and the corresponding modal inertia. For each length scale, the rigid body moments of inertia are calculated directly from the mass matrix of the corresponding full finite element model. The rigid body moments of inertia are depicted as functions of length scale in Fig. 8.2.

Each dominant-mode frequency and modal inertia are determined from a modal analysis of the corresponding full finite element model. For a single axis slew, the so-called dominant mode is the mode with the highest modal inertia about the slew axis. The modal inertia is the main diagonal entry corresponding to the slew axis in the modal mass matrix from Sec. 3.3. Figures 8.3a and 8.3b compare the first-mode

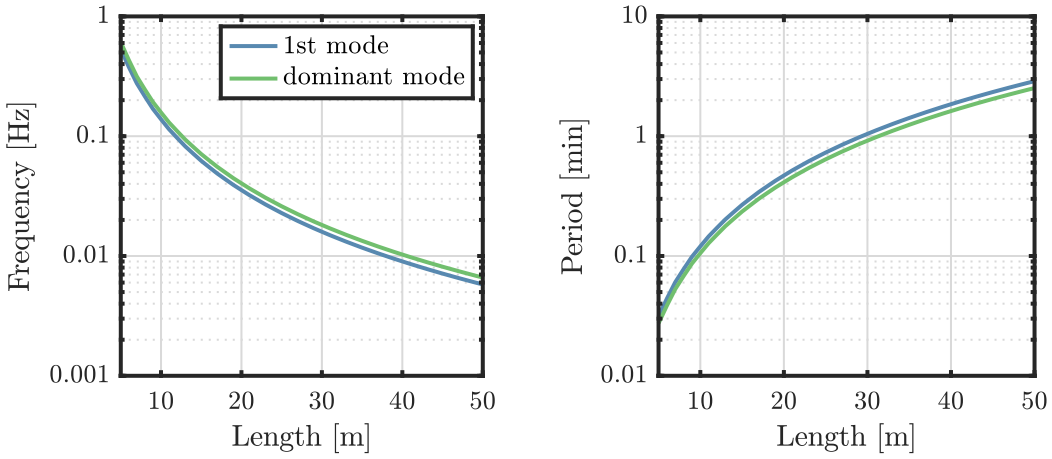

Figure 8.3: Comparison of first mode and dominant mode (a) natural frequencies and (b) natural periods. The dominant mode for the slew maneuver has the highest modal inertia.

and dominant-mode natural frequencies and periods as functions of the spacecraft size. Based on Fig. 8.3a, the lowest natural frequency of the 24 m × 24 m spacecraft is approximately 25 mHz. The figures also emphasize that the first mode is not the dominant mode for a single-axis slew. The dominant mode instead corresponds with either mode 2 or mode 3.

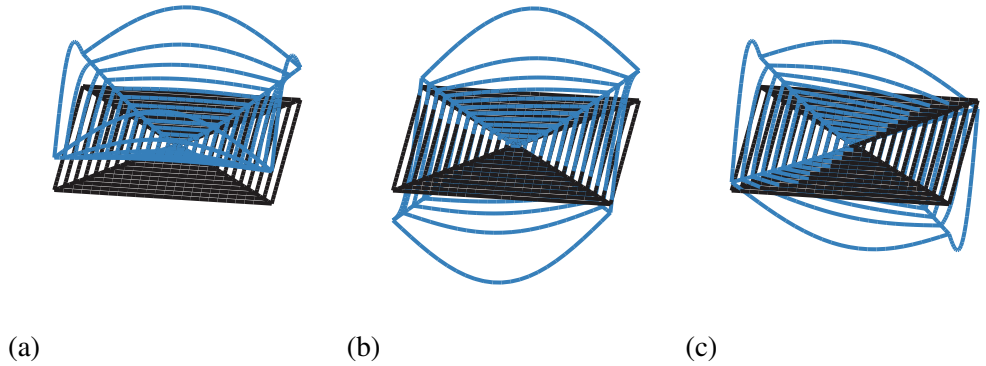

Figure 8.4: (a) 1st mode, (b) dominant mode, and (c) symmetric mode at dominant-mode frequency for the 24 m × 24 m SSPP-like spacecraft.

Modes 2 and 3 are symmetric, meaning they share the same natural frequency. Moreover, mode 3 is the same as mode 2 after a transformation by the appropriate symmetry operation. To see this, Fig. 8.4 depicts the first three vibration modes for the 24 m × 24 m spacecraft. These modes are representative of the modes across the full range of length scales, from 5 m to 50 m. The first mode (Fig. 8.4a) excites

symmetric bending deflections across all four quadrants. In contrast, modes 2 and 3 excite antisymmetric bending deflections; mode 2 is the same as mode 3 after a 90 deg counterclockwise rotation about the spacecraft's out-of-plane axis. Since modes 2 and 3 are symmetric, each reduced-order modal model must include the total modal inertia in modes 2 and 3. Thus, the reduced-order models take the form of Eq. (3.47). Due to symmetry, these models have two degrees of freedom but include three modes: a rigid body mode and two symmetric flexible modes.

The reduced-order modal models are used to predict slew times for the SSPP-like flexible spacecraft with integer length scales between 5 m and 50 m. The slew time calculations require two additional inputs: a slew maneuver and a slew performance metric. In this case, the slew maneuver is the 90 deg smooth slew from Chapter 3 (see Fig. 3.8). Likewise, the slew performance metric is a requirement on the maximum amplitude of the residual angular velocity, also from Chapter 3 (see Sec. 3.4, and in particular, Sec. 3.4.4). The amplitude of the residual angular velocity is a measure of the residual flexible dynamics after the completion of the slew. Two requirements on the residual angular velocity are considered, 0.01 deg/sec and 0.001 deg/sec, which respectively correspond to relatively coarse and fine pointing requirements. The minimum slew time corresponds to the fastest slew that guarantees that the residual angular velocity is always less than or equal to the specified requirement. In what follows, the resulting slew times are referred to as the structure-based slew performance limits.

The structure-based slew performance limits are also compared to slew performance limits associated with the available momentum and torque of reaction wheels for representative attitude control systems. Two reaction wheels are considered. The first is a baseline wheel with a maximum torque of 0.2 N m and a 100 N m s angular momentum storage capacity. This is representative of large, commercially available reaction wheels. The second is a reaction wheel with five times the maximum torque and momentum of the baseline wheel. This is larger than typical reaction wheels, but still likely within the realm of feasibility. Additionally, it is assumed that only 60% of the total momentum and torque are available for slews. Momentum and torque are allocated with margins for different attitude control system functions, including feedforward control (slews), feedback control, and to account for wheel friction and gyroscopic effects. As a result, only a fraction of the total momentum and torque are ever available for slews. For example, the Cassini spacecraft allocated 12.5% of its total torque for slews [258]; more agile spacecraft require higher momentum

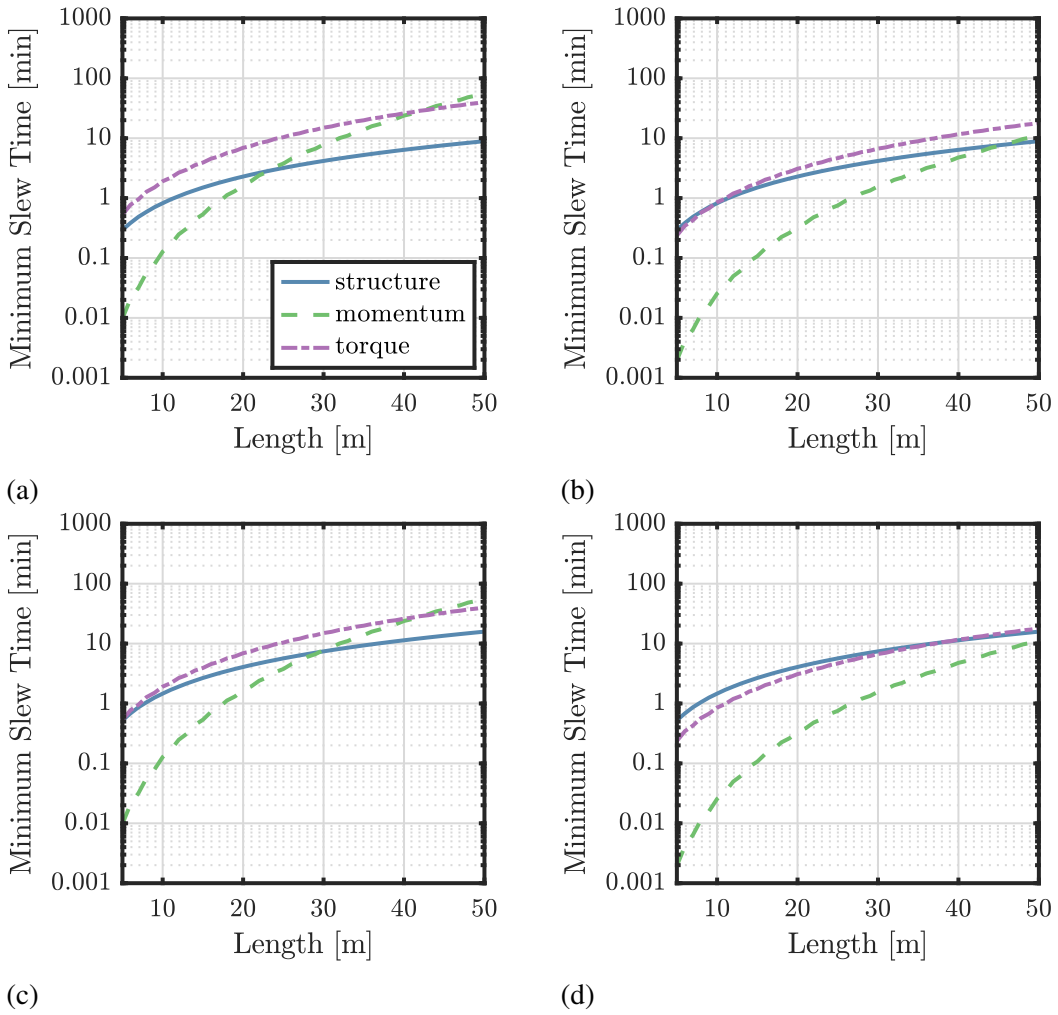

Figure 8.5: Comparison of minimum slew times for smooth slew maneuver. (a) baseline reaction wheel, 0.01 deg/sec; (b) 5× baseline reaction wheel, 0.01 deg/sec; (c) baseline reaction wheel, 0.001 deg/sec; (d) 5× baseline reaction wheel, 0.001 deg/sec.

and torque allocations for slews. However, 60% is likely overly generous because increasing the available angular momentum storage for a slew requires increasing its depth of desaturation before the slew, which for large spacecraft usually drives a requirement for more propellant. For a given slew maneuver and spacecraft, i.e., moment of inertia, the momentum and torque limits constrain the maximum angular velocity and acceleration, which in turn constrain the minimum slew time.

Figure 8.5 depicts the minimum slew times as a function of the spacecraft size. In each sub-figure, the top-most curve is the most-restrictive constraint on slew performance, and hence, specifies the minimum slew time. With the baseline reaction wheel, Figs. 8.5a and 8.5c demonstrate that the slew performance limit

is due to either the available torque or momentum, not the structure, regardless of the requirement on the residual angular velocity. Similarly, with the larger reaction wheel and the coarser pointing requirement, Fig. 8.5b shows that the available torque again drives the minimum slew time. The only exception is the case with the larger reaction wheels and the finer pointing requirement; see Fig. 8.5d. In this case, the structure-based performance limit constrains the minimum slew time for spacecraft at length scales below approximately 40 m. Above 40 m, the slew times are again torque-constrained. Even so, below the crossover point, the structure-based performance limit results in minimum slew times on the same order of magnitude as those from the torque limit.

Decreasing either the fraction of the momentum and torque available for slews or the maximum momentum and torque shifts the corresponding curves in Fig. 8.5 up. Similarly, decreasing the requirement on the amplitude of the residual angular velocity also shifts the corresponding curves in Fig. 8.5 up. Increasing the maximum momentum and torque is likely to require replacing reaction wheels with control moment gyroscopes.

Based on Fig. 8.5, the capabilities of each spacecraft's attitude control system are often significantly more limiting than the dynamics of the structure. When this is the case, the results suggest that a lighter-weight, less-stiff, and lower-cost structure can be used to shift the structure-based performance limit closer to that of the attitude control system, at least as far as slewing is concerned. The figure likewise emphasizes that SSPP-like flexible spacecraft can likely achieve slew times on the order of 10 min or less for 90 deg, single-axis maneuvers at length scales as large as 50 m. If this is indeed the case, these slew times are realistically an order of magnitude or more faster than the existing state-of-practice. To gain confidence in these results, Sec. 8.4 compares the predictions from the reduced-order model for the 24 m $\times$ 24 m spacecraft with those from geometrically nonlinear simulations of the corresponding full finite element model. In the interim, Sec. 8.3 develops the optimization approach for determining the viscoelastic damping coefficients that are inputs to the full finite element model.

8.3 Determination of Kelvin-Voigt Damping Coefficients

The goal of this section is to generalize standard linear damping models, e.g., modal damping or Rayleigh damping, to geometrically exact finite element formulations. This allows modal damping to be reproduced in the geometrically exact finite element

simulations in Sec. 8.4.

Unlike linear finite element formulations, where it is straightforward to determine a global damping matrix, geometrically exact finite element formulations require modifications at the element level to guarantee that the damping formulation is invariant to superposed rigid body motions. Invariant damping formulations only directly dissipate energy associated with the elastic motion. A recent numerical study demonstrates that these formulations are important for correctly modeling damping effects in large-deformation simulations [259]. However, these damping models are often troublesome due to the difficulties associated with determining appropriate damping coefficients [260]. To that end, this section proposes an optimization-based approach for determining these coefficients. Even though this section focuses on geometrically exact beam finite elements, the approach readily generalizes to other types of geometrically exact finite elements (e.g., plates or shells) by appropriately modifying the tangent damping matrix.

The simplest damping model for geometrically exact finite elements is referred to as Kelvin-Voigt damping. For geometrically exact beams, Kelvin-Voigt damping augments the constitutive relation [Eq. (4.42)] for the force resultant $\mathbf{N}$ and moment resultant $\mathbf{M}$ with terms proportional to the material strain rate $\dot{\mathbf{\Gamma}}$ and the material curvature rate $\dot{\mathbf{K}}$ [148]. In other words,

$$\mathbf{S} = \mathbf{C}\mathbf{E} + \mathbf{D}\dot{\mathbf{E}} \tag{8.1}$$

where $\mathbf{S}^T = \left(\mathbf{N}^T, \mathbf{M}^T\right)$, $\mathbf{E}^T = \left(\mathbf{\Gamma}^T, \mathbf{K}^T\right)$, $\mathbf{C} \in \mathbb{R}^{6\times6}$ is the sectional stiffness matrix, and $\mathbf{D} \in \mathbb{R}^{6\times6}$ is the matrix of to-be-determined sectional damping coefficients. To the author's knowledge, there are two systematic approaches in the literature for determining $\mathbf{D}$, although most studies instead tend to use "reasonable guesses" [213] or sensitivity studies. The first approach [261] derives closed-form expressions for the damping coefficients for geometrically exact beams with homogeneous, isotropic material properties. However, these expressions assume the availability of viscoelastic material properties, specifically the viscoelastic bulk and shear viscosities. These material properties are unavailable for the equivalent beam models of the strips, and hence, this approach is not applicable here. The second approach [213] applies modal analysis to the linearized partial differential equations governing the dynamics of geometrically exact beams with simple boundary conditions to derive expressions for the unknown damping coefficients. The optimization-based approach developed here generalizes this approach to finite element models of arbitrary complexity.

The formulation of the optimization problem starts from the dynamic equilibrium equations for a nonlinear finite element model:

$$\mathbf{F}_{\text{iner}}(\mathbf{g}, \dot{\mathbf{g}}, \ddot{\mathbf{g}}) + \mathbf{F}_{\text{int}}(\mathbf{g}, \dot{\mathbf{g}}) = \mathbf{F}_{\text{ext}} \tag{8.2}$$

where $\mathbf{g} \in \mathbb{R}^n$ is the vector of generalized coordinates, $\mathbf{F}_{\text{iner}}(\mathbf{g}, \dot{\mathbf{g}}, \ddot{\mathbf{g}}) \in \mathbb{R}^n$ is the vector of generalized inertia forces, $\mathbf{F}_{\text{int}}(\mathbf{g}, \dot{\mathbf{g}}) \in \mathbb{R}^n$ is the vector of generalized viscoelastic forces, and $\mathbf{F}_{\text{ext}} \in \mathbb{R}^n$ is the vector of generalized external forces. The tangent damping matrix $\mathbf{C}_T \in \mathbb{R}^{n \times n}$ then follows as

$$\mathbf{C}_T(\mathbf{g}) = \frac{\partial \mathbf{F}_{\text{int}}(\mathbf{g}, \dot{\mathbf{g}})}{\partial \dot{\mathbf{g}}}. \tag{8.3}$$

For simplicity (and without any loss of generality), these developments only consider generalized coordinates in a vector space and neglect external constraints, e.g., due to the joints in flexible multibody systems. The treatment of generalized coordinates in a Lie group entails straightforward modifications to Eq. (8.3) and what follows. The formulation is independent of any external constraints on the system.

The tangent damping matrix $\mathbf{C}_T$ for a finite element model with n_e elements is defined by a standard finite assembly step. Thus,

$$\mathbf{C}_T(\mathbf{g}) = \sum_{e=1}^{n_e} \mathbf{L}_e^T \mathbf{C}_T^e(\mathbf{L}_e \mathbf{g}) \mathbf{L}_e \tag{8.4}$$

where $e \in \{1,\ 2,\ \ldots,\ n_e\}$; $\mathbf{L}_e \in \mathbb{R}^{n_c^e \times n}$ is the Boolean matrix that indexes the element nodal coordinates $\mathbf{g}_e \in \mathbb{R}^{n_c^e}$ from the generalized coordinates $\mathbf{g}$, i.e., $\mathbf{g}_e = \mathbf{L}_e \mathbf{g}$; and $\mathbf{C}_T^e \in \mathbb{R}^{n_c^e \times n_c^e}$ is the elemental tangent damping matrix. For a geometrically exact beam element of length ℓ_e, $\mathbf{C}_T^e$ is given by

$$\mathbf{C}_T^e(\mathbf{g}_e) = \int_0^{\ell_e} \mathbf{B}^T(\mathbf{g}_e, s) \mathbf{D}_e \mathbf{B}(\mathbf{g}_e, s)\, \mathrm{d}s \tag{8.5}$$

where $\mathbf{B} \in \mathbb{R}^{6 \times 12}$ is the discrete strain gradient matrix [Eq. (5.48)], $\mathbf{D}_e \in \mathbb{R}^{6 \times 6}$ is the unknown matrix of viscoelastic damping coefficients for element e, and s is the arc length coordinate along the element's reference axis. The integral in Eq. (8.5) is normally approximated by a quadrature rule with n_q weights w_i at arc lengths s_i. It follows that

$$\mathbf{C}_T(\mathbf{g}) = \sum_{e=1}^{n_e} \mathbf{L}_e^T \left(\frac{\ell_e}{2} \sum_{i=1}^{n_q} w_i \mathbf{B}^T(\mathbf{L}_e \mathbf{g}, s_i) \mathbf{D}_e \mathbf{B}(\mathbf{L}_e \mathbf{g}, s_i) \right) \mathbf{L}_e \tag{8.6}$$

which is a linear function of $\mathbf{D}_e$.

From here, an optimization problem determines the n_e unknown matrices of elemental damping coefficients $\mathbf{D}_e$ that minimize the error between the global tangent damping matrix $\mathbf{C}_T$ and a reference damping matrix $\mathbf{C}_{\text{ref}}$. In doing so, the finite element model inherits the damping characteristics of $\mathbf{C}_{\text{ref}}$ in the specified configuration (here, the initial configuration). A particularly simple choice for $\mathbf{C}_{\text{ref}}$ is stiffness-proportional damping; i.e.,

$$\mathbf{C}_{\text{ref}} = \beta \mathbf{K}_T \tag{8.7}$$

where $\beta = 2\zeta_1/\omega_1$, ω_1 is the first-mode natural frequency, ζ_1 is the desired fraction of critical damping in the first mode, and $\mathbf{K}_T = \partial \mathbf{F}_{\text{int}}/\partial \mathbf{g}$ is the tangent stiffness matrix. With stiffness-proportional damping, successive modes are more heavily damped. Specifically, the fraction of critical damping in the ith mode is $\zeta_i = \zeta_1(\omega_i/\omega_1)$ where ω_i is the ith mode's natural frequency; $i = 1, \ldots, n$; and n is the number of modes. In the undeformed configuration, only the material tangent stiffness [Eq. (5.55)] contributes to $\mathbf{K}_T$, from which it follows that $\mathbf{C}_T$ and $\mathbf{K}_T$ share the same matrix structure (sparsity pattern). This implies that there is an optimal set of elemental damping coefficients that results in negligible errors between $\mathbf{C}_T$ and $\mathbf{C}_{\text{ref}}$. For this reason, stiffness-proportional damping is used to determine the elemental damping coefficients for the dynamic simulations in Sec. 8.4.

Following Sec. 7.3.1 and [243], the optimization problem enforces constraints on the structure of $\mathbf{D}_e$. In general, $\mathbf{D}_e$ is a symmetric positive definite matrix, i.e., $\mathbf{D}_e > 0$ [148, 261, 262]. For simplicity, however, $\mathbf{D}_e$ is taken to be diagonal, i.e., $\mathbf{D}_e = \text{diag}\,\{\mathbf{d}_e\}$, where the coefficients of $\mathbf{d}_e$ are strictly positive. With diagonal $\mathbf{D}_e$, the optimization problem takes the form

$$\underset{\mathbf{d}_e \;\forall\; e \,\in\, \{1,\,2,\,\ldots,\,n_e\}}{\text{minimize}} \qquad \|\mathbf{C}_T(\mathbf{g}_0, \mathbf{d}_e) - \mathbf{C}_{\text{ref}}\|_F \tag{8.8}$$

subject to $\mathbf{d}_e > \mathbf{0}_{6\times 1}$. Here,

$$\mathbf{C}_T(\mathbf{g}_0, \mathbf{d}_e) = \sum_{e=1}^{n_e} \mathbf{L}_e^T \left(\frac{\ell_e}{2} \sum_{i=1}^{n_q} w_i \mathbf{B}^T(\mathbf{L}_e \mathbf{g}_0, s_i)\, \text{diag}\,\{\mathbf{d}_e\}\, \mathbf{B}(\mathbf{L}_e \mathbf{g}_0, s_i) \right) \mathbf{L}_e, \tag{8.9}$$

the subscript 0 denotes the initial (undeformed) configuration, and F denotes the Frobenius norm.

To solve Eq. (8.8), the constraint $\mathbf{d}_e > \mathbf{0}_{6\times 1}$ is relaxed from strictly positive to simply nonnegative, i.e., $\mathbf{d}_e - \epsilon \mathbf{1}_{6\times 1} > \mathbf{0}_{6\times 1}$ where $\mathbf{1}_{6\times 1}$ is a vector of ones and $\epsilon \ll 1$ is a small positive scalar. This results in a convex program with a unique, globally

optimal solution. Since $\mathbf{C}_T(\mathbf{g}_0, \mathbf{d}_e)$ is linear in $\mathbf{d}_e$, the convex program can then be manipulated into the more standard form of a constrained least squares problem, i.e., an optimization problem of the form

$$\underset{\mathbf{d}}{\text{minimize}} \quad \|\mathbf{A}\mathbf{d} - \mathbf{b}\|_F \tag{8.10}$$

subject to $\mathbf{d} - \epsilon \mathbf{1}_{6n_e \times 1} > \mathbf{0}_{6n_e \times 1}$ where $\mathbf{d}^T = \left(\mathbf{d}_1^T, \ \ldots, \ \mathbf{d}_e^T\right) \in \mathbb{R}^{6n_e}$. Equation (8.10) is solved numerically using convex programming, in this case implemented using CVX [244, 245] with the SDPT3 solver [246, 247].

8.4 Dynamic Simulations of Reference Slew Maneuver

This section uses the full finite element model and the Lie group generalized-α method [36–38] to simulate the spacecraft's dynamics during a nominally rest-to-rest slew maneuver through an angle of 90 deg about the $\mathbf{y}'$ axis depicted in Fig. 8.1. Secs. 8.4.1 and 8.4.2 respectively describe the approach to and results from these simulations.

8.4.1 Approach to Dynamic Simulations

The slew maneuver simulations consider the 24 m $\times$ 24 m SSPP-like flexible spacecraft with the "soft" booms from Chapter 7. The booms and strips are both discretized using the objective, quaternion-based geometrically exact beam finite elements from Chapter 5. The boom-strip interface constraints are then modeled using revolute joints [180] and enforced via the method of Lagrange multipliers. This results in a holonomically-constrained flexible multibody dynamics model. The structure is unrestrained to simulate a free-flying spacecraft. Viscoelastic Kelvin-Voigt damping [148] is incorporated to replicate the very low modal damping characteristic of large space structures [90]. The Kelvin-Voigt damping coefficients are calculated for stiffness-proportional damping with 0.25% of critical damping in the lowest frequency mode using the optimization-based approach from Sec. 8.3. For additional details regarding the spacecraft model and its finite element implementation, see Chapters 5 and 7.

The dynamic simulations integrate the full finite element model using a quaternion-based implementation of the Lie group generalized-α method [36–38]. As is standard, the integrator evaluates the response at the discrete time steps $t_{k+1} = t_k + h$ for all $k \in \{0, \ 1, \ \ldots, \ N-1\}$ where $t_0 = 0$ is the initial time, $t_f = t_{N-1}$ is the final time, $h = 0.01$ s is the time step size, and $N = t_f/h + 1$ is the number of discrete solution points. Larger time steps lead to numerical instabilities for faster slew ma-

neuvers. The solver uses the infinity-norm-based convergence criterion [Eq. (5.58)] with an absolute convergence tolerance of 10^{-6} for both the generalized force and constraint residuals. To avoid numerical ill-conditioning, the integrator implements the optimal scaling strategy from [179].

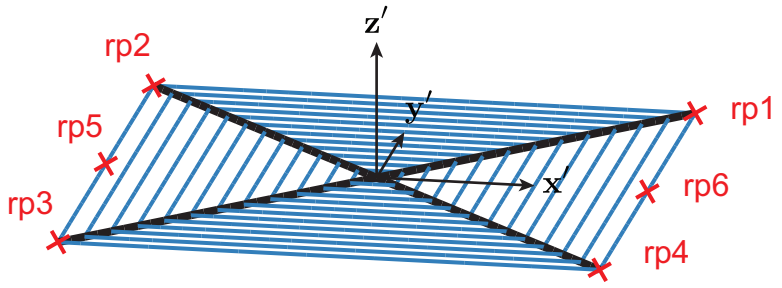

Figure 8.6: Reference point locations for displacements. rp1 through rp4 are located at the tips of the booms. rp5 and rp6 are located at the midpoints of the outermost strips parallel to the rotation axis $\mathbf{y}'$.

The slew maneuver simulations are subdivided into three steps:

1. for $t < 0$, the spacecraft is at rest in its undeformed configuration;
2. for $0 \leq t < T$, the spacecraft is actuated by an external moment $M_{y'}$ applied at its central node; and
3. for $t \geq T$, the spacecraft is unforced and undergoes damped free vibrations due to the residual energy remaining from the slew.

The external moment $M_{y'}$ about the $\mathbf{y}'$ axis from Fig. 8.1 is materially-fixed (i.e., fixed in the spacecraft's body frame) and given by

$$M_{y'}(t) = I_{y'y'}\ddot{\theta}(t) \tag{8.11}$$

where $I_{y'y'}$ is the spacecraft's rigid body inertia about the $\mathbf{y}'$ axis from Fig. 8.2 and $\ddot{\theta}(t)$ is the angular acceleration for the smooth slew maneuver from Chapter 3 (see Fig. 3.8). The simulations terminate at some time $t_f > T$ to study the residual flexible dynamics after the completion of the slew. At each time step t_k, the simulations output the displacements at the 6 reference points labeled in Fig. 8.6, along with the internal bending moments in the strips and the energy. The simulations consider 90 deg, single-axis slew maneuvers with durations ranging from 1 min to 20 min. A 1 min slew is comparable to the fundamental period of the 24 m $\times$ 24 m structure; see Fig. 8.3b.

The Lie group generalized-α method includes numerical dissipation specified by the spectral radius at infinity $\rho_\infty \in [0, 1]$ [25]. For flexible multibody systems, this numerical dissipation (i) eliminates the high-frequency numerical oscillations associated with the solution of numerically stiff differential equations and (ii) stabilizes the weak numerical instability attributed to the constraints [178]. Physically accurate simulations often require both physical (in this case, viscoelastic) damping to attenuate low frequencies and numerical damping to attenuate higher ones [263]. Since physical damping dominates at lower frequencies [263], the small amount of viscoelastic damping in the finite element model desensitizes the simulations to ρ_∞. For this reason, the simulations use $\rho_\infty = 0.7$. This results in a low-to-moderate amount of high-frequency numerical dissipation and is sufficient to stabilize the simulations, even for fast slew maneuvers.

As noted in Chapter 6, numerical dissipation can introduce non-physical energy decay. For this reason, conservation of energy is used as a proxy for accuracy [70]. In particular, the more exactly energy is conserved during the simulations, the more accurate the simulations. The total energy E at time t_k is

$$\mathcal{E}(t_k) = \mathcal{T}(t_k) + \mathcal{U}(t_k) + \mathcal{W}_{\text{visc}}(t_k) - \mathcal{W}_{\text{ext}}(t_k) \tag{8.12}$$

where $\mathcal{T}$ is the kinetic energy, $\mathcal{U}$ is the strain energy, $\mathcal{W}_{\text{visc}}$ is the work done by the Kelvin-Voigt damping, and $\mathcal{W}_{\text{ext}}$ is the external work. $\mathcal{W}_{\text{visc}}$ and $\mathcal{W}_{\text{ext}}$ are both evaluated using quadrature rules consistent with the Newmark-β formulas used for the time-discretization in the generalized-α method. Since the spacecraft is initially at rest and undeformed, energy conservation implies $\mathcal{E}(t_k) = 0$ for all $k \in \{0,\ 1,\ \ldots,\ N-1\}$, but numerical dissipation and the accumulation of numerical errors both contribute to non-conservation of energy.

8.4.2 Simulation Results

Dynamic simulations with the full finite element model are used to develop insights into the slew maneuver dynamics of the reference spacecraft and to validate the slew time calculations from the reduced-order modal models in Sec. 8.2. The simulations consider 90 deg, single-axis slew maneuvers with durations from 1 min to 20 min. Initially, the results in this section focus on the most aggressive slew maneuver: the 90 deg slew in 1 min. This maneuver features the highest structural loads and the fastest dynamics of all the simulated maneuvers, and hence, is the most dynamically interesting. The results then consider a wider range of slew times to validate some of the slew time calculations from Sec. 8.2.

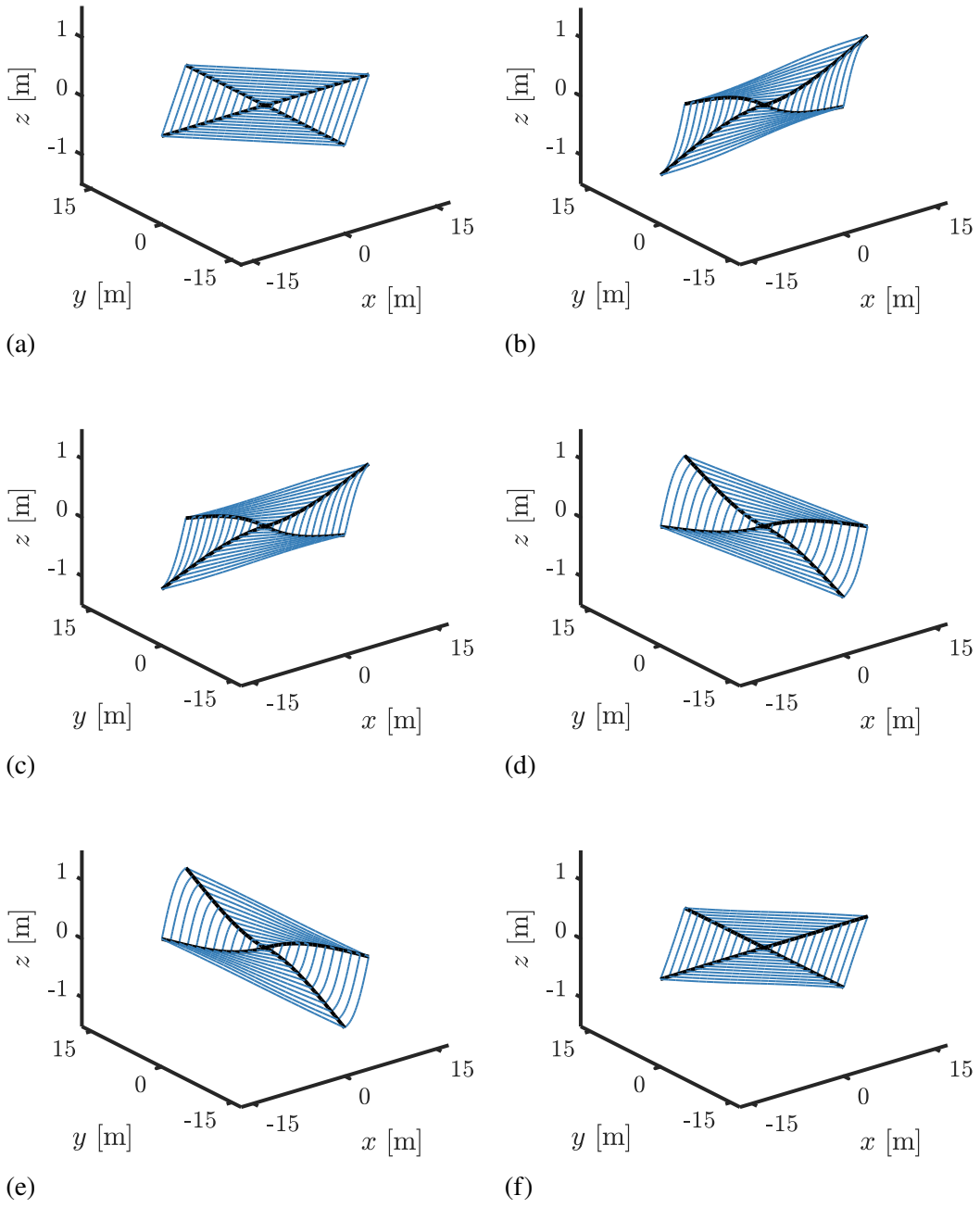

Figure 8.7: Elastic deformations in spacecraft body frame for 90 deg, single-axis slew maneuver. (a) t = 0 s, (b) t = 12 s, (c) t = 24 s, (d) t = 36 s, (e) t = 48 s, and (f) t = 60 s.

The 1 min slew is initially used to develop intuition into the slew maneuver dynamics. Figure 8.7 depicts snapshots of the deformed configurations of the spacecraft in the body frame at 12 s intervals. The origin of the body frame is at the center of the

spacecraft. Initially, the spacecraft is at rest and undeformed (Fig. 8.7a) with an orientation of 0 deg about the rotation axis. For 0 s $\leq t <$ 30 s, the spacecraft is accelerating to its peak angular velocity. The peak angular acceleration occurs at approximately $t = 16.6$ s, which implies that the peak displacements occur shortly after the second snapshot (Fig. 8.7b) taken at $t = 12$ s. The displacements subsequently decrease (Fig. 8.7c) as the angular acceleration decreases to zero at $t = 30$ s. The angular acceleration retraces its steps in reverse for 30 s $\leq t <$ 60 s. Hence, the deformed configurations at times $t = 36$ s (Fig. 8.7d) and $t = 48$ s (Fig. 8.7e) are comparable to those at times $t = 24$ s and $t = 12$ s, respectively. Peak deceleration occurs at approximately $t = 43.4$ s. At $t = 60$ s, the spacecraft has small residual elastic displacements due to its flexible dynamics. Due to symmetry, there are no deformations along the rotation axis. For longer slew maneuvers, the deformed configurations in the body frame are comparable to those in Fig. 8.7, except the peak displacements decrease as the slew time increases.

Figure 8.8 depicts the individual contributions to the energy balance [Eq. (8.12)] during the 90 deg slew in 1 min. Altogether, these results are as expected. In particular, both the kinetic energy (Fig. 8.8a) and external work (Fig. 8.8c) peak at about the same time the slew angular velocity peaks (in this case, $t = 30$ s). Likewise, the strain energy (Fig. 8.8b) peaks at approximately the same times as the angular acceleration, i.e., in the vicinities of $t = 16.6$ s and $t = 43.4$ s. The second strain energy peak is lower than the first, likely due to the viscoelastic dissipation. The work done by the viscoelastic forces (Fig. 8.8d) continuously dissipates strain energy. The energy behavior is similar for longer slew maneuvers, except the peak kinetic and strain energies decrease as the slew time increases.

As a proxy for simulation accuracy, Fig. 8.9 studies the energy balance [Eq. (8.12)] during the 90 deg, 1 min slew. Since the spacecraft is initially at rest in its undeformed configuration, $\mathcal{E}(0) = 0$. Conservation of energy then requires $\mathcal{E}(t_k) = 0$ for all $k \in \{0, 1, \ldots, N-1\}$; any deviations from zero correspond to errors, the significance of which depends on the magnitude. Typically, accuracy requires the errors to be at least several orders of magnitude smaller than the individual energy terms. In Fig. 8.9, the energy errors peak at approximately 40 s, then decrease in magnitude to a steady-state on the order of approximately 10^{-6} J. The peak energy error is approximately four orders of magnitude smaller than the smallest term in the energy balance (the viscoelastic dissipation, Fig. 8.8d). Hence, this simulation is likely accurate, at least for most engineering applications. Unsurprisingly, the energy

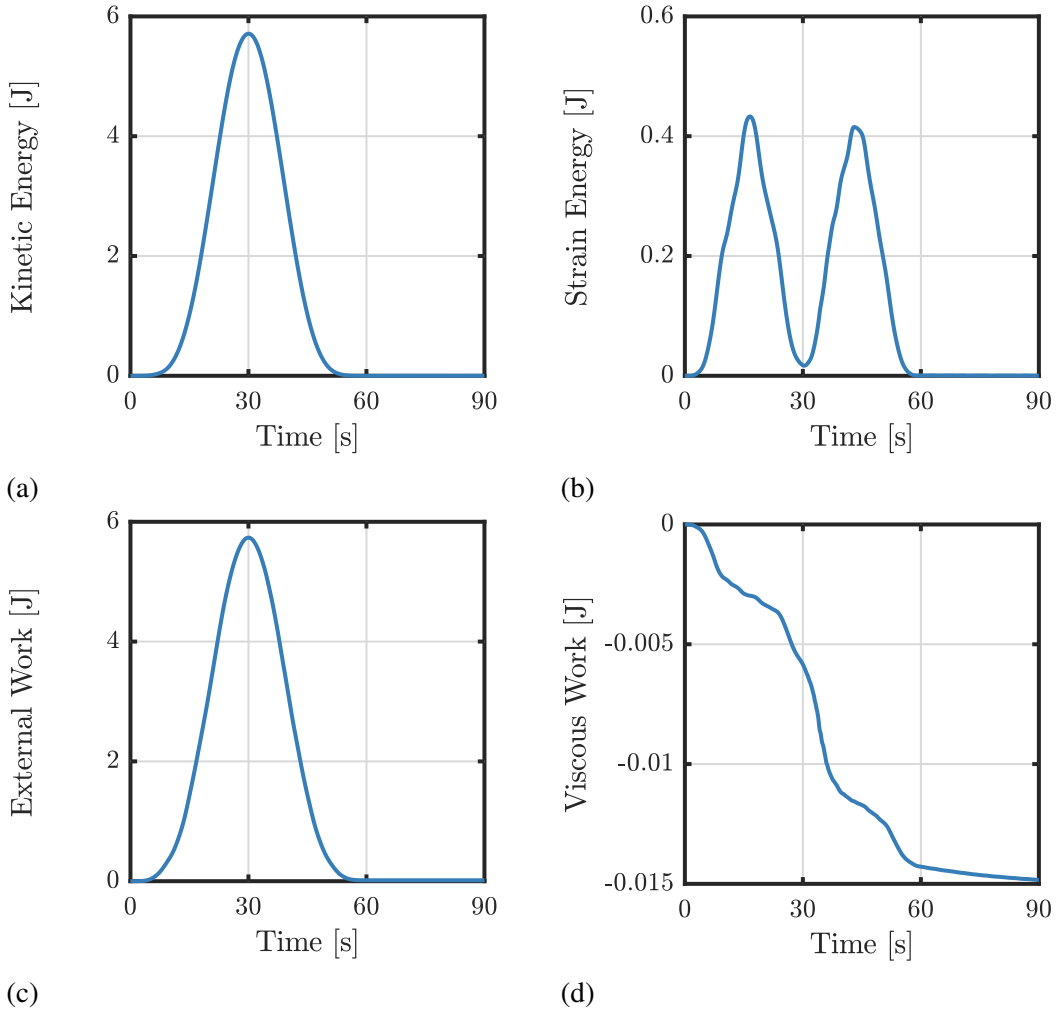

Figure 8.8: (a) kinetic energy, (b) strain energy, (c) external work, and (d) viscoelastic dissipation for a 90 deg slew maneuver in 1 min.

errors decrease as the slew time increases; e.g., for the 90 deg slew in 20 min, the peak energy error is on the order of 10^{-11} J. In other words, accuracy increases as the slew time increases due to the smaller structural loads and slower dynamics. Negative values of the energy balance imply that small amounts of energy are lost converting the external work into kinetic and strain energy.

The discussion now turns to several structural parameters of practical interest: the boom tip displacements (Fig. 8.10a), the strip midpoint displacements (Fig. 8.10b), and the peak out-of-plane bending moments in the strips (Fig. 8.11). In Fig. 8.10a, the displacements are measured relative to the center of the spacecraft. Due to symmetry, the displacements at reference points rp2 and rp3 are equal in magnitude but opposite in direction to those at rp1 and rp4; see Fig. 8.6. Similarly, the

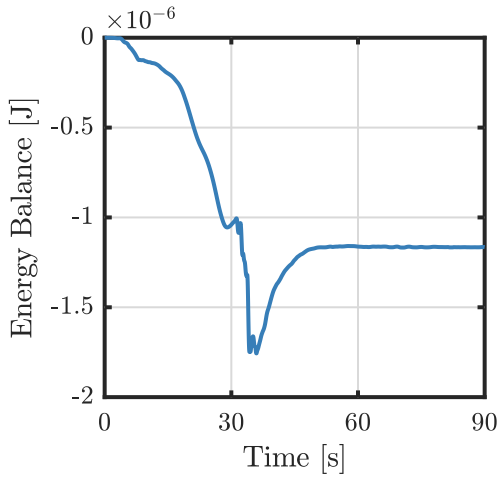

Figure 8.9: Energy balance [Eq. (8.12)] for a 90 deg slew maneuver in 1 min.

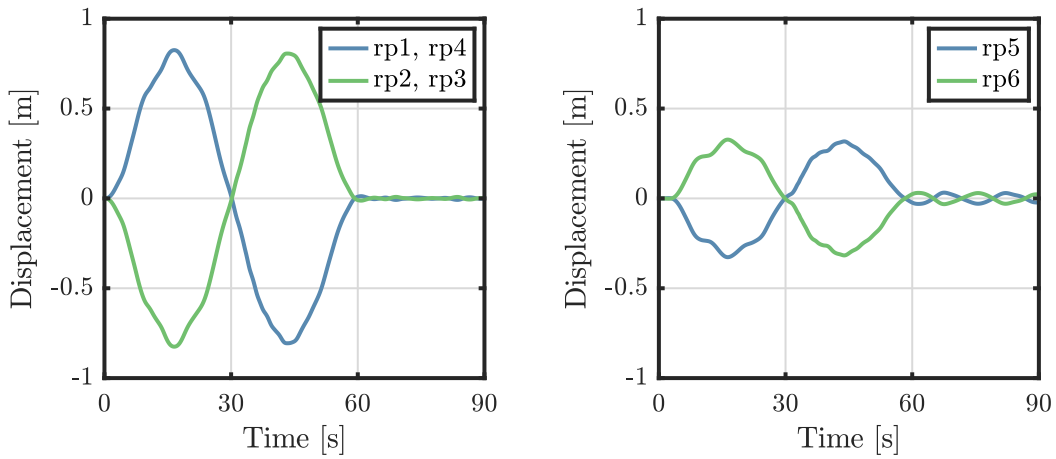

Figure 8.10: Displacements at (a) boom tips and (b) strip midpoints during a 90 deg slew maneuver of the 24 m×24 m SSPP-like spacecraft in 1 min. The strip midpoint displacements are measured relative to the boom tips.

displacements at rp6 are equal in magnitude but opposite in direction to those at rp5. The peak displacements at the boom tip are approximately 0.8 m. The strip midpoint displacements in Fig. 8.10b are measured relative to the tips of the booms. Thus, while the peak relative displacements at the midpoints of the strips are only approximately 0.35 m, the total displacements are approximately 1.15 m.

Figure 8.11 depicts the peak out-of-plane bending moments in the strips. The bending moments in the strips determine the onset of localization and buckling [24, 217]. The critical out-of-plane buckling moment for the TRAC longerons in the strips is approximately 0.1 N m [215]. Assuming that the critical buckling

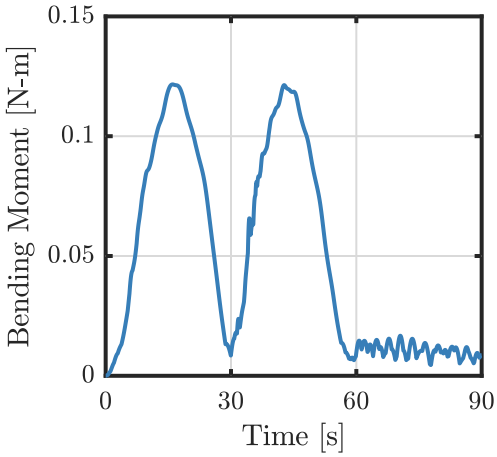

Figure 8.11: Peak out-of-plane internal bending moments for strips during a 90 deg slew maneuver in 1 min.

moment for a strip is approximately twice the critical buckling moment for the individual longerons, then it can be concluded that the strips likely do not buckle out-of-plane. Thus, the assumptions implicit in the equivalent beam models for the strips are likely reasonable, at least for the sake of preliminary design and analysis. In-plane buckling, however, is more complex due to the additional bending stiffness contributed by the battens. Consequently, it is difficult to draw any meaningful conclusions about in-plane localization and buckling. Additionally, the strips may experience premature localization and buckling due to the combination of both in-plane and out-of-plane moments. As a result, a more detailed study of localization and buckling during slew maneuvers is warranted. This is left to future work.

Due to symmetry, the peak bending moments occur at the midpoints of the strips parallel to the rotation axes, i.e., on the line connecting reference points rp5 and rp6. The peak bending moments are a function of both the inertial loads and the deflections of the booms. For these reasons, the simulations predict that the peak bending moments do not necessarily occur in the outermost strips.

Lastly, the geometrically nonlinear finite element simulations are used to validate the slew time calculations from Sec. 8.2. This involves comparing the amplitudes of the residual angular velocities predicted by the reduced-order model for the 24 m$\times$24 m spacecraft with the predictions from the full finite element model as a function of slew time. For the full finite element model, the amplitude of the residual angular velocity, denoted Ω, is calculated from

$$\mathcal{T}(T) + \mathcal{U}(T) = \frac{1}{2} I_{y'y'} \Omega^2 \tag{8.13}$$

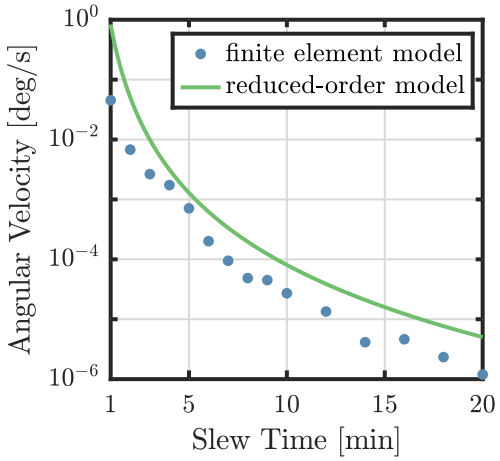

Figure 8.12: Amplitude of the residual spacecraft bus angular velocity as a function of slew time.

where T is the slew time and $I_{y'y'}$ is the moment of inertia about the slew axis from Fig. 8.2. In other words, Ω is the angular velocity that results from converting all the residual strain energy in the structure into kinetic energy about the slew axis. Figure 8.12 compares the results. Based on the figure, the predictions from the reduced-order model show excellent agreement with the full finite element model, especially considering that the reduced-order model only includes two symmetric flexible modes and is undamped. However, some caution is warranted here. Even though the reduced-order model provides accurate predictions of the residual angular velocity, this by no means guarantees that the reduced-order model is also going to provide accurate predictions of other figures of merit, e.g., the internal forces and moments in the structure. Regardless, these results suggest that the elastic deformations stay within the small-deflection regime despite the large rigid body rotation during the slew maneuver. Moreover, since the reduced-order model consistently overestimates Ω, the results demonstrate that its predictions are both accurate and conservative, at least at the 24 m $\times$ 24 m scale. Thus, it appears feasible to slew a 24 m $\times$ 24 m flexible spacecraft with a first-mode frequency of approximately 25 mHz 90 deg about a single-axis in 10 min or less. This is significantly faster than the current state-of-practice.

8.5 Application of Variational Integrator to Slew Maneuver Dynamics

This last section repeats the simulations from Sec. 8.4 using the variational integrator from Chapter 6. This facilitates comparisons of the accuracy and energy behavior of the more traditional structural dynamics integrator, the Lie group generalized-

α method [36–38], with the variational integrator for a larger-scale engineering problem. Unlike the Lie group generalized-α method, the variational integrator achieves stability without numerical dissipation for the simulated slew maneuvers. For brevity, this section focuses on the most numerically challenging slew maneuver simulation, the 1 min slew, which features the highest structural loads and the fastest dynamics of the simulated maneuvers.

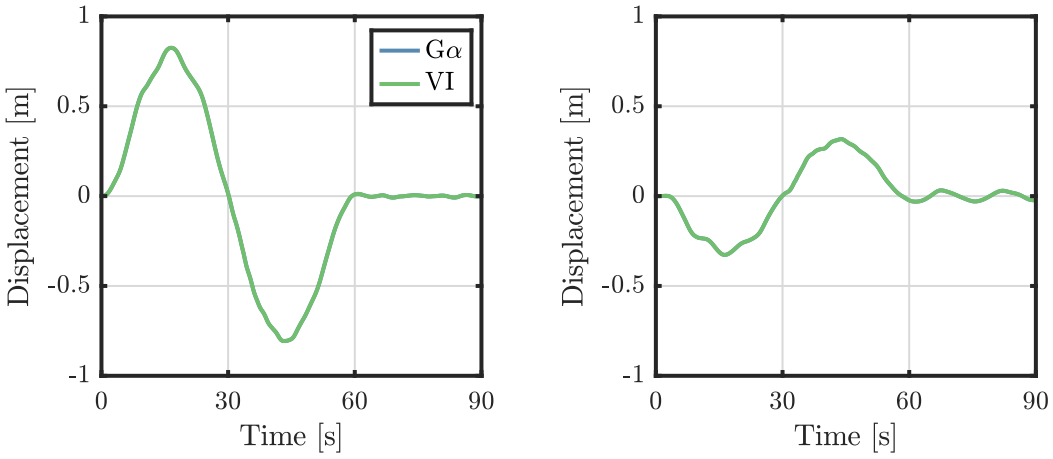

Figure 8.13: Comparison of (a) boom tip displacements at rp1 and (b) strip midpoint displacements at rp5 from generalized-α method (Gα) and variational integrator (VI). Due to symmetry, the displacements at rp4 are the same as rp1.

Figures 8.13a and 8.13b compare the displacements calculated from the generalized-α method and the variational integrator at reference points rp1 (the boom tip) and rp5 (the strip midpoint); see Fig. 8.6. Due to symmetry, the displacements at rp4 are the same as those at rp1. Likewise, the displacements at rp2, rp3, and rp6 are the negatives of those at rp1, rp4, and rp5. Both integrators predict virtually the same boom tip and strip midpoint displacements throughout the simulation. The displacement predictions at other points on the structure show similarly good agreement. Thus, both integrators exhibit comparable accuracies, at least as far as the displacements are concerned.

As an initial comparison of the energy behavior, Fig. 8.14 compares the kinetic energy (Fig. 8.14a), strain energy (Fig. 8.14b), external work (Fig. 8.14c), and viscous work (Fig. 8.14d) for the generalized-α method and the variational integrator. Here, the kinetic energy at t_k for the variational integrator is evaluated from the discrete generalized momenta $\mathbf{h}_k$ using $\mathcal{T}_k = \mathbf{h}_k^T \mathbf{M}^{-1}(\mathbf{g}_k)\mathbf{h}_k/2$ where $\mathbf{M}(\mathbf{g})$ is

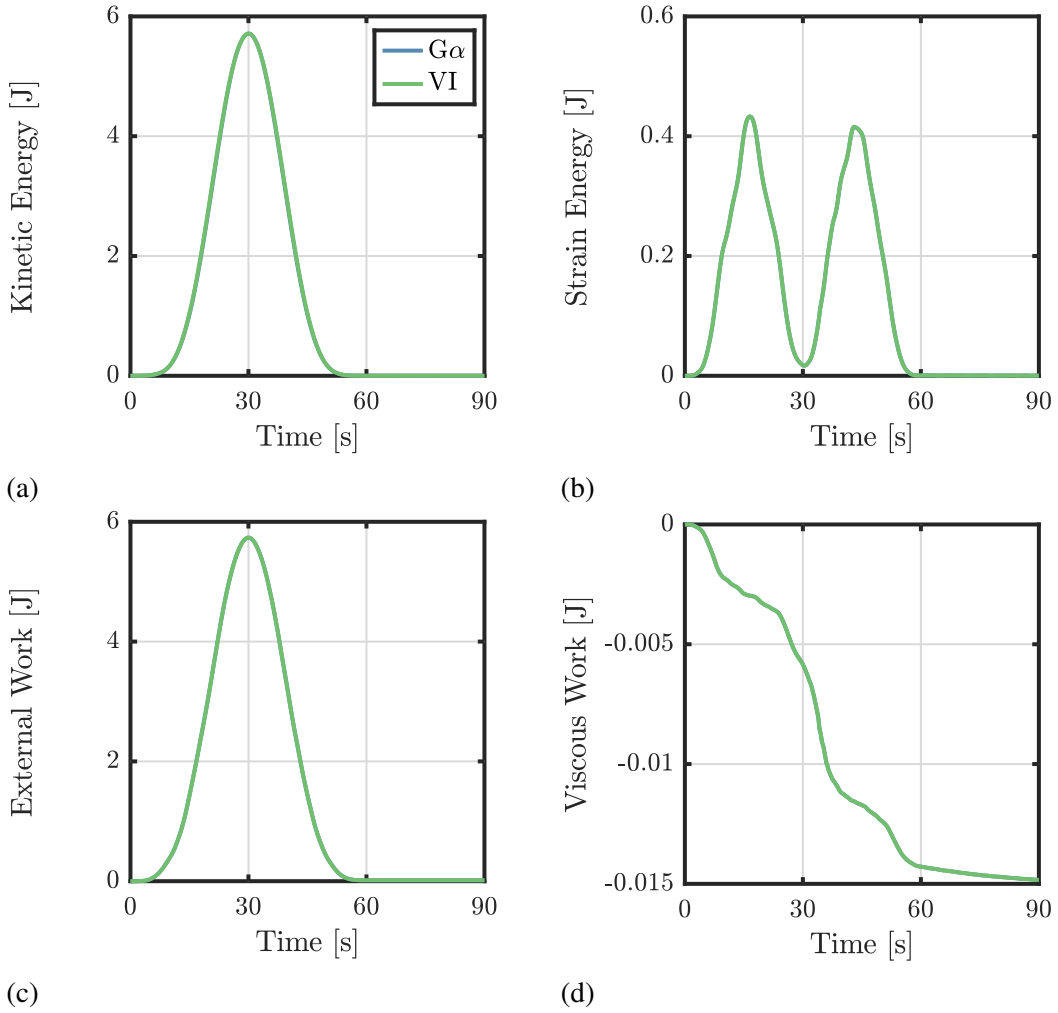

Figure 8.14: Comparison of (a) kinetic energy, (b) strain energy, (c) external work, and (d) viscous work from generalized-α method (Gα) and variational integrator (VI).

the configuration-dependent mass matrix [Eq. (5.57)]. In each case, the energy predictions from both integrators are virtually identical.

To highlight the discrepancies between each integrator's energy behavior, Fig. 8.15 compares their energy balances [Eq. (8.12)]. Since the spacecraft initially starts at rest in its undeformed configuration, perfect energy conservation implies $\mathcal{E}(t_k) = 0$ for all $k \in \{0,\ 1,\ \ldots,\ N-1\}$. For the generalized-$\alpha$ method, the errors in the energy balance are on the order of 10^{-6} J, which is approximately four orders of magnitude smaller than the viscous work and five or six orders of magnitude smaller than the other energy components. In contrast, the errors in the energy balance for the variational integrator are on the order of 10^{-2} J, i.e., they are of the same order

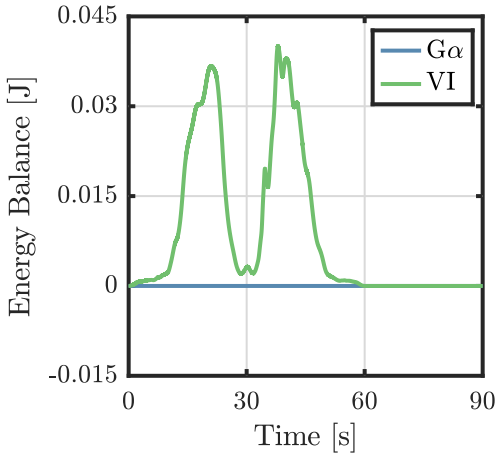

Figure 8.15: Comparison of energy balance [Eq. (8.12)] from generalized-α method (Gα) and variational integrator (VI).

of magnitude as the viscous work. Hence, the energy errors associated with the variational integrator are not negligible.

These results emphasize the disconnect between the fundamental theory of discrete mechanics underlying the variational integrator and its practical implementation. The theory demonstrates that the long-duration energy behavior of a variational integrator usually remains small and bounded [28]. However, theoretical guarantees are just that, theoretical, and are by no means immune to practical numerical problems. Here, the variational integrator's inferior energy behavior is likely due to its worse numerical conditioning than the generalized-α method. For implicit integrators, conditioning refers to the value of the condition number of the dynamic tangent matrix inverted during each Newton-Raphson iteration. With the generalized-α method, these condition numbers are typically on the order of 10^9, whereas with the variational integrator, they are typically on the order of 10^{13}. The higher the condition number, the worse the accuracy of the configuration update calculated from each matrix inversion. As a result, it is not surprising that the variational integrator's four order of magnitude increase in condition number translates into a proportional increase in its energy error. Similar relative errors between the generalized-α method and the variational integrator are observed across the range of simulated slew maneuvers. For a detailed discussion of related issues pertaining to the solvability of each Newton-Raphson iteration for Lie group variational integrators in rigid body dynamics, see [264].

As a final remark, the comparison of these two integrators is not entirely fair. The implementation of the Lie group generalized-α method uses the optimal precondi-

tioner from [179]. The variational integrator, on the other hand, does not benefit from any sort of preconditioner (aside from a multiplication of the linearized momentum balance by the time step h), let alone an optimal one, for the simple reason that an optimal preconditioner is currently unavailable in the literature. For that matter, the author is unaware of any examples in the literature of preconditioners for variational integrators. For these reasons, the results in this section do not invalidate the variational integrator. Instead, they emphasize that there are important practical developments required for variational integrators to reach the requisite level of maturity for wide-scale adoption in engineering.

8.6 Discussion

This chapter has studied the dynamics of ultralight flexible spacecraft during slew maneuvers. It first derived reduced-order modal models for a representative ultralight flexible spacecraft based on the Caltech Space Solar Power Project (SSPP) architecture with length scales between 5 m and 50 m. It subsequently used these reduced-order models to predict feasible slew times for a 90 deg, single-axis slew maneuver. These results compared the structure-based slew performance limits with those due to the available momentum and torque from the spacecraft's attitude control system. Consequently, they suggest that the attitude control system often imposes more restrictive slew limits than the structure. When the structure is not the limit, spacecraft can potentially fly lighter-weight, less-stiff, and lower-cost structures that result in structure-based performance limits closer to those of the rest of the system.

The chapter then demonstrated the feasibility of using geometrically nonlinear finite element models for simulating flexible spacecraft attitude dynamics during slew maneuvers. To facilitate these simulations, the chapter proposed a systematic approach for determining viscoelastic damping coefficients for geometrically exact finite element models. Simulations for a 24 m $\times$ 24 m SSPP spacecraft slewing 90 deg in as fast as 1 min showed that the peak deflections at the tips of the booms do not exceed 1 m. Similarly, the maximum out-of-plane bending moments in the strips do not exceed 0.15 N m, a value likely comparable to their critical buckling moments. Thus, the critical buckling moment imposes a lower bound on the slew time. Simulations for 90 deg slew maneuvers with durations from 1 min to 20 min subsequently established that the slew time predictions from the reduced-order models are both accurate and conservative. The excellent agreement between the reduced-order model and the full finite element model implies that the elastic deformations remain

in the small-deflection regime despite the large overall motions.

Taken together, these results indicate that a 24 m $\times$ 24 m flexible spacecraft with an approximately 25 mHz first mode can be slewed 90 deg in 10 min or less. This is one to two orders of magnitude faster than the current state-of-practice. For this reason, existing spacecraft designs are likely overly stiff with overly conservative design margins, which suggests that there are opportunities to either slew flexible spacecraft faster or fly less-conservative, lighter-weight spacecraft structures. Nevertheless, efforts to fly these structures must acknowledge the reality that many other design drivers (e.g., launch loads and propulsive maneuvers) also impose constraints on the structural design. These constraints may ultimately limit the achievable performance gains.

Lastly, the chapter has compared the performance of a more traditional structural dynamics integrator, the Lie group generalized-α method [36–38], with the variational integrator from Chapter 6 for simulating slew maneuver dynamics. Structure-preserving integrators like variational integrators initially appeared promising for these simulations due to their usually excellent long-duration energy behavior. However, contrary to expectations (and the results in Chapter 6), the variational integrator actually exhibited inferior energy behavior during the slew maneuver simulations. This is likely a numerical artifact associated with the variational integrator's comparatively poor numerical conditioning, which suggests that there are important practical considerations currently limiting the utility of variational integrators for some larger-scale engineering problems.

Chapter 9

CONCLUSION

9.1 Summary and Contributions

This thesis has studied the feasibility and limitations of slewing next-generation, ultralight flexible spacecraft with natural frequencies up to several orders of magnitude lower than the current state-of-the-art. The results demonstrate that contrary to common assumptions, structure-based slew performance limits are often less-restrictive than those associated with other constraints on the spacecraft. In particular, they show that the available momentum and torque capacities of the spacecraft's attitude control system are often significantly more limiting than the structure. This suggests that current spacecraft structural designs for many applications are overly stiff with overly conservative design margins. Thus, the results emphasize that flexible spacecraft can either be maneuvered faster (if sufficiently capable actuators are available) or be constructed with lighter-weight, less-stiff, and lower-cost structures that achieve structure-based performance limits closer to those of the rest of the system. Ultimately, geometrically nonlinear finite element simulations illustrate how a 24 m $\times$ 24 m flexible spacecraft with a first-mode frequency of approximately 25 mHz can be slewed 90 deg about a single axis in 10 min or less. This is significantly faster than the current state-of-practice.

The specific contributions of each chapter of the thesis are as follows:

Chapter 2 provided a motivating example for much of the rest of the thesis: the Caltech Space Solar Power Project (SSPP) [13]. The Caltech SSPP concept is predicated on the use of ultralight flexible spacecraft to achieve an order of magnitude reduction in mass, and hence, cost, compared to more traditional space solar power concepts. However, maximizing the transmitted power requires two approximately 90 deg, single-axis slew maneuvers per orbit [40]. The results emphasize that the slew time has a significant effect on the average power transmission efficiency, with faster slew maneuvers being more efficient. For example, decreasing the slew time from 2 h to 10 min is found to be comparable to increasing the photovoltaic cell efficiency from 25% to 26%.

Chapter 3 demonstrated the use of the Craig-Bampton method [30, 31] to rigorously derive low-order modal models for flexible spacecraft and addressed issues pertain-

ing to mode selection and model reduction for symmetric structures. The chapter then showed that settling time is a poor metric for determining flexible spacecraft slew maneuver requirements. This is because settling times can lead to slew times that are hundreds of times or more longer than the spacecraft's fundamental natural period. Instead, the chapter proposed using a new performance metric based on the amplitude of the residual angular velocity after a slew for determining slew maneuver requirements. The fundamental idea underlying this metric is that it is more advantageous to maintain any residual flexible dynamics to a tolerable level than it is to wait for them to dissipate. Finally, the results emphasized that both the "shape" of a slew maneuver and the ratio T/T_n between the slew time T and fundamental natural period T_n drive the dynamics during and after a slew. As an example, it illustrated how a simple "smooth" slew can reduce the amplitude of the residual angular velocity by several orders of magnitude compared to a more standard "bang-bang" one.

Chapters 4, 5, and 6 proposed two novel quaternion-based geometrically exact beam finite elements. Chapter 5 specifically proposed a continuous-time, quaternion-based reparameterization of the geometrically exact beam finite element from [121]. The quaternion parameterization yields a finite element with several incremental improvements over much of the existing state-of-the-art. Chapter 6 then proposed a quaternion-based variational integrator for simulating the dynamics of geometrically exact beams. The derivation used a structure-preserving temporal discretization of the continuous-time variational principle based on a geometric interpretation of the midpoint quaternion. Both formulations are objective [129, 153, 154], i.e., their spatial discretizations (which in this case are based on spherical linear interpolation [133, 140]) preserve the invariance of the 1D continuum strain measures to superposed rigid body motions. This invariance is important for accurately simulating the dynamics of flexible spacecraft during large-rotation slew maneuvers. The variational integrator exhibited near-perfect energy conservation during long-duration simulations of several standard benchmark problems, whereas a more traditional structural dynamics integrator, the Lie group generalized-α method [36–38], exhibited significant non-physical energy decay. A major feature of both formulations is their use of recent results from quaternion calculus [139] to account for the Lie group structure of the rotational degrees of freedom. The mathematical approach is conceptually much simpler than more traditional approaches rooted in differential geometry, and hence, intended to be more straightforward to derive and implement than many existing geometrically exact beam finite elements.

Chapter 7 used the finite elements from Chapter 5 to develop and implement a flexible multibody dynamics finite element model of a representative ultralight flexible spacecraft based on the Caltech SSPP structural architecture [13]. To increase its computational tractability, the model replaced the thin-shell, ladder-like structures called strips [35] from the original SSPP architecture with equivalent beams. A modal analysis of the complete finite element model then showed that the boom stiffness drives the dynamic properties of the structure. In particular, decreasing the boom stiffness increases the coupling between the vibrations of the booms and strips. Additionally, the modal analysis demonstrated that despite the structure's complexity, only a small number of modes (typically less than 10) are still responsible for the majority of the modal participation. This justified the subsequent use of reduced-order modal models in Chapter 8.

Chapter 8 described the most important results of the thesis. The chapter first used the methods from Chapter 3 and the finite element model from Chapter 7 to derive reduced-order modal models of the representative ultralight flexible spacecraft. These reduced-order models were then used to evaluate the slew performance metric from Chapter 3 and predict minimum slew times. Comparisons with the slew performance limits imposed by the capabilities of the spacecraft's attitude control system stressed that the structure is often not the limit on slew performance. Instead, the available momentum and torque were shown to often be significantly more limiting than the structure. The chapter then demonstrated the use of geometrically nonlinear finite element models for simulating flexible spacecraft attitude dynamics. These simulations revealed insights into the spacecraft's slew maneuver dynamics and confirmed both the accuracy and conservatism of the reduced-order models. Based on these results, it was concluded that a 24 m $\times$ 24 m flexible spacecraft with an approximately 25 mHz first mode can feasibly be slewed 90 deg about a single axis in 10 min or less. This is significantly faster than the current state-of-practice. Finally, the chapter applied the variational integrator from Chapter 6 to the slew maneuver problem and compared the results with those from the Lie group generalized-α method. The results were unexpected. The variational integrator exhibited similar displacement accuracies but inferior energy behavior due to its comparatively poor numerical conditioning. This provides the motivation for some of the future work in Sec. 9.2.

Collectively, the results in Chapter 8 emphasize that existing spacecraft designs are likely overly stiff and overly conservative, opening the door to the deployment of

lighter-weight, less-stiff, lower-cost, and higher-performance spacecraft structures. However, any attempts to improve structural performance must acknowledge the reality that slewing is just one of many important structural design drivers. The constraints associated with other structural design drivers (e.g., launch loads and propulsive maneuvers) may ultimately limit the achievable performance gains.

9.2 Future Research Directions

This thesis is a proof of concept for demonstrating the feasibility of slewing larger and more flexible spacecraft faster. However, there is substantial future work required to advance the requisite technologies towards flight. To that end, possible directions for future research are outlined below.

1. Design for dynamics

Much of the work in this thesis emphasizes the close relationship between structural design and dynamic performance. Achieving higher performance likely requires more careful consideration of the interactions between the structural design and its dynamics. A recent study by Lee and Pellegrino [24] proposes a framework for the optimal quasi-static design of ultralight spacecraft structural architectures. Thus, a possible avenue for future work involves extending their design framework to include dynamic effects, e.g., how the boom stiffness determines the peak internal bending moments in the strips. Ideally, any such design framework should also include slew maneuver performance, and potentially even the slew maneuver itself, as design variables in the optimization. Ultimately, more tightly coupling the structure, dynamic, and slew maneuver designs is likely to result in more efficient, higher-performing space systems.

2. Robust slew maneuvers

Chapter 3 demonstrates that even simple "smooth" slew maneuvers can significantly reduce the impact of the residual flexible dynamics, in this case, by several orders of magnitude relative to a baseline "bang-bang" slew. This result suggests that there is an opportunity to use modern robust optimal control methods [100–103] (likely in conjunction with the types of reduced-order models discussed in this thesis) to design slew maneuvers that are simultaneously robust to the uncertainties inherent to flexible spacecraft structures, minimize the impact of the residual flexible dynamics, and satisfy any constraints on the system. Importantly, these maneuvers can likely be flown using existing spacecraft attitude control systems, making them a potentially low-risk approach for improving the performance of flexible spacecraft.

3. Dynamics and control experiments

There are considerable difficulties associated with doing representative, laboratory-scale experiments of ultralight flexible spacecraft dynamics. It is particularly difficult to replicate both their low-frequency flexible dynamics and the absence of gravity. For example, even though the Caltech SSPP has developed several laboratory-scale prototypes of their spacecraft structural architecture [7, 218], these prototypes are too stiff to use in representative experiments of the full-scale flight system. For these reasons, the work in this thesis is purely computational. However, the costs and complexities associated with in-space technology demonstrations motivate the development of experiments to support technology maturation and risk reduction. Several recent studies [265, 266] are proofs of concept for the requisite experiments, albeit with structural dynamics several orders of magnitude higher in frequency than those studied here. Initial experiments should focus on model development, validation, and uncertainty quantification for simple slew maneuvers of very flexible structures. Subsequent experiments can study more complex slew maneuvers and structures, like those susceptible to localized nonlinearities [217], and should include the requisite hardware and software for closed-loop attitude control. Additionally, these experiments can demonstrate the use of reduced-order models during the design, analysis, and real-time implementation of complex slew maneuvers and optimal controllers for ultralight flexible spacecraft.

4. Computational modeling

Due to the difficulties associated with testing large, flexible spacecraft in representative 0-g environments before launch [14–18], computational modeling is likely to play an outsize role in their verification, validation, and risk reduction. As a result, efficient, high-fidelity simulations are expected to be paramount throughout the design and operation of these spacecraft. Since high-fidelity finite element models are traditionally used for analysis, not design, increasing their computational efficiency has the potential to promote their more widespread use throughout the spacecraft design life cycle.

The numerical methods developed in this thesis are limited to the prediction of macroscale structural phenomena, and hence, are unable to capture the small-scale nonlinearities like localization and buckling that are characteristic of ultralight composite spacecraft structures [24, 215, 217, 227]. High-fidelity models are important for accurately predicting the structural dynamic effects of these localized nonlinearities, for expanding a spacecraft's flight envelope to include more aggressive

on-orbit maneuvers, and for validating reduced-order models. Nonlinear model order reduction techniques, like those based on nonlinear Galerkin projections [267] and hyper-reduction [268], are potentially promising for efficiently modeling these localized nonlinearities, although these techniques are predicated on the availability of a sufficiently high-fidelity finite element model. An alternative approach is to incorporate localized nonlinearities into geometrically exact beam finite element formulations, e.g., by using a Carrera-type formulation that models cross-sectional deformations [122] or by using nonlinear homogenization techniques to derive nonlinear, deformation-dependent constitutive relations.

Additionally, the results in this thesis highlight several limitations of existing structure-preserving numerical methods. Current structure-preserving spatial discretizations for rotational degrees of freedom, like spherical linear interpolation [133, 140], are analogous to linear interpolation on a Lie group. This leads to low-order finite element formulations. Higher-order Lie group interpolation methods can improve both the accuracy and efficiency of the resulting finite elements. Similarly, the quaternion-based variational integrator for geometrically exact beams developed in Chapter 6 exhibits poor numerical conditioning for larger-scale problems. This emphasizes the importance of addressing the numerous practical considerations required for these types of integrators to reach sufficient maturity for their more widespread adoption in engineering. Here, possible lines of inquiry include the development of optimal preconditioners to reduce problems associated with ill-conditioning and a study of the relationship between the temporal discretization of the variational principle and the numerical properties of the resulting discrete-time propagation equations.

BIBLIOGRAPHY

[1] V. J. Modi, "Attitude Dynamics of Satellites with Flexible Appendages — A Brief Review," *Journal of Spacecraft and Rockets*, vol. 11, no. 11, pp. 743–751, 1974. DOI: 10.2514/3.62172.

[2] P. Likins, "The New Generation of Dynamic Interaction Problems," *Journal of the Astronautical Sciences*, vol. 27, no. 2, pp. 103–113, 1979.

[3] M. Mobrem and D. S. Adams, "Deployment Analysis of the Lenticular Jointed Antennas Onboard the Mars Express Spacecraft," *Journal of Spacecraft and Rockets*, vol. 46, no. 2, pp. 394–402, 2009. DOI: 10.2514/1.36890.

[4] H. M. Y. C. Mallikarachchi and S. Pellegrino, "Deployment Dynamics of Ultrathin Composite Booms with Tape-Spring Hinges," *Journal of Spacecraft and Rockets*, vol. 51, no. 2, pp. 604–613, 2014. DOI: 10.2514/1.A32401.

[5] M. K. Chamberlain, S. H. Kiefer, M. LaPointe, and P. LaCorte, "On-orbit flight testing of the Roll-Out Solar Array," *Acta Astronautica*, vol. 179, pp. 407–414, 2021. DOI: 10.1016/j.actaastro.2020.10.024.

[6] A. Pedivellano and S. Pellegrino, "Deployment Dynamics of Thin-Shell Space Structures," *Journal of Spacecraft and Rockets*, 2022. DOI: 10.2514/1.A35172.

[7] E. Gdoutos, A. Truong, A. Pedivellano, F. Royer, and S. Pellegrino, "Ultralight Deployable Space Structure Prototype," in *AIAA SciTech Forum*, AIAA 2020-0692, Orlando, Florida, 2020. DOI: 10.2514/6.2020-0692.

[8] A. Pedivellano, E. Gdoutos, and S. Pellegrino, "Sequentially Controlled Dynamic Deployment of Ultra-Thin Shell Structures," in *AIAA SciTech Forum*, AIAA 2020-0690, Orlando, Florida, 2020. DOI: 10.2514/6.2020-0690.

[9] J. M. Fernandez, G. Rose, O. R. Stohlman, C. J. Younger, G. D. Dean, J. E. Warren, J. H. Kang, R. G. Bryant, and K. W. Wilkie, "An Advanced Composites-Based Solar Sail System for Interplanetary Small Satellite Missions," in *AIAA SciTech Forum*, AIAA 2018-1437, Kissimmee, Florida, 2018. DOI: 10.2514/6.2018-1437.

[10] T. R. Lockett, J. Castillo-Rogez, L. Johnson, J. Matus, J. Lightholder, A. Marinan, and A. Few, "Near-Earth Asteroid Scout Flight Mission," *IEEE Aerospace and Electronic Systems Magazine*, vol. 35, no. 3, pp. 20–29, 2020. DOI: 10.1109/MAES.2019.2958729.

[11] K. Kobayashi, L. Johnson, H. D. Thomas, S. McIntosh, D. McKenzie, J. Newmark, A. Heaton, J. Carr, M. Baysinger, Q. Bean, L. Fabisinski, P. Capizzo, K. Clements, S. Sutherlin, J. Garcia, K. Medina, and D. Turse, *The High Inclination Solar Mission*, https://arxiv.org/abs/2006.03111, arXiv:2006.03111. Accessed June 4, 2021, 2020.

[12] M. R. M. Hashemi, A. C. Fikes, M. Gal-Katziri, B. Abiri, F. Bohn, A. Safaripour, M. D. Kelzenberg, E. L. Warmann, P. Espinet, N. Vaidya, E. E. Gdoutos, C. Leclerc, F. Royer, S. Pellegrino, H. A. Atwater, and A. Hajimiri, "A flexible phased array system with low areal mass density," *Nature Electronics*, vol. 2, pp. 195–205, 2019. DOI: 10.1038/s41928-019-0247-9.

[13] M. Arya, N. Lee, and S. Pellegrino, "Ultralight Structures for Space Solar Power Satellites," in *AIAA SciTech Forum*, AIAA 2016-1950, San Diego, California, 2016. DOI: 10.2514/6.2016-1950.

[14] D. A. Rey, E. F. Crawley, H. L. Alexander, R. M. Glaese, and P. Gaudenzi, "Gravity and Suspension Effects on the Dynamics of Controlled Structures," in *34th Structures, Structural Dynamics and Materials Conference*, AIAA 93-1662-CP, La Jolla, California, 1993. DOI: 10.2514/6.1993-1662.

[15] R. M. Glaese and D. W. Miller, "Derivation of 0-g structural control models from analysis and 1-g experimentation," in *36th Structures, Structural Dynamics and Materials Conference*, AIAA 95-1121-CP, New Orleans, Louisiana, 1995. DOI: 10.2514/6.1995-1121.

[16] M. E. Campbell and E. F. Crawley, "Development of Structural Uncertainty Models," *Journal of Guidance, Control, and Dynamics*, vol. 20, no. 5, pp. 841–849, 1997. DOI: 10.2514/2.4133.

[17] A. Fischer and S. Pellegrino, "Interaction Between Gravity Compensation Suspension System and Deployable Structure," *Journal of Spacecraft and Rockets*, vol. 31, no. 1, pp. 93–99, 2000. DOI: 10.2514/2.3531.

[18] A. Fratian, S. K. Jeon, K. Cheung, J. C. Griffee, B. Urioste, and C. Box, "Gravity Off-Load Follower (GOLF) Cart System for Ground-Based Spacecraft Testing," in *AIAA SciTech Forum*, AIAA 2020-1440, Orlando, Florida, 2020. DOI: 10.2514/6.2020-1440.

[19] T. R. Kane and D. A. Levinson, "Formulation of Equations of Motion for Complex Spacecraft," *Journal of Guidance, Control, and Dynamics*, vol. 3, no. 2, pp. 99–112, 1980. DOI: 10.2514/3.55956.

[20] S. N. Atluri and A. K. Amos, Eds., *Large Space Structures: Dynamics and Control*, 1st. Berlin, Heidelberg: Springer, 1988. DOI: 10.1007/978-3-642-83376-2.

[21] V. J. Modi, "Spacecraft attitude dynamics: Evolution and current challenges," *Acta Astronautica*, vol. 21, no. 10, pp. 689–718, 1990. DOI: 10.1016/0094-5765(90)90097-5.

[22] A. K. Banerjee, *Flexible Multibody Dynamics: Efficient Formulations and Applications*, 1st. Chichester, United Kingdom: John Wiley & Sons, Ltd., 2016. DOI: 10.1002/9781119015635.

[23] P. C. Hughes, "Space structure vibration modes: How many exist? Which ones are important?" *IEEE Control Systems Magazine*, vol. 7, no. 1, pp. 22–28, 1987. DOI: 10.1109/MCS.1987.1105241.

[24] A. J. Lee and S. Pellegrino, "Architectures for lightweight deployable plate-like space structures," *International Journal of Solids and Structures*, 2022, under review.

[25] J. Chung and G. M. Hulbert, "A Time Integration Algorithm for Structural Dynamics With Improved Numerical Dissipation: The Generalized-α Method," *Journal of Applied Mechanics*, vol. 60, no. 2, pp. 371–375, 1993. DOI: 10.1115/1.2900803.

[26] H. Sharma, M. Patil, and C. Woolsey, "A review of structure-preserving numerical methods for engineering applications," *Computer Methods in Applied Mechanics and Engineering*, vol. 366, p. 113 067, 2020. DOI: 10.1016/j.cma.2020.113067.

[27] G. Zhong and J. E. Marsden, "Lie-Poisson Hamilton-Jacobi theory and Lie-Poisson integrators," *Physics Letters A*, vol. 133, no. 3, pp. 134–139, 1988. DOI: 10.1016/0375-9601(88)90773-6.

[28] J. E. Marsden and M. West, "Discrete mechanics and variational integrators," *Acta Numerica*, vol. 10, pp. 357–514, 2001. DOI: 10.1017/S096249290100006X.

[29] A. Lew, J. E. Marsden, M. Ortiz, and M. West, "Variational time integrators," *International Journal for Numerical Methods in Engineering*, vol. 60, no. 1, pp. 153–212, 2004. DOI: 10.1002/nme.958.

[30] R. R. Craig Jr. and M. C. C. Bampton, "Coupling of Substructures for Dynamic Analyses," *AIAA Journal*, vol. 6, no. 7, pp. 1313–1319, 1968. DOI: 10.2514/3.4741.

[31] R. R. Craig Jr. and A. J. Kurdila, "Component-Mode Synthesis," in *Fundamentals of Structural Dynamics*, 2nd. Hoboken, New Jersey: John Wiley & Sons, 2001, ch. 17, pp. 531–575.

[32] E. Reissner, "On One-Dimensional Large-Displacement Finite-Strain Beam Theory," *Studies in Applied Mathematics*, vol. 52, no. 2, pp. 87–95, 1973. DOI: 10.1002/sapm197352287.

[33] E. Reissner, "On finite deformations of space-curved beams," *Journal of Applied Mathematics and Physics (ZAMP)*, vol. 32, pp. 734–744, 1981. DOI: 10.1007/BF00946983.

[34] J. C. Simo, "A finite strain beam formulation. The three-dimensional dynamic problem. Part I," *Computer Methods in Applied Mechanics and Engineering*, vol. 49, no. 1, pp. 55–70, 1985. DOI: 10.1016/0045-7825(85)90050-7.

[35] F. Royer and S. Pellegrino, "Ultralight Ladder-type Coilable Space Structures," in *AIAA SciTech Forum*, AIAA 2018-1200, Kissimmee, Florida, 2018. DOI: 10.2514/6.2018-1200.

[36] O. Brüls and A. Cardona, "On the Use of Lie Group Time Integrators in Multibody Dynamics," *Journal of Computational and Nonlinear Dynamics*, vol. 5, no. 3, p. 031 002, 2010. DOI: 10.1115/1.4001370.

[37] O. Brüls, A. Cardona, and M. Arnold, "Lie group generalized-α time integration of constrained flexible multibody systems," *Mechanism and Machine Theory*, vol. 48, pp. 121–137, 2012. DOI: 10.1016/j.mechmachtheory.2011.07.017.

[38] M. Arnold, O. Brüls, and A. Cardona, "Error analysis of generalized-α Lie group time integration methods for constrained mechanical systems," *Numerische Mathematik*, vol. 129, pp. 149–179, 2015. DOI: 10.1007/s00211-014-0633-1.

[39] M. A. Marshall, A. Goel, and S. Pellegrino, "Attitude maneuver design for planar space solar power satellites," in *29th AAS/AIAA Space Flight Mechanics Meeting*, AAS 19-287, Ka'anapali, Maui, Hawaii, 2019.

[40] M. A. Marshall, A. Goel, and S. Pellegrino, "Power-Optimal Guidance for Planar Space Solar Power Satellites," *Journal of Guidance, Control, and Dynamics*, vol. 43, no. 3, pp. 518–535, 2020. DOI: 10.2514/1.G004643.

[41] A. Goel, N. Lee, and S. Pellegrino, "Trajectory design of formation flying constellation for space-based solar power," in *IEEE Aerospace Conference*, Big Sky, Montana, 2017. DOI: 10.1109/AERO.2017.7943711.

[42] A. Goel, S.-J. Chung, and S. Pellegrino, "Trajectory Design of a Spacecraft Formation for Space-Based Solar Power Using Sequential Convex Programming," in *Proceedings of the 9th International Workshop on Satellites Constellations and Formation Flying (IWSCFF)*, Boulder, Colorado, 2017.

[43] I. Asimov, "Reason," in *I, Robot*, 1941, pp. 59–77.

[44] P. E. Glaser, "Power from the Sun: Its Future," *Science*, vol. 162, no. 3856, pp. 857–861, 1968. DOI: 10.1126/science.162.3856.857.

[45] C. Carrington, J. Fikes, M. Gerry, D. Perkinson, H. Feingold, and J. Olds, "The Abacus/Reflector and Integrated Symmetrical Concentrator: Concepts for Space Solar Power Collection and Transmission," in *35th Intersociety Energy Conversion Engineering Conference and Exhibit*, AIAA-2000-3067, Las Vegas, Nevada, 2000. DOI: 10.2514/6.2000-3067.

[46] J. C. Mankins, "A Technical Overview of the 'SunTower' Solar Power Satellite Concept," *Acta Astronautica*, vol. 50, no. 6, pp. 369–377, 2002. DOI: 10.1016/S0094-5765(01)00167-9.

[47] S. Sasaki, K. Tanaka, K. Higuchi, N. Okuizumi, S. Kawasaki, N. Shinohara, K. Senda, and K. Ishimura, "A new concept of solar power satellite: Tethered-SPS," *Acta Astronautica*, vol. 60, no. 3, pp. 153–165, 2007. DOI: 10.1016/j.actaastro.2006.07.010.

[48] E. E. Gdoutos, C. Leclerc, F. Royer, M. D. Kelzenberg, E. C. Warmann, P. Espinet-Gonzalez, N. Vaidya, F. Bohn, B. Abiri, M. R. Hashemi, M. Gal-Katziri, A. Fikes, H. Atwater, A. Hajimiri, and S. Pellegrino, "A Lightweight Tile Structure Integrating Photovoltaic Conversion and RF Power Transfer for Space Solar Power Applications," in *AIAA SciTech Forum*, AIAA-2018-2022, Kissimmee, Florida, 2018. DOI: 10.2514/6.2018-2202.

[49] E. C. Warmann, P. Espinet-Gonzalez, N. Vaidya, S. Loke, A. Naqavi, T. Vinogradova, M. Kelzenberg, C. Leclerc, E. Gdoutos, S. Pellegrino, and H. A. Atwater, "An ultralight concentrator photovoltaic system for space solar power harvesting," *Acta Astronautica*, vol. 170, pp. 443–451, 2020. DOI: 10.1016/j.actaastro.2019.12.032.

[50] J. Li, A. Aierken, Y. Liu, Y. Zhuang, X. Yang, J. H. Mo, R. K. Fan, Q. Y. Chen, S. Y. Zhang, Y. M. Huang, and Q. Zhang, "A Brief Review of High Efficiency III-V Solar Cells for Space Application," *Frontiers in Physics*, vol. 8, 2021. DOI: 10.3389/fphy.2020.631925.

[51] J. M. Raya-Armenta, N. Bazmohammadi, J. C. Vasquez, and J. M. Guerrero, "A short review of radiation-induced degradation of III-V photovoltaic cells for space applications," *Solar Energy Materials and Solar Cells*, vol. 233, p. 111 379, 2021. DOI: 10.1016/j.solmat.2021.111379.

[52] B. M. Kayes, L. Zhang, R. Twist, I.-K. Ding, and G. S. Higashi, "Flexible Thin-Film Tandem Solar Cells With >30% Efficiency," *IEEE Journal of Photovoltaics*, vol. 4, no. 2, pp. 729–733, 2014. DOI: 10.1109/JPHOTOV.2014.2299395.

[53] J.-S. Huang, M. D. Kelzenberg, P. Espinet-González, C. Mann, D. Walker, A. Naqavi, N. Vaidya, E. Warmann, and H. A. Atwater, "Effects of Electron and Proton Radiation on Perovskite Solar Cells for Space Solar Power Application," in *2017 IEEE 44th Photovoltaic Specialist Conference (PVSC)*, Washington, DC, 2017, pp. 1248–1252. DOI: 10.1109/PVSC.2017.8366410.

[54] I. Cardinaletti, T. Vangerven, S. Nagels, R. Cornelissen, D. Schreurs, J. Hruby, J. Vodnik, D. Devisscher, J. Kesters, J. D'Haen, A. Franquet, V. Spampinato, T. Conard, W. Maes, W. Deferme, and J. V. Manca, "Organic and perovskite solar cells for space applications," *Solar Energy Materials and Solar Cells*, vol. 182, pp. 121–127, 2018. DOI: 10.1016/j.solmat.2018.03.024.

[55] A. W. Y. Ho-Baillie, H. G. J. Sullivan, T. A. Bannerman, H. P. Talathi, J. Bing, S. Tang, A. Xu, D. Bhattacharyya, I. H. Cairns, and D. R. McKenzie, "Deployment Opportunities for Space Photovoltaics and the Prospects for Perovskite Solar Cells," *Advanced Materials Technologies*, vol. 7, no. 3, p. 2 101 059, 2022. DOI: 10.1002/admt.202101059.

[56] P. Espinet-Gonzalez, E. Barrigón, G. Otnes, G. Vescovi, C. Mann, R. M. France, A. J. Welch, M. S. Hunt, D. Walker, M. D. Kelzenberg, I. Åberg, M. T. Borgström, L. Samuelson, and H. A. Atwater, "Radiation Tolerant Nanowire Array Solar Cells," *ACS Nano*, vol. 13, pp. 12 860–12 869, 2019. DOI: 10.1021/acsnano.9b05213.

[57] P. Espinet-Gonzalez, E. Barrigón, Y. Chen, G. Otnes, G. Vescovi, C. Mann, J. V. Lloyd, D. Walker, M. D. Kelzenberg, I. Åberg, M. Borgström, L. Samuelson, and H. A. Atwater, "Nanowire Solar Cells: A New Radiation Hard PV Technology for Space Applications," *IEEE Journal of Photovoltaics*, vol. 10, no. 2, pp. 502–507, 2020. DOI: 10.1109/JPHOTOV.2020.2966979.

[58] M. Gal-Katziri, "Precision at Scale: System Design from Tiny Biosensors to Giant Arrays," Ph.D. dissertation, California Institute of Technology, Pasadena, California, 2021. DOI: 10.7907/t3cz-c785.

[59] C. A. Balanis, *Antenna Theory: Analysis and Design*, 3rd. Hoboken, New Jersey: John Wiley & Sons, Inc., 2005.

[60] W. H. Press, B. P. Flannery, S. A. Teukolsky, and W. T. Vetterling, in *Numerical Recipes in C: The Art of Scientific Computing*, 2nd. New York: Cambridge University Press, 1992, ch. 10, pp. 397–402.

[61] A. C. Fikes, "Future Microwave Arrays Take Shape," Ph.D. dissertation, California Institute of Technology, Pasadena, California, 2022. DOI: 10.7907/h541-3e28.

[62] T. Bayer, M. Bittner, B. Buffington, G. Dubos, E. Ferguson, I. Harris, M. Jackson, G. Lee, K. Lewis, J. Kastner, R. Morillo, R. Perez, M. Salami, J. Signorelli, O. Sindiy, B. Smith, M. Soriano, K. Kirby, and N. Laslo, "Europa Clipper Mission: Preliminary Design Report," in *IEEE Aerospace Conference*, Big Sky, Montana, 2019. DOI: 10.1109/AERO.2019.8741777.

[63] J. T. Spanos., "Control-Structure Interaction in Precision Pointing Servo Loops," *Journal of Guidance, Control, and Dynamics*, vol. 12, no. 2, pp. 256–263, 1989. DOI: 10.2514/3.20399.

[64] B. Wie, *Space Vehicle Dynamics and Control*, 2nd. Reston, Virginia: American Institute of Aeronautics and Astronautics, 2008.

[65] K. Ogata, *System Dynamics*, 4th. Upper Saddle River, New Jersey: Pearson Education, Inc., 2004.

[66] T. R. Sutter, P. A. Cooper, J. W. Young, and D. K. McCutchen, "Dynamic and Attitude Control Characteristics of an International Space Station," in *28th Structures, Structural Dynamics and Materials Conference*, AIAA 87-0931, Monterey, California, 1987. DOI: 10.2514/6.1987-931.

[67] P. E. Nikravesh, "Understanding mean-axis conditions as floating reference frames," in *Advances in Computational Multibody Systems*, vol. 2, Dordrecht, Netherlands: Springer, 2005, pp. 185–203. DOI: 10.1007/1-4020-3393-1.

[68] A. A. Shabana, *Dynamics of Multibody Systems*, 4th. New York: Cambridge University Press, 2013. DOI: 10.1017/CBO9781107337213.

[69] A. Zwölfer and J. Gerstmayr, "A concise nodal-based derivation of the floating frame of reference formulation for displacement-based solid finite elements," *Multibody System Dynamics*, vol. 49, pp. 291–313, 2020. DOI: 10.1007/s11044-019-09716-x.

[70] M. Géradin and A. Cardona, *Flexible Multibody Dynamics: A Finite Element Approach*, 1st. Chichester, United Kingdom: John Wiley & Sons, 2001.

[71] D. C. Kammer and M. J. Triller, "Ranking the Dynamic Importance of Fixed Interface Modes Using a Generalization of Effective Mass," *International Journal of Analytical and Experimental Modal Analysis*, vol. 9, no. 2, pp. 77–98, 1994.

[72] M. J. Triller and D. C. Kammer, "Controllability and Observability Measures for Craig-Bampton Substructure Representations," *Journal of Guidance, Control, and Dynamics*, vol. 17, no. 6, pp. 1198–1204, 1994. DOI: 10.2514/3.21333.

[73] A. M. A. Hamdan and A. H. Nayfeh, "Measures of Modal Controllability and Observability for First- and Second-Order Linear Systems," *Journal of Guidance, Control, and Dynamics*, vol. 12, no. 3, pp. 421–428, 1989. DOI: 10.2514/3.20424.

[74] D. C. Kammer and M. J. Triller, "Selection of Component Modes for Craig-Bampton Substructure Representations," *Journal of Vibration and Acoustics*, vol. 118, no. 2, pp. 264–270, 1996. DOI: 10.1115/1.2889657.

[75] B. C. Moore, "Principal component analysis in linear systems: Controllability, observability, and model reduction," *IEEE Transactions on Automatic Control*, vol. 26, no. 1, pp. 17–32, 1981. DOI: 10.1109/TAC.1981.1102568.

[76] E. A. Jonckheere, "Principal component analysis of flexible systems–Open-loop case," *IEEE Transactions on Automatic Control*, vol. 29, no. 12, pp. 1095–1097, 1984. DOI: 10.1109/TAC.1984.1103457.

[77] C. Z. Gregory Jr., "Reduction of Large Flexible Spacecraft Models Using Internal Balancing Theory," *Journal of Guidance, Control, and Dynamics*, vol. 7, no. 6, pp. 725–732, 1984. DOI: 10.2514/3.19919.

[78] K.-J. Bathe and E. L. Wilson, "Solution methods for eigenvalue problems in structural mechanics," *International Journal for Numerical Methods in Engineering*, vol. 6, no. 2, pp. 213–226, 1973. DOI: 10.1002/nme.1620060207.

[79] A. Zingoni, "Group-theoretic exploitations of symmetry in computational solid and structural mechanics," *International Journal for Numerical Methods in Engineering*, vol. 79, no. 3, pp. 253–289, 2009. DOI: 10.1002/nme.2576.

[80] C. R. McInnes, "Satellite attitude slew manoeuvres using inverse control," *The Aeronautical Journal*, vol. 102, no. 1015, pp. 259–266, 1998. DOI: 10.1017/S0001924000065295.

[81] M. Muenchhof and T. Singh, "Desensitized Jerk Limited-Time Optimal Control of Multi-Input Systems," *Journal of Guidance, Control, and Dynamics*, vol. 25, no. 3, pp. 474–481, 2002. DOI: 10.2514/2.4933.

[82] T. A. Hindle and T. Singh, "Robust Minimum Power/Jerk Control of Maneuvering Structures," *Journal of Guidance, Control, and Dynamics*, vol. 24, no. 4, pp. 816–826, 2001. DOI: 10.2514/2.4783.

[83] J.-J. Kim and B. Agrawal, "Experiments on Jerk-Limited Slew Maneuvers of a Flexible Spacecraft," in *AIAA Guidance, Navigation, and Control Conference*, AIAA 2006-6187, Keystone, Colorado, 2006. DOI: 10.2514/6.2006-6187.

[84] F. A. Leve, B. J. Hamilton, and M. A. Peck, "Requirements Development for Momentum Control Systems," in *Spacecraft Momentum Control Systems*, 1st. Cham, Switzerland: Springer, 2015, ch. 3, pp. 35–55. DOI: 10.1007/978-3-319-22563-0_3.

[85] N. C. Singer and W. P. Seering, "Preshaping Command Inputs to Reduce System Vibration," *Journal of Dynamic Systems, Measurement, and Control*, vol. 112, no. 1, pp. 76–82, 1990. DOI: 10.1115/1.2894142.

[86] A. K. Banerjee, N. Pedreiro, and W. E. Singhose, "Vibration Reduction for Flexible Spacecraft Following Momentum Dumping With/Without Slewing," *Journal of Guidance, Control, and Dynamics*, vol. 24, no. 3, pp. 417–427, 2001. DOI: 10.2514/2.4737.

[87] T. Singh and W. Singhose, "Tutorial on Input Shaping/Time Delay Control of Maneuvering Flexible Structures," in *Proceedings of the 2002 American Control Conference*, vol. 3, Anchorage, Alaska, 2002, pp. 1717–1731. DOI: 10.1109/ACC.2002.1023813.

[88] W. Singhose, "Command Shaping for Flexible Systems: A Review of the First 50 Years," *International Journal of Precision Engineering and Manufacturing*, vol. 10, pp. 153–168, 2009. DOI: 10.1007/s12541-009-0084-2.

[89] J. M. Longuski, J. J. Guzmán, and J. E. Prussing, "Bounded Control Problems," in *Optimal Control with Aerospace Applications*, 1st. New York: Springer, 2013, ch. 9, pp. 175–191. DOI: 10.1007/978-1-4614-8945-0_9.

[90] M. Balas, "Trends in large space structure control theory: Fondest hopes, wildest dreams," *IEEE Transactions on Automatic Control*, vol. 27, no. 3, pp. 522–535, 1982. DOI: 10.1109/TAC.1982.1102953.

[91] B. C. Stiltner, B. Diedrich, C. Becker, I. Bertaska, A. Heaton, and J. Orphee, "Cold Gas Reaction Control System for the Near Earth Asteroid Scout Cubesat," in *AIAA SPACE and Astronautics Forum*, AIAA 2017-5185, Orlando, Florida, 2017. DOI: 10.2514/6.2017-5185.

[92] J. Orphee, B. Diedrich, B. C. Stiltner, and A. Heaton, "Solar Torque Management for the Near Earth Asteroid Scout CubeSat Using Center of Mass Position Control," in *AIAA SciTech Forum*, AIAA 2018-1326, Kissimmee, Florida, 2018. DOI: 10.2514/6.2018-1326.

[93] A. Y. Lee, J. W. Yu, P. B. Kahn, and R. L. Stoller, "Space Interferometry Mission Spacecraft Pointing Error Budgets," *IEEE Transactions on Aerospace and Electronic Systems*, vol. 38, no. 2, pp. 502–514, 2002. DOI: 10.1109/TAES.2002.1008982.

[94] D. S. Bayard, "Spacecraft Pointing Control Criteria for High Resolution Spectroscopy," *IEEE Transactions on Aerospace and Electronic Systems*, vol. 35, no. 2, pp. 637–644, 1999. DOI: 10.1109/7.766944.

[95] M. E. Pittelkau and W. G. McKinley, "Optical transfer functions, weighting functions, and metrics for images with two-dimensional line-of-sight motion," *Optical Engineering*, vol. 55, no. 6, p. 063 108, 2016. DOI: 10.1117/1.OE.55.6.063108.

[96] J. M. Hedgepeth, "Critical Requirements for the Design of Large Space Structures," in *2nd AIAA Conference on Large Space Platforms: Toward Permanent Manned Occupancy in Space*, AIAA-81-0443, San Diego, California, 1981. DOI: 10.2514/6.1981-443.

[97] R. W. Clough and J. Penzien, *Dynamics of Structures*, 1st. New York: McGraw-Hill, Inc., 1975.

[98] J. M. Biggs, *Introduction to Structural Dynamics*, 1st. New York: McGraw-Hill, Inc., 1964.

[99] J. R. Wertz, *Spacecraft Attitude Determination and Control*, 1st. Dordrecht, Netherlands: Springer, 1978. DOI: 10.1007/978-94-009-9907-7.

[100] I. M. Ross, R. J. Proulx, M. Karpenko, and Q. Gong, "Riemann–Stieltjes Optimal Control Problems for Uncertain Dynamic Systems," *Journal of Guidance, Control, and Dynamics*, vol. 38, no. 7, pp. 1251–1263, 2015. DOI: 10.2514/1.G000505.

[101] G. I. Boutselis, Y. Pan, and E. A. Theodorou, "Numerical Trajectory Optimization for Stochastic Mechanical Systems," *SIAM Journal on Scientific Computing*, vol. 41, no. 4, A2065–A2087, 2019. DOI: 10.1137/17M116272X.

[102] Z. Manchester and S. Kuindersma, "Robust direct trajectory optimization using approximate invariant funnels," *Autonomous Robots*, vol. 43, pp. 375–387, 2019. DOI: 10.1007/s10514-018-9779-5.

[103] Y. K. Nakka and S.-J. Chung, "Trajectory Optimization of Chance-Constrained Nonlinear Stochastic Systems for Motion Planning and Control," *IEEE Transactions on Robotics*, 2022, under review.

[104] C. M. Shearer and C. E. S. Cesnik, "Nonlinear Flight Dynamics of Very Flexible Aircraft," *Journal of Aircraft*, vol. 44, no. 5, pp. 1528–1545, 2007. DOI: 10.2514/1.27606.

[105] R. Palacios, J. Murua, and R. Cook, "Structural and Aerodynamic Models in Nonlinear Flight Dynamics of Very Flexible Aircraft," *AIAA Journal*, vol. 48, no. 11, pp. 2648–2659, 2010. DOI: 10.2514/1.J050513.

[106] D. H. Hodges, "Review of Composite Rotor Blade Modeling," *AIAA Journal*, vol. 28, no. 3, pp. 561–565, 1990. DOI: 10.2514/3.10430.

[107] D. L. Kunz, "Survey and Comparison of Engineering Beam Theories for Helicopter Rotor Blades," *Journal of Aircraft*, vol. 31, no. 3, pp. 473–479, 1994. DOI: 10.2514/3.46518.

[108] V. V. Volovoi, D. H. Hodges, C. E. S. Cesnik, and B. Popescu, "Assessment of beam modeling methods for rotor blade applications," *Mathematical and Computer Modelling*, vol. 33, no. 10–11, pp. 1099–1112, 2001. DOI: 10.1016/S0895-7177(00)00302-2.

[109] D. H. Hodges and W. Yu, "A rigorous, engineer-friendly approach for modelling realistic, composite rotor blades," *Wind Energy*, vol. 10, no. 2, pp. 179–193, 2007. DOI: 10.1002/we.215.

[110] Q. Wang, M. A. Sprague, J. Jonkman, N. Johnson, and B. Jonkman, "BeamDyn: A high-fidelity wind turbine blade solver in the FAST modular framework," *Wind Energy*, vol. 20, no. 8, pp. 1439–1462, 2017. DOI: 10.1002/we.2101.

[111] C. Damaren and I. Sharf, "Simulation of Flexible-Link Manipulators With Inertial and Geometric Nonlinearities," *Journal of Dynamic Systems, Measurement, and Control*, vol. 117, no. 1, pp. 74–87, 1995. DOI: 10.1115/1.2798525.

[112] J. Martins, M. A. Botto, and J. Sá da Costa, "Modeling of Flexible Beams for Robotic Manipulators," *Multibody System Dynamics*, vol. 7, pp. 79–100, 2002. DOI: 10.1023/A:1015239604152.

[113] C. Armanini, F. Dal Corso, D. Misseroni, and D. Bigoni, "From the elastica compass to the elastica catapult: An essay on the mechanics of soft robot arm," *Proceedings of the Royal Society A: Mathematical, Physical and Engineering Sciences*, vol. 473, no. 2198, 2017. DOI: 10.1098/rspa.2016.0870.

[114] S. Grazioso, G. Di Gironimo, and B. Siciliano, "A Geometrically Exact Model for Soft Continuum Robots: The Finite Element Deformation Space Formulation," *Soft Robotics*, vol. 6, no. 6, pp. 790–811, 2019. DOI: 10.1089/soro.2018.0047.

[115] A. A. Shabana, "Flexible Multibody Dynamics: Review of Past and Recent Developments," *Multibody System Dynamics*, vol. 1, pp. 189–222, 1997. DOI: 10.1023/A:1009773505418.

[116] T. M. Wasfy and A. K. Noor, "Computational strategies for flexible multibody systems," *Applied Mechanics Reviews*, vol. 56, no. 6, pp. 553–613, 2003. DOI: 10.1115/1.1590354.

[117] Y. Yang, I. Tobias, and W. K. Olson, "Finite element analysis of DNA supercoiling," *The Journal of Chemical Physics*, vol. 98, no. 2, pp. 1673–1686, 1993. DOI: 10.1063/1.464283.

[118] W. K. Wilkie, J. Warren, L. G. Horta, K. H. Lyle, J.-N. Juang, S. C. Gibbs, E. Dowell, D. V. Guerrant, and D. A. Lawrence, "Recent Advances in Heliogyro Solar Sail Structural Dynamics, Stability, and Control Research," in *AIAA SciTech Forum*, AIAA 2015-0431, Kissimmee, Florida, 2015. DOI: 10.2514/6.2015-0431.

[119] R. A. Laskin, P. W. Likins, and R. W. Longman, "Dynamical equations of a free-free beam subject to large overall motions," *Journal of the Astronautical Sciences*, vol. 31, no. 4, pp. 507–528, 1983.

[120] T. R. Kane, and A. K. Banerjee, "Dynamics of a Cantilever Beam Attached to a Moving Base," *Journal of Guidance, Control, and Dynamics*, vol. 10, no. 2, pp. 139–151, 1987. DOI: 10.2514/3.20195.

[121] A. Cardona and M. Géradin, "A beam finite element non-linear theory with finite rotations," *International Journal for Numerical Methods in Engineering*, vol. 26, no. 11, pp. 2403–2438, 1988. DOI: 10.1002/nme.1620261105.

[122] Z. Soltani and M. J. Santer, "Efficient geometrically-nonlinear analysis of tape spring flexures using a unified beam formulation," in *AIAA SciTech Forum*, AIAA 2021-1149, Virtual Event, 2021. DOI: 10.2514/6.2021-1149.

[123] M. A. Crisfield, "A consistent co-rotational formulation for non-linear, three-dimensional, beam-elements," *Computer Methods in Applied Mechanics and Engineering*, vol. 81, no. 2, pp. 131–150, 1990. DOI: 10.1016/0045-7825(90)90106-V.

[124] D. H. Hodges, "A mixed variational formulation based on exact intrinsic equations for dynamics of moving beams," *International Journal of Solids and Structures*, vol. 26, no. 11, pp. 1253–1273, 1990. DOI: 10.1016/0020-7683(90)90060-9.

[125] D. H. Hodges, "Geometrically Exact, Intrinsic Theory for Dynamics of Curved and Twisted Anisotropic Beams," *AIAA Journal*, vol. 41, no. 6, pp. 1131–1137, 2003. DOI: 10.2514/2.2054.

[126] I. Romero, "A comparison of finite elements for nonlinear beams: The absolute nodal coordinate and geometrically exact formulations," *Multibody System Dynamics*, vol. 20, pp. 51–68, 2008. DOI: 10.1007/s11044-008-9105-7.

[127] O. A. Bauchau, S. Han, A. Mikkola, and M. K. Matikainen, "Comparison of the absolute nodal coordinate and geometrically exact formulations for beams," *Multibody System Dynamics*, vol. 32, pp. 67–85, 2014. DOI: 10.1007/s11044-010-9223-x.

[128] C. Meier, A. Popp, and W. A. Wall, "Geometrically Exact Finite Element Formulations for Slender Beams: Kirchhoff-Love Theory Versus Simo-Reissner Theory," *Archives of Computational Methods in Engineering*, vol. 26, pp. 163–243, 2019. DOI: 10.1007/s11831-017-9232-5.

[129] M. A. Crisfield and G. Jelenić, "Objectivity of strain measures in the geometrically exact three-dimensional beam theory and its finite-element implementation," *Proceedings of the Royal Society A*, vol. 455, no. 1983, pp. 1125–1147, 1999. DOI: 10.1098/rspa.1999.0352.

[130] J. Argyris, "An excursfion into large rotations," *Computer Methods in Applied Mechanics and Engineering*, vol. 32, no. 1–3, pp. 85–155, 1982. DOI: 10.1016/0045-7825(82)90069-X.

[131] M. D. Shuster, "A Survey of Attitude Representations," *Journal of the Astronautical Sciences*, vol. 41, no. 4, pp. 439–517, 1993.

[132] F. L. Markley and J. L. Crassidis, "Matrices, Vectors, Frames, Transforms," in *Fundamentals of Spacecraft Attitude Determination and Control*, 1st. New York: Springer-Verlag, 2014, ch. 2, pp. 17–65. DOI: 10.1007/978-1-4939-0802-8_2.

[133] J. Solá, *Quaternion kinematics for the error-state Kalman filter*, https://arxiv.org/abs/1711.02508, arXiv:1711.02508. Accessed January 6, 2021, 2017.

[134] R. Zanetti, "Rotations, Transformations, Left Quaternions, Right Quaternions?" *Journal of the Astronautical Sciences*, vol. 66, pp. 361–381, 2019. DOI: 10.1007/s40295-018-00151-2.

[135] J. E. Marsden and T. S. Ratiu, *Introduction to Mechanics and Symmetry*, 2nd. New York: Springer, 1999. DOI: 10.1007/978-0-387-21792-5.

[136] H. Sommer, I. Gilitschenski, M. Bloesch, S. Weiss, R. Siegwart, and J. Nieto, "Why and How to Avoid the Flipped Quaternion Multiplication," *Aerospace*, vol. 5, no. 3, p. 72, 2019. DOI: 10.3390/aerospace5030072.

[137] R. A. Spurrier, "Comment on 'Singularity-Free Extraction of a Quaternion from a Direction-Cosine Matrix'," *Journal of Spacecraft and Rockets*, vol. 15, no. 4, p. 255, 1978. DOI: 10.2514/3.57311.

[138] F. L. Markley, "Unit Quaternion from Rotation Matrix," *Journal of Guidance, Control, and Dynamics*, vol. 31, no. 2, pp. 440–442, 2008. DOI: 10.2514/1.31730.

[139] B. E. Jackson, K. Tracy, and Z. Manchester, "Planning with attitude," *IEEE Robotics and Automation Letters*, vol. 6, no. 3, pp. 5658–5664, 2021. DOI: 10.1109/LRA.2021.3052431.

[140] E. B. Dam, M. Koch, and M. Lillholm, "Quaternions, Interpolation and Animation," University of Copenhagen, Copenhagen, Denmark, Tech. Rep. DIKU-TR-98/5, 1998.

[141] I. Romero and F. Armero, "An objective finite element approximation of the kinematics of geometrically exact rods and its use in the formulation of an energy-momentum conserving scheme in dynamics," *International Journal for Numerical Methods in Engineering*, vol. 54, no. 12, pp. 1683–1716, 2002. DOI: 10.1002/nme.486.

[142] P. Betsch and P. Steinmann, "Frame-indifferent beam finite elements based upon the geometrically exact beam theory," *International Journal for Numerical Methods in Engineering*, vol. 54, no. 12, pp. 1775–1788, 2002. DOI: 10.1002/nme.487.

[143] S. R. Eugster, C. Hesch, P. Betsch, and C. Glocker, "Director-based beam finite elements relying on the geometrically exact beam theory formulated in skew coordinates," *International Journal for Numerical Methods in Engineering*, vol. 97, no. 2, pp. 111–129, 2014. DOI: 10.1002/nme.4586.

[144] G. Jelenić and M. A. Crisfield, "Geometrically exact 3D beam theory: Implementation of a strain-invariant finite element for statics and dynamics," *Computer Methods in Applied Mechanics and Engineering*, vol. 171, no. 1–2, pp. 141–171, 1999. DOI: 10.1016/S0045-7825(98)00249-7.

[145] F. A. McRobie and J. Lasenby, "Simo-Vu Quoc rods using Clifford algebra," *International Journal for Numerical Methods in Engineering*, vol. 45, no. 4, pp. 377–398, 1999. DOI: 10.1002/(SICI)1097-0207(19990610)45:4<377::AID-NME586>3.0.CO;2-P.

[146] S. Ghosh and D. Roy, "Consistent quaternion interpolation for objective finite element approximation of geometrically exact beam," *Computer Methods in Applied Mechanics and Engineering*, vol. 198, no. 3–4, pp. 555–571, 2008. DOI: 10.1016/j.cma.2008.09.004.

[147] E. Zupan, M. Saje, and D. Zupan, "The quaternion-based three-dimensional beam theory," *Computer Methods in Applied Mechanics and Engineering*, vol. 198, no. 49–52, pp. 3944–3956, 2009. DOI: 10.1016/j.cma.2009.09.002.

[148] H. Lang, J. Linn, and M. Arnold, "Multi-body dynamics simulation of geometrically exact Cosserat rods," *Multibody System Dynamics*, vol. 25, pp. 285–312, 2011. DOI: 10.1007/s11044-010-9223-x.

[149] V. Sonneville, A. Cardona, and O. Brüls, "Geometrically exact beam finite element formulated on the special euclidean group SE(3)," *Computer Methods in Applied Mechanics and Engineering*, vol. 268, pp. 451–474, 2014. DOI: 10.1016/j.cma.2013.10.008.

[150] J. Stuelpnagel, "On the Parametrization of the Three-Dimensional Rotation Group," *SIAM Review*, vol. 6, no. 4, pp. 422–430, 1964. DOI: 10.1137/1006093.

[151] G. R. Cowper, "The Shear Coefficient in Timoshenko's Beam Theory," *Journal of Applied Mechanics*, vol. 33, no. 2, pp. 335–340, 1966. DOI: 10.1115/1.3625046.

[152] J. R. Hutchinson, "Shear Coefficients for Timoshenko Beam Theory," *Journal of Applied Mechanics*, vol. 68, no. 1, pp. 87–92, 2001. DOI: 10.1115/1.1349417.

[153] A. Ibrahimbegovic and R. L. Taylor, "On the role of frame-invariance in structural mechanics models at finite rotations," *Computer Methods in Applied Mechanics and Engineering*, vol. 191, no. 45, pp. 5159–5176, 2002. DOI: 10.1016/S0045-7825(02)00442-5.

[154] I. Romero, "The interpolation of rotations and its application to finite element models of geometrically exact rods," *Computational Mechanics*, vol. 34, pp. 121–133, 2004. DOI: 10.1007/s00466-004-0559-z.

[155] E. Kreyszig, *Advanced Engineering Mathematics*, 9th. Hoboken, New Jersey: John Wiley & Sons, 2006.

[156] M. Ritto-Corrêa and D. Camotim, "Work-conjugacy between rotation-dependent moments and finite rotations," *International Journal of Solids and Structures*, vol. 40, no. 11, pp. 2851–2873, 2003. DOI: 10.1016/S0020-7683(03)00078-7.

[157] J. C. Simo and L. Vu-Quoc, "A three-dimensional finite-strain rod model. Part II: Computational aspects," *Computer Methods in Applied Mechanics and Engineering*, vol. 58, no. 1, pp. 79–116, 1986. DOI: 10.1016/0045-7825(86)90079-4.

[158] J. Mäkinen, "Total Lagrangian Reissner's geometrically exact beam element without singularities," *International Journal for Numerical Methods in Engineering*, vol. 70, no. 9, pp. 1009–1048, 2007. DOI: 10.1002/nme.1892.

[159] H. Zhong, R. Zhang, and N. Xiao, "A quaternion-based weak form quadrature element formulation for spatial geometrically exact beams," *Archive of Applied Mechanics*, vol. 84, pp. 1825–1840, 2014. DOI: 10.1007/s00419-014-0889-z.

[160] C. Bottasso, "A non-linear beam space-time finite element formulation using quaternion algebra: Interpolation of the Lagrange multipliers and the appearance of spurious modes," *Computational Mechanics*, vol. 10, pp. 359–368, 1992. DOI: 10.1007/BF00364256.

[161] E. Celledoni and N. Säfström, "A Hamiltonian and multi-Hamiltonian formulation of a rod model using quaternions," *Computer Methods in Applied Mechanics and Engineering*, vol. 199, no. 45–48, pp. 2813–2819, 2010. DOI: 10.1016/j.cma.2010.04.017.

[162] İ. Tunay, "Spatial Continuum Models of Rods Undergoing Large Deformation and Inflation," *IEEE Transactions on Robotics*, vol. 29, no. 2, pp. 297–307, 2013. DOI: 10.1109/TRO.2012.2232532.

[163] E. Zupan, M. Saje, and D. Zupan, "Dynamics of spatial beams in quaternion description based on the Newmark integration scheme," *Computational Mechanics*, vol. 51, pp. 47–64, 2013. DOI: 10.1007/s00466-012-0703-0.

[164] E. Zupan, M. Saje, and D. Zupan, "On a virtual work consistent three-dimensional Reissner-Simo beam formulation using the quaternion algebra," *Acta Mechanica*, vol. 224, pp. 1709–1729, 2013. DOI: 10.1007/s00707-013-0824-3.

[165] E. Zupan and D. Zupan, "On conservation of energy and kinematic compatibility in dynamics of nonlinear velocity-based three-dimensional beams," *Nonlinear Dynamics*, vol. 95, pp. 1379–1394, 2019. DOI: 10.1007/s11071-018-4634-y.

[166] D. Lolić, D. Zupan, and M. Brojan, "A consistent strain-based beam element with quaternion representation of rotations," *Computational Mechanics*, vol. 65, pp. 1397–1412, 2020. DOI: 10.1007/s00466-020-01826-0.

[167] H. Ren, W. Fan, and W. D. Zhu, "An Accurate and Robust Geometrically Exact Curved Beam Formulation for Multibody Dynamic Analysis," *Journal of Vibration and Acoustics*, vol. 140, no. 1, p. 011 012, 2018. DOI: 10.1115/1.4037513.

[168] S. P. Bhat and D. S. Bernstein, "A topological obstruction to continuous global stabilization of rotational motion and the unwinding phenomenon," *Systems & Control Letters*, vol. 39, no. 1, pp. 63–70, 2000. DOI: 10.1016/S0167-6911(99)00090-0.

[169] C. G. Mayhew, R. G. Sanfelice, and A. R. Teel, "Quaternion-Based Hybrid Control for Robust Global Attitude Tracking," *IEEE Transactions on Automatic Control*, vol. 56, no. 11, pp. 2555–2566, 2011. DOI: 10.1109/TAC.2011.2108490.

[170] K. Sherif, K. Nachbagauer, and W. Steiner, "On the rotational equations of motion in rigid body dynamics when using Euler parameters," *Nonlinear Dynamics*, vol. 81, pp. 343–352, 2015. DOI: 10.1007/s11071-015-1995-3.

[171] H. M. Hilber, T. J. R. Hughes, and R. L. Taylor, "Improved numerical dissipation for time integration algorithms in structural dynamics," *Earthquake Engineering & Structural Dynamics*, vol. 5, no. 3, pp. 283–292, 1977. DOI: 10.1002/eqe.4290050306.

[172] N. M. Newmark, "A Method of Computation for Structural Dynamics," *Journal of the Engineering Mechanics Division*, vol. 85, no. 3, pp. 67–94, 1959. DOI: 10.1061/JMCEA3.0000098.

[173] H. D. Hibbit, "Some follower forces and load stiffness," *International Journal for Numerical Methods in Engineering*, vol. 14, no. 6, pp. 937–941, 1979. DOI: 10.1002/nme.1620140613.

[174] T. Rahman and J. Valdman, "Fast MATLAB assembly of FEM matrices in 2D and 3D: Nodal elements," *Applied Mathematics and Computation*, vol. 219, no. 13, pp. 7151–7158, 2013. DOI: 10.1016/j.amc.2011.08.043.

[175] F. Cuvelier, C. Japhet, and G. Scarella, *An efficient way to perform the assembly of finite element matrices in Matlab and Octave*, https://arxiv.org/abs/1305.3122, arXiv:1305.3122. Accessed October 12, 2021, 2013.

[176] F. Cuvelier, C. Japhet, and G. Scarella, "An efficient way to assemble finite element matrices in vector languages," *BIT Numerical Mathematics*, vol. 56, pp. 833–864, 2016. DOI: 10.1007/s10543-015-0587-4.

[177] J. H. Manton, "A framework for generalising the Newton method and other iterative methods from Euclidean space to manifolds," *Numerische Mathematik*, vol. 129, pp. 91–125, 2015. DOI: 10.1007/s00211-014-0630-4.

[178] A. Cardona and M. Géradin, "Time integration of the equations of motion in mechanism analysis," *Computers & Structures*, vol. 33, no. 3, pp. 801–820, 1989. DOI: 10.1016/0045-7949(89)90255-1.

[179] C. L. Bottasso, D. Dopico, and L. Trainelli, "On the optimal scaling of index three DAEs in multibody dynamics," *Multibody System Dynamics*, vol. 19, pp. 3–20, 2008. DOI: 10.1007/s11044-007-9051-9.

[180] A. Cardona, M. Géradin, and D. B. Doan, "Rigid and flexible joint modelling in multibody dynamics using finite elements," *Computer Methods in Applied Mechanics and Engineering*, vol. 89, no. 1–3, pp. 395–418, 1991. DOI: 10.1016/0045-7825(91)90050-G.

[181] G. Jelenić and M. A. Crisfield, "Non-linear 'master-slave' relationships for joints in 3-D beams with large rotations," *Computer Methods in Applied Mechanics and Engineering*, vol. 135, no. 3–4, pp. 211–228, 1996. DOI: 10.1016/0045-7825(96)01017-1.

[182] A. Ibrahimbegović and S. Mamouri, "On rigid components and joint constraints in nonlinear dynamics of flexible multibody systems employing 3D geometrically exact beam model," *Computer Methods in Applied Mechanics and Engineering*, vol. 188, no. 4, pp. 805–831, 2000. DOI: 10.1016/S0045-7825(99)00363-1.

[183] N. Carpenter, T. Belytschko, and H. Stolarski, "Locking and shear scaling factors in C^0 bending elements," *Computers & Structures*, vol. 22, no. 1, pp. 39–52, 1986. DOI: 10.1016/0045-7949(86)90083-0.

[184] R. H. MacNeal, "A simple quadrilateral shell element," *Computers & Structures*, vol. 8, no. 2, pp. 175–183, 1978. DOI: 10.1016/0045-7949(78)90020-2.

[185] G. Garcea, G. A. Trunfio, and R. Casciaro, "Mixed formulation and locking in path-following nonlinear analysis," *Computer Methods in Applied Mechanics and Engineering*, vol. 165, no. 1–4, pp. 247–272, 1998. DOI: 10.1016/S0045-7825(98)00068-1.

[186] G. Garcea, G. Salerno, and R. Casciaro, "Extrapolation locking and its sanitization in Koiter's asymptotic analysis," *Computer Methods in Applied Mechanics and Engineering*, vol. 180, no. 1–2, pp. 137–167, 1999. DOI: 10.1016/S0045-7825(99)00053-5.

[187] D. Magisano, L. Leonetti, and G. Garcea, "How to improve efficiency and robustness of the Newton method in geometrically non-linear structural problem discretized via displacement-based finite elements," *Computer Methods in Applied Mechanics and Engineering*, vol. 313, pp. 986–1005, 2017. DOI: 10.1016/j.cma.2016.10.023.

[188] A. Ibrahimbegovic, "On finite element implementation of geometrically nonlinear Reissner's beam theory: Three-dimensional curved beam elements," *Computer Methods in Applied Mechanics and Engineering*, vol. 122, no. 1–2, pp. 11–26, 1995. DOI: 10.1016/0045-7825(95)00724-F.

[189] K.-J. Bathe and S. Bolourchi, "Large displacement analysis of three-dimensional beam structures," *International Journal for Numerical Methods in Engineering*, vol. 14, no. 7, pp. 961–986, 1979. DOI: 10.1002/nme.1620140703.

[190] I. Stewart, "Warning — handle with care!" *Nature*, vol. 355, pp. 16–17, 1992. DOI: 10.1038/355016a0.

[191] J. M. Sanz-Serna, "Symplectic integrators for Hamiltonian problems: An overview," *Acta Numerica*, vol. 1, pp. 243–286, 1992. DOI: 10.1017/S0962492900002282.

[192] D. Donnelly and E. Rogers, "Symplectic integrators: An introduction," *American Journal of Physics*, vol. 73, pp. 938–945, 2005. DOI: 10.1119/1.2034523.

[193] J. C. Simo and N. Tarnow, "The discrete energy-momentum method. Conserving algorithms for nonlinear elastodynamics," *Z angew Math Phys*, vol. 43, pp. 757–792, 1992. DOI: 10.1007/BF00913408.

[194] J. C. Simo and O. Gonzalez, "Assessment of Energy-Momentum and Symplectic Schemes for Stiff Dynamical Systems," in *Proceedings of the ASME Winter Annual Meeting*, New Orleans, Louisiana, 1993.

[195] J. C. Simo, N. Tarnow, and M. Doblare, "Non-linear dynamics of three-dimensional rods: Exact energy and momentum conserving algorithms," *International Journal for Numerical Methods in Engineering*, vol. 38, no. 9, pp. 1431–1473, 1995. DOI: 10.1002/nme.1620380903.

[196] O. Gonzalez and J. C. Simo, "On the stability of symplectic and energy-momentum algorithms for non-linear Hamiltonian systems with symmetry," *Computer Methods in Applied Mechanics and Engineering*, vol. 134, no. 3–4, pp. 197–222, 1996. DOI: 10.1016/0045-7825(96)01009-2.

[197] S. Leyendecker, J. E. Marsden, and M. Ortiz, "Variational integrators for constrained dynamical systems," *Z angew Math Mech*, vol. 88, no. 9, pp. 677–708, 2008. DOI: 10.1002/zamm.200700173.

[198] P. Betsch, C. Hesch, N. Sänger, and S. Uhlar, "Variational Integrators and Energy-Momentum Schemes for Flexible Multibody Dynamics," *Journal of Computational and Nonlinear Dynamics*, vol. 5, no. 3, p. 031 001, 2010. DOI: 10.1115/1.4001388.

[199] S. Ascher Uri M.and Reich, "On Some Difficulties in Integrating Highly Oscillatory Hamiltonian Systems," in *Computational Molecular Dynamics: Challenges, Methods, Ideas*, P. Deuflhard, J. Hermans, B. Leimkuhler, A. E. Mark, S. Reich, and R. D. Skeel, Eds., Berlin, Heidelberg: Springer, 1999, pp. 281–296. DOI: 10.1007/978-3-642-58360-5_15.

[200] M. Ortiz, "A note on energy conservation and stability of nonlinear time-stepping algorithms," *Computers & Structures*, vol. 24, no. 1, pp. 167–168, 1986. DOI: 10.1016/0045-7949(86)90346-9.

[201] C. Kane, J. E. Marsden, and M. Ortiz, "Symplectic-energy-momentum preserving variational integrators," *Journal of Mathematical Physics*, vol. 40, no. 7, pp. 3353–3371, 1999. DOI: 10.1063/1.532892.

[202] H. Sharma, M. Patil, and C. Woolsey, "Energy-preserving variational integrators for forced Lagrangian systems," *Communications in Nonlinear Science and Numerical Simulation*, vol. 64, pp. 159–177, 2018. DOI: 10.1016/j.cnsns.2018.04.015.

[203] F. Demoures, F. Gay-Balmaz, S. Leyendecker, S. Ober-Blöbaum, T. S. Ratiu, and Y. Weinand, "Discrete variational Lie group formulation of geometrically exact beam dynamics," *Numerische Mathematik*, vol. 130, pp. 73–123, 2015. DOI: 10.1007/s00211-014-0659-4.

[204] P. M. Almonacid, "Explicit symplectic momentum-conserving time-stepping scheme for the dynamics of geometrically exact rods," *Finite Elements in Analysis and Design*, vol. 96, pp. 11–22, 2015. DOI: 10.1016/j.finel.2014.10.003.

[205] Z. R. Manchester and M. A. Peck, "Quaternion Variational Integrators for Spacecraft Dynamics," *Journal of Guidance, Control, and Dynamics*, vol. 39, no. 1, pp. 69–76, 2016. DOI: 10.2514/1.G001176.

[206] A. Saccon, "Midpoint rule for variational integrators on Lie groups," *International Journal for Numerical Methods in Engineering*, vol. 78, no. 11, pp. 1345–1364, 2009. DOI: 10.1002/nme.2541.

[207] E. S. Gawlik, P. Mullen, D. Pavlov, J. E. Marsden, and M. Desbrun, "Geometric, variational discretization of continuum theories," *Physica D: Nonlinear Phenomena*, vol. 240, no. 21, pp. 1724–1760, 2011. DOI: 10.1016/j.physd.2011.07.011.

[208] P. Betsch, "The discrete null space method for the energy consistent integration of constrained mechanical systems: Part I: Holonomic constraints," *Computer Methods in Applied Mechanics and Engineering*, vol. 194, no. 50–52, pp. 5159–5190, 2005. DOI: 10.1016/j.cma.2005.01.004.

[209] P. Betsch and S. Leyendecker, "The discrete null space method for the energy consistent integration of constrained mechanical systems. Part II: Multibody dynamics," *International Journal for Numerical Methods in Engineering*, vol. 67, no. 4, pp. 499–552, 2006. DOI: 10.1002/nme.1639.

[210] S. Leyendecker, P. Betsch, and P. Steinmann, "The discrete null space method for the energy-consistent integration of constrained mechanical systems. Part III: Flexible multibody dynamics," *Multibody System Dynamics*, vol. 19, pp. 45–72, 2008. DOI: 10.1007/s11044-007-9056-4.

[211] J. C. Simo and L. Vu-Quoc, "On the dynamics in space of rods undergoing large motions — A geometrically exact approach," *Computer Methods in Applied Mechanics and Engineering*, vol. 66, no. 2, pp. 125–161, 1988. DOI: 10.1016/0045-7825(88)90073-4.

[212] G. Jelenić and M. A. Crisfield, "Interpolation of rotational variables in nonlinear dynamics of 3D beams," *International Journal for Numerical Methods in Engineering*, vol. 43, no. 7, pp. 1193–1222, 1998. DOI: 10.1002/(SICI)1097-0207(19981215)43:7<1193::AID-NME463>3.0.CO;2-P.

[213] H. Lang, S. Leyendecker, and J. Linn, "Numerical experiments for viscoelastic Cosserat rods with Kelvin-Voigt damping," in *ECCOMAS Multibody Dynamics 2013*, University of Zagreb, Croatia, 2013.

[214] A. Manan, R. Hodges, J. F. Sauder, S. Horst, M. Mobrem, A. Pedivellano, A. Wen, A. Truong, and S. Pellegrino, "Lightweight Composite Reflectarray that can be Flattened, Folded, and Coiled for Compact Stowage," in *AIAA SciTech Forum*, AIAA 2022-1886, San Diego, California, 2022. DOI: 10.2514/6.2022-1886.

[215] C. Leclerc and S. Pellegrino, "Nonlinear elastic buckling of ultra-thin coilable booms," *International Journal of Solids and Structures*, vol. 203, pp. 46–56, 2020. DOI: 10.1016/j.ijsolstr.2020.06.042.

[216] W. Luo and S. Pellegrino, "Propagating Instabilities in Coilable Booms," in *AIAA SciTech Forum*, AIAA 2022-0407, San Diego, California, 2022. DOI: 10.2514/6.2022-0407.

[217] F. Royer and S. Pellegrino, "Probing the Stability of Ladder-Type Coilable Space Structures," *AIAA Journal*, vol. 60, no. 4, pp. 2000–2012, 2022. DOI: 10.2514/1.J060820.

[218] E. E. Gdoutos, C. F. Sommer, A. Truong, A. Wen, A. Pedivellano, U. K. Ubamanyu, R. G. Madonna, and S. Pellegrino, "Development of the Deployable on-Orbit ultraLight Composite Experiment (DOLCE) for the Space Solar Power Project Demonstration Mission," in *AIAA SciTech Forum*, AIAA 2022-1266, San Diego, California, 2022. DOI: 10.2514/6.2022-1266.

[219] J. S. Przemieniecki, *Theory of Matrix Structural Analysis*. Mineola, New York: Dover Publications, Inc., 2012.

[220] H. Matsumoto, "Research on Solar Power Satellites and Microwave Power Transmission in Japan," *IEEE Microwave Magazine*, vol. 3, no. 4, pp. 36–45, 2002. DOI: 10.1109/MMW.2002.1145674.

[221] P. Jaffe and J. McSpadden, "Energy Conversion and Transmission Modules for Space Solar Power," *Proceedings of the IEEE*, vol. 101, no. 6, pp. 1424–1437, 2013. DOI: 10.1109/JPROC.2013.2252591.

[222] J. Hamley, J. Sankovic, J. R. Miller, P. Lynn, M. O'Neill, and S. Oleson, "Hall thruster direct drive demonstration," in *33rd Joint Propulsion Conference and Exhibit*, AIAA 1997-2787, Seattle, Washington, 1997. DOI: 10.2514/6.1997-2787.

[223] T. W. Kerslake and L. P. Gefert, "Solar Power System Analyses for Electric Propulsion Missions," *IEEE Aerospace and Electronic Systems Magazine*, vol. 16, no. 1, pp. 3–9, 2001. DOI: 10.1109/62.894171.

[224] J. T. Howell, M. J. O'Neill, and J. C. Mankins, "High-voltage array ground test for direct-drive solar electric propulsion," *Acta Astronautica*, vol. 59, no. 1–5, pp. 206–215, 2006. DOI: 10.1016/j.actaastro.2006.02.050.

[225] J. S. Snyder, J. R. Brophy, R. R. Hofer, D. M. Goebel, and I. Katz, "Experimental Investigation of a Direct-Drive Hall Thruster and Solar Array System," *Journal of Spacecraft and Rockets*, vol. 51, no. 1, pp. 360–373, 2014. DOI: 10.2514/1.A32479.

[226] T. W. Murphey and J. Banik, *Triangular rollable and collapsible boom*, US Patent 7,895,795, 2011.

[227] T. W. Murphey, D. Turse, and L. Adams, "TRAC Boom Structural Mechanics," in *AIAA SciTech Forum*, AIAA 2017-0171, Grapevine, Texas, 2017. DOI: 10.2514/6.2017-0171.

[228] M. A. Marshall, R. G. Madonna, and S. Pellegrino, "Investigation of Equatorial Medium Earth Orbits for Space Solar Power," *IEEE Transactions on Aerospace and Electronic Systems*, 2021. DOI: 10.1109/TAES.2021.3122790.

[229] S. Klarmann, F. Gruttmann, and S. Klinkel, "Homogenization assumptions for coupled multiscale analysis of structural elements: Beam kinematics," *Computational Mechanics*, vol. 65, pp. 635–661, 2020. DOI: 10.1007/s00466-019-01787-z.

[230] J. Jones and C. E. Cesnik, "Nonlinear Aeroelastic Analysis of the X-56 Multi-Utility Aeroelastic Demonstrator," in *AIAA SciTech Forum*, AIAA 2016-1799, San Diego, California, 2016. DOI: 10.2514/6.2016-1799.

[231] R. Palacios and A. Cea, "Nonlinear Modal Condensation of Large Finite Element Models: Application of Hodges's Intrinsic Theory," *AIAA Journal*, vol. 57, no. 10, pp. 4255–4268, 2019. DOI: 10.2514/1.J057556.

[232] C. Riso, D. Sanghi, C. E. Cesnik, F. Vetrano, and P. Teufel, "Parametric Roll Maneuverability Analysis of a High-Aspect-Ratio-Wing Civil Transport Aircraft," in *AIAA SciTech Forum*, AIAA 2020-1191, Orlando, Florida, 2020. DOI: 10.2514/6.2020-1191.

[233] D. Sarojini, M. Gupta, D. H. Hodges, and D. N. Mavris, "An Efficient Method to Dimensionally Reduce Aperiodic Inhomogeneous 3-D Structures to 1-D Beam-Like Structures," in *AIAA SciTech Forum*, AIAA 2020-0272, Orlando, Florida, 2020. DOI: 10.2514/6.2020-0272.

[234] C. Riso and C. E. Cesnik, "Low-Order Geometrically Nonlinear Aeroelastic Modeling and Analysis of the Pazy Wing Experiment," in *AIAA SciTech Forum*, AIAA 2022-2313, San Diego, California and Virtual, 2022. DOI: 10.2514/6.2022-2313.

[235] D. J. Malcolm and D. L. Laird, "Extraction of equivalent beam properties from blade models," *Wind Energy*, vol. 10, no. 2, pp. 135–157, 2007. DOI: 10.1002/we.213.

[236] A. K. Noor, "Continuum Modeling for Repetitive Lattice Structures," *Applied Mechanics Reviews*, vol. 41, no. 7, pp. 285–296, 1988. DOI: 10.1115/1.3151907.

[237] M. Webster and W. Vander Velde, "Modelling beam-like space trusses with nonlinear joints," in *32nd Structures, Structural Dynamics, and Materials Conference*, AIAA 91-1225-CP, Baltimore, Maryland, 1991. DOI: 10.2514/6.1991-1225.

[238] O. R. Stohlman, M. E. Zander, and J. M. Fernandez, "Characterization and modeling of large collapsible tubular mast booms," in *AIAA SciTech Forum*, AIAA 2021-0903, Virtual Event, 2021. DOI: 10.2514/6.2021-0903.

[239] Y. Wang, H. Yang, H. Guo, R. Liu, and K. Liu, "Equivalent Dynamic Model for Triangular Prism Mast with the Tape-Spring Hinges," *AIAA Journal*, vol. 59, no. 2, pp. 690–699, 2021. DOI: 10.2514/1.J059398.

[240] H. Chen, W. Yu, and M. Capellaro, "A critical assessment of computer tools for calculating composite wind turbine blade properties," *Wind Energy*, vol. 13, no. 6, pp. 497–516, 2010. DOI: 10.1002/we.372.

[241] W. Yu, V. V. Volovoi, D. H. Hodges, and X. Hong, "Validation of the Variational Asymptotic Beam Sectional Analysis," *AIAA Journal*, vol. 40, no. 10, pp. 2105–2112, 2002. DOI: 10.2514/2.1545.

[242] W. Yu and D. H. Hodges, "Generalized Timoshenko Theory of the Variational Asymptotic Beam Sectional Analysis," *Journal of the American Helicopter Society*, vol. 50, no. 1, pp. 46–55, 2005. DOI: 10.4050/1.3092842.

[243] Z. R. Manchester and M. A. Peck, "Recursive Inertia Estimation with Semidefinite Programming," in *AIAA SciTech Forum*, AIAA 2017-1902, Grapevine, Texas, 2017. DOI: 10.2514/6.2017-1902.

[244] M. C. Grant and S. P. Boyd, "Graph implementations for nonsmooth convex programs," in *Recent Advances in Learning and Control*, ser. Lecture Notes in Control and Information Sciences, V. D. Blondel, S. P. Boyd, and H. Kimura, Eds., http://stanford.edu/~boyd/graph_dcp.html,

Springer-Verlag Limited, 2008, pp. 95–110. DOI: 10.1007/978-1-84800-155-8_7.

[245] CVX Research, Inc., *CVX: Matlab Software for Disciplined Convex Programming, version 2.0*, http://cvxr.com/cvx, Aug. 2012.

[246] K. C. Toh, M. J. Todd, and R. H. Tütüncü, "SDPT3 — A Matlab software package for semidefinite programming, Version 1.3," *Optimization Methods and Software*, vol. 11, no. 1–4, pp. 545–581, 1999. DOI: 10.1080/10556789908805762.

[247] R. H. Tütüncü, K. C. Toh, and M. J. Todd, "Solving semidefinite-quadratic-linear programs using SDPT3," *Mathematical Programming*, vol. 95, no. 2, pp. 189–217, 2003. DOI: 10.1007/s10107-002-0347-5.

[248] G. Greschik and M. M. Mikulas, "Design Study of a Square Solar Sail Architecture," *Journal of Spacecraft and Rockets*, vol. 39, no. 5, pp. 653–661, 2002. DOI: 10.2514/2.3886.

[249] D. M. Murphy, M. E. McEachen, B. D. Macy, and J. L. Gaspar, "Demonstration of a 20-m Solar Sail System," in *46th AIAA/ASME/ASCE/AHS/ASC Structures, Structural Dynamics and Materials Conference*, AIAA 2005-2126, Austin, Texas, 2005. DOI: 10.2514/6.2005-2126.

[250] J.-S. Fuh and S.-Y. Chen, "Constraints of the Structural Modal Synthesis," *AIAA Journal*, vol. 24, no. 6, pp. 1045–1047, 1986. DOI: 10.2514/3.9387.

[251] S.-M. Yang, "Modal Analysis of Structures with Holonomic Constraints," *AIAA Journal*, vol. 30, no. 10, pp. 2526–2531, 1992. DOI: 10.2514/3.11256.

[252] A. A. Pantelous and A. Pirrotta, "Modal Analysis of Multi-Degrees-of-Freedom Systems with Singular Matrices: Analytical Dynamics Approach," *Journal of Engineering Mechanics*, vol. 143, no. 6, p. 06 017 005, 2017. DOI: 10.1061/(ASCE)EM.1943-7889.0001232.

[253] C. Hente, C. G. Gebhardt, D. Pache, and R. Rolfes, "On the modal analysis of nonlinear beam and shell structures with singular mass and stiffness matrices," *Thin-Walled Structures*, vol. 144, p. 106 310, 2019. DOI: 10.1016/j.tws.2019.106310.

[254] K.-J. Bathe, *Finite Element Procedures*, 2nd. Watertown, Massachusetts: K.J. Bathe, 2014.

[255] K.-J. Bathe, "The subspace iteration method – Revisited," *Computers & Structures*, vol. 126, pp. 177–183, 2013. DOI: 10.1016/j.compstruc.2012.06.002.

[256] L. Vu-Quoc and J. C. Simo, "Dynamics of Earth-Orbiting Flexible Satellites with Multibody Components," *Journal of Guidance, Control, and Dynamics*, vol. 10, no. 6, pp. 549–558, 1987. DOI: 10.2514/3.20255.

[257] Q. Li, Z. Deng, K. Zhang, and H. Huang, "Unified Modeling Method for Large Space Structures Using Absolute Nodal Coordinate," *AIAA Journal*, vol. 56, no. 10, pp. 4146–4157, 2018. DOI: 10.2514/1.J057117.

[258] G. A. Macala, "Design of the Reaction Wheel Attitude Control System for the Cassini Spacecraft," in *AAS/AIAA Space Flight Mechanics Meeting*, AAS 02-121, San Diego, California, 2002.

[259] M. Artola, A. Wynn, and R. Palacios, "Generalized Kelvin-Voigt Damping for Geometrically Nonlinear Beams," *AIAA Journal*, vol. 59, no. 1, pp. 356–365, 2021. DOI: 10.2514/1.J059767.

[260] M. Gupta, K. Sarkar, and D. H. Hodges, "Dynamic Analysis of Nonlinear Composite Beams with 3-D Structural Damping," in *AIAA SciTech Forum*, AIAA 2019-0211, San Diego, California, 2019. DOI: 10.2514/6.2019-0211.

[261] J. Linn, H. Lang, and A. Tuganov, "Geometrically exact Cosserat rods with Kelvin-Voigt type viscous damping," *Mechanical Sciences*, vol. 4, pp. 79–96, 2013. DOI: 10.5194/ms-4-79-2013.

[262] S. S. Antman, "Invariant Dissipative Mechanisms for the Spatial Motion of Rods Suggested by Artificial Viscosity," *Journal of Elasticity*, vol. 70, pp. 55–64, 2003. DOI: 10.1023/B:ELAS.0000005549.19254.17.

[263] F. Dewalque, P. Rochus, and O. Brüls, "Importance of structural damping in the dynamic analysis of compliant deployable structures," *Acta Astronautica*, vol. 111, pp. 323–333, 2015. DOI: 10.1016/j.actaastro.2015.03.003.

[264] M. Kobilarov, "Solvability of Geometric Integrators for Multi-body Systems," in *Multibody Dynamics: Computational Methods and Applications*, Z. Terze, Ed., Cham, Switzerland: Springer, 2014, ch. 7, pp. 145–174. DOI: 10.1007/978-3-319-07260-9_7.

[265] M. Sabatini, G. B. Palmerini, N. Leonangelia, and P. Gasbarri, "Analysis and experiments for delay compensation in attitude control of flexible spacecraft," *Acta Astronautica*, vol. 104, no. 1, pp. 276–292, 2014. DOI: 10.1016/j.actaastro.2014.08.006.

[266] S. Laurenzi, D. Rufo, M. Sabatini, P. Gasbarri, and G. B. Palmerini, "Characterization of deployable ultrathin composite boom for microsatellites excited by attitude maneuvers," *Composite Structures*, vol. 220, pp. 502–509, 2019. DOI: 10.1016/j.compstruct.2019.04.003.

[267] H. G. Matthies and M. Meyer, "Nonlinear Galerkin methods for the model reduction of nonlinear dynamical systems," *Computers & Structures*, vol. 81, no. 12, pp. 1277–1286, 2003. DOI: 10.1016/S0045-7949(03)00042-7.

[268] C. Farhat, P. Avery, T. Chapman, and J. Cortial, "Dimensional reduction of nonlinear finite element dynamic models with finite rotations and energy-based mesh sampling and weighting for computational efficiency," *International Journal for Numerical Methods in Engineering*, vol. 98, no. 9, pp. 625–662, 2014. DOI: 10.1002/nme.4668.

[269] M. S. Lake, L. D. Peterson, and M. B. Levine, "Rationale for Defining Structural Requirements for Large Space Telescopes," *Journal of Spacecraft and Rockets*, vol. 39, no. 5, pp. 674–681, 2002. DOI: 10.2514/2.3889.

[270] M. S. Lake, L. D. Peterson, and M. M. Mikulas, "Space Structures on the Back of an Envelope: John Hedgepeth's Design Approach," *Journal of Spacecraft and Rockets*, vol. 43, no. 6, pp. 1174–1183, 2006. DOI: 10.2514/1.21076.

Appendix A

HEDGEPETH'S SLEW MANEUVER REQUIREMENT

The goals of this appendix are twofold: (i) to derive the first-mode natural frequency requirement for a slewing flexible spacecraft presented in Hedgepeth [96], and (ii) to compare this requirement with the requirements from Sec. 3.4.3. The derivations in this appendix are based on the canonical flexible spacecraft model [Eq. (3.1)] with the notation and conventions for attitude slew maneuvers from Sec. 3.4. For these reasons, this appendix assumes familiarity with the material from Chapter 3.

Per [96], the relationship between the fixed-base natural frequency f_n (in hertz) and the peak slew acceleration $\ddot{\theta}$ for the canonical flexible spacecraft is

$$f_n = \sqrt{\frac{1}{2\pi^2}\frac{J_2/J_1}{1+J_2/J_1}\frac{\ddot{\theta}}{|\theta_{1,f}|}} \tag{A.1}$$

where J_1 and J_2 respectively denote the rotational inertias of the "bus" and flexible "appendage" and $|\theta_{1,f}|$ is the amplitude of the residual angular position disturbance on the bus due to the motion of the appendage. Equation (A.1) is derived from the undamped solution to Eq. (3.1) with the initial conditions

$$\theta_1(0) = 0, \tag{A.2}$$

$$\dot{\theta}_1(0) = 0, \tag{A.3}$$

$$\theta_2(0) = \ddot{\theta}\big/\left(4\pi^2 f_n^2\right), \tag{A.4}$$

$$\dot{\theta}_2(0) = 0. \tag{A.5}$$

These initial conditions correspond to a spacecraft initially at rest with an elastically deformed appendage. The initial elastic deformation $\theta_2(0)$ is the peak quasi-static deformation of the appendage due to an inertial load with acceleration $\ddot{\theta}$; for a general derivation of Eq. (A.4) for a structure with an arbitrary number of modes, see [269, 270]. Importantly, Eq. (A.1) does not explicitly account for the dynamics of the slew maneuver. Instead, it assumes that the residual bus motion $\theta_1(t)$ after the slew is entirely due to the maximum deflection of the appendage during the slew. The derivation of Eq. (A.1) does not explicitly consider the appendage motion $\theta_2(t)$. Hence, only the solution to Eq. (3.1) for $\theta_1(t)$ appears in what follows.

The solution to Eq. (3.1) for the bus motion $\theta_1(t)$ with the initial conditions [Eqs. (A.2)–(A.5)] is

$$\theta_1(t) = \frac{J_2/J_1}{1 + J_2/J_1} \frac{\ddot{\theta}}{4\pi^2 f_n^2} \left[1 - \cos\left(2\pi\sqrt{1 + J_2/J_1}\ f_n t\right)\right]. \tag{A.6}$$

The amplitude of $\theta_1(t)$ then follows as

$$|\theta_{1,f}| = \frac{J_2/J_1}{1 + J_2/J_1} \frac{\ddot{\theta}}{2\pi^2 f_n^2} \tag{A.7}$$

where the subscript f emphasizes that the motion of the spacecraft bus is entirely due to the flexibility of the appendage. Solving Eq. (A.7) for f_n results in Hedgepeth's requirement [Eq. (A.1)]. Equation (A.1) defines the minimum natural frequency f_n such that the maximum disturbance on the spacecraft bus due to an initial static appendage deflection $\theta_2(0)$ is guaranteed to be less than or equal to $|\theta_{1,f}|$.

The slew maneuver requirements developed in Chapter 3 are based on the amplitude of the residual angular velocity $|\dot{\theta}_{1,f}|$, not $|\theta_{1,f}|$. To facilitate comparisons with Chapter 3, Hedgepeth's approach is also used to derive an expression analogous to Eq. (A.1) in terms of $|\dot{\theta}_{1,f}|$. The time derivative of $\theta_1(t)$ is

$$\dot{\theta}_1(t) = \frac{J_2/J_1}{\sqrt{1 + J_2/J_1}} \frac{\ddot{\theta}}{2\pi f_n} \sin\left(2\pi\sqrt{1 + J_2/J_1}\ f_n t\right), \tag{A.8}$$

from which it follows that the amplitude of $\dot{\theta}_1(t)$ is

$$|\dot{\theta}_{1,f}| = \frac{J_2/J_1}{\sqrt{1 + J_2/J_1}} \frac{\ddot{\theta}}{2\pi f_n}. \tag{A.9}$$

Solving Eq. (A.9) for f_n then yields

$$f_n = \frac{1}{2\pi} \frac{J_2/J_1}{\sqrt{1 + J_2/J_1}} \frac{\ddot{\theta}}{|\dot{\theta}_{1,f}|} \tag{A.10}$$

which is analogous to Eq. (A.1). Of note is that in Eq. (A.1), f_n is proportional to $\ddot{\theta}^{1/2}$, whereas here, f_n is proportional to $\ddot{\theta}$.

For a bang-bang slew (see Fig. 3.2), the peak acceleration for a maneuver through an angle $\Delta\theta$ in time T is $\ddot{\theta} = 4\Delta\theta/T^2$ [Eq. (3.50)]. It follows that for a bang-bang slew, Eq. (A.10) takes the form

$$\frac{|\dot{\theta}_{1,f}|}{(\Delta\theta/T)} = \frac{2}{\pi} \frac{J_2/J_1}{\sqrt{1 + J_2/J_1}} \left(\frac{T}{T_n}\right)^{-1} \tag{A.11}$$

where $T_n = 1/f_n$ is the natural period. Comparing Eq. (A.11) with the analogous expression for a bang-bang slew from Chapter 3 [Eq. (3.54)] then reveals that

$$\frac{T^H}{T^{BB}} = \frac{1}{2} \tag{A.12}$$

where the superscripts H and BB denote the slew times from Eqs. (A.11) and (3.54), respectively. Thus, given a requirement on $|\dot{\theta}_{1,f}|$, Hedgepeth's approach predicts a slew time two times faster for a bang-bang slew than the analysis from Chapter 3. Said another way, for a fixed slew time T, Hedgepeth's approach underpredicts $|\dot{\theta}_{1,f}|$ by a factor of four. The takeaway is that it is insufficient to simply consider the peak quasi-static inertial loads during the definition of structure-based slew maneuver requirements. Instead, any analysis of these requirements must take into account both the modal properties of the structure and the slew maneuver profile.

Appendix B

SPHERICAL LINEAR INTERPOLATION

The purpose of this appendix is to catalog identities related to the spherical linear interpolation (slerp) [133, 140] of the quaternion degrees of freedom in the finite element formulations from Chapters 5 and 6. All the derivatives and Jacobians in this appendix are straightforward (albeit often tedious) to derive, and hence, are stated without proof. They likewise assume that $\theta \leq \pi/2$, i.e.., the interpolation traces the shortest arc between two quaternions $\mathbf{p}_1$ and $\mathbf{p}_2$. Due to its geometrical interpretation on the unit three-sphere, slerp and the formulas compiled here are independent of the chosen quaternion conventions.

The set of unit quaternions is equivalent to the unit three-sphere. The simplest interpolation on the unit three-sphere is along the arc of a great circle (a geodesic) at a constant angular rate. This corresponds to linear interpolation on the unit three-sphere, meaning it is the quaternion analogue of linear interpolation in Euclidean space. Hence, it is referred to as spherical linear interpolation. The slerp formula reads [133, 140]

$$\mathbf{p}(\sigma) = N_1(\sigma)\mathbf{p}_1 + N_2(\sigma)\mathbf{p}_2 \tag{B.1}$$

where $\sigma \in [0, 1]$ parameterizes the arc of the great circle, $\mathbf{p}(\sigma)$ is the interpolated quaternion, and $N_1(\sigma)$ and $N_2(\sigma)$ are given by

$$N_1(\sigma) = \sin\left((1-\sigma)\theta\right)\csc(\theta), \tag{B.2}$$

$$N_2(\sigma) = \sin\left(\sigma\theta\right)\csc(\theta). \tag{B.3}$$

The parameter θ is the angle between $\mathbf{p}_1$ and $\mathbf{p}_2$ on the unit three-sphere, i.e.,

$$\cos(\theta) = \mathbf{p}_2^T\mathbf{p}_1. \tag{B.4}$$

A detailed derivation of slerp is outside the scope of this appendix; instead, interested readers are referred to the existing literature, e.g., [133, 140] and the references therein. For the initially straight beam finite elements studied in Chapters 5 and 6, $\mathbf{p}_1$ and $\mathbf{p}_2$ define the element's nodal orientations and $\sigma = s/\ell$ where s is the arc length along the element's longitudinal axis of length ℓ.

For plane rotations, slerp is equivalent to linear interpolation. This is straightforward to show by substituting

$$\mathbf{p}_1 = (0, 0, 0, 1)^T,$$
$$\mathbf{p}_2 = (0, 0, \sin(\phi/2), \cos(\phi/2))^T$$

into Eq. (B.1) and simplifying, which corresponds to the interpolation of the relative rotation ϕ between the two quaternions. Similarly, in the limit as $\theta \to 0$,

$$\lim_{\theta \to 0} N_1(\sigma) = 1 - \sigma, \tag{B.5}$$
$$\lim_{\theta \to 0} N_2(\sigma) = \sigma. \tag{B.6}$$

Thus, slerp reduces to standard linear interpolation when $\theta = 0$, as occurs, e.g., in the initial (undeformed) configuration of an initially straight beam.

In what follows, gradients are expressed using the numerator-layout (Jacobian) convention; i.e., for a function $f(\mathbf{x}) : \mathbb{R}^n \to \mathbb{R}$, $\partial f/\partial \mathbf{x} \in \mathbb{R}^{1\times n}$. The symbol $\mathbf{I}_{n\times n}$ denotes the identity matrix in $\mathbb{R}^{n\times n}$. Dot and prime notation are respectively used to denote derivatives with respect to time t and space σ. Since spatial derivatives are evaluated with respect to σ, not s, the corresponding derivatives with respect to s can be recovered from the chain rule, i.e.,

$$\frac{\partial}{\partial s} = \frac{\partial}{\partial \sigma}\frac{\partial \sigma}{\partial s} = \frac{1}{\ell}\frac{\partial}{\partial \sigma}. \tag{B.7}$$

To simplify notation, explicit dependencies on σ are dropped in what follows.

B.1 Spatial Derivative

The spatial derivative of Eq. (B.1) is

$$\mathbf{p}' = N_1'\mathbf{p}_1 + N_2'\mathbf{p}_2 \tag{B.8}$$

where $N_1' = -\theta \csc(\theta) \cos((1-\sigma)\theta)$ and $N_2' = \theta \csc(\theta) \cos(\sigma\theta)$.

B.2 Temporal Derivatives

The temporal derivatives of Eq. (B.1) are

$$\dot{\mathbf{p}} = \dot{N}_1\mathbf{p}_1 + N_1\dot{\mathbf{p}}_1 + \dot{N}_2\mathbf{p}_2 + N_2\dot{\mathbf{p}}_2, \tag{B.9}$$
$$\ddot{\mathbf{p}} = \ddot{N}_1\mathbf{p}_1 + 2\dot{N}_1\dot{\mathbf{p}}_1 + N_1\ddot{\mathbf{p}}_1 + \ddot{N}_2\mathbf{p}_2 + 2\dot{N}_2\dot{\mathbf{p}}_2 + N_2\ddot{\mathbf{p}}_2 \tag{B.10}$$

where

$$\dot{N}_i = \dot{\theta}\frac{\partial N_i}{\partial \theta}, \tag{B.11}$$

$$\ddot{N}_i = \ddot{\theta}\frac{\partial N_i}{\partial \theta} + \dot{\theta}^2\frac{\partial^2 N_i}{\partial \theta^2} \tag{B.12}$$

for $i = 1,\ 2$ and the temporal derivatives of θ are given by

$$\dot{\theta} = -\csc(\theta)\left(\dot{\mathbf{p}}_2^T\mathbf{p}_1 + \mathbf{p}_2^T\dot{\mathbf{p}}_1\right), \tag{B.13}$$

$$\ddot{\theta} = -\cot(\theta)\dot{\theta}^2 - \csc(\theta)\left(\ddot{\mathbf{p}}_2^T\mathbf{p}_1 + 2\dot{\mathbf{p}}_2^T\dot{\mathbf{p}}_1 + \mathbf{p}_2^T\ddot{\mathbf{p}}_1\right). \tag{B.14}$$

Likewise, the derivatives of N_1 and N_2 with respect to θ are

$$\frac{\partial N_i}{\partial \theta} = \csc(\theta)\left(\sigma_i\cos\left(\sigma_i\theta\right) - \cot(\theta)\sin\left(\sigma_i\theta\right)\right), \tag{B.15}$$

$$\frac{\partial^2 N_i}{\partial \theta^2} = \csc(\theta)\left(\left(\cot^2(\theta) + \csc^2(\theta) - \sigma_i^2\right)\sin\left(\sigma_i\theta\right) - 2\sigma_i\cot(\theta)\cos\left(\sigma_i\theta\right)\right) \tag{B.16}$$

which hold for $i = 1,\ 2$. Here, $\sigma_1 = 1 - \sigma$ and $\sigma_2 = \sigma$.

B.3 Jacobians

The following Jacobians appear in the linearization of slerp and its derivatives:

$$\frac{\partial \mathbf{p}}{\partial \mathbf{p}_1} = \frac{\partial \dot{\mathbf{p}}}{\partial \dot{\mathbf{p}}_1} = \frac{\partial \ddot{\mathbf{p}}}{\partial \ddot{\mathbf{p}}_1} = \mathbf{p}_1\frac{\partial N_1}{\partial \mathbf{p}_1} + \mathbf{p}_2\frac{\partial N_2}{\partial \mathbf{p}_1} + N_1\mathbf{I}_{4\times 4}, \tag{B.17}$$

$$\frac{\partial \mathbf{p}}{\partial \mathbf{p}_2} = \frac{\partial \dot{\mathbf{p}}}{\partial \dot{\mathbf{p}}_2} = \frac{\partial \ddot{\mathbf{p}}}{\partial \ddot{\mathbf{p}}_2} = \mathbf{p}_1\frac{\partial N_1}{\partial \mathbf{p}_2} + \mathbf{p}_2\frac{\partial N_2}{\partial \mathbf{p}_2} + N_2\mathbf{I}_{4\times 4}, \tag{B.18}$$

$$\frac{\partial \mathbf{p}'}{\partial \mathbf{p}_1} = \mathbf{p}_1\frac{\partial N_1'}{\partial \mathbf{p}_1} + \mathbf{p}_2\frac{\partial N_2'}{\partial \mathbf{p}_1} + N_1'\mathbf{I}_{4\times 4}, \tag{B.19}$$

$$\frac{\partial \mathbf{p}'}{\partial \mathbf{p}_2} = \mathbf{p}_1\frac{\partial N_1'}{\partial \mathbf{p}_2} + \mathbf{p}_2\frac{\partial N_2'}{\partial \mathbf{p}_2} + N_2'\mathbf{I}_{4\times 4} \tag{B.20}$$

where the corresponding Jacobians of N_1 and N_2 are

$$\frac{\partial N_1}{\partial \mathbf{p}_1} = \frac{\partial \dot{N}_1}{\partial \dot{\mathbf{p}}_1} = \frac{\partial \ddot{N}_1}{\partial \ddot{\mathbf{p}}_1} = -\csc(\theta)\frac{\partial N_1}{\partial \theta}\mathbf{p}_2^T, \tag{B.21}$$

$$\frac{\partial N_1}{\partial \mathbf{p}_2} = \frac{\partial \dot{N}_1}{\partial \dot{\mathbf{p}}_2} = \frac{\partial \ddot{N}_1}{\partial \ddot{\mathbf{p}}_2} = -\csc(\theta)\frac{\partial N_1}{\partial \theta}\mathbf{p}_1^T, \tag{B.22}$$

$$\frac{\partial N_2}{\partial \mathbf{p}_1} = \frac{\partial \dot{N}_2}{\partial \dot{\mathbf{p}}_1} = \frac{\partial \ddot{N}_2}{\partial \ddot{\mathbf{p}}_1} = -\csc(\theta)\frac{\partial N_2}{\partial \theta}\mathbf{p}_2^T, \tag{B.23}$$

$$\frac{\partial N_2}{\partial \mathbf{p}_2} = \frac{\partial \dot{N}_2}{\partial \dot{\mathbf{p}}_2} = \frac{\partial \ddot{N}_2}{\partial \ddot{\mathbf{p}}_2} = -\csc(\theta)\frac{\partial N_2}{\partial \theta}\mathbf{p}_1^T. \tag{B.24}$$

Similarly, the Jacobians of N_1' and N_2' are

$$\frac{\partial N_1'}{\partial \mathbf{p}_1} = -\csc(\theta)\frac{\partial N_1'}{\partial \theta}\mathbf{p}_2^T, \tag{B.25}$$

$$\frac{\partial N_1'}{\partial \mathbf{p}_2} = -\csc(\theta)\frac{\partial N_1'}{\partial \theta}\mathbf{p}_1^T, \tag{B.26}$$

$$\frac{\partial N_2'}{\partial \mathbf{p}_1} = -\csc(\theta)\frac{\partial N_2'}{\partial \theta}\mathbf{p}_2^T, \tag{B.27}$$

$$\frac{\partial N_2'}{\partial \mathbf{p}_2} = -\csc(\theta)\frac{\partial N_2'}{\partial \theta}\mathbf{p}_1^T \tag{B.28}$$

where

$$\frac{\partial N_i'}{\partial \theta} = (-1)^{i-1}\csc(\theta)\left((\theta\cot(\theta) - 1)\cos(\sigma_i\theta) + \sigma_i\theta\sin(\sigma_i\theta)\right) \tag{B.29}$$

for $i = 1,\ 2$.

Appendix C

GEOMETRIC TANGENT STIFFNESS MATRIX

This appendix derives the geometric tangent stiffness matrix $\mathbf{K}_G$ for the geometrically exact beam finite element developed in Chapter 5. The geometric tangent stiffness matrix is defined by Eq. (5.56) (reproduced below):

$$\mathbf{K}_G = \int_0^\ell \frac{\partial \mathbf{B}^T}{\partial \mathbf{g}} \mathbf{S}^h \, \mathrm{d}s \tag{C.1}$$

where $\mathbf{B}$ is the discrete strain gradient matrix [Eq. (5.37)] and $\mathbf{S}^h$ contains the discrete internal force and moment resultants. Equivalently, since $\mathbf{S}^T = \left(\mathbf{N}^T, \mathbf{M}^T\right)$,

$$\mathbf{K}_G = \int_0^\ell \frac{\partial \mathbf{B}^T}{\partial \mathbf{g}} \begin{bmatrix} \mathbf{N}^h \\ \mathbf{M}^h \end{bmatrix} \mathrm{d}s. \tag{C.2}$$

To simplify notation, the superscript h is dropped in what follows, i.e., $\mathbf{N}^h \rightarrow \mathbf{N}$ and $\mathbf{M}^h \rightarrow \mathbf{M}$.

The quantity $\partial \mathbf{B}^T / \partial \mathbf{g}$ is a third-order tensor. To simplify its evaluation, a matrix $\mathbf{W}$ is defined such that

$$\mathbf{W} = \frac{\partial \mathbf{B}^T}{\partial \mathbf{g}} \begin{bmatrix} \mathbf{N} \\ \mathbf{M} \end{bmatrix} = \frac{\partial}{\partial \mathbf{g}} \left(\mathbf{B}^T \begin{bmatrix} \mathbf{N} \\ \mathbf{M} \end{bmatrix} \right) \tag{C.3}$$

where $\mathbf{N}$ and $\mathbf{M}$ are treated as constants with respect to the differentiation. Hence,

$$\mathbf{K}_G = \int_0^\ell \mathbf{W} \, \mathrm{d}s. \tag{C.4}$$

Substituting $\mathbf{B}$ [Eq. (5.37)] into Eq. (C.3) then gives

$$\mathbf{W} = \frac{\partial}{\partial \mathbf{g}} \left(\mathbf{P}^T \begin{bmatrix} \boldsymbol{\Lambda}(\mathbf{p})\mathbf{N} \\ 2\mathbf{G}(\mathbf{p})\mathbf{M} \\ -2\mathbf{L}(\mathbf{T}\mathbf{x}')\mathbf{G}(\mathbf{p})\mathbf{N} - 2\mathbf{G}(\mathbf{p}')\mathbf{M} \end{bmatrix} \right) \tag{C.5}$$

where the strain interpolation matrix $\mathbf{P}$ [Eq. (5.34)] depends on $\mathbf{g}$ through the slerp shape functions. Assuming $\partial \mathbf{P}^T / \partial \mathbf{g}$ is negligible, i.e., that the geometric stiffness is insensitive to small changes in $\theta = \cos^{-1}\left(\mathbf{p}_1^T \mathbf{p}_2\right)$, then $\mathbf{W}$ becomes

$$\mathbf{W} = \mathbf{P}^T \frac{\partial}{\partial \mathbf{g}} \begin{bmatrix} \boldsymbol{\Lambda}(\mathbf{p})\mathbf{N} \\ 2\mathbf{G}(\mathbf{p})\mathbf{M} \\ -2\mathbf{L}(\mathbf{T}\mathbf{x}')\mathbf{G}(\mathbf{p})\mathbf{N} - 2\mathbf{G}(\mathbf{p}')\mathbf{M} \end{bmatrix}. \tag{C.6}$$

Further simplifications of $\mathbf{W}$ require the following identities involving a quaternion $\mathbf{p} \in \mathbb{H}_1$ and a vector $\mathbf{v} \in \mathbb{R}^3$:

$$\mathbf{R}(\mathbf{Tv}) = -\mathbf{R}^T(\mathbf{Tv}), \tag{C.7}$$

$$\mathbf{G}(\mathbf{p})\mathbf{v} = \mathbf{R}(\mathbf{Tv})\mathbf{p}, \tag{C.8}$$

$$\mathbf{H}^T(\mathbf{p})\mathbf{v} = \mathbf{L}(\mathbf{Tv})\mathbf{p}, \tag{C.9}$$

$$\mathbf{L}(\mathbf{Tv}_1)\mathbf{G}(\mathbf{p})\mathbf{v}_2 = \mathbf{R}(\mathbf{Tv}_2)\mathbf{H}^T(\mathbf{p})\mathbf{v}_1, \tag{C.10}$$

$$\delta(\mathbf{\Lambda}(\mathbf{p})\mathbf{v}) = -2\mathbf{H}^T(\mathbf{p})\mathbf{R}^T(\mathbf{Tv})\delta\mathbf{p}. \tag{C.11}$$

From these identities, it is straightforward to derive the variations

$$\delta\left(\mathbf{\Lambda}(\mathbf{p})\mathbf{N}\right) = 2\mathbf{H}^T(\mathbf{p})\mathbf{R}(\mathbf{TN})\delta\mathbf{p}, \tag{C.12}$$

$$\delta\left(\mathbf{G}(\mathbf{p})\mathbf{M}\right) = \mathbf{R}(\mathbf{TM})\delta\mathbf{p}, \tag{C.13}$$

$$\delta\left(\mathbf{L}(\mathbf{Tx}')\mathbf{G}(\mathbf{p})\mathbf{N}\right) = -\mathbf{R}^T(\mathbf{TN})\mathbf{H}^T(\mathbf{p})\delta\mathbf{x}' - \mathbf{R}^T(\mathbf{TN})\mathbf{L}(\mathbf{Tx}')\delta\mathbf{p}, \tag{C.14}$$

$$\delta\left(\mathbf{G}(\mathbf{p}')\mathbf{M}\right) = -\mathbf{R}^T(\mathbf{TM})\delta\mathbf{p}'. \tag{C.15}$$

Using these variations and Eq. (5.33) then results in the following expression for $\mathbf{W}$:

$$\mathbf{W} = 2\mathbf{P}^T \begin{bmatrix} \mathbf{0}_{3\times3} & \mathbf{0}_{3\times4} & \mathbf{H}^T(\mathbf{p})\mathbf{R}(\mathbf{TN}) \\ \mathbf{0}_{4\times3} & \mathbf{0}_{4\times4} & \mathbf{R}(\mathbf{TM}) \\ \mathbf{R}^T(\mathbf{TN})\mathbf{H}^T(\mathbf{p}) & \mathbf{R}^T(\mathbf{TM}) & \mathbf{R}^T(\mathbf{TN})\mathbf{L}(\mathbf{Tx}') \end{bmatrix} \mathbf{P}. \tag{C.16}$$

Since $\mathbf{R}^T(\mathbf{Tv}_1)\mathbf{L}(\mathbf{Tv}_2) = \mathbf{L}^T(\mathbf{Tv}_2)\mathbf{R}(\mathbf{Tv}_1)$ for all $\mathbf{v}_1, \mathbf{v}_2 \in \mathbb{R}^3$, $\mathbf{W}$ is symmetric. Thus, $\mathbf{K}_G$ is also symmetric.